

# **Bio-tribology of Total Disc Replacements of the Lumbar Spine**

Philip James Hyde

Submitted in accordance with the requirements for the degree of Doctor of  
Philosophy

The University of Leeds  
School of Mechanical Engineering

September, 2012

The candidate confirms that the work submitted is his own, except where work which has formed part of jointly-authored publications has been included. The contribution of the candidate and the other authors to this work has been explicitly indicated below. The candidate confirms that appropriate credit has been given within the thesis where reference has been made to the work of others.

Results from Chapter 3 were published as jointly authored journal publications. Some experiments were assisted by undergraduate students as part of their level three project reports: Tristan Phillips – motion track component drawings and rotational Charité data; Zhian Tan – some motion track results (Prodisc) and ‘Callaghan’ data; Alex Doddy – some motion track results (Charité). Theoretical results for the Prodisc motion tracks were computed by Dr Feng Liu. Pin-on-plate cross shear calculations were computed by Dr Abdellatif Abdelgaied.

This copy has been supplied on the understanding that it is copyright material and that no quotation from the thesis may be published without proper acknowledgement.

The right of Philip James Hyde to be identified as Author of this work has been asserted by him in accordance with the Copyright, Designs and Patents Act 1988.

© 2012 The University of Leeds and Philip James Hyde

## **Acknowledgements**

I would like to thank my supervisors, Professor Richard Hall and Professor John Fisher CBE, for giving me the opportunity to work in a world-class institution and for their guidance and support. This research was supported by the EPSRC and a NIH grant, I acknowledge the great opportunity afforded by this.

It has been a pleasure to work in the company of all in room 442C plus many others in the school of mechanical engineering. I can't list everyone who has given me help or advice, but Dr Claire Brockett is someone who has given particularly sound advice when needed; Dr Rachel Vicars helped me to get settled into lab work and explained the spine simulator's foibles; Dr Abdul Abdelgaied and Dr Feng Liu's computational knowledge was also much appreciated; Mazen Al-Hajaar's hip wear advice was gratefully received; and Mr Adrian Eagles M.Phil is thanked for sharing his expert surface profilometry knowledge. I would also like to acknowledge the late J E Gordon, for writing such brilliantly accessible engineering books.

To anyone else who has ever given me a helping hand I thank you most sincerely and hope to be able to repay the favour someday.

Thank you to my mother in supporting my studies and also my late father (Alan Hyde) for answering all my childhood 'how does it work' questions so well.

I am eternally grateful my wife (Mona Manan) and my step-daughter (Rowan) for their support.

## **Abstract**

Total disc replacements (TDR) of the lumbar spine offer a direct replacement to the natural intervertebral disc (IVD). Possible indications for replacement would typically include severe discogenic pain that has not responded to conservative treatment. Until relatively recently the preferred surgical intervention was removal of the pain-causing disc and creation of a bony mass between the adjacent vertebrae – known as a fusion. Concerns over removing motion at one level and the effect of compensated motion at other levels was a driver in the development of motion preservation surgery using TDR. Most popular designs rely on technology directly translated from total hip replacement (THR) and total knee replacement (TKR). However, the design rationales used vary considerably and the operating regime in the spine is different to other joints which work by articulation in synovial fluid. Furthermore, the successes of the original generation of THRs were countered by late failures due to loosening (osteolysis); a result of adverse tissue reactions to particulate wear debris. Therefore pre-clinical simulation using a stratified approach (including parametric studies) should be a goal in development of both better understanding of present TDR performance and in aiding in design of the next generation devices and avoiding sub-optimal design.

The aim of this thesis was to examine performance of two different devices, representing opposing design rationales, and use parametric studies based on the international testing standard (ISO18192-1) to assess performance characteristics. The TDRs were challenged by altering the phasing, loading and amplitude of the cyclical input motions. Further to this the effects of short strokes encountered in spinal motions were investigated. To compliment these results, experiments investigating contact pressure, motion paths, friction and lubrication were completed.

The resultant rates of wear (in mg/million cycles (mg/MC)  $\pm$  standard deviation) of Prodisc and Charité TDR devices were comparable, demonstrating wear rates of  $16.1 \pm 1.4$  mg/MC and  $13.4 \pm 2.0$  mg/MC respectively for the standard ISO study. The following ISO-based experiments highlighted the impact that small perturbations of the testing regime can have. Surface profilometry and secondary

electron microscopy demonstrated a wear phenomenon not observed *in vivo*, where micron-sized particles of ultra-high molecular weight polyethylene (UHMWPE) appeared to be re-attached to the surface. Edge-effects on the UHMWPE surfaces adjacent to the radii of curvature of the fillets of the metallic endplates produced burnishing and deformation which were quantitatively recorded in terms of roughness parameters. Motion tracking of TDR components highlighted the similarity between ISO motions and *in vivo* based kinematics from Callaghan et al. [1]. Frictional characteristics were studied and found to be in the range 0.05-0.09 which is similar to those reported in MoP hips. Lubrication was theoretically studied and found to be boundary in nature for contemporary TDR designs.

Neither TDR design excelled over the other when tested under the parametric studies described here. Rates of wear, though lower than historic THR and TKR wear rates, were high enough to raise the concern about possible future osteolysis development. Even small amounts of cross shear (ratio 0.03) were enough to cause significant mass loss and hence debris production. Reduced loading did not reduce the wear substantially and may indicate that patient weight will not affect TDR performance in terms of rates of wear alone. Surface topography was monitored for the two devices and input kinetics. This highlighted the correlation between axial loading and roughening of the pole area of the PE components; caused by particles of re-attached debris at the bearing surface. Edge-effects were measured in terms of surface features around the PE bearing perimeter and related to the higher than expected contact stress in this region. Frictional torques were investigated and found to be in the region of 1.5 Nm. This is not of concern per se, however, the artificial TDR and the natural IVD differ in two key respects: 1) in the articulating TDR the resistance to rotation is reasonably constant; 2) is not proportional to angle of flexion. The *in vivo* effects of this difference are as yet unknown. In conclusion, the bio-tribological operating regime is harsh and therefore future bearing design should consider how to be more resilient to this at the design stage.

# Contents

<b>Acknowledgements .....</b>	<b>i</b>
<b>Abstract .....</b>	<b>ii</b>
<b>Contents.....</b>	<b>iv</b>
<b>List of Figures .....</b>	<b>vii</b>
<b>List of Tables.....</b>	<b>xii</b>
<b>Nomenclature .....</b>	<b>xiii</b>
<b>1 Background and Literature Review .....</b>	<b>1</b>
1.1 Introduction.....	1
1.2 Clinical Context of Low Back Pain.....	2
1.2.1 Epidemiology.....	3
1.3 The Spine.....	5
1.3.1 Vertebral Column .....	5
1.3.2 Lumbar Spine.....	7
1.3.3 Ligaments and Muscles .....	7
1.3.4 Vertebral Anatomy .....	11
1.3.4.1 Vertebral End Plates.....	15
1.3.4.2 Zygapophysial Joints (Facet Joint).....	16
1.3.5 The Natural Intervertebral Disc .....	17
1.4 The Functional Spinal Unit and Load Transfer .....	19
1.4.1 Lumbar Spinal Biomechanics .....	21
1.5 Surgical Interventions for Lower Back Pain.....	26
1.5.1 Fusion between Vertebrae .....	27
1.5.2 Total Disc Replacement.....	29
1.6 Tribology Theory.....	30
1.6.1 Lubrication Regimes.....	33
1.6.1.1 Hydrodynamic Lubrication .....	34
1.6.1.2 Boundary Lubrication .....	35
1.6.1.3 Mixed Lubrication.....	36
1.6.2 Friction.....	36
1.6.3 Wear.....	37
1.6.4 Bio-tribology Considerations in Total Joint Replacements .....	37
1.6.4.1 Cross Shear Motion.....	38
1.7 Total Disc Replacement.....	40
1.7.1 Design Rationales .....	40
1.7.1.1 The Meaning of Constraint.....	42
1.7.1.2 Material Combinations.....	44
1.7.2 Indications and Contraindications for Surgery .....	45
1.7.3 Clinical Results.....	46
1.8 Wear in Total Disc Replacement.....	47
1.8.1 Wear Testing.....	48
1.8.2 Typical Rates of Wear In Vitro.....	48
1.8.3 The Risk of Osteolysis.....	51
1.9 Aim and Objectives.....	53
<b>2 Spine Simulator Methodology.....</b>	<b>55</b>
2.1 Introduction to Spine Simulation.....	55

2.2	<i>Spine Simulator Calibration</i> .....	59
2.2.1	Load Verification.....	59
2.2.2	Flexion-Extension.....	62
2.2.3	Dynamic Verification of FE Motion.....	63
2.2.4	Lateral Bend.....	64
2.2.5	Axial Rotation.....	66
2.2.6	Anterior-Posterior Load and Displacement .....	67
2.2.7	Test Cell Temperature Calibration.....	69
2.2.8	Phase calibration.....	70
2.3	<i>Materials and Methods: Spine Simulator Wear Testing</i> .....	70
2.3.1	Introduction.....	70
2.3.2	Materials .....	71
2.3.2.1	TDR Samples .....	71
2.3.2.2	Wear Testing Lubricant Medium .....	72
2.3.2.3	Gravimetric Measurement.....	73
2.3.2.4	Surface Profilometry .....	73
2.3.3	Methods .....	76
2.3.3.1	Standard Testing Conditions .....	76
2.3.3.2	Spine Simulation Method.....	78
2.3.3.3	Statistical Analysis.....	80
2.3.3.4	Use of Perturbations of the Standard Testing Conditions .....	81
2.4	<i>Spine Simulator Verification</i> .....	82
2.4.1	Results of Verification .....	82
2.4.2	Feedback and Tolerance Limits .....	85
2.4.3	Discussion.....	85
<b>3</b>	<b>In Vitro TDR Simulation</b> .....	<b>87</b>
3.1	<i>Introduction</i> .....	87
3.2	<i>Method</i> .....	87
3.2.1	Wear Simulation .....	87
3.2.2	Profilometry and Imagery .....	93
3.3	<i>Results (Wear)</i> .....	96
3.3.1	Standard ISO Input Motions .....	96
3.3.1.1	Low Cross Shear Input Motions.....	103
3.3.1.2	Low Load Input Motions.....	105
3.3.1.3	Half Flexion-Extension (Prodisc only).....	106
3.3.1.4	Standard ISO Verification Study (Initial and final ISO studies compared).....	106
3.3.2	Profilometry and Imagery .....	114
3.3.2.1	<i>Prodisc</i> .....	114
3.3.2.2	<i>Charité</i> .....	118
3.3.2.3	SEM Analysis.....	122
3.4	<i>Discussion</i> .....	125
3.4.1	Rates of Wear .....	125
3.4.2	Relation to Damage Observed Ex Vivo .....	131
3.4.3	Biological Implications.....	138
3.4.4	Summary.....	142
<b>4</b>	<b>Tracking of Motion Paths</b> .....	<b>144</b>
4.1	<i>Introduction</i> .....	144
4.2	<i>Methods</i> .....	145
4.3	<i>Results</i> .....	149
4.4	<i>Discussion</i> .....	153
4.4.1	Summary.....	154
<b>5</b>	<b>Investigation of Short Stroke Effects</b> .....	<b>156</b>

5.1	<i>Introduction</i> .....	156
5.1.1	Theoretical Prediction of Contact Pressure.....	158
5.1.2	Experimental Contact Pressure Measurement .....	162
5.1.3	Experimental Contact Pressure Results .....	165
5.2	<i>Pin on Plate Methodology</i> .....	168
5.3	<i>Results</i> .....	172
5.4	<i>Discussion</i> .....	179
5.4.1	TDR Surface Contact Pressure .....	179
5.4.2	PoP Experiment .....	180
5.4.3	Summary.....	182
<b>6</b>	<b>Frictional Characteristics of TDR</b> .....	<b>183</b>
6.1	<i>Introduction</i> .....	183
6.2	<i>Methods</i> .....	183
6.2.1	Component Alignment.....	184
6.2.2	Input Kinetics.....	186
6.2.3	Output Data.....	188
6.2.4	Control Sample .....	189
6.3	<i>Results</i> .....	190
6.3.1	Applied Load .....	190
6.3.2	Rotational Velocity .....	191
6.3.3	Serum Concentration and Input Frequency .....	193
6.4	<i>Discussion (Friction Studies)</i> .....	194
6.4.1	Summary.....	196
6.5	<i>Computation of Lubrication Regimes</i> .....	198
6.5.1	Introduction.....	198
6.5.2	Method.....	199
6.5.3	Results .....	201
6.5.4	Discussion (computational lubrication) .....	204
6.5.5	Summary.....	206
<b>7</b>	<b>General Discussion</b> .....	<b>207</b>
7.1	<i>Overview of Experiments</i> .....	207
7.2	<i>Use of Leeds Spine Simulators</i> .....	207
7.3	<i>Summary</i> .....	208
7.3.1	Key Results.....	212
<b>8</b>	<b>Conclusions and Future Work</b> .....	<b>215</b>
8.1	<i>Conclusions</i> .....	215
8.2	<i>Future Work</i> .....	219
	<b>References</b> .....	<b>221</b>
	<b>Appendix A: Publications Arising From Thesis</b> .....	<b>235</b>
	<b>Appendix B: Motion Tracking Equipment</b> .....	<b>237</b>
	<b>Appendix C: Curvature of Motion Path Measurement</b> .....	<b>240</b>
	<b>Appendix D: Possible Source of Error in Friction Simulator Design</b> .....	<b>242</b>
	<b>Appendix E: Friction Simulator Drawings</b> .....	<b>244</b>
	<b>Appendix F: MATLAB Code for Lubrication Regime</b> .....	<b>248</b>



## List of Figures

Figure 1-1 The anatomical planes and positioning .....	2
Figure 1-2 Sagittal view of the vertebral column [24] .....	6
Figure 1-3 The spinal ligaments in posterior oblique view [24] .....	8
Figure 1-4 Iliolumbar ligament connecting L5 to the ilium .....	9
Figure 1-5 Superior view (left) and lateral view (right) of cervical (A), thoracic (B) and lumbar (C) vertebrae [34] .....	12
Figure 1-6 Superior view of a lumbar vertebra showing processes and facets [36] .....	13
Figure 1-7 CT-scan cross-section of a vertebra showing trabecular struts [image: A Liddle] .....	14
Figure 1-8 Superior view of vertebrae highlighting orientation of articular facets shown in grey (left: transverse plane, right: sagittal view) [46] .....	16
Figure 1-9 An FSU showing nucleus (centre) and surrounding annulus [36] .....	17
Figure 1-10 Intervertebral disc diagram showing section in coronal and transverse planes [32] (VEP: vertebral end plate, AF: annulus fibrosus, NP: nucleus pulposus) .....	19
Figure 1-11 Intra-discal pressure (IDP) shown diagrammatically with opposing tensile annulus forces (AF) .....	21
Figure 1-12 Diagrammatical disc showing dehydrated nucleus and inner annulus lamellae leaning inwards .....	21
Figure 1-13 Axes definition for the functional spinal unit [54] .....	23
Figure 1-14 Standard ISO input cycle used in wear testing .....	24
Figure 1-15 Plot of Loading (bottom) and kinematics (top three) from Callaghan et al. [1] with overlaid sinusoidal cycles .....	25
Figure 1-16 Fused vertebra – disc space filled with new bone growth and secured with plates [Image modified from University of Maryland] .....	28
Figure 1-17 X-ray images of a fusion using pedicle screws and rods (left) and an implanted TDR device (right) [image: Orthopaedic Center of Southern Illinois] .....	29
Figure 1-18 Types of wear: adhesive, abrasive, fatigue and tribo-chemical .....	31
Figure 1-19 Lubrication regimes showing asperity contact in mixed and boundary lubrication, where $\lambda$ is the film thickness (h) divided by $R_o$ .....	33
Figure 1-20 The Stribeck Curve Shows Friction as a function of film thickness caused by the effects of viscosity, velocity and load (logarithmic plot) .....	36
Figure 1-21 Example motion paths at a bearing surface and the principle direction of motion .....	39
Figure 1-22 Principle total disc replacement design examples: Charité (left), Prodisc-L (right) .....	41
Figure 1-23 Locus of instantaneous axis of rotation points through flexion-extension of the functional spinal unit [32] .....	43
Figure 2-1 Leeds spine simulator showing left hand bank of 3 stations and right hand bank of 3 stations (soak control to right of bank 2, computer control cabinet to right of picture) .....	56
Figure 2-2 Schematic of a group of three stations showing the linkage of the FE motor and actuating rods .....	57
Figure 2-3 Schematic of assembly of axial load application mechanism of the Leeds spine simulator, cam and spring are operated by the motor behind .....	58
Figure 2-4 Schematic showing assembly of the AP load application mechanism – the two springs give anterior and posterior force .....	58
Figure 2-5 Axial load measured using an independent load cell and special jig .....	59
Figure 2-6 Plot of simulator load cell versus independent load cell: the gradient and intercept are used in order to adjust the calibration constants of gain and gain offset .....	61
Figure 2-7 Revised Calibration plot: the simulator load cell now within the tolerance limits stipulated by the ISO standard .....	61
Figure 2-8 Digital inclinometer pictured measuring input flexion of one station (fitted with dummy sample) .....	63
Figure 2-9 Dynamic checking of FE motion under standard ISO conditions using dial gauge .....	64
Figure 2-10 Lateral bending measured at the gimbal (schematic shown in Figure 2-11) - links all three stations in one group .....	65
Figure 2-11 Schematic of simulator from end (posterior looking to anterior) view with lateral input motion gimbal which moves all three stations per bank .....	66

Figure 2-12 Axial rotation calibration checking.....	67
Figure 2-13 Jig used to hold independent load cell perpendicular to vertical axis.....	68
Figure 2-14 AP control depends on the attachment of bolt A (AP input configured) and bolt B (AP load configured), pictured schematically on right.....	68
Figure 2-15 LVDT mounted adjacent to a station sample holder and used to read deflection readings from an oscilloscope.....	69
Figure 2-16 The most common topographical function is average roughness (Ra) (image altered from Taylor-Hobson presentation).....	74
Figure 2-17 A pictorial demonstration of wavelength in relation to surface roughness.....	75
Figure 2-18 Positions of profile traces on PE components.....	76
Figure 2-19 TDR test cell submerged in serum contained in a flexible silicone gaiter.....	79
Figure 2-20 Gravimetric data showing wear rates per MC (simulator B = blue, simulator A = red) ±95% confidence limits.....	84
Figure 2-21 Feedback data averaged over three cycles is shown together with the tolerances allowed (±5 %) (AF1 = Axial Force 1 etc).....	85
Figure 3-1 Charité (left) and Prodisc (right) test components shown assembled.....	88
Figure 3-2 Both TDR designs allow FE but the unconstrained Charité device allows translation in the transverse plane – red dots depict example CoR positions.....	89
Figure 3-3 ISO 18192-1 lumbar TDR wear testing standard input motions and loads.....	91
Figure 3-4 ISO 18192-1 lumbar TDR wear testing standard with FE and LB placed in-phase to produce a low cross-shear wear path.....	91
Figure 3-5 An example Charité core component with solid lines showing stylus trace positions and dotted line showing approximate position of the metallic cup contact area.....	94
Figure 3-6 Example trace start/finish positions for the Charité PE component showing how the initial long trace was truncated for overall roughness measurement.....	95
Figure 3-7 An example Charité core (11 MC) showing profile trace and the truncating of the trace used to assess specific area profile phenomena (central roughened pole area shown).....	95
Figure 3-8 Soak control results for the entire spine simulator experimentation period for Prodisc (top) and Charité (bottom).....	97
Figure 3-9 Soak control results for the entire spine simulator experimentation period for Prodisc (top) and Charité (bottom).....	97
Figure 3-10 Soak control mass calculated as difference between end-point and start-point mass for each parametric study.....	98
Figure 3-11 Prodisc tested under standard ISO conditions showing cumulative wear rate ± standard deviation (also shown is a linear regression and R <sup>2</sup> correlation coefficient).....	99
Figure 3-12 Charité tested under standard ISO conditions showing cumulative wear rate ± standard deviation (also shown is a linear regression and R <sup>2</sup> correlation coefficient).....	100
Figure 3-13 Mean wear rates for the Prodisc and Charité disc designs (0-5 and 1-5 million cycle points shown for the Charité).....	101
Figure 3-14 Prodisc and Charité wear scars particularly pronounced towards the circumference of the UHMWPE bearing and toward the anterior of the Prodisc (scale 2mm).....	102
Figure 3-15 x25 magnification LOM image of the dome area of the Prodisc showing predominantly linear wear tracks (scale shown is 0.01 mm per division).....	102
Figure 3-16 x50 magnification LOM image of the pole area at the edge of the roughened section of the Prodisc – the islands of debris have been reapplied the surface (scale shown is 0.01 mm per division).....	103
Figure 3-17 Prodisc low CS average wear rate compared to the standard ISO (± standard deviation).....	104
Figure 3-18 Prodisc low CS average wear rate compared to the standard ISO (Charité results shown are 2-5 MC average).....	105
Figure 3-19 Prodisc half FE (HF) average wear rate compared to the standard ISO cycle.....	106
Figure 3-20 ISO and repeated ISO (ISO2) wear rates for the Prodisc device (note that the repeated ISO test was completed after a gap of 6 MC).....	107
Figure 3-21 ISO and repeated ISO (ISO2) wear rates for the Charité device (note that the repeated ISO test was completed after a gap of 8 MC).....	109
Figure 3-22 Spread of data of entire spine simulator experiments showing widening of spread for the secondary Charité studies (bottom) compared to the Prodisc (top).....	111

Figure 3-23 Schematic depicting (exaggerated) machining marks on the surface of a TDR bearing surface and the postulated increased contact area after bedding-in.....	113
Figure 3-24 Close up of surface profile demonstrating periodic profile resulting from machining of the Charité core (1.6 mm length shown) .....	114
Figure 3-25 Image of the pole area of the dome of a Prodisc (ISO test) showing the roughened area of the disc and penetration of ink (circled) under some of the debris .....	115
Figure 3-26 Prodisc disc $R_a$ trace results separated into entire disc length (ALL), edge wear (RIM) and roughened area on the pole of the dome (POLE).....	117
Figure 3-27 Prodisc metallic cups before and after wear testing for 15 MC of various parametric tests .....	117
Figure 3-28 Left: Prodisc wear scar (2MC ISO2) Right: Measurement after form removal (posterior to left) .....	118
Figure 3-29 Increased symmetry of wear for the lateral profile across a Prodisc (ISO2).....	118
Figure 3-30 Charité superior core $R_a$ trace results separated into entire disc length (ALL), edge wear (RIM) and roughened area on the pole of the dome (POLE).....	121
Figure 3-31 Charité inferior core $R_a$ trace results separated into entire disc length (ALL), edge wear (RIM) and roughened area on the pole of the dome (POLE).....	122
Figure 3-32 Charité superior (SUP) and infer (INF) cups surface profiled before and after 13 MC of wear testing.....	122
Figure 3-33 Charité SEM images of roughened area around the pole (descending increase in magnification), showing appearance of built up layers of particles.....	123
Figure 3-34 Comparing absolute results from Prodisc in vitro simulation and Prodisc finite element wear prediction (Dr Feng Liu) .....	130
Figure 3-35 Normalised comparison of Prodisc wear rate between different kinetic inputs showing the relative changes of the computation closely following the simulation .....	130
Figure 3-36 Motion paths of standard ISO and ½ FE modified ISO demonstrating shortened path length of the ½ FE input [Dr Feng Lui].....	131
Figure 3-37 Rim entrapment of Charité explants [131] .....	132
Figure 3-38 Radiograph image showing the anterior shear present at L5-S1 (left) when subject to flexion [171] - tilt of core appears to be caused by anterior shear.....	133
Figure 3-39 Image modified from O’Leary with anterior shear displacement visible when in flexion (circled) .....	134
Figure 3-40 SEM of ex vivo Charité PE core ([170]).....	135
Figure 3-41 LOM image of a Charité PE core surface (0.1 mm per division). .....	136
Figure 3-42 SEM image from Choma et al. [172] taken from the pole area of a Prodisc explant (scale not visible in original paper) – shows similarity to the SEM image of Figure 3-43 from the in vitro test .....	137
Figure 3-43 SEM image of a Charité (ISO tested) core showing overlapping re-attached debris plus linear multidirectional scratching .....	137
Figure 4-1 Sectional schematic of Charité motion track components .....	146
Figure 4-2 Sectional schematic of Prodisc motion track components – single sided scribes.....	147
Figure 4-3 Prodisc motion track measurements for all input cycles ( $\pm$ standard deviation).....	150
Figure 4-4 Prodisc motion tracks images, ISO (left) and LXS (right) .....	150
Figure 4-5 Charité motion track measurements for superior and inferior surfaces for all input cycles ( $\pm$ standard deviation) .....	151
Figure 4-6 Continuous motion paths on an actual Charité core (left) showing the spiral motion path (indent from scribes) and replicate PE core (right) as a result of scratching ink off the surface.....	152
Figure 4-7 Comparison between motion tracks of low CS (LXS) input (left) and pure ISO (right) .....	152
Figure 5-1 Example TDR (left) shown in close up section (right) with wear particles (red) shown accumulating at the pole and escaping at the edges .....	157
Figure 5-2 Plan view schematic of the PoP system showing two tests, (a) is 20 mm stroke length and (b) is 13.5 mm stroke length, the pin moves cyclically.....	157
Figure 5-3 Hertzian contact theory showing stress distribution, peak stress ( $P_o$ ), shear stress ( $\tau$ ) and width of contact ( $2a$ ) for a sphere on an infinite flat plane.....	159
Figure 5-4 Hertzian analysis showing maximum contact pressure ( $P_o$ ), shear stress ( $\tau$ ) and contact width ( $2a$ ) .....	161
Figure 5-5 A Charité device with Fujifilm in place before compression .....	163

Figure 5-6 The resultant contact pattern was recorded on the petal-patterned Fujifilm next to a scale and analysed in measurement software .....	163
Figure 5-7 Diagrammatical representation of a convex bearing surface, showing the measurement of arc length (s) as the measured contact width .....	164
Figure 5-8 Charité mobile core translated and tilted between its endplates (mounted in cement) ..	165
Figure 5-9 Compressive contact pressure and contact area results for the Prodisc TDR bearing .....	166
Figure 5-10 Theoretical pressure distribution (left) and actual plug shaped distribution (right) .....	166
Figure 5-11 Compressive contact pressure and contact area results for the Charité TDR bearing ...	167
Figure 5-12 PoP pin design for a wide contact area bearing face (all units in mm, material GUR 1020) .....	168
Figure 5-13 PoP theoretical CS ratios based on two pinion gear sizes used on the PoP machine for a 20 mm and 13.5 mm stroke length producing the same CS value.....	170
Figure 5-14 A single station from a six station rack and pinion system of a PoP wear rig showing UHMWPE pin in contact with a CoCr plate .....	171
Figure 5-15 Long stroke study: per measurement time point wear removal from pins 1-6 showing the high wearing pin .....	173
Figure 5-16 Short stroke study: per measurement time point wear volume removal from pins 1-6 showing the high wearing pin.....	173
Figure 5-17 Box plot showing the average wear factor for both tests and the outliers (both pin number 6, * indicates possible outlier in SPSS).....	175
Figure 5-18 Per million cycle point wear factor values as an average (n=5) for a 20 mm stroke length and 13.5 mm stroke length.....	176
Figure 5-19 Long stroke: Average roughness for the pins and plates before and after testing to approximately 1 MC showing no change for the plates but a polishing of the pins.....	177
Figure 5-20 Short stroke: Average roughness for the pins and plates before and after testing to approximately 1 MC showing no change for the plates but a polishing of the pins.....	178
Figure 5-21 Long stroke: Average skewness for the pins and plates before and after testing .....	178
Figure 5-22 Short stroke: Average skewness for the pins and plates before and after testing (*an outlier value was found and deleted from the skew analysis for the plates 1 MC data set) .....	179
Figure 5-23 Results of 20 mm long stroke and 13.5 mm short stroke compared to a study by Kang et al: Kang20 = 20 mm stroke length and Kang12 = 12 mm stroke length (note Kang et al used 8 mm diameter pins and 3.18 MPa contact stress) .....	181
Figure 6-1 Friction simulator schematic showing set-up of MoP hip control [197] .....	184
Figure 6-2 Charité endplates mounted in cement and the bath used to contain the lubricant .....	185
Figure 6-3 Typical friction simulator output – example shows TDR ISO waveform (Demand Motor = FE) .....	188
Figure 6-4 Hip control subject to hip input compared to Prodisc samples under hip input and constant load .....	190
Figure 6-5 Prodisc: varying static load from 500 N – 2750 N .....	191
Figure 6-6 Charité: varying static load from 500 N – 3000 N .....	191
Figure 6-7 Prodisc TDR under varying bearing surface velocities (slew rate) .....	192
Figure 6-8 Charité TDR under varying bearing-surface velocity (slew rate) .....	193
Figure 6-9 Prodisc: varying serum concentration .....	193
Figure 6-10 Prodisc – ISO 18192-1 input at 1, 1.5, and 2 Hz.....	194
Figure 6-11 Schematic demonstration of the difference in bearing coverage of a THR (left) and TDR (right), also showing same centre of rotation (CoR).....	198
Figure 6-12 Shaheen-Shepherd plot of lubrication regime for a 14mm radius and 0.05mm clearance – the CoCrMo/UHMWPE plot was used to verify the matlab plot [Figure 6-13].....	200
Figure 6-13 Simple MatLab plot used to verify calculations against existing data.....	201
Figure 6-14 MoM (blue) and MoP (red) lubrication regime plots for a 14mm radius TDR device.....	202
Figure 6-15 MoM (blue) and MoP (red) lubrication regime for reduced FE velocity and increased load (2000 N).....	203
Figure 6-16 The lubrication regime for a MoM TDR after changing the roughness from 80nm (red) to 5nm (blue).....	204
Figure 8-1 Bearing surface with motion path length shown Y mm away from the central position .	240

*Figure 8-2 Simplified friction simulator with TDR cup and dome components – the cup is loaded (offset centre loading shown) and rotated against the dome with the resulting torque on the dome measured at the transducer (F+Fe).....242*

*Figure 8-3 The free body diagram shows the forces required to prevent the (mass less) beam falling .....243*

## List of Tables

<i>Table 1-1 Inclusion and exclusion criteria for enrolment in FDA TDR study (modified from Blumenthal et al. [99])</i> .....	45
<i>Table 1-2 Comparison of patient clinical assessment scores, back to work rate and patient satisfaction rates</i> .....	47
<i>Table 2-1 Lot numbers of Charité devices (endplate ref 75-6400-12, core ref 75-6411-02 )</i> .....	72
<i>Table 2-2 Lot numbers of Prodisc devices (superior endplate ref PDL-M-IP00S, inferior endplate ref SSX534K, PE inlay ref PDL-M-PE14S)</i> .....	72
<i>Table 2-3 Tolerances in Lumbar ISO standard</i> .....	77
<i>Table 2-4 Comparison of mean wear rates for simulator A and simulator B</i> .....	83
<i>Table 2-5 Inter-simulator statistical difference between accumulative mean wear rates</i> .....	83
<i>Table 2-6 Inter-simulator statistical difference between each million cycle time point (per each MC rather than overall mean)</i> .....	84
<i>Table 3-1 Experimental studies: four input cycles applied to Prodisc; three input cycles applied to Charité</i> .....	90
<i>Table 3-2 ISO 18192-1 (standard ISO) input cycle parameters – alterations to the standard ISO cycle are highlighted</i> .....	90
<i>Table 3-3 Test inputs were coded: I = ISO, X = low cross shear, I2 = repeat ISO, L = low load, H = half load; P = Prodisc, C = Charité</i> .....	92
<i>Table 3-4 Prodisc million cycle measurement points showing significance levels (using Tukey HSD test for homogenous variances)</i> .....	108
<i>Table 3-5 Prodisc ISO studies showing minimum and maximum wearing test cells (mg/MC)</i> .....	108
<i>Table 3-6 Charité million cycle measurement points showing significance levels (using Tamhane’s test for non-homogenous variances)</i> .....	110
<i>Table 3-7 Charité ISO studies showing minimum and maximum wearing test cells (mg/MC)</i> .....	110
<i>Table 3-8 Full <math>R_a</math> results for the Prodisc PE components (average and standard deviation)</i> .....	115
<i>Table 3-9 Superior and inferior surface <math>R_a</math> results for the Charité PE components (average and standard deviation)</i> .....	120
<i>Table 3-10 Summary of wear results for both in vitro and computational</i> .....	126
<i>Table 4-1 List of input cycles used in motion track study</i> .....	148
<i>Table 4-2 Rotation of the Charité mobile core under differing inputs and of two design types</i> .....	153
<i>Table 5-1 Prostheses material properties</i> .....	159
<i>Table 5-2 Prodisc results obtained from using Hertzian contact theory (highlighted are peak pressure, <math>P_o</math>, width of contact, <math>2a</math>, and shear stress, <math>\tau</math>)</i> .....	160
<i>Table 5-3 Charité results obtained from using Hertzian contact theory (highlighted are peak pressure, <math>P_o</math>, width of contact, <math>2a</math>, and shear stress, <math>\tau</math>)</i> .....	160
<i>Table 5-4 Grades of Fujifilm used</i> .....	162
<i>Table 5-5 A check for spurious results obtained from test station pin wear – based on pin wear factor at each 1/3 MC compared to the mean wear factor</i> .....	174
<i>Table 5-6 Comparison of spine simulator and PoP wear values and wear factors (HF: half FE, LS: long stroke, SS: short stroke)</i> .....	176
<i>Table 6-1 Order of application of constant load tests in order to limit the influence of one test affecting another</i> .....	187
<i>Table 6-2 MoP control hip friction factor displayed in relation to oil warmth and period of data point selection (90 seconds or 5 minutes)</i> .....	189
<i>Table 6-3 Frictional torque for constant load inputs, Prodisc and Charité</i> .....	190
<i>Table 6-4 Values of constants and variables in lubrication analysis (modified from Shaheen &amp; Shepherd [83])</i> .....	200

## Nomenclature

a	Contact half width
2a	Contact width
$\alpha$	Probability significance level
ADR	Artificial disc replacement
ALL	Anterior longitudinal ligament
ALDD	Adjacent level disc disease
ASTM	American Society for Testing and Materials
ANOVA	Analysis of variance
AP	Anterior posterior
AR	Axial rotation, or;
AR	Aspect ratio
BW	Body weight
Callaghan	Refers to use of Callaghan-based motions
CI	Confidence interval
CoR	Centre of rotation
CoC	Ceramic on ceramic
CoCrMo or CoCr	Cobalt chromium molybdenum
CS	Cross shear
DDD	Degenerative disc disease
DoF	Degrees of freedom
EHL	Elastohydrodynamic lubrication
IDE	Investigational device exemption
f	Frequency
<i>f</i>	Friction factor
F	Friction force
f(---)	A function of ---
FBA	Functional biological activity
FDA	Federal Food and Drug Administration
FE	Flexion extension
FSU	Functional spinal unit
h	Fluid film thickness
HF	Half flexion-extension
IAR	Instantaneous axis of rotation
IDP	Intra-discal pressure
ISO	International Organisation for Standardisation, or;
ISO	Standard ISO input cycle
ISO2	Repeated standard ISO input cycle
ISO+AP	ISO motion plus AP shear component
IVD	Intervertebral disc (natural)
K	Wear factor ( $\text{mm}^3/\text{Nm}$ )
$\lambda$	Lubrication ratio ( $h/R_a$ )
L1, L2 etc.	Lumbar vertebra 1, vertebra 2 etc.
LB	Lateral bend
LBP	Low back pain
LL	Low load
LXS	Low cross shear
LXS+AP	LXS plus AP shear component
$\mu\text{CT}$	Micro computed tomography
mg/MC	Milligrams per million cycles

MoM	Metal on metal
MoP	Metal on polyethylene
NHS	National Health Service
NIH	National Institutes of Health (USA)
NIHR	National Institute for Health Research (UK)
ODI	Oswestry disability index
$P_o$	Peak contact pressure
$p$	Probability
PE	Polyethylene
PMO	Principle molecular orientation
PoM	Polyethylene on metal
$R_a$	Average roughness
RoM	Range of motion
$R_{sk}$	Average roughness skew
S1, S2 etc.	Sacral vertebra 1, vertebra 2 etc.
SD	Standard deviation
SE	Standard error
$\tau$	Shear stress
T	Torque
TDA	Total disc arthroplasty
TDR	Total disc replacement
THR	Total hip replacement
TKR	Total knee replacement
UHMWPE	Ultra-high molecular weight polyethylene
V	Volumetric wear volume
VEP	Vertebral end plate
$\omega$	Angular velocity
W	Work done



# **1 Background and Literature Review**

Late failures of hip and knee joint replacements have been linked to wear and consequent adverse tissue reactions resulting from wear debris production. Concerns regarding the use of articulating artificial discs in the spine have prompted an increased need for a better understanding of the bio-tribological performance of these devices, which is the subject of this thesis. In the following sections the reader is introduced to spinal anatomy, basic principles of tribology, artificial disc replacements and finally; the aim of the experimental studies.

## ***1.1 Introduction***

Back pain can affect anyone at any age and approximately 70% of the population will suffer from lower back pain in their lifetime [2]. The most common age group affected is 35-55 years of age and it is the most prevalent reason for lost days in the work-place [2]. The lower part of the back, known as the lumbar region, is the most susceptible to back pain as it carries more than the full weight of the upper body and limbs and so is subject to large compressive loads and torques [3]. Most occurrences of lumbar back pain resolve with time, but in the most severe cases it may be necessary to perform surgery such as a fusion procedure or total disc replacement (TDR). Fusion refers to the removal of the natural disc and fusing the adjacent vertebra together with a bone graft and instrumentation. Total disc replacement refers to the removal of the natural disc and replacement with a prosthetic. The reason for removal of the disc may be disease (degenerative disc disease) or a mechanically damaged disc due overloading or trauma.

During this review, many anatomical descriptions of planes of view and positioning are used. For the reader's benefit, the anatomical planes are shown in Figure 1-1.

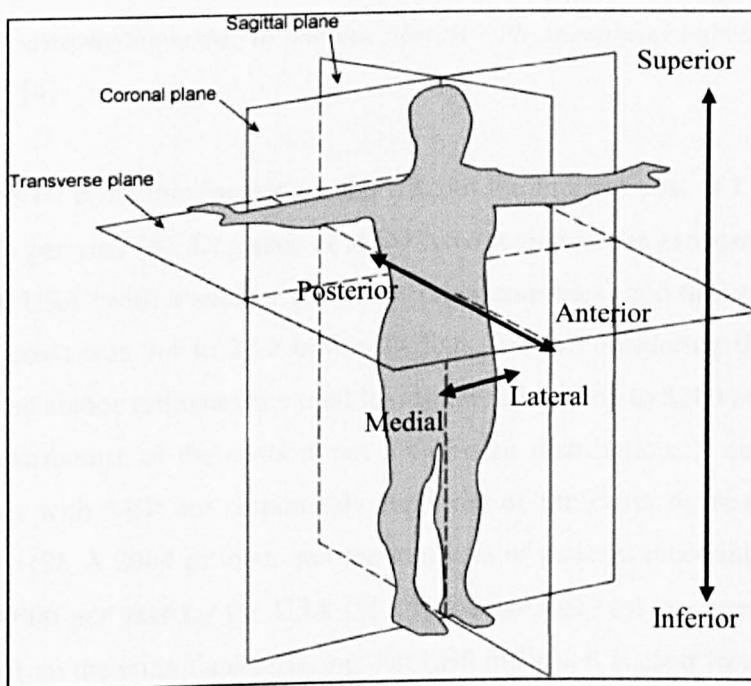


**Figure 1-1 The anatomical planes and positioning**

## **1.2 Clinical Context of Low Back Pain**

The link between low back pain and degenerative disc disease (DDD) is not closely correlated and is the subject of debate. Most people from middle age onwards will have degenerated discs, however, they are usually not painful. The term ‘disease’ is therefore a misnomer since this is a natural aging process. In a similar way, ‘degenerative’ also sounds alarming, but actually the process is age dependant and may not result in pain. However, for those people with pain that does not improve by the use of conservative treatments the acronym DDD is used and the removal of the intervertebral disc (IVD) can be a solution. This is commonly achieved by a fusion procedure but more recently a total disc replacement (TDR) has become an option where indications allow. Lower back pain that is attributable to a degeneration of the disc has been more concisely defined as discogenic back pain with the following factors:

- *”contained herniated nucleus pulposus*
- *paucity of facet joint degeneration changes*
- *decrease in IVD disc height of at least 4mm and/or*

- *scarring/thickening of annulus fibrosis with osteophytes indicating osteoarthritis*" [4]

Reports on economic impact for the UK put the indirect cost of LBP at 10.7 billion pounds per year [5]. Dagenais et al [6] have reviewed the economic impact of LBP for the USA (with a smaller review of other countries) and the spread of estimated direct costs was 7.4 to 28.2 billion Dollars. When considering the total impact of LBP one author estimates the total loss to the USA at up to \$200 billion per year [7]. The distribution of the costs is not a Gaussian distribution. A small proportion of patients with LBP are responsible for most of the costs by requiring substantial surgery [8]. A 2004 estimate put the numbers of patients receiving a fusion surgery at 250,000 per year for the USA [9] and the average cost per operation at \$34,000. Apart from the individual suffering that LBP inflicts, it is clear from the data that the wider impact to the whole of society through indirect economic costs is large. These costs are met by all of the working population, whether through taxes or insurance premiums. Therefore it is of importance that long-term clinical solutions for the treatment of severe discogenic back pain be realised.

### **1.2.1 Epidemiology**

The present long standing method of treating unresponsive DDD is spinal fusion, where the adjacent vertebra are fused together, commonly referred to as the 'gold standard' treatment [10]. However, there is no consensus in the literature as to the efficacy of fusion. A systematic review by Gibson et al. [11] found that there was no evidence to support spinal fusion as an alternative treatment. Carreon et al. [12] completed a meta-analysis of results from fusion (anterior and posterior) from 25 studies and compared outcomes to those of non-surgically treated patients. They found that there was substantial improvement with all fusion types, but that the indication had to be clear; patients with chronic low back pain but no specific pathology did not improve as much. Fritzell et al. [13] conducted a multicentre controlled trial comparing non-surgical and fusion results (with evidence of degenerative changes) at lumbar level four (L4) to the sacrum (S1). At 2 years in the fusion group 63 % of patients rated themselves much better or better versus 29 % of the non-surgical group – a significant difference with a 83 % successful fusion rate

at two years. A later review of this paper by Kwon et al. [14] attempted to clarify the validity of these favourable results by comparing data with Brox et al. [15]. The main drawback of Fritzell et al., described by Kwon et al., was the non-specific definition of chronic low back pain and its comparison with “usual non-operative” care. However, Kwon came to the conclusion that even with certain analysis weaknesses the Fritzell et al. conclusions were sound. Brox et al. compared posterolateral fusion with a more rigorous non-surgical intervention at a specialist centre. Their conclusions were that fusion patients showed no significantly better outcomes than non-surgical ones, although the follow-up period was only one year and the sample size was smaller – hence the review by Kwon et al.

A hypothesised drawback of fusion is the increased stress placed on adjacent disc and the risk of advancing DDD in those levels. Total disc replacement has been advocated as an alternative to fusion as a way of managing the risk of DDD in adjacent level discs. It has been theorised that the preservation of natural functional spinal unit (FSU) biomechanics will decrease the risk of adjacent level DDD [16-19]. The most common current types are based on present arthroplasty knowledge, gained from total hip replacement (THR) and total knee replacements (TKR). However, long-term wear related issues from spine arthroplasty are a potential serious outcome, as has already been seen in THR and TKR.

In the last decade, it was thought that TDRs would herald a paradigm shift in the treatment of DDD [20]. TDRs were seen as an attractive alternative to fusion and that patients would benefit from the perceived advantage of preserved motion at adjacent levels. However, although there are a large number of potential lumbar TDR procedure candidates, the number of people rejected due to contraindications is very large. Huang et al. [21] reported an epidemiological study that found 95% of the patients selected as potential TDR candidates were actually excluded due to contraindications. Two recent investigations of TDR candidacy showed indication rates of between 0.5 – 5% [21, 22]. If only a maximum of 5% of lumbar patients are indicated for this procedure then the enthusiasm for lumbar TDR over the past decade may have been premature.

The sections ahead will guide the reader through spinal anatomy, back pain and treatments, introduce TDR devices and examine the bio-tribological implications of using such devices.

## **1.3 The Spine**

### **1.3.1 Vertebral Column**

The vertebral column connects pelvis to skull and transports the weight of the trunk and head to the pelvis and hence through the legs to the ground. The flexible pre-sacral part is made up of 24 bony sections called vertebra, separated by 23 flexible IVDs, which are connected together by ligaments and muscles. Altogether the spine is made up of 33 vertebra, where 9 of the vertebra are fused together to form a solid base in the pelvic region. The five regions of the spine and the vertebra numbers are:

1. Seven cervical; making up the neck
2. Twelve thoracic; having ribs attached and make up the thorax
3. Five lumbar; support the torso and attach to the sacrum
4. Five sacral (fused)
5. Three to four coccyx (fused)

The five vertebrae that make up the lumbar spine are labelled L1 to L5 with the base of the spine where it joins the sacrum labelled S1. Intervertebral discs are labelled according to their relative position between vertebrae in the spine: L1-2, L2-3 etc. White and Panjabi [3] have defined the function of the spine as in points 1-3 below. Harms and Tabasso [23] also added a fourth:

1. protect the spinal cord
2. provide stability
3. provide mobility
4. control the transmittance of movement of upper and lower extremities

The arrangement of the vertebral column in relation to the torso is shown in Figure 1-2.

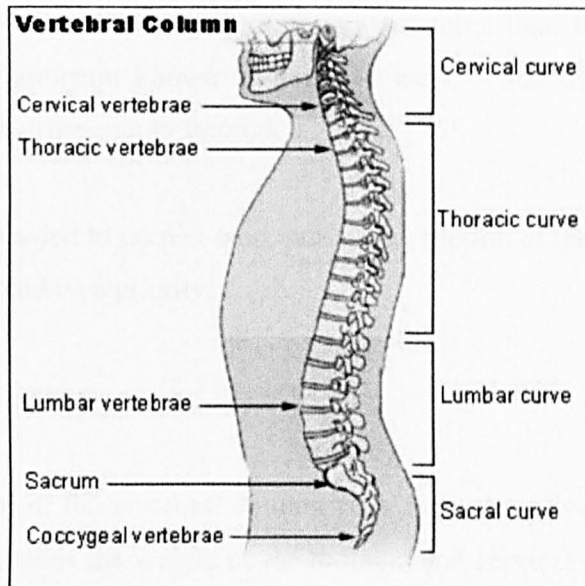


**Figure 1-2 Sagittal view of the vertebral column [24]**

The column has a characteristic shape of a shallow S shaped curve when viewed in the sagittal plane, with lordosis at lumbar and cervical regions and kyphosis at the thoracic region. This shape enables bipedal locomotion [25], but because of this upright posture there is a greater proportion of body weight placed on the lumbar lordotic section. The muscle-reaction forces to bending at the spinal curves give a degree of elasticity necessary to absorb shock loads associated with walking, running, etc. [26]. It has been estimated that, as a proportion of the input loads to the body from heel strike, the legs absorb and dissipate 84% of these energies with the remaining 16% being absorbed by the spine [27]. For patients suffering from ankylosing spondylitis (a natural fusion of parts of the spine by disease) the amount of absorption available drops to around 1% [27]. Although in surgically fused cases the number of levels fused is 3-4 at most, it could be argued that fusion, whether caused by natural disease or fusion-surgery, must decrease the ability of the spine to absorb and dissipate energy from loads without injury or pain. Since this ability is directly governed by the flexibility of the FSU (and the muscles that control it), the case for an artificial TDR device rather than a fusion procedure is strengthened. The nature of heel-strike energy dissipation is by bending of the FSUs and the consequent muscle action (energy dissipation) of the erector spinae group of muscles that help control the spine [26]. The muscles therefore act as the primary energy dissipaters (or shock absorbers), rather than the discs. Muscles are known to

be able to absorb around 40% greater amount of force than they can output – a physiological phenomenon known as negative work – and this accounts for the dissipation of heel-strike energy through the spine [26].

When surgery is needed to correct pain, preserving motion of the spine and function of the muscles should be a priority.

### **1.3.2 Lumbar Spine**

The lumbar region of the vertebral column rises from the pelvis to the area of the abdomen and so carries the weight of the thoracic and cervical spine as well as the weight of the rest of the upper body. This static weight is approximately 2/3 of full body weight [3]. However, once we consider the tension in the muscles, tendons and ligaments that keep the flexible spine upright, this rises to approximately 2-3 times body weight. Under heavy loading conditions this can rise to 4-5 times body weight [3]. The lumbar spine is lordotically curved which aids the distribution of transient impact-loads by flexing in the sagittal plane. All other mammals have vertebral columns that display no lordosis or some kyphosis and as such are limited to a prone posture. If humans had straight lumbar spines, our bipedal posture would result in excessive axial loads going directly through the vertebrae and IVDs. FSU bending allows the application of muscle and ligament forces to absorb some transient loading [28].

### **1.3.3 Ligaments and Muscles**

#### *Ligaments*

Ligaments are fibrous connective tissues that link bones together. There are seven main types of ligament in the spine, some link vertebra to vertebra and others traverse several vertebrae. The L5 vertebra of the lumbar spine is subject to larger anterior shear forces and has an additional ligament attaching it to the ilium. The positioning of the ligaments is shown in Figure 1-3.

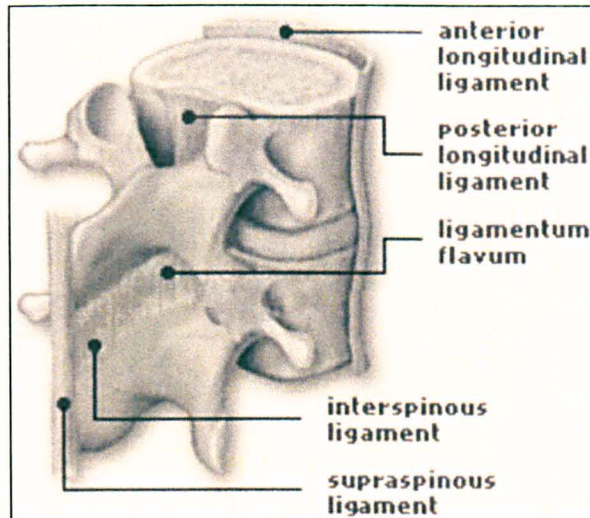
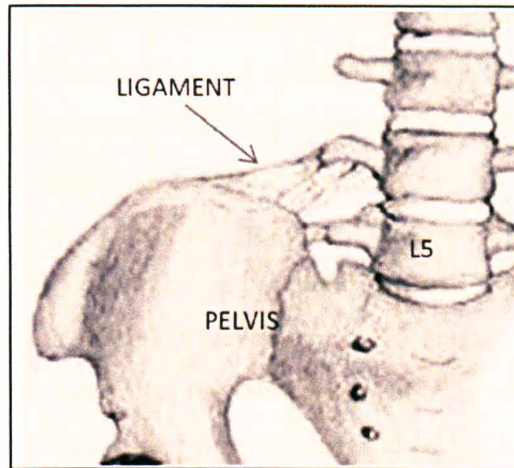


Figure 1-3 The spinal ligaments in posterior oblique view [24]

Ligaments in the lumbar spine either connect intersegmentally, holding several vertebrae together including the ligamentum flavum, interspinous and intertransverse, or; intrasegmentally, holding adjacent vertebrae together including the anterior and posterior longitudinal ligaments and the supraspinous ligaments [29]. The two longest ligaments are the anterior longitudinal ligament and the posterior longitudinal ligament. These traverse many vertebrae and attach to the front and rear of the vertebral bodies – the anterior and bottom of the neural arch. These help to reinforce the column and are attached to the vertebral bones and the cartilaginous discs. The ligamentum flavum connect adjacent laminae (in the vicinity of the vertebral arch) and has to be very elastic so that when the spine rotates from full flexion to full extension the ligament cannot become trapped in the vertebral canal and cause impingement on the spinal cord. For this reason they contain a large proportion of elastin which ensures that a high degree of deformation is possible without causing residual deformation [3]. The iliolumbar ligament [Figure 1-4] attaches the L5 vertebra’s transverse process to the ilium (superior part of the pelvis) and so serves to anchor the L5 vertebra and protect its disc from the increased shear forces experienced due to the angle of inclination there. For this reason it is the strongest ligament [30]. Interspinous ligaments attach the opposing faces of the spinous processes and do not contain elastin.





**Figure 1-4 Iliolumbar ligament connecting L5 to the ilium**

Some ligaments in the spine are deemed not true ligaments by some authors, in that they don't connect bone to bone or are too weak to do so [31, 32]. The supraspinous ligament in the lumbar spine is an example. It is only well developed in the upper region but by L4 it terminates in 73% of individuals [33]. It is thought that this ligament is derived largely from back muscle fibres and therefore not truly a ligament [32].

### *Muscles*

Without control of the spine by the muscles, the vertebral column would be a passive structure vulnerable to collapse and damage. A strong control by muscle groups is essential in protecting the back by stabilising the spinal structure. They are the main tissue that surrounds and protects the back and provide motion and stability. The lumbar spine is enclosed by several muscles groups. As with the ligaments, some muscles connect vertebra to vertebra and others connect across multiple vertebrae, or to other bones such as the femur. For clarity, Bogduk [32] has ordered these muscles into three main groups, on descriptive and functional grounds:

- psoas major, covering anterolateral aspects of the lumbar spine
- intertransversarii laterals and quadratus lumborum, which connect the transverse processes and covers them anteriorly
- the lumbar back muscles, lying behind and covering the posterior elements of the lumbar spine

The psoas major arises from the anteriolateral aspect of the lumbar spine where it attaches to vertebrae and discs from T12 to L5. It continues downward through the pelvis and attaches to the tendon of the lesser trochanter of the femur. The psoas major is not thought to exert large flexion-extension (FE) forces on the lumbar spine due to its proximity to the centre of rotation of the vertebrae [32]. The function therefore is to exert a flexion force on the femur by using the lumbar spine as an anchoring base. However, because the line of force action through the muscle is close to the vertebral body centre, the compression forces on the lumbar spine are amplified by its action [31, 32] and this compression of the lordotic curve results in extension of the lumbar spine [28]. Anterior flexor forces are largely controlled by abdominal wall musculature.

The intertransversarii laterals connect the transverse processes. It has been postulated that they could feebly assist in lateral flexion but their function has not been experimentally determined [32]. It could be that like the interspinales they give a proprioceptive function or help in stabilisation of the spine. The quadratus lumborum muscles lie lateral to each side of the spine and connect the 12<sup>th</sup> rib, lumbar transverse processes of L1 to L4 and the ilium. Acting individually the muscle can flex the spine laterally. Acting together, the muscles help extend the lumbar spine.

The posterior lumbar back muscles include the erector spinae, multifidus, intertransversarii medialis and interspinales. The erector spinae consists of two main groups: the longissimus thoracis and the iliocostalis lumborum. The longissimus muscles arise from the around the dorsal surface of the transverse processes and end caudally forming tendons at the medial vicinity of the ilium. The iliocostalis are similar to the longissimus but the attachment points at the transverse processes and at the ilium are positioned more laterally, affording increased unilateral axial rotation (though this cannot be applied without extension – the oblique abdominal muscles are the primary rotators). The longissimus and iliocostalis muscles produce both vertical and horizontal force components and so they can also resist anterior shear. The line of action of the longissimus and iliocostalis is close to the sagittal axis of rotation and therefore their ability to apply extension is less than the multifidus. The multifidus muscle group fills the channel either side of the transverse processes. It is

primarily an extensor of the lumbar spine with little lateral force component. The fibres of the multifidus pull down on the transverse process from multiple attachment points at vertebrae two to five levels below plus the ilium and posterior surface of the sacrum. The lumbar interspinales connect each spinous process to its adjacent process. The lumbar region has four pairs. Although they are positioned in such a way as to give the impression of applying extension forces, it is believed they apply little force and could be a form of feedback transducer (proprioceptive function) for the body [31].

#### *Muscle Damage during Posterior Spine Surgery*

During posterior spine surgery, such as for posterior fusion procedures, the posterior paraspinal muscles have to be moved aside to gain access to the vertebrae. During this process it is possible that some muscle and nerve damage will occur. If nerves are damaged through swelling or scar tissue, this can affect the action of the muscle supplied by those nerves causing loss of sensation or weakness. Because the muscles are cut and lifted away from the vertebrae resulting in disruption to the blood supply, the reattached muscles may be weaker and fatigue more easily resulting in greater back instability [10].

### **1.3.4 Vertebral Anatomy**

There are usually 33 vertebrae, 24 of which are free to articulate. They are subdivided into three groups depending on position and morphology [Figure 1-5]:

- Seven cervical vertebrae between the skull and the thorax. These are characterised by small size and each transverse process has a foramen (opening).
- Twelve thoracic vertebrae are primarily characterised by the articular processes where ribs attach.
- Five lumbar vertebrae lead to the base of the spine (sacrum) and take the greatest share of the upper body weight; hence they are larger than the others.
- Five sacral vertebra below the lumbar vertebra are fused together to form the sacrum which forms part of the pelvis.

- Usually there are four vertebrae below the sacrum that are also fused to form the coccyx.

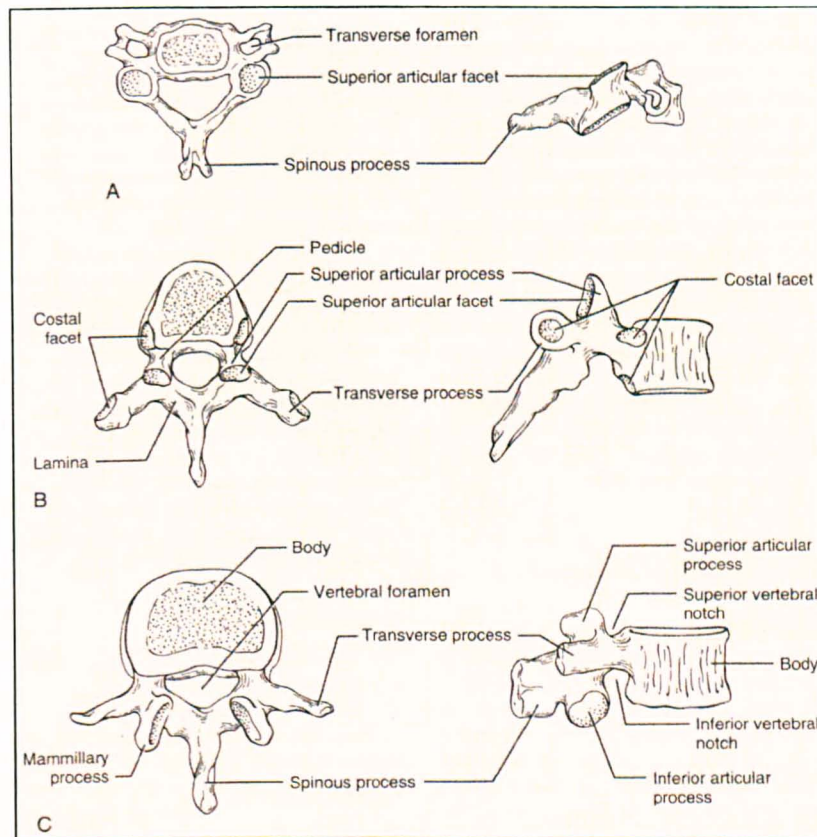


**Figure 1-5 Superior view (left) and lateral view (right) of cervical (A), thoracic (B) and lumbar (C) vertebrae [34]**

Apart from the first two cervical vertebrae that support extreme physiological motions of the head – the atlas and axis - the remaining mobile vertebra share common features. The vertebral body lies to the anterior in the torso and is the principle load bearer. The lumbar bodies support approximately 80% of the loads when in a neutral position with the facet joints supporting the remaining 20% [35]. Two pedicles extend posteriorly and together with the lamina form the neural arch within which the spinal cord is protected [Figure 1-6]. Processes are protrusions from the vertebra that serve as attachment points for ligaments and muscles and as lever arms for the application of forces. There are seven principle processes:

- One spinous process
- Two transverse processes

- Four articular processes: two superior and two inferior which come together to form a synovial facet joint between adjacent vertebrae.

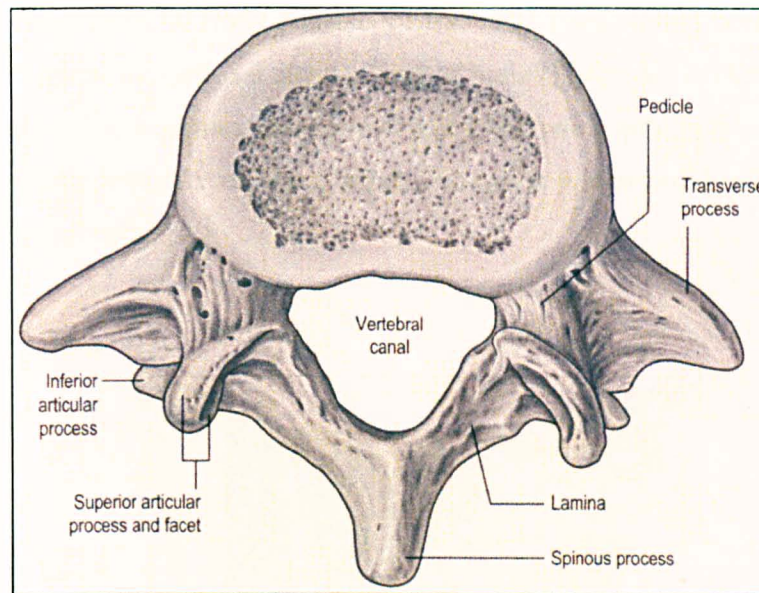


**Figure 1-6 Superior view of a lumbar vertebra showing processes and facets [36]**

Small accessory processes are also present on the transverse processes and serve as attachment sites for muscle groups. Each spinal segment is separated by IVDs and connected together by muscle and ligament. The makeup of the load bearing part of a vertebra is an outer shell of stiff cortical bone surrounding an inner matrix of softer cancellous bone [31]. The cancellous bone is vascularised and a source of bone marrow, the nutrients of which are thought to diffuse across the vertebral end plates to the IVD nucleus [37].

The strength characteristics of vertebral bone (and also long bones) are due to their composite structure. Bone consists of a fibrous organic matrix (approx 50% organic phase by weight; 25 % by volume) containing embedded cells. Within the organic matrix, an inorganic mineral component of hydroxyapatite (calcium phosphate) forms hydroxyapatite crystals ~5-10 nm in size. The calcium phosphate gives strength in compression while the collagen provides flexibility and resilience in tension [38]. O'Brian et al. [39] have shown that at the micro scale, secondary osteons (functional units of compact bone) act as crack growth limiters - cracks instigate most failures in stiff structures [40]. The macro scale composite structure

consists of an outer layer of cortical bone (compact and hard) with the inner being cancellous (spongy) bone. Cancellous bone is also found at the end of long bones and helps distribute forces imparted to the articular cartilage from the high contact loads. The inner vertebral body consists of trabecula (cancellous) bone and tissue. The trabecula element itself is a slender strut of bone [Figure 1-7]. Their orientation appears random but becomes anisotropic when following principle stress vectors [41]. They create a matrix of bone filled with voids which provide nourishment; blood vessels and cells.

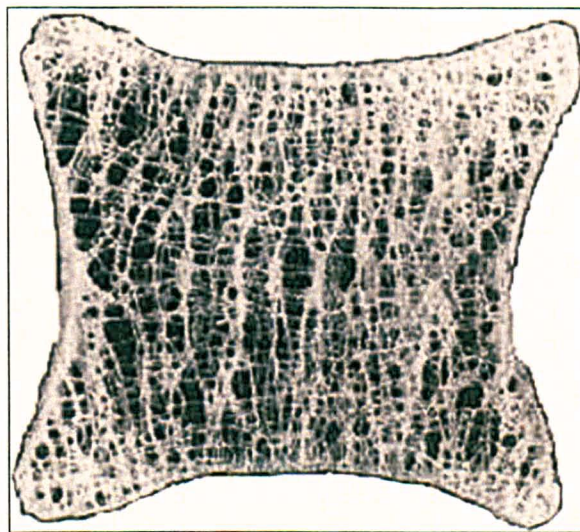


**Figure 1-7 CT-scan cross-section of a vertebra showing trabecular struts [image: A Liddle]**

The posterior part of the lumbar vertebra has a number of processes which are designed to manage the very large loads that would otherwise make the vertebral column unstable and liable to buckling. Moving posteriorly away from the main vertebral body, there is an opening surrounded by an arch (foramen) where the spinal cord runs from the brain to around L1-2 and continues as the corda equine to the base of the column. The facets of the superior articular processes of the lower vertebrae glide on the inferior processes of the upper vertebra. This facet joint arrangement allows the FSU to resist excessive types of shear force and torsion. The nature of the shear force being resisted is dependent on the level of the vertebra. Lumbar vertebra resist anterior-posterior (AP) shear loads and therefore have facets arranged so that shear is controlled. A single spinous process at the medial posterior

position gives an anchor point for muscle forces to be applied to the vertebra in order to apply or moderate FE. This is necessary because the centre of mass of the torso lies to the anterior of the spine and therefore has a constant forward bending moment applied.

Movement of vertebra relative to each other helps control shock absorption. The main way in which shock absorption is achieved in everyday activities is by way of small flexions of adjacent vertebra as a result of the overall compressive bending of the spine's S-curve shape. For larger shocks, the vertebral end plates themselves may deform [26, 27, 42]. The muscles that control the vertebrae act as dampers with some shock absorption also done by the vertebrae themselves. During heavy loading the vertebral end plates are deflected by the resisting pressure of the nucleus pulposus and this deflection deforms and stresses the vertebra trabecula matrix thereby storing energy which can be released elastically to reform the shape of the end plate [43 , 44].

#### **1.3.4.1 Vertebral End Plates**

The disc is positioned between adjacent vertebrae and the vertebral end plates are attached to the disc. The plates are cartilaginous with a bony base of subchondral bone. The end plates serve to transmit mechanical forces from vertebra to disc to vertebra and also to form a permeable barrier (cribriform plate) so that fluid and nutrients can pass from the vertebra which are vascular, to the disc, which from early adulthood is not [31, 45].

Fixation of a TDR device to the end plates is achieved by removing the cartilaginous end plate surface as far as the subchondral bone. The roughened surface of the TDR end plate is then inserted and the vertebral end plate bone is expected to grow into the device. Initial fixation is achieved by keels or spikes on the TDR endplates combined with roughening of the surfaces, typically by blasting. These stabilise the device until bone fixation occurs. To facilitate longer term boney ingrowth, coatings such as plasma sprayed titanium (e.g. Prodisc, Synthes) or hydroxyapatite (e.g. Charite, dePuy) are used to create porous surfaces favourable to bone in-growth.

### 1.3.4.2 Zygapophysial Joints (Facet Joint)

The facet joint is a synovial joint like most articulating joints in the body such as the knee and hip. It is comprised of articular hyaline cartilage lined facets that face each other and are lubricated with synovial fluid contained in a synovial membrane. The broad function of the facet joints is to resist certain motions - depending on whether they are located in the cervical, thoracic or lumbar region. The average alignment of facet joints for the cervical, thoracic and lumbar vertebrae is shown in Figure 1-8.

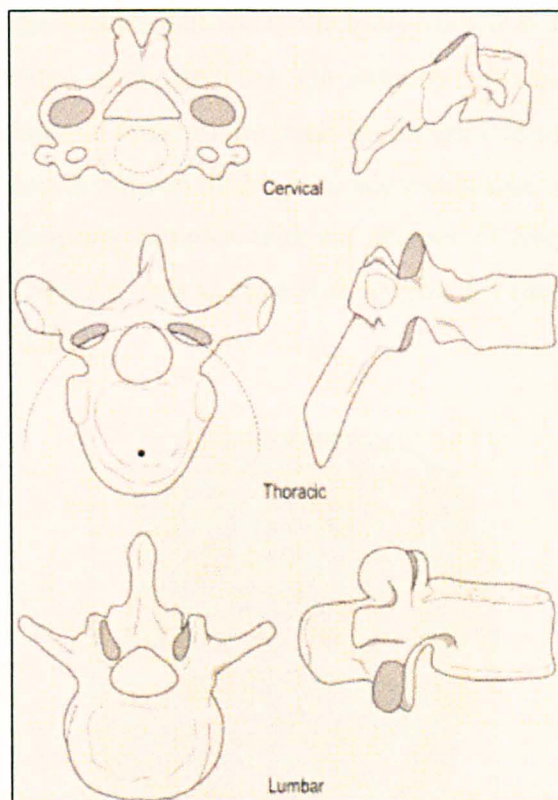


**Figure 1-8 Superior view of vertebrae highlighting orientation of articular facets shown in grey (left: transverse plane, right: sagittal view) [46]**

In the cervical region the facet joints are arranged in an oblique angle to the sagittal plane which allows a greater degree of movement in all directions. In the thoracic region the facet joints are arranged more vertically and are angled in the horizontal plane such that the faces have a centre of rotation in the vertebral body, this allows more axial rotation but limits anterior shear displacement. In the lumbar region the



facet joints are positioned approximately vertically and slope obliquely with curved mating surfaces which allows FE and lateral bending (LB) [46]. Perhaps most importantly, the lumbar facets limit torsion and reduce the shear force component of body weight on the lower lumbar discs [3, 37].

### 1.3.5 The Natural Intervertebral Disc

The function of the IVD is to allow movement between vertebrae. Most articulating joints between bones of the body are synovial in nature. The disc is unusual in that the movement is achieved through deformation of the joint itself. The disc consists of two main parts, the annulus fibrosus (commonly known as the annulus), and the nucleus pulposus (known as the nucleus). The annulus surrounds the nucleus. These two components interact to transmit the loads in the spine from vertebra to vertebra [Figure 1-9]. The unusual makeup of this joint occurs because the motions and loads of the spine are particularly complex with six degrees of freedom (3 translational and three rotational) and also has to cope with approx 2-5 times body weight loads in daily activity [1, 3, 47].

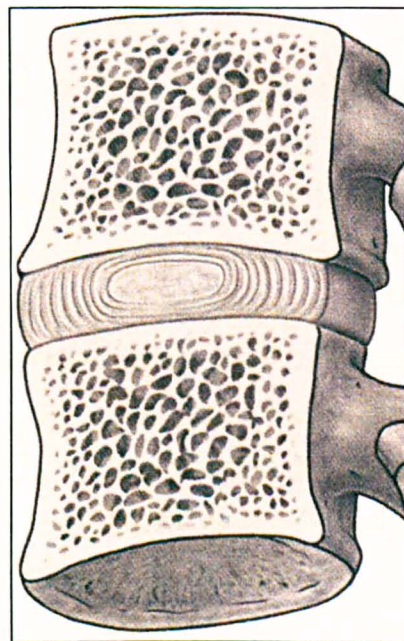


Figure 1-9 An FSU showing nucleus (centre) and surrounding annulus [36]

### *Annulus Fibrosus*

The annulus is made up of concentric layers or lamellae of collagen fibres and a proteoglycan gel which binds them together [28]. The layers run parallel to each other and at an oblique angle between fibres, with every other layer having its direction of obliqueness changed to form an intersecting crossing pattern. The outer layers contain a greater proportion of collagen which is thought to provide extra strength when under torsion where the outer annulus will have to resist a greater movement [28]. The strength of this structure is therefore anisotropic. If the fibres were not aligned in this fashion then there would be little stiffness in shear. The angle of the fibres vary as load is applied thus allowing the annulus to deform and also giving it visco-elasticity when compressed under load [32]. As the layers of collagen are arranged as alternate sheets, it can be imagined that such a structure, under load, would be susceptible to buckling. However, buckling inwards is resisted by the hydraulic pressure exerted by the nucleus. This pressure creates a hoop stress in the annulus which helps prevent buckling [31]. The construct of the annulus and nucleus is shown in Figure 1-10.

### *Nucleus Pulposus*

The nucleus consists of a jelly-like substance of high water content that serves to transmit load hydraulically in all directions. Some of the vertical load is transferred outwards to the annulus which is then loaded radially in hoop stress [3]. The nucleus acts as a piston that pushes against the vertebral end plates (VEP), deforming them, which in turn is resisted by the internal trabeculae of the vertebra. The nucleus has the ability to deform under pressure but retain its volume. This pressure keeps the annulus from buckling inwards which would otherwise damage the nucleus and de-strengthen the annulus. The nucleus accounts for 40-60% of the disc [28]. In a healthy IVD the loads acting axially are transferred radially by the internal pressure of the pulposus (intradiscal pressure) to the annulus. With aging, the proteoglycan content of the nucleus decrease and so the water binding ability reduces [48]. This alters the intradiscal pressure and load transfer mechanism. Therefore, as the pressure in the nucleus drops the load on the annulus increases [49]. This exposes the annulus to increased risk of tears or fissures with in turn can lead to herniation of nucleus material; a possible cause of inflammation and cord or nerve root

compression. Miller et al. [50] found that by 50 years of age 97 % of discs examined from 600 autopsy specimens were found to be degenerative [50].

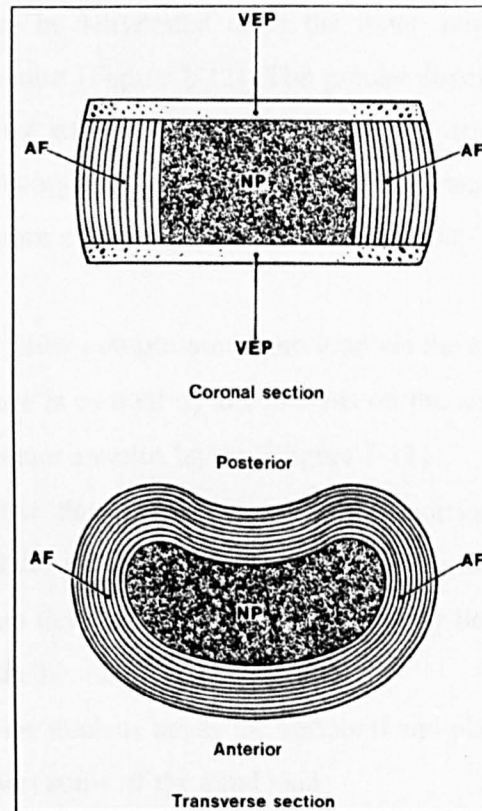


Figure 1-10 Intervertebral disc diagram showing section in coronal and transverse planes [32]  
(VEP: vertebral end plate, AF: annulus fibrosis, NP: nucleus pulposus)

#### **1.4 The Functional Spinal Unit and Load Transfer**

When considering the motions and loads in the spine, it is helpful in analysis to reduce the levels under consideration to a single functional spinal unit (FSU) as described by White & Panjabi [3]. The FSU consists of a vertebra-disc-vertebra section considered separately to the entire vertebral column. This makes analysis of motions simpler although at a cost in terms of accuracy of analysis. The mechanism of load transfer from vertebra to vertebra is via the IVD. The healthy IVD transfers pressure, resulting from the vertebral load, evenly across its entire surface [51]. However, the vertebral endplates are strongest at the periphery (supported by cortical bone) and weakest at the centre. In this region the nucleus can deform the plates when under extreme load. Traumatic high-loading usually results in damaged

vertebra rather than damaged discs. The nucleus is in hydrostatic compression and this puts the annulus lamellae in tension [Figure 1-11]. This tension diminishes towards the exterior lamellae. The annulus is therefore able to resist compressive load without buckling. In dehydrated discs the inner annulus layers can buckle inwards towards the centre [Figure 1-12]. The precise function and reaction of the FSU will depend on the nature of the loading regime: magnitude of load, steady state (standing), oscillatory (walking/running), shock (trauma or harsh landing or heavy lifting). Under normal loading the IVD behaves thus:

- The nucleus is under compression from load via the adjacent IVD endplate
- A radial pressure is exerted by the nucleus on the annulus resulting in hoop stresses in the inner annulus layers [Figure 1-11]
- In a healthy disc the annulus supports a proportion of the load from the adjacent end plates without buckling inwards towards the nucleus
- The annulus can deform to allow FSU flexion by bulging outwards, but not inwards towards the nucleus
- Pressure from the nucleus bends the vertebral end plates in the central region and helps support some of the axial load
- The load over the surface of the endplates is evenly distributed [37]

In transient, high-load IVD shocks, it has been suggested that:

- Endplate deformation induces blood flow out of the vertebra [43, 44]
- When this flow velocity is insufficient for the rate of deformation (volume reduction), burst fracture can occur [52]
- However, more recent work by Ochia and Ching [53] has not demonstrated the hypothesised increase in hydraulic pressure necessary in the flow-dependant burst fracture theory.

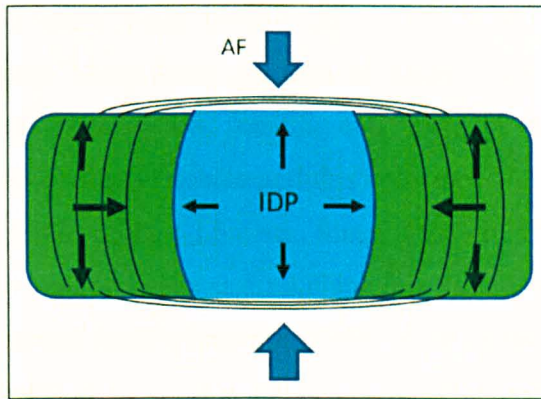


Figure 1-11 Intra-discal pressure (IDP) shown diagrammatically with opposing tensile annulus forces (AF)

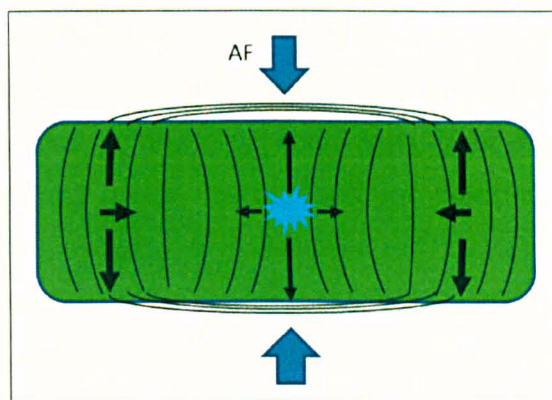


Figure 1-12 Diagrammatical disc showing dehydrated nucleus and inner annulus lamellae leaning inwards

Transmittance of forces through the vertebrae themselves takes place in the cancellous trabecula bone that makes up the bulk of the vertebra. Each strut of trabecula bone will transmit forces depending on its orientation. Vertically aligned struts are under compression while horizontally aligned struts help stabilise the vertical loaded ones [Section 1.3.4].

### 1.4.1 Lumbar Spinal Biomechanics

Loading of the lumbar spine is complicated by its lordotic curvature, the positioning of the centre of mass (CoM) anterior to the torso, and the complex action of the ligaments and muscles that provide stability and motion. As the CoM is anterior to the spine, the unsupported spine would tend to fall forward. To counteract this turning moment, tension is required in the posterior muscles and ligaments and this

tends to increase the spinal loads axially, due to the short lever arms that these muscle forces act upon. These loads can then be many times body weight even in static equilibrium conditions such as standing and sitting [1, 47]. The highest loads are experienced by the lowest vertebrae and this coincides with the higher incidence of DDD seen in the L5-S1 and L4-L5 discs. Since these discs have a higher loading and greater kinematic motion in the sagittal plane it is speculated that these facts are related [3]. The maximum range of motion (RoM) in FE of the lumbar vertebrae has been estimated to be 12° at L1-L2 and 17° at L5-S1 [3]. For everyday activity such as walking and sitting these values will be much less [1, 47].

In order to define a testing regime for artificial discs, a consensus on the description of the biomechanical coordinates is needed. The lumbar motions and loads are difficult to precisely measure due to the complexity of the area under investigation and difficulty in imaging access - as opposed, for example, to hip biomechanics which are more clearly understood. Because the FSU contains a visco-elastic joint, rather than a synovial joint (with constrained axes of motion), there is much more complexity to the motions. Hence, when all rotations, flexions and loads are considered, it is necessary to include all six degrees of freedom (three axial and three translational). Wilke [54] and White [3] have defined coordinate systems for describing kinematics of the spine. The coordinate system that has since been adopted by ASTM and ISO for spinal disc testing criteria is based on the Wilke axis system [Figure 1-13]. For the translational motions: x axis = AP shear, z axis = axial load, y axis = lateral shear. Rotational motions: x axis = LB, y axis = FE, z axis = AR.

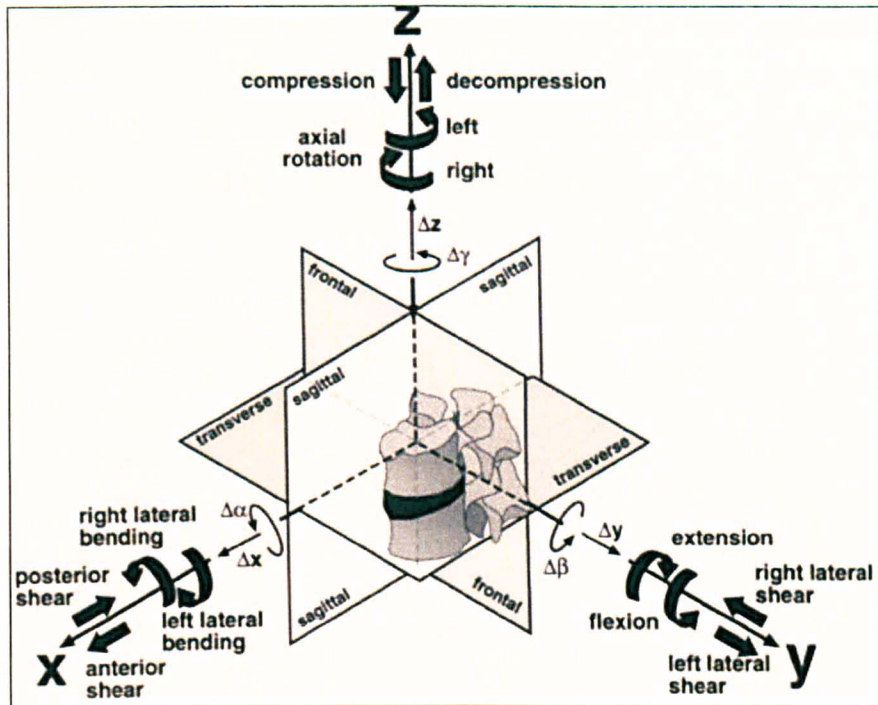


Figure 1-13 Axes definition for the functional spinal unit [54]

Approximately 2/3 body weight (BW) is supported by the lumbar spine [3] but there can also be several times body weight caused by compressive loads imparted by the spinal muscles. Walking results in approximately three times BW loads in the lumbar spine [1] and even inactivity can result in 1½ -2 times BW [47]. The kinetic motions defined by ISO 18192-1 are a sinusoidal approximation of reality. For example, the maximum axial load of 2000 N is approximately three times BW of an average weight person. The real *in vivo* motions have most thoroughly been reported by Callaghan et al [1]. The kinetic results were for the lumbar spine relative to the pelvis and the small sample number (n=6) was of healthy young men only. Callaghan et al. measured the range of motion for average walking cadence to be a mean of 6.46° for the lumbar spine in total. Figure 1-14 shows the standard ISO 18192-1 cycle and pictured in Figure 1-15 are the biomechanical measurements by Callaghan et al. compared with overlaid lines representing idealised motions and loads that show how sinusoidal approximation could be interpreted. The biomechanics simulated by the ISO standard are explained in section 1.5.

Morlock et al. (2000) [55] reported dynamics of the lumbar spine for nurses with and without low back pain. Their results showed that 0-15° flexion was the most

common magnitude of bend for 42 % of the time. This was followed by extension of 0-15° and flexion of 15-30° for 21 and 22 % of the time. If it is possible to simply divide by five (five discs) then this would equate to 0-3° as the most common bending flexion followed by a less often extension also of 0-3°.

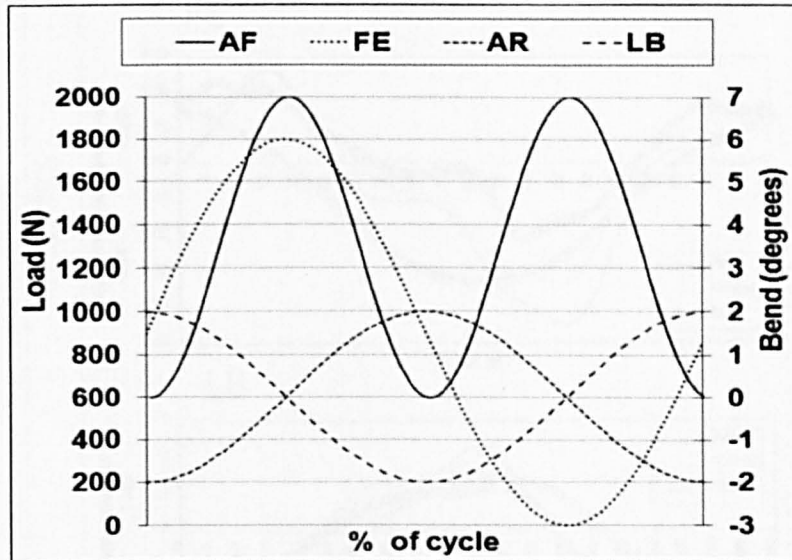


Figure 1-14 Standard ISO input cycle used in wear testing



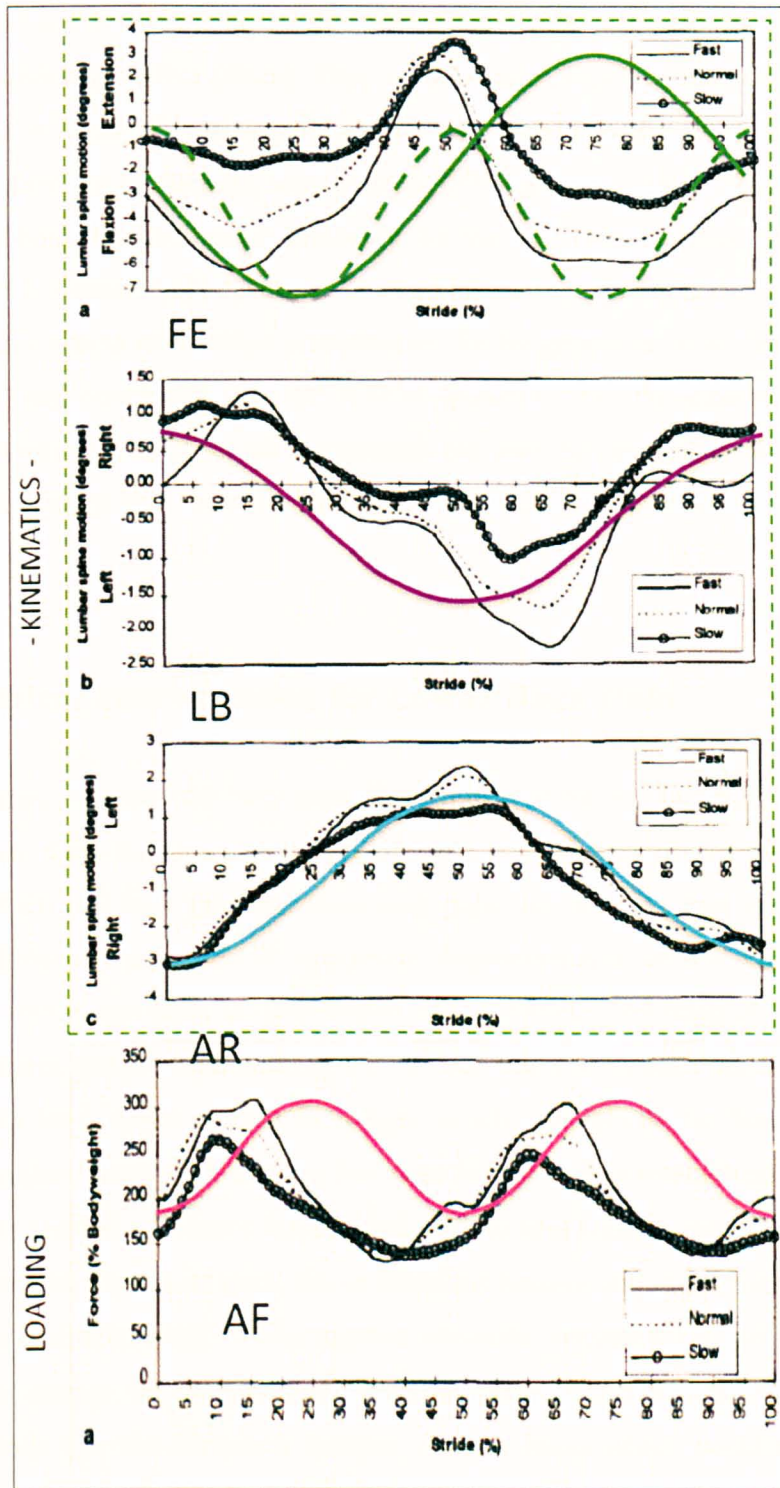


Figure 1-15 Plot of Loading (bottom) and kinematics (top three) from Callaghan et al. [1] with overlaid sinusoidal cycles

More recently, Cobian et al. [56] found similar overall amplitudes of motion to Callaghan et al. (and also not sinusoidal data). They found that the most frequent motions were those of small amplitude (5-15° for the full lumbar segment). The

median RoM at L4-5 was 2.2°, but this was calculated by reducing the full segment motion by dividing by five (discs). They went on to extrapolate their data for a full year *in vivo* in terms of total degrees moved and found that the ISO standard most closely matched the FE motion; whereas the ASTM guidance most closely matched the LB; and both standards were in-between for the AR. Total motions per year were found to be 2-3 times more than the standard, assuming 1 million cycles (MC per year), but this was in some ways compensated for by greater angular flexions in the standards. They concluded that the ASTM guideline was the closest to *in vivo* motion in terms of total angle moved through per year, however, they noted that the effects on tribology that these larger flexions have compared to *in vivo* reality are unknown.

## **1.5 Surgical Interventions for Lower Back Pain**

There are many reasons for back pain, from injury or trauma to natural aging and degeneration. One fundamental aspect of LBP is the onset of degenerative disc disease (DDD) and how this correlates with pain. As the disc ages it degenerates naturally, however, advanced or aggressive degeneration is termed DDD. This is correlated with issues such as dehydration of the nucleus, lowering of disc height, annular fissures and the herniation of the nucleus material through the annulus. The disc nucleus loses water content as it ages which can disturb the function of the nucleus-annulus interface. A nucleus that is no longer able to hydraulically force the annulus into tension will leave the annulus open to abnormal loading that may lead to an increase in fissures or tears. Nerve roots can become impinged because of disc height loss and also when a disc nucleus becomes herniated and presses onto a nerve. The change in biomechanics resulting from DDD will also have other manifestations like the abnormal loading of facet joints which could cause early onset of facet degeneration and pain from arthritis.

The annulus of the disc has small blood vessels and nerves on the surface which have limited penetration [57]. Healthy IVDs are innervated to a depth of approximately 1/3 of the annulus thickness [58]. Since degenerated IVDs do not always result in pain (degeneration is a natural aging process) it is difficult to

correlate the two. It has been reported in work by Freemont et al. [58, 59] that in discs removed because of LBP, the discs were found to be more highly innervated and vascularised to the inner 1/3 of the disc and pulposus, suggesting that painful degeneration is connected with nerve ingrowth deeper into the disc. This ingrowth is postulated to be because of an increase in vascularisation due to damage [58]. From approximately the 3rd decade of life the end plates become steadily more avascular and ossified, which limits the transition of nutrients in their diffusional process across the disc tissues [57]. The disc is primarily made of fibrocartilage that has a very low density of cells per unit volume so as the supply of nutrients to the end plate of the disc decreases, so does its ability to naturally repair. In attempting to repair, it has been hypothesised that an increase in blood vessels and nerve ingrowth is encouraged, but, because of the low density of cells, this process mainly results in pain, rather than repair [58].

The most common IVD degenerative levels are between L4-S1 [60] and this is the indicated level for most TDRs. Recent research by Siemionow et al. [61] has confirmed that L5-S1 has a pace of degeneration greater than other lumbar levels showing degeneration much more rapid before 40 years and slower after 40 years.

### **1.5.1 Fusion between Vertebrae**

Fusion is considered the 'gold standard' of treating severe back pain due to discogenic pain that has been incurable through conservative methods. Discogenic refers to pain related to the disc itself rather than radiculopathy from herniation. Spinal fusion is the fusing or immobilising of a painful joint by ossification (arthrodesis) of the adjacent bones to prevent motion and therefore reduce pain. The pain-causing disc is usually (but not always) removed with the long-term goal of inducing bone growth in the disc space which will prevent motion at that level. When fusion rods and screws are used in conjunction (Figure 1-16), there is a risk of stress shielding that can result in a loading regime that is not biologically favourable to bone healing. The stress shielded healing bone may not have adequate stress needed to produce bone growth (Wolff's Law). This can result in bone resorption producing a weakening of the fusion site and non-union with the onset of pseudoarthrosis where the unsuccessfully fused area becomes painful due to movement.

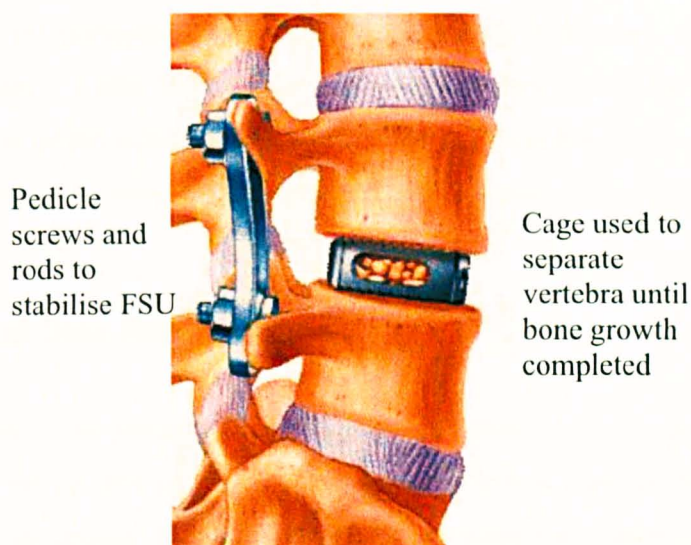


**Figure 1-16 Fused vertebra – disc space filled with new bone growth and secured with plates**  
 [Image modified from University of Maryland]

Obviously a fused spinal unit can no longer flex. This has to be compensated for by extra flexion of the adjacent spinal units and thus increased stress is introduced which is hypothesised to speed up the onset of DDD in other discs [62-66]. Lee et al. [63] found five of 18 fusion patients had adjacent level disc disease (ALDD) after an average of 8.5 years. In comparison, a systematic review of the literature by Freemon et al. [67] compared Prodisc and Charité results (comprising eleven retrospective cohort studies, eight case series, seven prospective cohort studies, two randomised trials, and two systematic reviews) found no evidence of reduced ALDD compared to fusion. But since then other reviews by Harrop et al. [65] have found that 34 % of fusion and 9 % of arthroplasty patients developed ALDD and concluded there was a reduced risk of ALDD after TDR.

One of the primary reasons for developing an alternative to fusion is to maintain as closely as possible the normal FSU kinematics. After a fusion the dynamics of the FSU are drastically altered. The fusion restores stability, but the kinematics of the adjacent FSUs are changed. They now have to compensate for the reduced motion at one FSU and consequently there may be an increased risk of adjacent level DDD. There are other disadvantages such as pain resulting from harvesting of bone from

the iliac crest and a reduction in the biomechanical motions of the spine that may lead to a reduction in patient comfort. The anterior replacement of damaged discs is advocated over posterior fusion surgery because the latter can result in paraspinal muscle damage. Using fusion there are also occurrences of iliac crest pain due to inflammation of the autograft site where bone has been harvested. This bone is used in order to facilitate new bone growth in the IVD space.

### 1.5.2 Total Disc Replacement

One solution to the perceived long-term degenerative problems presented by fusion is the TDR device. For an active younger patient this is believed to be a much more satisfactory procedure due to overcoming biomechanical limitations of fusion. The procedure requires the removal of the diseased disc and replacement with an artificial TDR. An example x-ray comparison between fusion and TDR is shown in Figure 1-17.

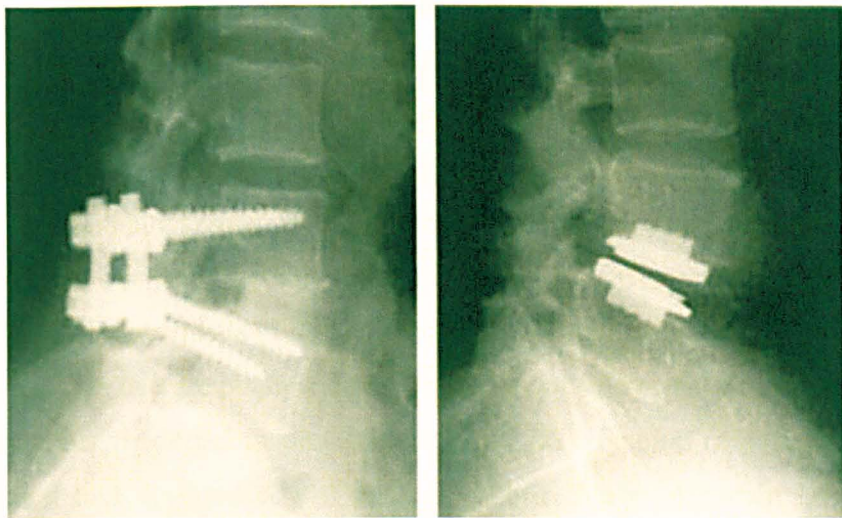


Figure 1-17 X-ray images of a fusion using pedicle screws and rods (left) and an implanted TDR device (right) [image: Orthopaedic Center of Southern Illinois]

By maintaining similar biomechanics to the natural FSU it is hypothesised that the risk of adjacent level DDD is reduced [17, 18]. Articulating, mechanical discs have no shock absorbing ability and although the natural IVD performs little shock absorbing duties, the ability of the nucleus to deform the endplate is lost. The long-term implications of this biomechanical change are unclear. The natural IVD also

has a dynamically changing (non-linear) resistance to rotation (torque) dependant on angle of flexion. The replacement articulating disc does not follow this dynamic and actually has a resistance to rotational motion that is quite different. Visco-elastic disc have been postulated to replicate the ‘quality’ of motion as well as the absolute kinematics, but so far the results *in vivo* have been poor [69, 70].

Due to the lack of suitable technologies required to manufacture a flexible natural-disc imitating device, most TDRs are of the articulating bearing type, relying on a technology based on hip and knee replacements. They are therefore a replacement that is different in concept to the natural function of the disc and subject to tribological problems.

## **1.6 Tribology Theory**

The name tribology covers the science and technology of interacting surfaces in sliding contact. The study of tribology includes wear, friction, fatigue and lubrication. Friction is the resistive tangential force that occurs when one body slides or rolls over another and it acts in the direction opposite to motion [71]. If two bodies are in contact and a tangential force is applied to one, the force preventing initiation of motion is the static friction force. Once this force is overcome, the force required to maintain sliding is the kinetic (or dynamic) friction force which is usually slightly less than the static force. In bearing systems, including natural joints and total joint replacements (TJR), friction is undesirable as it may be indicative of wear (though the two are not necessarily related as was demonstrated in low friction PTFE materials first tried in replacement hips [72]). Fatigue in TJR can lead to delamination in polyethylene (PE) surfaces. Lubrication is important for reducing friction and wear and is usually of critical importance in MoM TJR. Wear between surfaces in contact is the removal of material or damage of one or both surfaces. Usually wear takes place because of contact between asperities of the surfaces. Types of wear are categorised as, adhesive, abrasive, fatigue, and tribochemical [Figure 1-18].

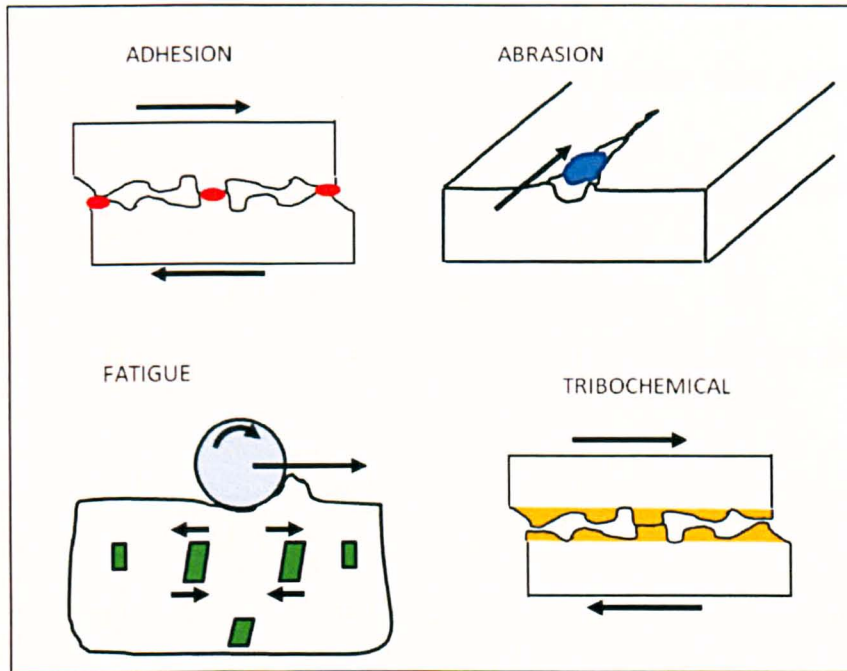


Figure 1-18 Types of wear: adhesive, abrasive, fatigue and tribo-chemical

#### *Adhesive wear*

Contacting asperities adhere (or weld) momentarily before sliding contact shears them. These fragments can then become attached to the opposing surface. As sliding continues, the fragments can then be re-transferred back to the original surface or form loose wear particles (debris). Adhesive wear is commonly associated with like-on-like bearing couples where the surface attraction and/or friction are high.

#### *Abrasive wear*

Asperities of a hard surface or hard particles embedded in a surface damage a softer surface in sliding contact which deforms by plastic flow or fracture. There are two types of this wear. Firstly, the harder surface asperities abrade the surface (two-body abrasion). Secondly, the hard particles are trapped between the surfaces and cause wear to one or both the surfaces (three-body abrasion).

#### *Fatigue wear*

Cyclic rolling or sliding contact repeatedly loads and unloads the surface and subsurface material. This may induce fatigue cracks below or at the surface which will eventually form large fragments leaving pits in the surface (pitting).

### *Tribo-chemical wear*

Corrosion of the sliding contact surfaces may occur. Under these conditions the surface film that is formed may:

- form a protective barrier that prevents further damage (e.g. TiO<sub>2</sub> layer that protects titanium artificial implants from corrosion)
- form a layer that has weak wear resistance (e.g. TiO<sub>2</sub>)
- form a layer that has strong wear resistance (cobalt-chrome passivation layer)

To reduce wear and friction, lubrication is used. In joint replacement this lubrication is either the body's own natural synovial fluid (a weaker version of the fluid is produced when a synovial membrane grows around the joint arthroplasty) or it is due to blood, interstitial fluid etc. Unlike the most common lubrication system examples such as car engine journal bearings, implanted device lubrication is passive, in that there is no scope to pump lubricating fluid between the articulating surfaces in an active way such as is done for the car engine bearings example (or in the natural synovial joint by boosted or biphasic lubrication). Bearing designs for arthroplasty should ideally be capable of entraining lubricant between the articulating surfaces in order to attempt to reduce direct asperity contact and resultant wear.

### **Bio-tribology**

The term bio-tribology was coined in 1973 by Dowson and Wright to cover all aspects of tribology concerning biological applications, be they natural synovial joints or artificial orthopaedic joints replacements [73]. The study of wear associated with joint arthroplasty doesn't just rely on the knowledge of wear and lubrication. The study of the wear debris has in recent years been shown to be of significant importance. Studies in hip joint replacements has linked osteolysis and aseptic loosening of femoral stems with the biologically non-inert wear debris produced by the articulating ball and socket joint [74, 75]. The wear of artificial joint replacements gives rise to two main problems:

- Wear may generate biologically active particles and/or metal ions



- Wear will yield a change in surface morphology that can affect function

The control of this wear mechanism by selecting suitable materials for the prostheses' environment and of understanding the biomechanics of operation is therefore very important.

### 1.6.1 Lubrication Regimes

Lubrication provides an inter-surface layer that ideally will separate the surface asperities, reduce friction and prevent wear. The natural synovial joint has a very low coefficient of friction and a combination of lubrication regimes that keep the joint surfaces apart. The natural IVD is not a synovial joint, however, the most common articulating bearing types of TDR attempt to use a design rationale that is known to work for replacement hips and knees. Lubrication regimes that characterise the inter-surface behaviour of bearings in motion are split into three groups [Figure 1-19]: hydrodynamic, mixed and boundary. The ratio  $\lambda$  is used to differentiate between them:  $\lambda = \frac{h}{R_a}$ , where  $h$  is the film thickness and  $R_a$  is the combined average roughness value of the surfaces. In terms of the load support provided by the lubricant, the most favourable is full separation enabled by hydrodynamic lubrication, followed by mixed lubrication where at least some of the surface asperity contact is reduced; and finally, the least ideal is boundary lubrication because this allows direct contact. However, in the presence of a solid lubricant adhered to the surface, the drawbacks of boundary lubrication can be mitigated. For example, it is believed that protein adherence to artificial bearing surfaces may reduce wear while increasing friction [76].

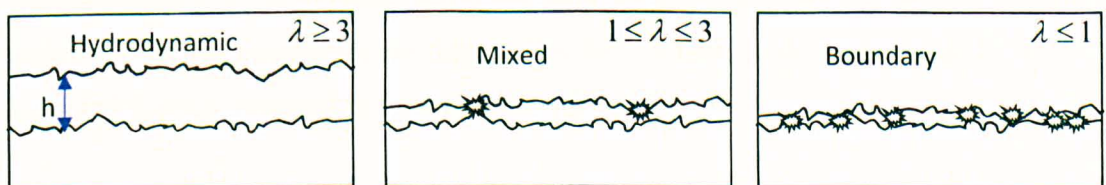


Figure 1-19 Lubrication regimes showing asperity contact in mixed and boundary lubrication, where  $\lambda$  is the film thickness ( $h$ ) divided by  $R_a$

### **1.6.1.1 Hydrodynamic Lubrication**

Hydrodynamic (or fluid film) lubrication is said to occur when a continuous film of lubricant is dragged (entrained) in between the surfaces that are moving relative to each other and fully separates the surface asperities from each other. It is similar to the type of lubrication that protects the natural synovial joint - Micro Elastohydrodynamic and squeeze-film lubrication [77]. The full fluid film occurs when the ratio of lubricant thickness to asperity height is greater than three. Hydrodynamic lubrication is an ideal regime for an artificial replacement joint to operate in as this would give virtually zero wear; however, this is unachievable in practice because in order to create enough separation of the surfaces, the lubricating medium needs to be pressurised or of very high viscosity.

#### **Elastohydrodynamic (EHL)**

This is a modified version of fluid film separation. The fluid film exists even though it appears to be too thin. One or both of the two surfaces deform due to the extremely high local pressure of the lubricant. This makes the surfaces more conforming and hence more likely to support a full fluid film. This mode of lubrication was theorised in order to explain the exceptionally long life of gears in gearboxes of machinery. Since then it has also been theorised to account for the very low friction and wear in articular cartilage [77].

#### *Lubrication in the Natural Synovial Joint*

##### **Micro EHL**

Micro EHL is theorised to exist on a microscopic level in the natural synovial joint. Cartilage roughness is too high to account for the seemingly hydrodynamic and low friction response of these joints. But it has been demonstrated that microscopic EHL, where the cartilage asperities are flattened by EHL action, could account for the low wear and friction observed in natural healthy joints [77].

### **Squeeze Film**

The process describes the response to the application of a temporary increase in force which is resisted by the viscosity of the lubricant. The finite time it takes the lubricant to escape helps the surfaces stay apart and therefore reduces wear.

### **Boosted Lubrication**

If the lubricating film becomes too thin, the water content of the synovial fluid reduces by entering the cartilage, leaving a highly viscous high molecular weight protein gel to protect at the boundary surfaces.

### **1.6.1.2 Boundary Lubrication**

Boundary lubrication is the opposite of hydrodynamic. This is a condition where there is no separation of the mating surfaces by a flow of viscous-shearing lubricant. Instead, the surface asperities carry the full load applied to the surfaces. This is similar to not having any lubrication at all except that it may be possible for surface layers to form by adsorption that then help protect them from wear. In MoM hip replacements it has been hypothesised that an metallo-organic boundary layer assists with favourable lubrication [78]. In MoP hips adsorbed albumin protein has been linked to increased friction due to the boundary layer effect [76].

The Stribeck plot can help visualise the lubrication regime, an idealised plot is shown in Figure 1-20. The coefficient of friction is plotted against the product of viscosity, sliding speed and radius divided by load. The initial section, with high coefficient of friction, indicates boundary lubrication. The mid-section shows a reduction of friction as the mixed lubrication regime separates the asperities. The rising point of the curve indicates that as the fluid film thickness increases, shearing force and hence friction increases.

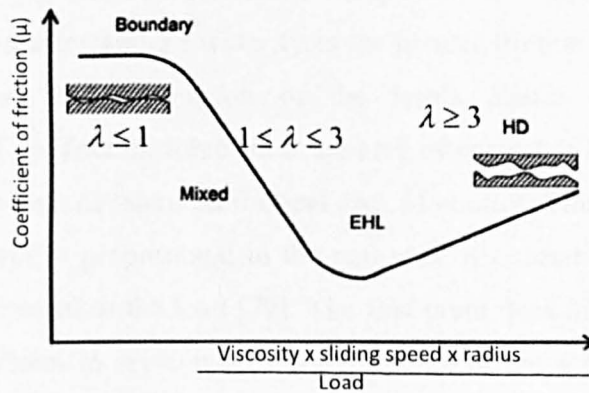


Figure 1-20 The Stribeck Curve Shows Friction as a function of film thickness caused by the effects of viscosity, velocity and load (logarithmic plot)

### 1.6.1.3 Mixed Lubrication

Mixed lubrication is said to exist when the load is shared between the contacting asperities on the surface and the pressure of the lubricant resulting in a partial separation of the surfaces. As this is a mixture of full fluid film and boundary lubrication it is called mixed lubrication. Increasing the loads on a joint or decreasing the angular velocity will cause the lubrication regime to fall from fluid film to mixed and, in severe cases, to boundary.

### 1.6.2 Friction

Fundamental to the study of tribology is the friction generated between bodies wholly or partly in contact. Da Vinci was the first recorded person to have formulated the modern understanding of frictional response but it was Amanton who rediscovered and published these laws and later Coulomb added a 3<sup>rd</sup>:

1. Frictional force is independent of surface area
2. Frictional force increases as the load is increased
3. The dynamic friction is independent of sliding velocity

The second point is intuitive but the first may be considered counter-intuitive but holds for relatively inelastic materials, though not for highly elastic ones. For example, performance cars use wider tyres for greater friction and hence cornering forces, generated by deformation of the tyre's elastic contact patch. The independence of the friction force from the area of contact is because the apparent area of contact is not the same as the real area of contact. This can be explained if the frictional force is proportional to the real area of contact and the real area of contact is proportional to the load [79]. The first point does not hold for extremely polished flat surfaces in dry contact where the ratio of the apparent to real area of contact is low.

Since the friction force ( $F$ ) is proportional to the applied perpendicular load (normal load,  $N$ ), there is a constant of proportionality,  $\mu$ . From point 1 we have  $F = \mu N$ .

### **1.6.3 Wear**

The consequence of two sliding surfaces under an applied load is that one or both will wear. Archard's wear equation [80] demonstrates the proportional relationship between the sliding distance ( $x$ ), the load on the surface ( $W$ ) and the amount of volumetric wear this creates ( $V$ ). The Archard wear law is shown in Equation 1-1, where  $K$  is the wear factor. This is an experimental constant and is related to the hardness of the surfaces as well as other tribological factors such as lubricant used, roughness, etc.

$$V = K.W.x$$

**Equation 1-1 Archard wear equation with wear factor  $K$**

### **1.6.4 Bio-tribology Considerations in Total Joint Replacements**

Total hip and knee replacements are the most prominent arthroplasty procedures and as such the knowledge gained from these devices is used when considering new designs such as TDRs. Total knee replacements have become as prevalent as THR and should probably be considered the most relevant technology when considering

the lubrication in mobile TDRs as the highly non-conforming bearing surfaces give rise to high stresses and boundary lubrication. Knee replacements utilise MoP bearing surfaces because other materials, such as ceramic-on-ceramic and metal-on-metal, will not work in non-conforming bearing design. Using the lubrication theory of Hamrock and Dowson [81] it can be shown in theory that the lubrication regime in all the TDR artificial articulating discs is boundary in nature [82, 83]. As such, it then needs to be assessed if the high wear rates associated with largely boundary lubricated devices is acceptable.

#### **1.6.4.1 Cross Shear Motion**

Contemporary joint replacements are available in various material combinations, principally ceramic, polyethylene and metal. Ultra-high molecular weight polyethylene (UHMWPE) has highly kinematic-dependant wear characteristics related to the input motions at the bearing surface. The effect those motions have on the material wear performance is indicated by cross-shear (CS) ratio. This refers to the ratio of the amount of work done (frictional force\*sliding distance, Equation 1-2) in the principle direction of sliding (the longest motion path direction, Figure 1-21) to the work done in total [84], shown in Equation 1-3. Sometimes the ‘aspect ratio’ is also referred to in explanation of motion patterns. This is the ratio of the shortest to longest width of the motion track and can be an approximate guide to the amount of crossing path motion present.

$$W = Fd$$

**Equation 1-2 Work done is the product of frictional force (F) and sliding distance (d)**

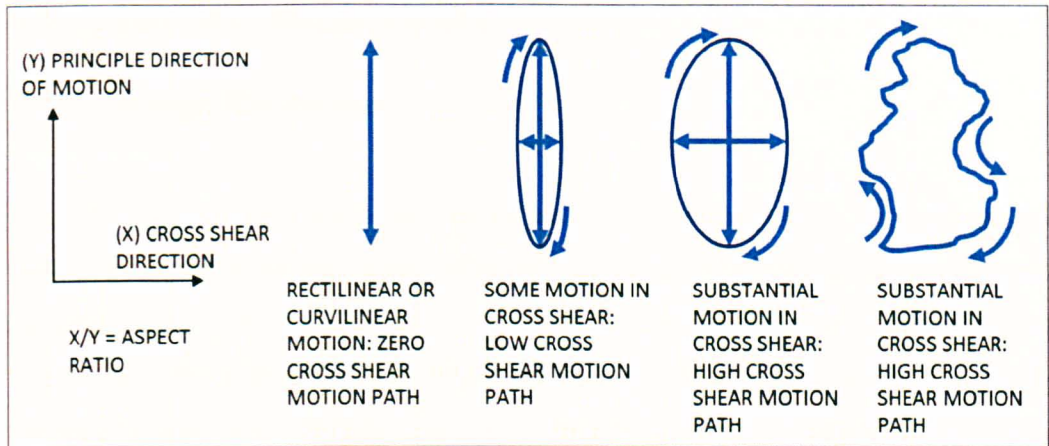


**Figure 1-21 Example motion paths at a bearing surface and the principle direction of motion**

$$CS = \frac{W_{cross-shear}}{W_{total}}$$

**Equation 1-3 Cross shear ratio is the quotient of work done (W) in cross shear and work done in total by the friction force**

UHMWPE is a semi-crystalline polymer with regions of amorphous polymer chains. When a hard material such as CoCr slides against it in a rectilinear manner, the polymer chains begin to align in the direction of sliding and hence strain hardening is said to occur. In this situation, extremely low wear rates can be achieved. However, in motions that have a component of motion orthogonal to the principle direction, strain softening takes place where the PE chains are sheared perpendicularly to the principle sliding direction and hence wear is increased. Input cycle motions that produce surface bearing slide tracks in a multi-directional are said to be of higher CS ratio. Input kinematics of a purely rectilinear nature (e.g., pin on plate tests) or curvilinear (e.g. flexion-extension only) are described as zero cross shear and hence very low wearing. Modern cross-linked UHMWPE aims to maximise resistance to crossing path motions by the application of cross-linking to some of the PE chains. This is done by gamma irradiation, causing some of the chains to break and reform connections between chains, therefore increasing resistance to strain softening.

## **1.7 Total Disc Replacement**

### **1.7.1 Design Rationales**

Over the past 25 years the fusion procedure has advanced to the stage where it is widely believed to be the 'gold standard' treatment. However, in other corrective surgeries of the joints, the aim is to not just to reduce pain but also maintain motion. With fusion the primary goal is to reduce pain by the elimination of motion. The theorised consequence of fusion (discussed in section 1.5) is the onset of DDD in the adjacent discs which can also cause more pain. This cascading effect is caused by the adjacent levels necessitating extra motion to accommodate the restricted motion at the fused site. A study by Huang et al. [85] found that TDR recipients after a mean period of 8.7 years had a lower level of ALDD. Patients with motions of 5° or greater had a 0 % prevalence of ALDD. Patients with motion less than 5° had a 34 % prevalence of ALDD. Therefore it is believed that the effect of ADDL could be reduced if maintenance of motion at the diseased site was possible. The treatment of severe discogenic back pain by surgery to replace a natural disc with a prosthesis that preserves motion is a concept that could revolutionise the treatment, and postponement, of the onset of degenerative disc disease.

The most successful designs for the lumbar spine use the articulating bearing design rationale familiar in knee and hip replacements. Elastomeric designs for the lumbar region, such as the Acroflex (DePuy Acromed), have so far proved unreliable [70] and more recent designs such as the M6 (Spinal Kinetics) and Cadisc-L (Ranier Technology Limited, Cambridge, UK) are yet to be proved in published clinical trial.

The most prevalent lumbar TDRs at this time are: Prodisc (Synthes Spine, Warsaw, Indiana, USA) and Charité (DePuy Spine, Raynham, MA, USA) [Figure 1-22]. The first TDR device to be implanted was the SB Charité in 1984. It was conceived and developed in the 1980s by Karin Buttner-Janzand and Kurt Schnellnack at the Charité hospital, Berlin. The Charité has a mobile UHMWPE core that is permitted to move between the two end plates in order to replicate the way the natural disc's nucleus and centre of rotation (CoR) moves in the AP axis during FE. The superior



and inferior end plates are of CoCrMo and have concave polished surfaces. The mobile centre is of UHMWPE and has a convex surface on each side. The device gained FDA approval in 2004.

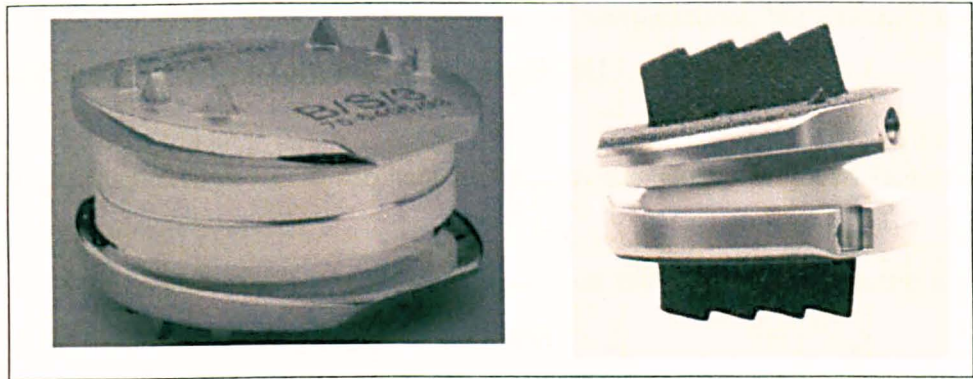


Figure 1-22 Principle total disc replacement design examples: Charité (left), Prodisc-L (right)

The first Prodisc design was conceived by Thierry Marnay in 1989 with the first implantation in 1990. In comparison to the Charité TDR, the Prodisc is an articulating bearing design with one bearing surface interface rather than two. The superior plate is concave and acts as one articulating bearing face. The inferior plate attaches a snap-fit UHMWPE core with a convex face that articulates against the superior plate. The device gained FDA approval in 2006.

Only two TDRs are approved in the US, but there are more TDR designs available in Europe. The Maverick (Medtronic, Minneapolis, MN, USA) design, conceived in 1990s by Denek medical and further developed in 2001 by Medtronic Sofamor Danek, uses the design rationale associated with MoM THR. The device was engaged in an FDA approval study until patent-related litigation forced a withdrawal from the US market. The Flexicore Disc (Stryker, Kalamazoo, MA, USA) is similar in concept to the MoM ball-and-socket Maverick device; the Mobidisc (LDR Médical, Troyes, France) and Activ L (Aesculap AG Tuttlingen, Germany) are similar to the Prodisc (ball-in-socket, MoP) but have the translational mobility of the Charité; the Kineflex (Spinal Motion, South Africa) is similar to the Charité design (mobile core) but has MoM bearing surfaces. All these disc designs are roughly separated in to two design rationales of articulating disc, dependant on the degree of constraint.

### 1.7.1.1 The Meaning of Constraint

In TDR technology the terms constrained, semi-constrained and unconstrained refer to the type of motion allowed by its design and is important when considering RoM, DoF and facet joint loading. There is no standard nomenclature, but a biomechanical description has been put forward by Bertagnoli [86]:

1. Constrained – has a mechanical limit to the motion allowed (e.g. visco-elastic devices)
2. Semi-constrained – has a mechanical limit that may be outside the normal RoM of the spinal segment (e.g. Prodisc)
3. Unconstrained – has no (or little) mechanical limit to the RoM permitted (e.g. Charité device)

Point 2 and 3 have also been described by Cunningham et al. [87] as referring to ball-in-socket and mobile core TDRs, although they also described mobile bearing devices as having six degrees of freedom, which is unfeasible in the case of the Charité (no axial translation). Palepu et al. [88] have described the three-rotation, fixed CoR TDR as a constrained design, but also describe the Prodisc as semi-constrained. Some confusion arises when the description of constraint of a device is not clearly in terms of RoM, lateral translation or number of DoF. Since the Prodisc and other ball-in-socket type devices have constraint in the transverse plane – and this is the main difference between these and the unconstrained design such as the Charité – it could be argued that the term constrained is more appropriate rather than semi-constrained. Also, visco-elastic prostheses offer limited constraint in all planes of motion and axes of rotation and are therefore more “semi-constrained” in nature.

For the purposes of this thesis, the most common term, “semi-constrained” will refer to the ball-in-socket (Prodisc) design of TDR and “unconstrained” will refer to mobile bearing (Charité) type design. Where the word “constrained” is used, it will refer to constraint in the transverse plane, especially in the AP direction.

The two most common TDR devices at present are the Prodisc (semi-constrained MoP) and the Charité (unconstrained MoP). The perceived advantage offered by the

unconstrained device is that it more closely resembles the physiological motion of the FSU. When flexed, the FSU has been shown to shift its CoR depending on the position moved to. At any one time it has an instantaneous axis of rotation (IAR) that may or may not shift as the biomechanics change with motion. The semi-constrained devices have a CoR and IAR that are the same, due to the fixed CoR. A plot of IVD centres produces a locus [Figure 1-23]; this has important implications as far as facet joint loading is concerned. If the CoR of the device is fixed then the facet joints now have to contend with altered biomechanics which may lead to increased or unnatural loads and therefore early degeneration of the facets [89, 90].

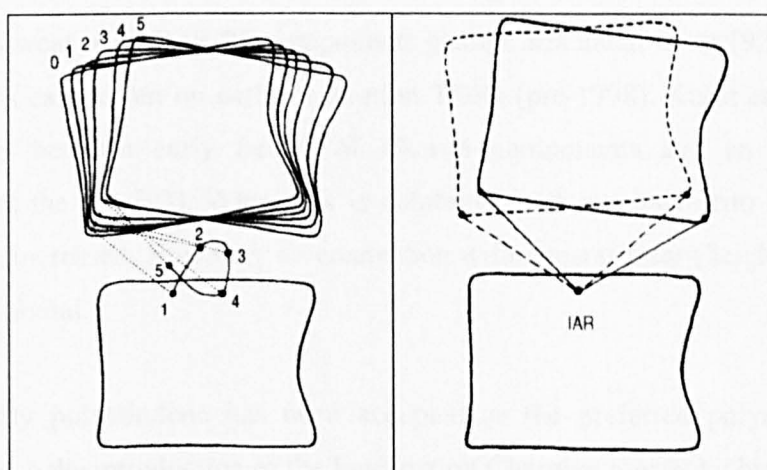


**Figure 1-23 Locus of instantaneous axis of rotation points through flexion-extension of the functional spinal unit [32]**

Rousseau et al [90] compared Prodisc and Charité replacement disc effects on 12 cadaveric spines. The facet forces were larger in lateral bending for the Charité device (though not significantly), while the Prodisc design seemed to protect the facets from overloading during high extension. Any analysis will be strongly dependant on surgical positioning of the device, which on a cadaver model will be easier than on a live patient. The positioning effect was discussed by Dooris et al [91] who found that the loads on the facet joints were sensitive to AP positioning of the centre of rotation of the TDR device.

### 1.7.1.2 Material Combinations

Material combinations used in articulating designs of TDR are similar to total hip and knee replacements: metal on polyethylene (MoP) and metal on metal (MoM). A ceramic on ceramic (CoC) design has yet to be created for the lumbar TDR. Metals used in joint prostheses bearings are predominantly cobalt chromium molybdenum (CoCrMo) alloys, due to this metal's superior wear resistance, high strength and anti-corrosive properties. It also polishes well, which increases the wear resistance further because of the lubrication improvement gained by low roughness.

Oxidation and embrittlement have historical significance in THR and TKR in accelerated wear of UHMWPE components gamma irradiated in air [92]. A similar process was carried out on early generation TDRs (pre-1998). Kurtz et al. found a relationship between early failure of Charité components and an increase in oxidation at the rim [93]. When this is combined with excessive rim loading, the failure rate increased. However, no connection with general wear (height loss at the dome) was found.

High density polyethylene has been accepted as the preferred polymer bearing material since the introduction of the low friction Charnley prosthetic hip joint in the early 1960s [94]. UHMWPE exhibits high wear resistance, inertness of wear debris (in general, but not for certain size particles) and "self lubricity (*in vivo*)" [94]. The inertness of the polymer to the biological host is compromised when the wear debris is generated at sizes that match the biological scale (typically 0.1-1  $\mu\text{m}$ ), whereby macrophages in the blood mistake the debris for foreign cells and try to consume it. As it is non-digestible the macrophages become giant cells (granuloma) and this can lead to osteolysis of the surrounding joint [75] leading to possible failure.

The MoP design used in the Charité and Prodisc and the MoM design seen in the Maverick TDR have been chosen because of the wealth of experience gained from MoP and MoM hip replacements that have exhibited acceptable wear results. Hip joints operate in the boundary or mixed lubrication regime for MoP and MoM [95, 96]. The design concept for total disc replacements has been based on this knowledge. However, the results from the MoM hip prostheses and results from

MoM disc replacements are not comparable, with TDR exhibiting much larger wear *in vitro* than THRs [97, 98]. This high wear might be explained by the difference in lubrication regime between MoM TDR and MoM THR.

## 1.7.2 Indications and Contraindications for Surgery

TDR is indicated for patients with discogenic pain associated with degeneration of the lumbar disc which has failed to improve after 6 months of conservative treatment. The age range is significantly younger than that seen in hip or knee replacements as back pain afflicts patients at an earlier age and older patients are contraindicated. This places more severe endurance demands on the disc due to the extended implant lifetime. A failure of a TDR device would lead to a more serious revision surgery than in a hip, i.e., necessitating disruption to the abdominal cavity, arteries and most importantly the spinal cord or nerves. Older patients who would theoretically benefit from TDR are contraindicated due to the need for healthy and strong intervertebral bone to minimise the risk of device subsidence or migration. A list of the salient FDA inclusion and exclusion criteria for the Prodisc are listed in Table 1-1.

**Table 1-1 Inclusion and exclusion criteria for enrolment in FDA TDR study (modified from Blumenthal et al. [99])**

<b>Inclusion Criteria</b>	<b>Exclusion Criteria</b>
DDD in 1 or 2 levels between L3 and S1	Greater than 2 levels of DDD
Back or leg pain	Vertebral end plate dimensions of < 34.5 mm ML or 27mm AP
Failure of at least 6 months of conservative treatment	Metal or PE allergies
Oswestry score >20/50 ( >40%)	Trauma at lumbar level
Radiographic evidence including:	Significant facet degeneration
1. 2mm disc height reduction	Osteoporosis or osteopenia
2. Instability of the IVD indicated by >3mm of AP translation or greater than 5° angulation	
3. MRI shows annular thickening	
4. Herniated nucleus	
5. Vacuum phenomenon	

### 1.7.3 Clinical Results

The Charité disc was the first disc of its type, being first implanted in 1984, and therefore has the longest period of *in vivo* performance. The success rates in non-controlled studies have been reported to be 77% for patients with no previous lower back surgery at a mean period of 3.2 years[100]; 79% at a mean period of 4.25 years [101]; and 70% at two years [102]. In a randomized FDA trial comparing Charité and fusion performance, the rate of patient satisfaction was found to be 74% vs. 53% respectively. The TDR patients had lower pain levels at all time intervals (except the 24 month point which was slightly lower), a decrease in re-operation procedures and an increase in back-to-work rates of 9.1% vs 7.2% respectively [99]. Zigler et al., reporting on the FDA exemption study, concluded that the Prodisc was superior to circumferential fusion for multiple clinical criteria. At two years post-operative, 92% of Prodisc patients and 85% of fusion patients reported an improvement in the Oswestry Low Back Pain Disability Questionnaire [103]. Although the fusion patients were satisfied, it should be recalled that the risk of ALDD for them may be greater [sec 1.5.1].

The initial Prodisc design was implanted into 64 patients (93 TDRs) with a period of approximately 5-8 years wait to see what the long-term outcome would be. A significant reduction in leg and back pain was recorded with 93% of patients reporting that they would have the procedure again [104]. In 2006 the Prodisc-L was granted Food and Drug Administration approval for implantation. Bertagnoli and Kumar reported a 100% excellent-to-fair patient satisfaction result for a cohort of 108 patients including 12 for multiple levels [105]. At a one year follow up Mayer et al. reported an 80% satisfactory outcome for a cohort of 34 patients [106]. Results from an FDA controlled randomised trial comparing Prodisc and a fusion procedure reported a significant improvement in the Oswestry disability score favouring the Prodisc TDR over fusion [107]. Maverick preliminary results by Le Huec et al [108] report a series of 64 patients with a follow up period of two years. They reported an improvement in the Oswestry disability score of 75% and found this improvement to be equivalent to that expected from an anterior fusion cage. An FDA trial of the Maverick has been taking place since 2003 but has not reached a conclusion.

Some studies comparing TDR to fusion have found equivalent or greater success rates for TDR in the short to medium term [99, 107, 109, 110]. Long-term results are not yet available. It is theorised that long-term results will be improved further by TDR because of the reduced probability of ALDD which may be inhibited by the preservation range of motion. A large long-term study of Charité patients (n=1,938) found that there was a significant difference between TDR and fusion outcomes for adjacent level degeneration at the 5 year point favouring TDR [111]. However, long-term results from the FDA Charité study analysed by Guyer et al. [109] at a 3-5 year follow-up period found that there was no significant statistical difference between patients receiving a TDR and those receiving an anterior inter body fusion. A summary of results is shown in Table 1-2.

**Table 1-2 Comparison of patient clinical assessment scores, back to work rate and patient satisfaction rates**

	ODI/VAS (% improvement)	Patient satisfaction (%)	No significant difference found
Fusion	84.5 [103]	62 [112]	Guyer et al. [109]
	25 [110]	53.1 [99]	
		81.4 [103]	
		78 [110]	
Prodisc	91.8 [103]	87 [112]	Guyer et al. [109]
		91.2 [103]	
Charité		73.7 [99]	
Maverick	71 [110]	95 [110]	

### **1.8 Wear in Total Disc Replacement**

First generation TDRs rely heavily on current hip and knee replacement technology, in particular the use of metal-UHMWPE bearings. Although articulating bearings provide excellent functionality in terms of reliability and longevity, they are subject to wear that produces debris in the form of sub-micron UHMWPE particles. Longer-term follow-up of TJR has highlighted the role of wear particles in the failure process, particularly in hip and knee prostheses [75, 113]. Here, UHMWPE debris can trigger a biological cascade with macrophage activation that instigates an inflammatory response and possible osteolysis within the surrounding bone [75,

114-116]. It is therefore necessary to wear test TDR designs in order to compare wear rates and volume of debris to existing designs.

### **1.8.1 Wear Testing**

Wear debris from spinal implants is hypothesised to play a role in the long-term clinical success rates for TDRs just as it has in THR and TKR [117]. Since long-term results are few, it is necessary to use *in vitro* testing to simulate *in vivo* response and analyse the response in terms of wear characteristics [118].

Two international testing documents have emerged: ISO 18192-1 (Sec 1.4.1) and ASTM F2423-05. Previous *in vitro* lumbar TDR wear simulations using the ISO 18192-1 standard or the ASTM F2423-05 guidance document have shown a wide variation in wear rates, in the range of 2-20 mg/MC for ISO-based inputs [97, 119-122] and between zero and ~0.1 mg/MC when ASTM guidelines were utilised [119, 123]. Whereas the ISO input motions run concurrently, those in the ASTM allow the user to input the test motions sequentially or in any combination chosen by the user, e.g. LB + FE. In the latter, the test conditions produce zero or very low cross-shear motion [84, 124-126] at the bearing surfaces, resulting in rates of wear that are typically two orders of magnitude lower than those observed in ISO defined (i.e. higher CS ratio) tests.

The difference in wear between curvilinear and cross-shear motion patterns has been demonstrated by Nechtow et al. [119] who showed that wear from cross-shear motions according to ISO-18192 produced 50-fold more wear than the same motions minus LB (i.e. curvilinear motions). The preferred test is the ISO-18192 standard [127] which is a sinusoidal approximation of known motion data gathered by Callaghan et al. [1], but also includes the option to apply an anterior shear force.

### **1.8.2 Typical Rates of Wear In Vitro**

#### **Prodisc (Synthes)**

The Prodisc is a semi-constrained design, in that the AP and lateral shear force experienced in the natural FSU is immobilised in the TDR. This alteration of



biomechanics compared to the natural disc is thought to have the desired effect of shielding the facet joints from these loads. However, this fixed CoR is also of concern as the facet joints may be forced to articulate in an unnatural way, especially if the TDR was mal-positioned. Further, assuming the device was perfectly positioned, the implant-bone interface will take more of the shear loads rather than the facets. Vicars et al. found *in vitro* wear rates of 12.2 mg/MC for the Prodisc using a Leeds spine simulator with 5 DoF [128]. A finite element model of wear for the Prodisc has shown simulated wear using ISO inputs of 11.77 mg/MC [129]. In the same paper they refer to an unreferenced *in vitro* validation test by Endolab that gave 9.82 mg/MC. These similar results suggest that 10-15mg/MC is a reasonable expectation of wear. In comparison, the Charité has shown *in vitro* results much higher when under additional AP shear displacement but with similar rates of wear for identical ISO inputs [130].

### **Charité (DePuy)**

The design of the Charité to some extent follows the kinematics of the natural disc, although not the load-deformation profile. The allowance of movement in the AP direction allows the CoR to more closely follow the natural FSU and hence reduce unwanted unnatural kinematics and forces. However, this means that the facet joints could potentially be loaded in the anterior direction. Although this is a natural physiological function, the facet joints of potential TDR patients could be at greater risk of arthrosis due to degeneration of the natural disc and so begin to fail at an accelerated rate. However, Rousseau et al. [90], using a cadaveric model, demonstrated that the Charité disc increased facet joint loads only in LB, although this in itself is a concern. One sided wear of the Charité disc has been muted as a potential flaw in terms of increased wear. Kurtz et al. have shown that one-sided wear took place in 45% of retrievals studied [131]. Assuming that the coefficient of friction is the same for upper and lower surfaces, this may result from a biomechanical mechanism that changes the way in which the end plates move. Kurtz et al. suggest that an instantaneous centre of rotation (ICR) that is not in the centre of the PE core will result in increased forces in one of the end faces resulting in one-sided wear. They confirmed this with an *in vitro* cadaveric test.

*In vitro* wear studies undertaken by Serhan et al. on behalf of the manufacturer showed wear rates of 0.13 mg/MC [123] which is much less than a study by Vicars et al [122] who found an average wear of 12.7 mg/MC, a two order of magnitude difference. Nechtow et al. have found wear rates of 19.35mg/MC [119] under ISO motions. The large difference is probably due to the fact that Serhan et al. ran their tests with FE and AR, then LB with rotation, but not all motions together. The inputs were taken from the ASTM guide, which does not stipulate phasing of motions. This avoided applying a crossing path motion pattern [Sec 1.6.4.1] and instead resulted in curvilinear kinematics. It has been demonstrated experimentally that omitting crossing path (cross-shear) motion can decrease wear rates considerably [119].

### **Maverick (Medtronic)**

In contrast to the Prodisc and Charité, the Maverick device owes its design to the knowledge gained from MoM THR. However, it is not clear whether that technology is transferable to the TDR concept. Bushelow et al. [97] reported a comparison of wear of a MoM TDR to a MoP TDR using the Maverick and Prodisc designs respectively, according to ISO 18192-1 inputs. Maverick steady state wear was 4.36mm<sup>3</sup>/MC compared to 9.78mm<sup>3</sup>/MC for the Prodisc. This was only a factor of two reduction in wear, even though a much harder material combination was used. This volume of metallic wear debris is unusual in THR devices except under extreme swing-phase loading [132] or rim impingement [133]. In a well-functioning THR the mixed lubrication regime helps to reduce wear by two orders of magnitude compared to a boundary lubricated MoP hip [134]. Furthermore, if the wear in mm<sup>3</sup> of a MoM device is converted to mg, then the wear is more alarming, as CoCr is approximately eight times heavier than UHMWPE. If it were assumed that the MoP TDR operates in the boundary lubrication regime, then a MoM TDR design should either be designed in a desire to achieve a mixed lubrication regime or to perhaps take advantage of the metallo-organic protective film that is thought to protect surfaces in MoM hip arthroplasties [78].

Bushelow et al. also noted that the wear was 15-50 times greater than that of typical THA tests [97] and four times greater than Mathews et al [135] and concluded that greater standardisation of wear testing was required. They also describe the running-

in period over the first one MC as having approximately half the wear rate of the steady-state. However, the graph supplied in the paper does not show a clear definition between running-in and steady-state. It appears more like a constant linear relationship, in keeping with a boundary lubricated device.

Previously to the Bushelow experiments, Mathews et al [135], reported a wear rate of 1.2 to 1.4 mm<sup>3</sup>/MC for the Maverick design which they thought favourable compared to THR. However, the *in vitro* testing details were not made clear except that they accelerated the test by using “10 million repetitions of significant bends, as opposed to 10 million walking cycles”. It could be that the low wear reported was partly due to these more extreme motions used. A more favourable lubrication regime might have existed for their MoM device, due to having a longer stroke length and therefore higher entraining velocity. One co-author of the test consults for the manufacturer.

Large numbers of metal particles in the disc space have been reported [136] which will be of concern in the long-term as the spine is an area of large nerve concentration and metal ions are cytotoxic [137].

### **1.8.3 The Risk of Osteolysis**

Recently, osteolysis has been reported in TDR revision surgery [138-142] which, although in low numbers presently, suggests that future problems may possibly be in stasis, as were the first reports of hip loosening and failure. Since it has been found that both volume of wear and size of the wear debris is of prime concern for prediction of failure [143] it is of importance to quantify both the volume and size of debris that may be released from these articulating bearing prostheses. The risk of osteolysis resulting from wear debris has so far been assumed to be very low in TDR compared to THR because of assumed lower wear rates, however this has not been quantified sufficiently and the long-term problems of wear are uncertain. Given this potential failure mechanism it seems prudent to use enhanced preclinical testing using *in vitro* spine simulation.

White macrophage cells interpret the debris as a foreign microbial intruder and try to digest and kill. It has been observed that debris which has a diameter in the range 0.1-1.0  $\mu\text{m}$  are the most biologically reactive, however, the PE itself is bio-inert and so remains in the cell. This can trigger more chemical messages (in the form of cytokines) to signal for help to deal with the intruder particles. This cyclic reaction results in the merging of macrophages into a giant nucleated cell with the intention of 'walling off' the foreign body from the host [75]. This cascade of adverse tissue reaction produces inflammation and accompanying pain in some THRs and TKRs [144].

A hip prosthesis that has loosened because of osteolysis can often be revised at least once, though the quality of the remaining bone that has undergone resorption may not be ideal. If this clinical scenario was repeated in the lumbar spine, the consequences would be much more difficult to treat. Operating on the spine is a procedure complicated by the presence of the central nervous system, aorta and venous cava. Most TDR failures are treated by a revision surgery that uses fusion to remedy the loose or pain causing TDR. However, revision of an osteolytic vertebra would be hampered by the fact that the bone volume of vertebrae is small and any resorption of the bone may not leave enough for revision.

Punt et al. [140] evaluated the periprosthetic tissues of 16 patients undergoing Charité revision for intractable pain after an average of eight years. They found that although only one incident out of 16 was found to be osteolytic, a positive correlation was found between the extent of chronic inflammatory reaction to the number of particles per  $\text{mm}^3$  in the periprosthetic fibrous tissue and the length of time the device had been implanted [140]. The moderate to high amounts of multinuclear giant cells found in seven patients was indicative of a worrying macrophage response that has the potential to become osteolytic. A Charité revision study by van Ooij et al. [142] involving four patients after 6.5 to 12.9 years of implantation reported osteolysis failure in one patient and PE debris in giant nucleated cells in all the others. The study was restricted to identifying  $>10 \mu\text{m}$  particles, which are not the optimum size for osteolysis reactions (being 0.1-1.0  $\mu\text{m}$  [144]), but the high risk of adverse reaction to TDR debris was thought to be high.

## 1.9 Aim and Objectives

### *Rationale*

In total joint replacement the study and understanding of the bio-tribological nature of the device is important for predicting performance *in vivo* and for selecting the right design rationale. By testing two different designs of contemporary TDR under varying loading and kinematic conditions a better understanding of what design and patient considerations are necessary may be achieved.

Data from reduced cross-shear tests will highlight any difference between semi-constrained and unconstrained devices. Low loads will challenge the existing classical wear theory used by some computational modellers and may indicate the extent to which patient weight will influence wear. Reduced FE motions will model the effect of very small motions believed to exist *in vivo*. At present, contact pressures are unknown; therefore knowledge of these may help explain certain wear phenomena. The effect of very short stroke lengths is postulated to be detrimental to the tribological regime; therefore a fundamental study using a simple PoP test may explain this further. The influence of motions other than standard ISO will be explored using motion tracking components using more realistic input data. Frictional characteristics will be studied in context to existing TJR knowledge and measurement of operating torques may help to explain articulating TDR limitations. The calculation of lubrication regimes will assist in the selection of bearing materials and indicate preferred material combinations and bearing dimensions.

### *Aim*

- Design a parametric study to investigate the bio-tribology of two different designs of artificial disc replacement with altered modes of input motion and supplement this with further basic science: pin-on-plate, contact pressures, motion path data, frictional response and lubrication regimes.

### *Objectives*

- Verify the new Leeds Spine simulator 'B' by completing standard ISO tests and comparing the results with existing data for Leeds Spine simulator 'A'
- Investigate the effect of altered phasing of motions

- Investigate effect of reduced/increased loading
- Investigate contact pressures in TDR
- Investigate effect of very short stroke lengths
- Investigate motion paths that more closely replicate Callaghan's low back motion data [1] and compare to ISO
- Investigate the bio-tribology of TDR in terms of frictional characteristics and lubrication regimes

## 2 Spine Simulator Methodology

To date, *in vitro* testing of orthopaedic implants has matured to a level where standard ISO inputs have been developed for the most common joint replacements such as hips and knees, and TDR has also recently achieved standardisation of testing input parameters. However, as the experience of hip and knee testing has grown, so too has the expectation that these joints should be subject to more challenging input conditions in order to try and replicate the outliers in performance that occur *in vivo*. Stratification of testing [145] and investigating wear rates will help indicate improvements to design by expanding results beyond the central-tendency. Improvements in materials and avoidance of sub-optimal design could then be made.

This chapter gives an overview of the testing methodologies used in this thesis for *in vitro* wear testing of TDR components. Supplementary experiments used while investigating characteristics of TDR design in terms of based basic science, including contact pressure, pin-on-plate, motion-track, friction, and lubrication, are expounded upon in their respective chapters.

### 2.1 Introduction to Spine Simulation

The simulator used for many of the experiments presented here was jointly developed by the Institute of Medical and Biological Engineering (IMBE), Leeds University, and Simulation Solutions Ltd, Manchester, UK. Leeds supplied the specification of the machine and Simsol Ltd carried out the detail design. The design uses fully electro-mechanically controlled actuators to control the input kinematics and loading. All inputs are operated by harmonic-drive motors that provide superior motion control. Axial loading uses motors connected to rotating-cam gearboxes fitted with compression springs that can be changed for different spring-constants depending on level of loading required.

The simulator is unique in that it allows six degrees of freedom with five degrees actively controlled (only medial-lateral shear is not controlled). This ability to apply

more detailed kinetics and a degree of ‘self-centring’ or ‘float’ is advantageous when trying to achieve more accurate simulation. Other commercially available simulators do not have the Leeds capability to add anterior shear, posterior shear, or a cyclically loaded AP shear. Furthermore the shear load can be changed to a displacement if this is more suitable for a test specimen. Machines such as the Endolab, AMTI Boston, Bose Endurotec and MTS Bionics can only accommodate four active degrees of freedom. Only the Bose and MTS machines incorporate full six degrees of freedom but this includes two passive axes in the transverse plane. The motions and loads in the transverse plane may be important parameters in simulating *in vivo* conditions.

The experimental simulations were all based on the standard ISO kinetics with the exception of the motion track work which also incorporated a waveform based on the Callaghan input [1] discussed in section 1.4.1. The simulator contains two banks of three stations [Figure 2-1] allowing six samples to be tested plus a stationary station which is purely axially loaded and used as a soak control.

Before commencement of experimental studies using simulators, it is necessary to calibrate motions and loads.



Figure 2-1 Leeds spine simulator showing left hand bank of 3 stations and right hand bank of 3 stations (soak control to right of bank 2, computer control cabinet to right of picture)



In the Leeds spine simulator, generation of the kinetic inputs is achieved through the following systems:

- Direct motor control
  - FE, LB, AR, AP displacement
- Indirect motor control:
  - Axial and AP load

The direct control of the kinematics is done by simple connecting rod arrangements to lever arms attached to the motors [Figure 2-2]. Indirect motor control uses Hook's Law principle to allow the application of a load by use of a compressed spring. This is done using a cam (rotated by a motor) and spring for the axial loads [Figure 2-3] and by four-bar link and compression of a captive spring for the AP load [Figure 2-4].

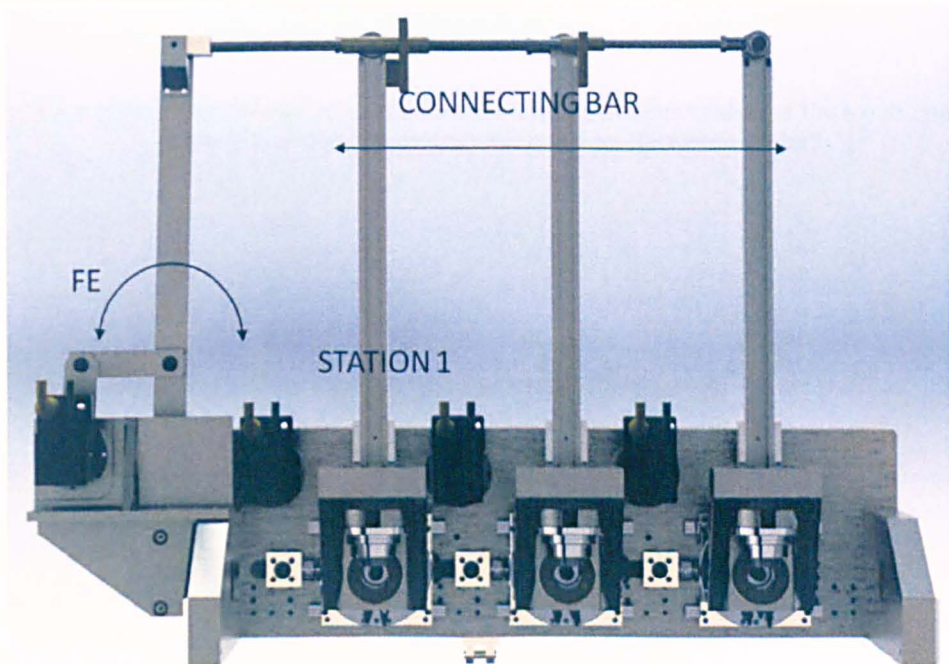


Figure 2-2 Schematic of a group of three stations showing the linkage of the FE motor and actuating rods

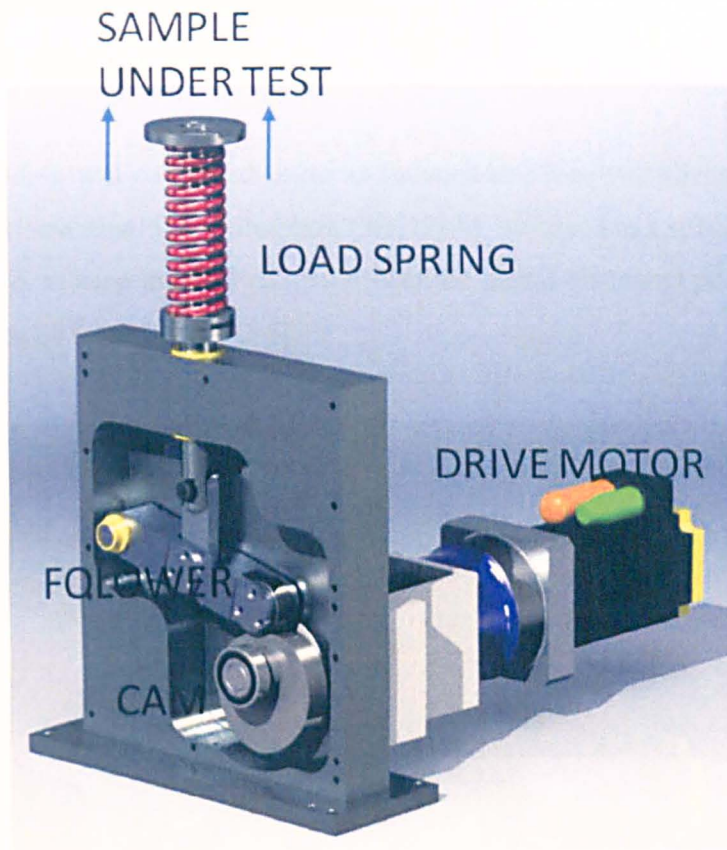


Figure 2-3 Schematic of assembly of axial load application mechanism of the Leeds spine simulator, cam and spring are operated by the motor behind

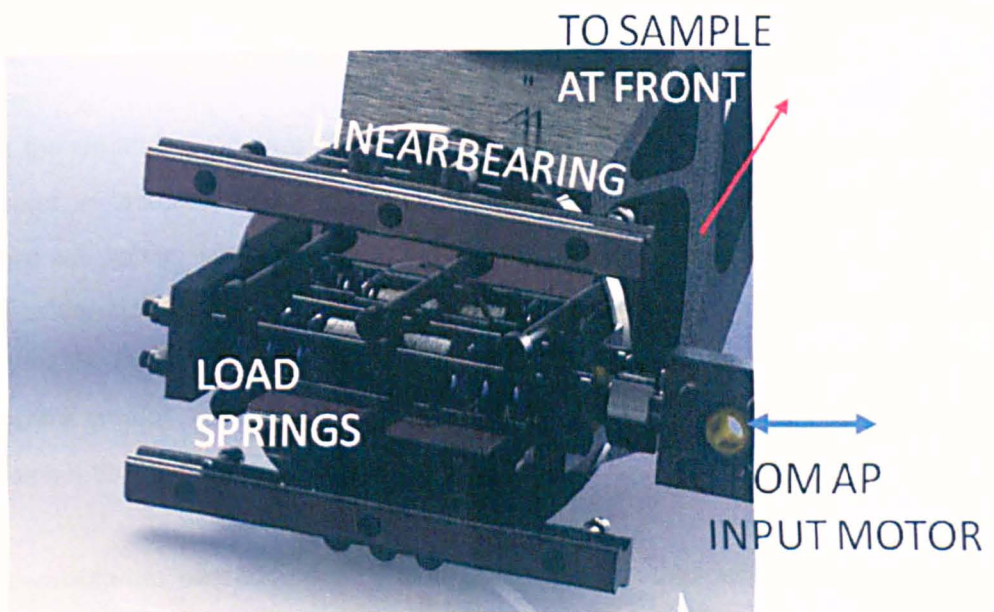


Figure 2-4 Schematic showing assembly of the AP load application mechanism – the two springs give anterior and posterior force

## 2.2 Spine Simulator Calibration

### 2.2.1 Load Verification

The axial loading was calibrated using an independent load cell (Sensotec 4.5 KN, Honeywell International Inc, Columbus, OH, USA) mounted in a specially designed fixture in order to keep the load cell parallel to the lateral plane and perpendicular to the application of force [Figure 2-5].

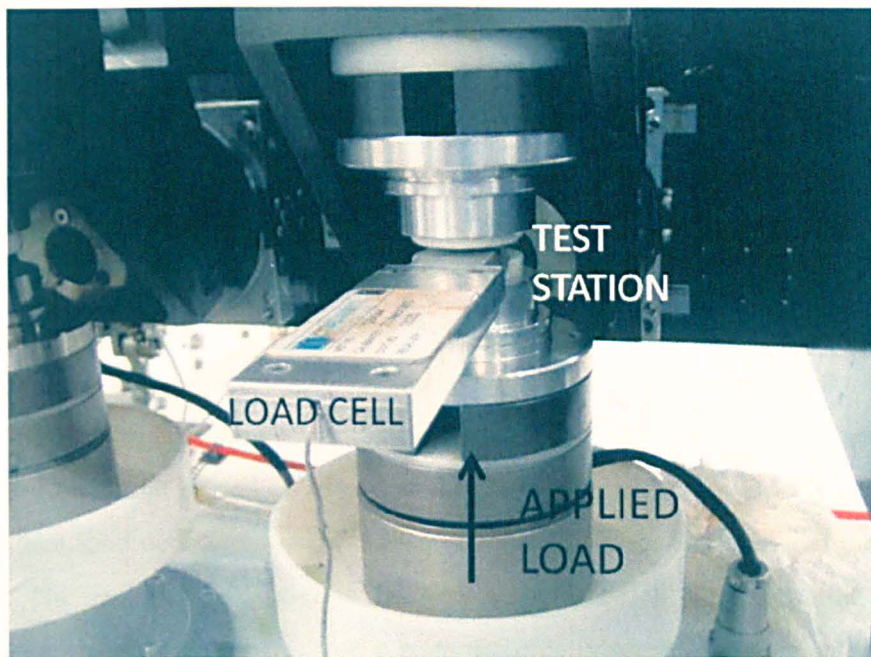


Figure 2-5 Axial load measured using an independent load cell and special jig

In the simulator software, the 'jog axes' function was used to move the axial force motor to incremental positions. The resulting simulator load cell and independent load cell values were compared in a specially designed spread-sheet for the purpose of calculating correction factors for the axial load motors. Where no difference was found between simulator and independent load cell value, a plot of these would show a gradient equal to the existing motor gain and an intercept of zero. Where this was not the case, recalibration was required.

Re-calibration was achieved by calculating the gain and offset values of the *force-motor position* plot and using these values to calculate new ones to be used in the calibration software [Equation 2-1].

$$F = CG + O$$

**Equation 2-1**

Where F is axial force, C is motor count (a feature of the motor control unit), G is gain (amplification of the motor input signal) and O is offset (nominal position control). These parameters can be adjusted in order to move the output into the tolerance band required from the ISO standard (or any other standard chosen by the user).

A source file (`_default.ssp`) is used by the control software to control the motors responsible for loading. The calculation of gain and offset were determined by using the gradient and intercept of the load cell plot. The gradient was then used to multiply the existing gain offset value to produce the new gain offset value. The intercept of the graph was subtracted from the existing gain offset value [Figure 2-6]. The new values (if change was necessary) were used to replace the existing values in the simulator control software source file (`_default.ssp`). This correction changed the simulator load cell to be within tolerance and more closely reflect the independent load cell. The load was then checked for a second time and the results plotted. The resulting plot should be within tolerance. If not, then this usually indicated a different source of error, e.g. an incorrectly seated independent load cell, non-zero position of FE or LB inputs which load the load cell off-centre, or operator error. An example of a revised calibration plot is shown in Figure 2-7.

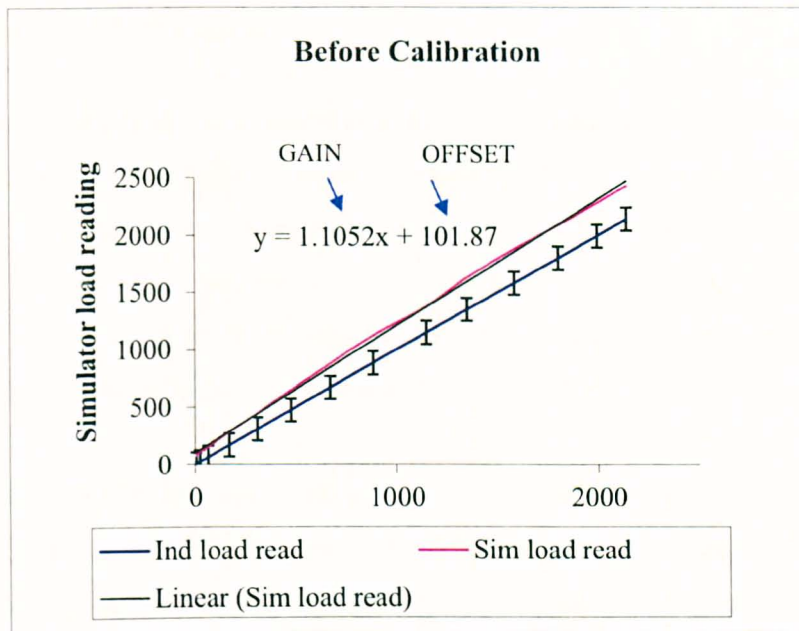


Figure 2-6 Plot of simulator load cell versus independent load cell: the gradient and intercept are used in order to adjust the calibration constants of gain and gain offset

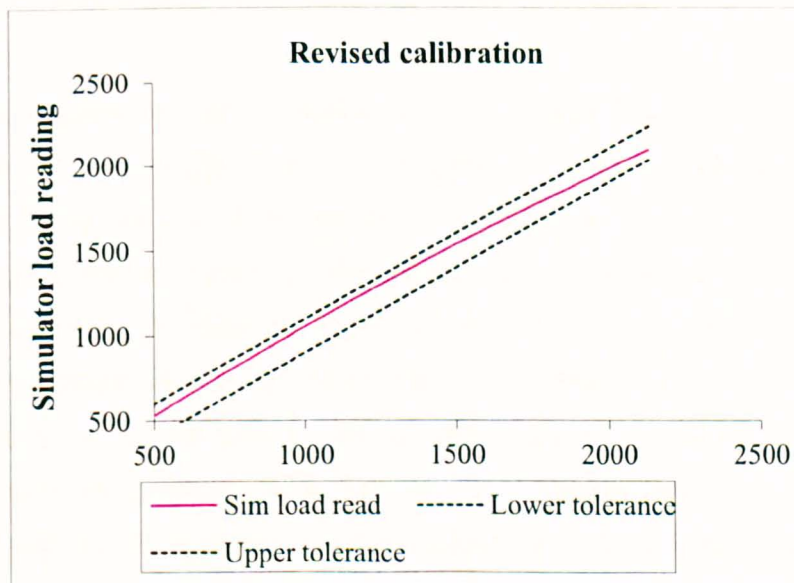


Figure 2-7 Revised Calibration plot: the simulator load cell now within the tolerance limits stipulated by the ISO standard

The tolerance stipulated by the ISO standard is 5 % of the maximum load, which for lumbar inputs is 2000 N, therefore limits of  $\pm 100$  N were used on the plotted graphs. The calibration method was repeated for test stations 1 to 7.

### 2.2.2 Flexion-Extension

The motors on the spine simulator do not have built in encoders and therefore cannot be automatically calibrated. A table of motor positions must be filled out by a process of moving a motor through an arc of motion. The demand inputs and actual simulator outputs from this are then recorded in a table stored as a text file. The simulator control software then uses this data as a look-up table to compute a linear motor input table so that the FE motion is accurate and linear.

The spine simulator FE inputs are grouped into two sets of mechanically linked stations. Stations 1 to 3 are operated by one motor drive as are stations 4 to 6. Station 7 is a soak control and has no kinematic output. Due to mechanical linkage between stations, the FE motion need only be calibrated from one station, the remaining two stations should follow the calibrated station. However, the other two stations should be checked for congruity with the calibrated station so that they are no more than  $\pm 0.1^\circ$  in difference when stationary. The value of  $\pm 0.1^\circ$  was chosen as the smallest possible tolerance that was practicable to measure.

In order to measure the angle of motion of the FE input, a digital inclinometer with a resolution on  $0.1^\circ$  (Pro 360 digital inclinometer, SmartTool Tech Inc., Oklahoma City, OK, USA) was placed on one station and taped in position [Figure 2-8]. To check the FE position accuracy the 'jog axes' instruction in the control software was used to move the FE motor in  $2^\circ$  increments from  $\pm 14^\circ$  and the independent inclinometer results were compared to this. If re-calibration was required, the 'jog axes' instruction in the control software was used to move the FE motor to approximately 45 positions from  $+15^\circ$  to  $-15^\circ$ . The inclinometer results were tabulated with the 45 positions and this formed the look-up table required by the control software. In order to check that the calibration was successful it was necessary to switch off and on the control software in order to make the new look up table take effect. The calibration procedure was then repeated and inputs of  $-14^\circ$ ,  $-12^\circ$ ,  $-10^\circ$  ...  $0^\circ$ ,  $+2^\circ$ ,  $+4^\circ$  ...  $+14^\circ$  were tried and checked for accuracy. An accuracy of  $\pm 0.5^\circ$  was required by ISO for the output cyclical motions but for the primary calibration a value of  $0.1^\circ$  was chosen so that it would be more probable that an output cyclic waveform would be within  $0.5^\circ$ .



Figure 2-8 Digital inclinometer pictured measuring input flexion of one station (fitted with dummy sample)

### 2.2.3 Dynamic Verification of FE Motion

A previous report has been made that the FE motions of the Leeds spine simulator become extended and hence inaccurate when operating dynamically rather than when being checked statically [122]. This error was found to be between  $1.1^{\circ}$  and  $3.1^{\circ}$  depending on the input cycle and test sample. The author hypothesised that this error could be due to inertia in the FE mechanism forcing the FE motors to overshoot their demand profile positions. Therefore a method of checking the FE motion under dynamic conditions was devised. A dial gauge was attached to the simulator so that light contact could be achieved between the FE arms and the pushrod of the gauge when the FE position was statically set to  $-3^{\circ}$  (maximum extension in the ISO cycle) [Figure 2-9]. At this point the gauge was set to zero. The input motions were adjusted so that only FE was running dynamically and the dial gauge was filmed (Canon Ixus 40, Canon Inc, Tokyo, Japan) and analysed. This

method was repeated with the AF load set to 300 N (to isolate the effect of an oscillating load) and also to 600-2000 N (effect of cyclical loading).

The motions were found to be accurate to  $\pm 0.1^\circ$  under dynamic inputs (FE only) and were therefore assumed to be accurate for the lesser motions of LB and AR. The error found in the original analysis may have been due to the video analysis method used which did not include calibration markers and used video analysis alone. This may have introduced parallax error due to the wide angle nature of the lens system. This would have the effect of widening the apparent rotation angle observed.

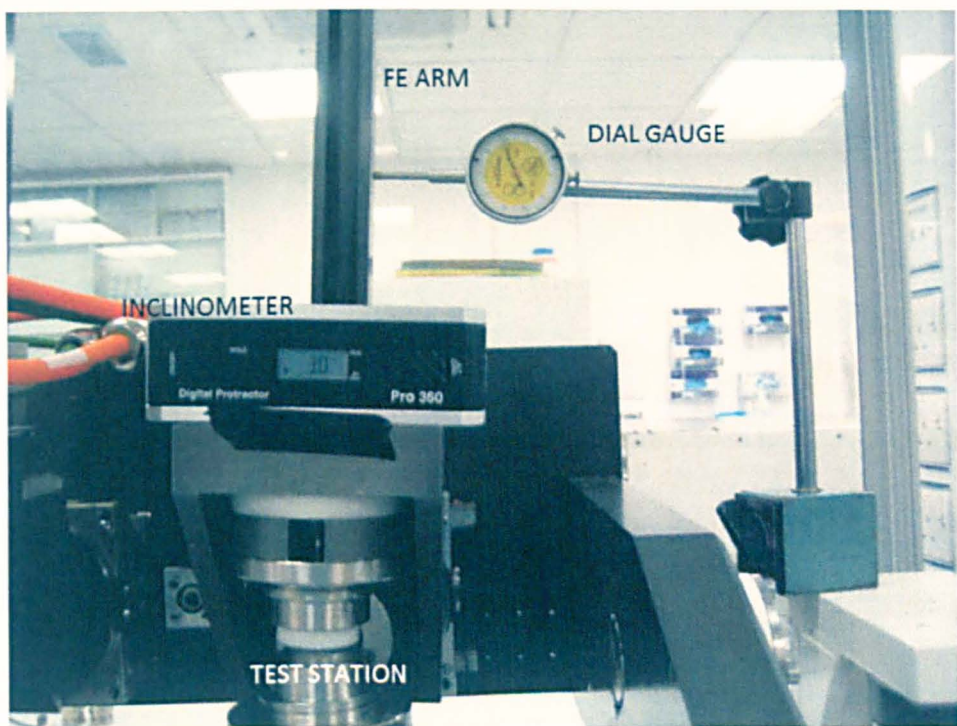


Figure 2-9 Dynamic checking of FE motion under standard ISO conditions using dial gauge

## 2.2.4 Lateral Bend

The calibration checking and adjustment procedure was similar to the FE motion method with the exception that the three stations are solidly connected to the LB motion by being incorporated into a gimbal system [Figure 2-10]. It was therefore unnecessary to check that each separate station was following its adjacent neighbour [Figure 2-11]. The ISO standard requires an input LB of  $\pm 2^\circ$  therefore the range of



motion checked was also smaller being approximately  $\pm 4^\circ$ . Group one and two had to be done separately.

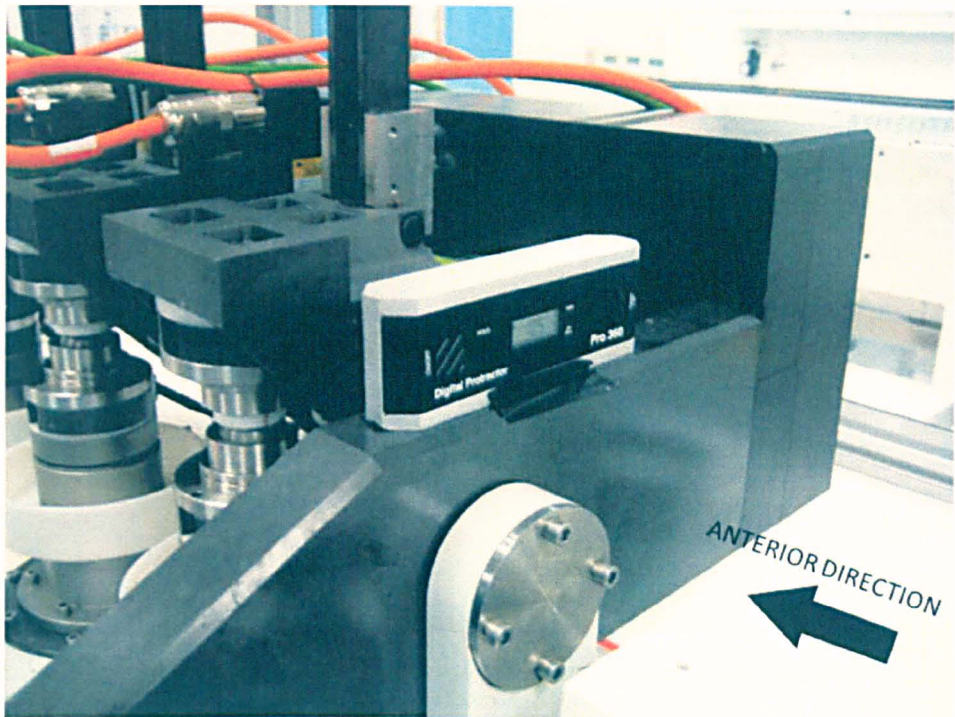


Figure 2-10 Lateral bending measured at the gimbal (schematic shown in Figure 2-11) - links all three stations in one group

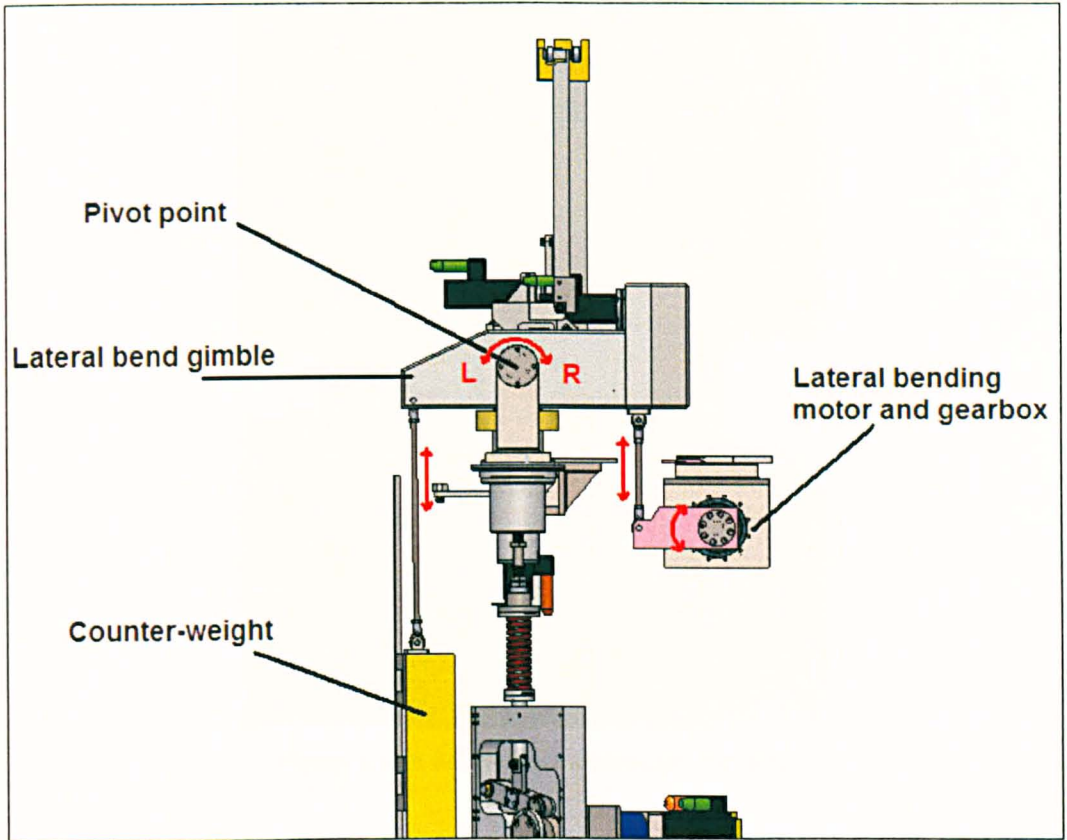


Figure 2-11 Schematic of simulator from end (posterior looking to anterior) view with lateral input motion gimbal which moves all three stations per bank

### 2.2.5 Axial Rotation

The method of calibration for the axial rotations followed the same principle as the FE/LB methods; however, the measurement of the rotation necessitated the use of a rotational scale. The angular increments necessary were converted to a rotational distance by use of the formula for an arc length of a circle ( $S = r\theta$ ).

Increments of  $2^\circ$  were used and since the radius of the spine simulator test station was 45 mm, the corresponding rotation would be known to be 1.57 mm. A scale of 1.57 mm divisions was used to compare input angle and output displacement [Figure 2-12]. The AR never required adjustment, probably because the rotation motor and station attachment mechanism are a simple parallelogram connection.

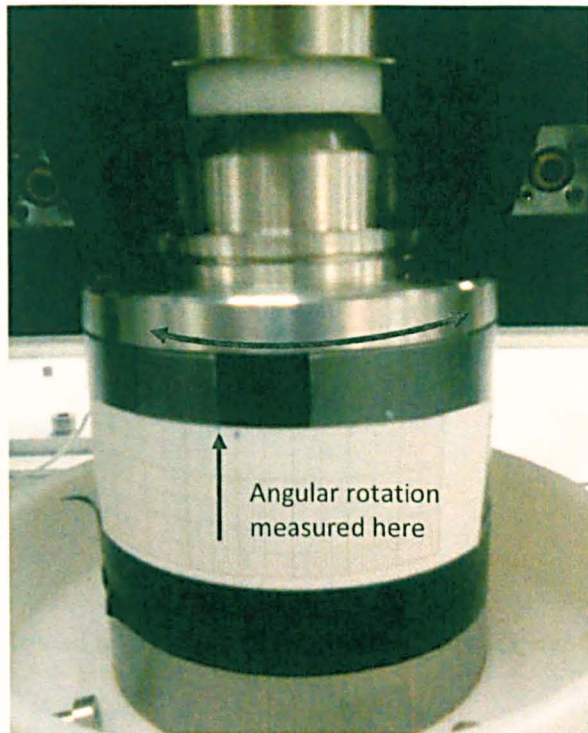


Figure 2-12 Axial rotation calibration checking

## 2.2.6 Anterior-Posterior Load and Displacement

The Leeds spine simulator design includes the ability to apply either an AP displacement or load and therefore calibration is required for the each possible input. A custom design hemi-cylindrical jig was used to hold either an independent load cell [Figure 2-13] or to facilitate displacement measurement with a digital calliper. In order to run the machine with AP control, bolt A [Figure 2-14] should be connected to the AP input motion arm. In displacement control, bolt B should be inserted in order to lock the AP compression spring [Figure 2-14].

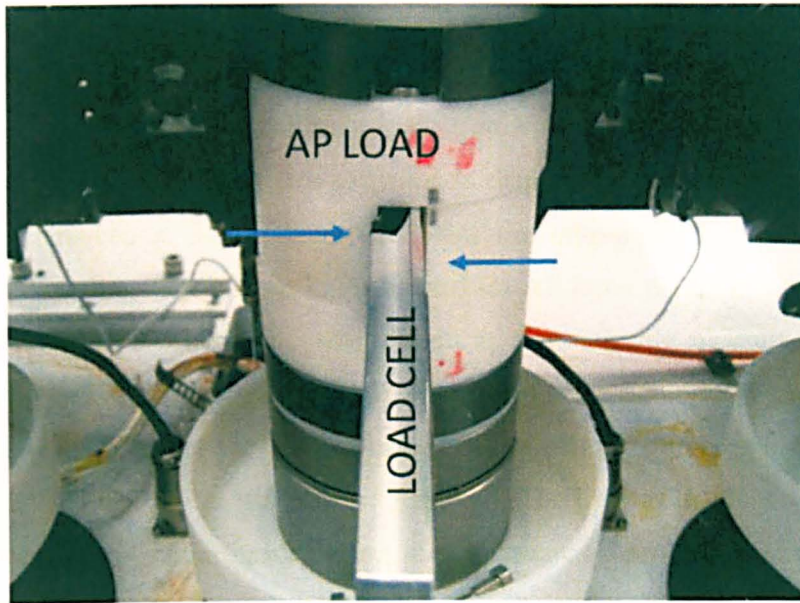


Figure 2-13 Jig used to hold independent load cell perpendicular to vertical axis

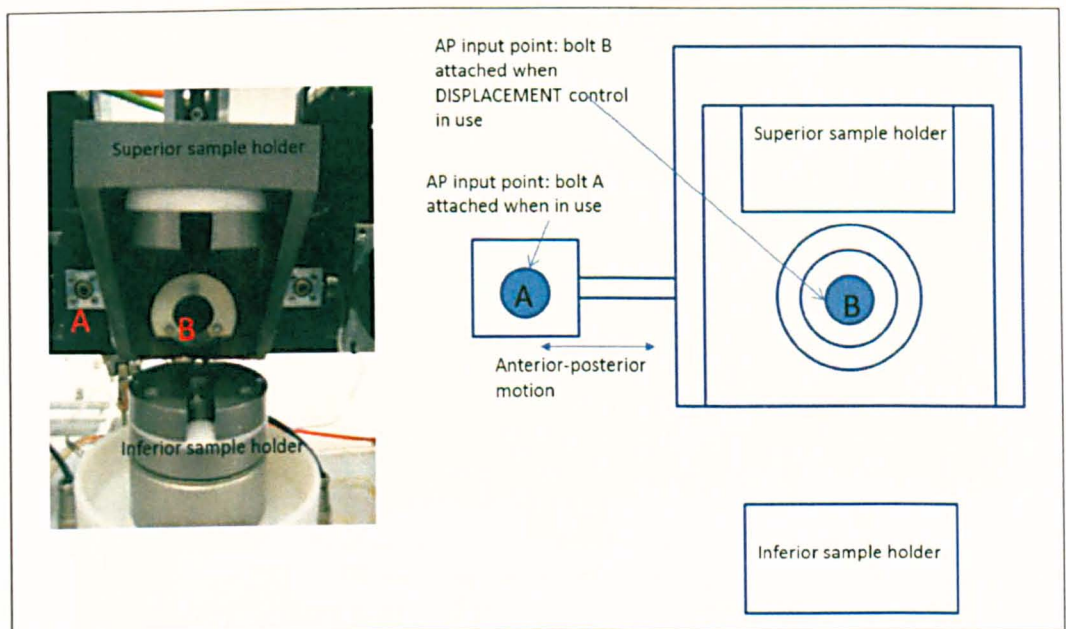


Figure 2-14 AP control depends on the attachment of bolt A (AP input configured) and bolt B (AP load configured), pictured schematically on right

Displacement measurement was accomplished by use of a specially made jig to hold a LVDT connected to an oscilloscope [Figure 2-15]. The displacement could then be measured accurately on an oscilloscope screen. The LVDT first had to be calibrated by clamping the LVDT above an engineering surface-plate to maintain a baseline reference surface and then using slip gauges to reference (for example) 3 mm

deflection with three divisions of the oscilloscope screen. The LVDT was then mounted adjacent to the station holder and the jog axes function used to move the AP application motors. When calibrating, the jig displacement was controlled by the 'jog axes' function of the simulator software. In displacement mode, inputs of 1 mm increments between  $\pm 3$  mm were used and the output position noted by the oscilloscope reading. There is no ISO standard for AP input therefore a tolerance of  $\pm 0.5$  mm was used. This value was chosen as a practicable measurement when using the jig and oscilloscope method. A similar calibration look-up table to the FE inputs was used to record the results for stations 1 – 6. For force input AP control the jig was used to hold an independent load cell. The jig was machined so that the load cell would not come loose during measurement. A procedure similar to the axial load calibration was then followed.

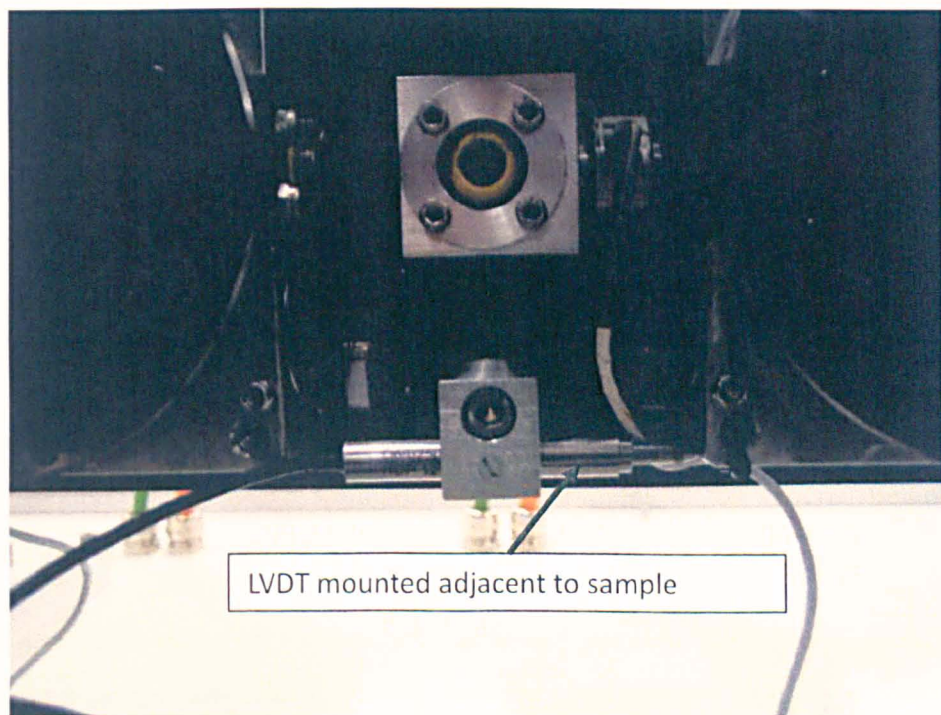


Figure 2-15 LVDT mounted adjacent to a station sample holder and used to read deflection readings from an oscilloscope.

### 2.2.7 Test Cell Temperature Calibration

The ISO standard stipulates that the test cells containing the samples under test should be heated to body temperature ( $37 \pm 2^\circ\text{C}$ ) in order to have a lubrication

regime at the same temperature as would be the case *in vivo*. On the simulator this is achieved by each station containing a heating element and a thermocouple to provide feedback. The thermocouples are factory calibrated at 0°C and 100°C using iced and boiling water respectively. In order to check the test cell temperature requirement was met, an independent thermocouple (Fluke 51 K/J, John Fluke Manufacturing Co. Inc, Everett, WA, USA) was employed to check the temperature of each lubricant filled test cell chamber. The demand temperature input and the actual output were compared and the output was found to be ~3°C less than the demand, therefore most station temperature demands were set at 40°C.

### **2.2.8 Phase calibration**

The frequency of the simulator was checked while performing a standard ISO cycle and a stop watch used to record the difference in cycle number and elapsed time. This was done periodically throughout experimentation to make sure frequency was not altered. Phase between the input demand profile and the output profile was checked at the start of each experiment.

## **2.3 Materials and Methods: Spine Simulator Wear Testing**

### **2.3.1 Introduction**

This section outlines the fundamental materials and methods used in wear testing of TDR devices on the Leeds spine simulator. Variations of the general method are reported in each relevant chapter or section.

Orthopaedic bearings are routinely wear tested prior to clinical use in order to validate a design rationale or bearing material combination, with the *in vitro* tests usually following existing standards, for example, the ISO standard for total hip replacements. However, experience from hip replacement *in vivo* versus *in vitro* data can show large variance in the data when compared to laboratory controlled conditions even though the overall central tendency may be similar. The standards for hip (ISO 14242) and knee replacements (ISO 14243) are relatively mature and are an accepted indicator of probable mean *in vivo* performance, whereas the TDR standards and guidelines are more recent and lack robust validation through explant

inspection and comparison. Existing TDR wear testing methods may be an indication of central tendency but the range of *in vivo* performance is not captured, therefore the following methodologies were developed to show an envelope of performance.

## **2.3.2 Materials**

### **2.3.2.1 TDR Samples**

Two distinct types of disc design were used for this study; a semi-constrained device represented by the Prodisc (donated by Synthes Spine) and an un-constrained device represented by the Charité (DePuy Spine). Both designs use articulating CoCr on UHMWPE bearings with the main difference between them being the level of stability in the transverse plane. The Charité device is constructed to allow a small amount of transverse motion which is designed to be beneficial to IAR positioning and hence reduce the possibility of facet joint overload due to a fixed CoR [87, 89, 90]. This is achieved by use of a mobile central core and two CoCr endplates as opposed to the ball-in-socket design of the Prodisc, hence the Charité device has two bearing interfaces. In contrast to the Charité manufacturer's claim, the manufacturers of the Prodisc say that the level of transverse stability in their device protects facet joints from overloading. There are many different device designs in the market place, but the decision to choose these two bearings as samples throughout the studies presented here was made due to the similarity of the material design (i.e. CoCr endplates and UHMWPE cores) and also because of the fundamental design differences which are meant to change behaviour when subject to four DoF or five DoF inputs. The latter has already been investigated [122] but other simulator input perturbations have yet to be explored.

#### *Charité*

No modifications were made to the samples and the discs were of implant quality. The TDRs were of size two with zero degrees offset. Table 2-1 denotes the lot numbers used in this study.

**Table 2-1 Lot numbers of Charité devices (endplate ref 75-6400-12, core ref 75-6411-02 )**

Sample Number	Superior Endplate	Inferior Endplate	UHMWPE Core
1	WL 048B092	WL 047B039	WL 043F014
2	WL 048D026	WL 047B039	WL 047B075
3	WL 048D026	WL 048E085	WL 047B075
4	WL 048D026	WL 048E085	WL 047B075
5	WL 047C007	WL 048B092	WL 047B075
6	WL 040C188	WL 048B092	WL 047B075
7 (soak control)	WL 040C160	WL 048B092	WL048D060

*Prodisc*

No modifications were made to the samples and the discs were of implant quality. The TDRs were size medium with six degrees offset applied to the superior endplate. For the Prodisc-L design the inferior endplate only acts as a base for the UHMWPE components and is therefore not a critical component. Table 2-2 denotes the lot numbers used in this study.

**Table 2-2 Lot numbers of Prodisc devices (superior endplate ref PDL-M-IP00S, inferior endplate ref SSX534K, PE inlay ref PDL-M-PE14S)**

Sample Number	Superior Endplate	Inferior Endplate	UHMWPE Core
1	5013250	51254876	5357444
2	4998137	5363445	5380650
3	4998137	51254876	5391202
4	5009723	51254876	5395329
5	5009723	51254876	5357444
6	4998137	51254876	5395329
7 (soak control)	51254876	5013249	5367390

**2.3.2.2 Wear Testing Lubricant Medium**

All spine simulator and pin-on-plate testing was completed using a diluted solution of new born calf serum (bovine serum) diluted with distilled water to 25 % (v/v) in order to give a protein concentration of 15 g/L. The serum protein concentration of



15 g/L was less than that stipulated by ISO 18192-1 and ASTM F2423-05 (30 g/L), however, the value of 15 g/L is in the central region of a range of concentrations that have been shown to produce clinically relevant wear data in TJR [146]. The perceived advantage of using this level of serum dilution is based on the fact that *in vivo* synovial fluid is less protein rich than a healthy joint. For both spine simulator and pin-on-plate experiments the lubricating medium was changed every 333,333 cycles. During this time the samples and their holders were cleaned with soapy water and disinfectant before refilling with diluted serum

### **2.3.2.3 Gravimetric Measurement**

The period of mass measurement was 1 MC. A Mettler-Toledo balance ( $d=0.01$  mg g) was used for all measurements. Before assessment the PE components were depolarised with an ion stream (Statattack IB8, Amersham Int, UK) to minimise the risk of static charge build up. A minimum of four readings were recorded, the balance was checked for zero reading between readings and the balance was stable before commencement. The mass loss of the components was then recorded but during analysis the mass change due to fluid uptake of the control pins was adjusted in the wear results.

### **2.3.2.4 Surface Profilometry**

The tribological performance assessment of the TDR components involved the measurement of surface roughness and comparison between the start and end of test results. The surface measurements were completed using a contact profilometer (Taylor-Hobson 120L or PGI800) using a diamond stylus. The principle of surface roughness computation relies on the amplification of the small deviations of a stylus dragged across the surface under investigation. These small perturbations are projected by a laser onto a sensitive screen and converted to a mathematical value. Various algorithms can then be used by the analysis software to display roughness parameters such as average roughness ( $R_a$ ). However,  $R_a$  does not distinguish between different topographies, as shown in Figure 2-16.

Roughness ( $R_a$ ) is defined as the average vertical deviation from the mean surface position. A high  $R_a$  value indicates that the deviations from the mean surface position are greater than a lower value  $R_a$ . However, the  $R_a$  value does not give an indication of the transverse properties, for example, the periodic nature of the roughness. Another property that can be described is the waviness of a surface. The descriptive algorithm is similar to  $R_a$  but the wavelength over which it is calculated is longer.

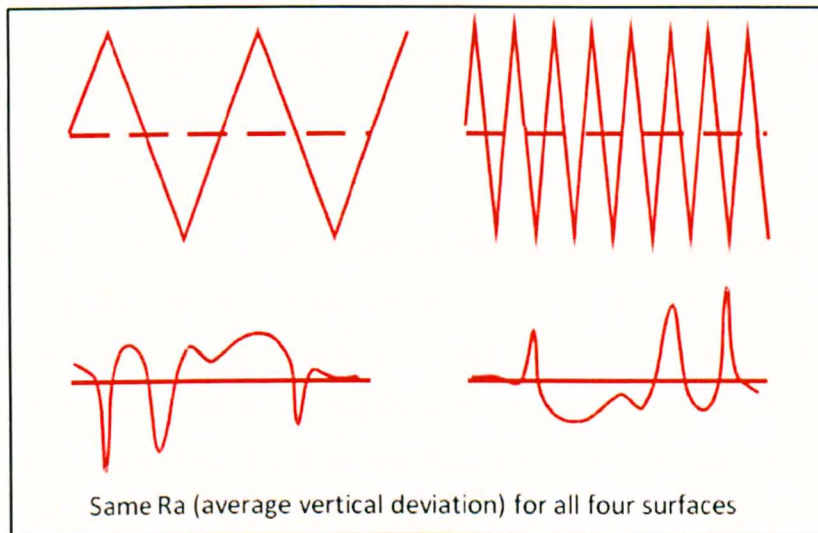


**Figure 2-16** The most common topographical function is average roughness ( $R_a$ ) (image altered from Taylor-Hobson presentation)

Cut-off and bandwidth limits are needed to correctly interpret roughness and must be adhered to when comparing sample data. Cut-off values (mm) refer to the measurement length at which the roughness value (i.e. average vertical height deviation; typically microns) changes. In general, for highly polished metallic components a cut-off of 0.25 mm was used and for UHMWPE samples a cut-off of 0.8 mm was preferable. These values take into consideration the underlying waviness of the surface under investigation. For example, UHMWPE components are typically 10-100 times rougher than CoCr components, if the same cut-off is used for the highly polished CoCr endplates the analysis software will interpret the waviness profile as roughness and give a higher value of  $R_a$ . The wavelength cut-off in relation to the roughness profile is shown in Figure 2-17.

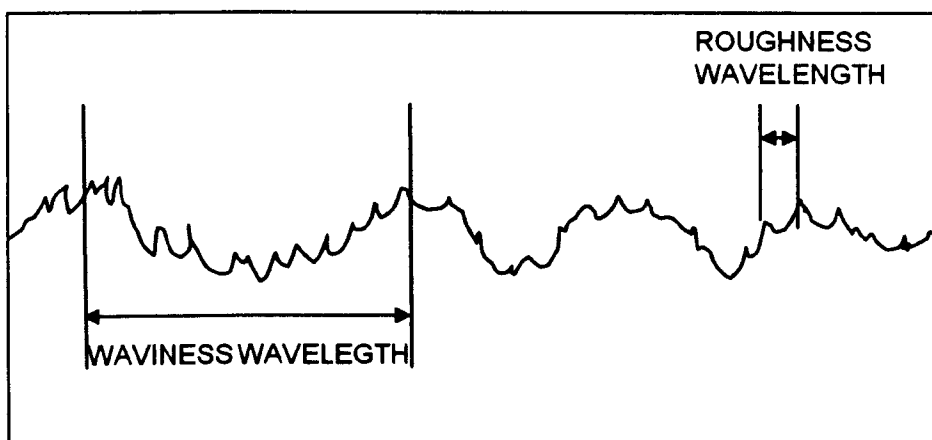


Figure 2-17 A pictorial demonstration of wavelength in relation to surface roughness

### *Convex UHMWPE components*

Due to the nuances of TDR wear performance under different input cycles, a method of quantifying the bearing surface performance was needed. Instead of taking several traces across the full bearing faces and computing average values, a more descriptive method was used whereby the changes elicited by wear effects could be distinguished. Values were taken for the three different wear zones present on the UHMWPE surfaces:

- Pole
- All (Full diameter)
- Rim

These positions were chosen from optical inspection of the wear scars, showing roughening of the pole area of the UHMWPE, rim (or edge loading) effects, abrasion of the majority of the PE area and burnishing of the contact area congruent with contact of the articulating concave CoCr component. A diagram of trace positions is shown in Figure 2-18.

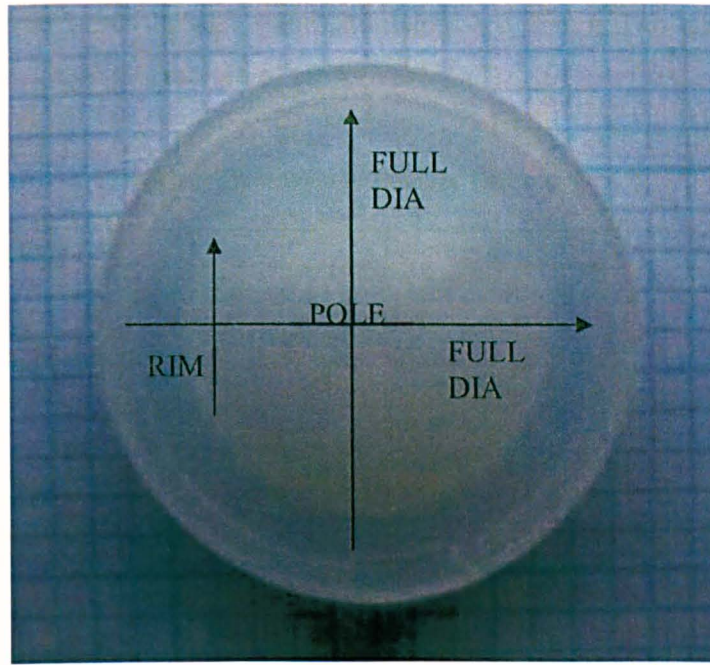


Figure 2-18 Positions of profile traces on PE components

### *Concave CoCr Components*

As has been observed in other wear simulations the CoCr components were not expected to change greatly over the course of the experiment. The position of traces was therefore limited to rim to rim profiles with no investigation of separate areas of interest.

## **2.3.3 Methods**

### **2.3.3.1 Standard Testing Conditions**

Standard ISO testing methodologies were adhered to, however, certain parameters were adjusted in order to isolate parametric effects of either kinematics and loading. One parameter in turn was adjusted for each study and the end performance recorded before another parameter was altered. This also allowed convenient comparison with results in the literature and with the other studies presented here.

Before a description of the parametric experimentation it is necessary to describe the standard ISO testing regime for TDR components. This dictates an error margin for the input motions and loads and other cycle parameters such as frequency and

temperature. The Leeds Prosim spine simulators are designed to accurately apply cycle inputs to within this margin of error (Table 2-3).

**Table 2-3 Tolerances in Lumbar ISO standard**

Load/Displacement	Tolerance
Axial load	$\pm 5 \%$
Transverse load	N/A
Transverse displacement	N/A
Flexion-extension	$\pm 0.5^\circ$
Lateral bend	$\pm 0.5^\circ$
Axial rotation	$\pm 0.5^\circ$
Cycle frequency	2 % of cycle time
Serum concentration	30 g $\pm$ 2 g protein/l (equivalent to 50 % diluted)*
Additives	
Temperature	37 $\pm$ 2 C°
CoR	Concurrent with simulator
Minimum sample number	n = 6

\*For the experiments presented here, all serum was diluted to 15 g/l protein concentration

The range of motions of disc prostheses and the corresponding standard are less than that seen in hip and knee replacements and therefore the tolerances are also reduced. However, other factors that are shared between ISO standards include serum concentration and anti-bacterial additives. The Leeds requirement extends beyond the standard ISO to include the facility to further the envelope of testing to include cervical inputs and also to perturb the lumbar inputs in order to investigate phenomena that may arise from altered inputs.

The original ISO kinematics were developed to reflect a reasonable scenario for implant wear and allow comparison between designs. The loading regime is 600-2000 N which is roughly one to three time body weight. This is within the order of loading found by Callaghan et al [1, 47] when investigating loads for walking and sitting. More extreme loading is known to occur, sometimes up to five times body weight [55], which are not normally simulated *in vitro*. These loads are transitory and patients receiving a TDR are not expected to perform strenuous activity. The kinematics of the ISO standard includes 9° rotations for FE, which, although within the typical range for RoM found in the literature, is probably not representative of a single index level. It could be argued that this is a ‘worst case scenario’ in that the

extended motions of the ISO standard will cause more wear. This could be true, but the tribological regime is affected by inputs such as entrainment velocity and this is directly proportional to rotational amplitude and frequency. An increase in bending angle is equivalent to an increase in velocity. If this entrains more fluid then a decrease in wear may result. Another parameter affected by rotational input magnitude is the amount of cross-shear present at the surface of the bearing, which will also affect wear

Before commencement of a wear test the simulator outputs were statically measured in order to calibrate the machine [Section 2.2].

### **2.3.3.2 Spine Simulation Method**

Before commencement of testing, the UHMWPE components were soaked in distilled water for a minimum of 14 days in order to stabilise fluid uptake. This was followed by drying with lint free tissue and storage in a temperature (20 °C) and humidity controlled metrology laboratory for 48 hours prior to mass measurement. The same period of stabilisation (48 h) was used at each wear measurement point within each test variation. After mass measurement the polyethylene components were assembled together with the endplates into sample test cell holders. The TDR fixtures consisted of seven pairs of Prodisc and Charité endplates each of which were mounted in lower and upper holders using PMMA bone cement. To reproduce the exact positioning of the endplates, special jigs were manufactured to enable precise setting in the PMMA cement mantle so that the CoR of each device matched that of the simulator. Axially and radially positioned grub screws allowed fine adjustment of the CoR using slip gauges set to the CoR height using a vertically mounted dial gauge. The Charité device has a variable CoR and therefore an arbitrarily fixed CoR was chosen to be at the centre of the polyethylene core when fully assembled (the same position used by Nechtow et al.). Prodisc polyethylene discs were inserted into their inferior endplate (by a snap-lock mechanism) and holder, and then assembled together with the superior endplate and holder. Charité polyethylene cores were placed between inferior and superior endplates and remained mobile. All polyethylene components were numbered and the test station cells were always replaced in the same positions after measurement. The test cell

assemblies were then enclosed in a silicone gaiter [Figure 2-19] to enable complete immersion in lubricant. FE and LB were applied to the upper holders of the simulator and hence to the superior components of the TDRs. Axial rotation (AR) was applied to the lower holders and hence to the inferior TDR components. The axial loading was vertically applied to the lower holders and hence to the inferior side of the TDRs.

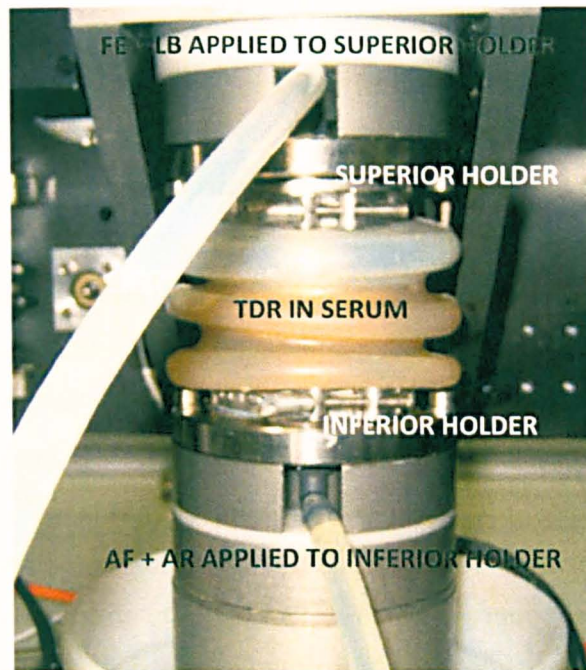


Figure 2-19 TDR test cell submerged in serum contained in a flexible silicone gaiter

The test cells were mounted in the holders which were in turn attached with screws to each station position. A flexible pipe connected to the lower holder of each test cell allowed filling with lubricant: bovine calf serum, diluted to 15 g/L protein concentration with 0.03% (wt/v) sodium azide added to limit bacterial growth between serum changes. In addition, a pipe connected to the upper holder improved the serum draining and refilling process by allowing intake of air. During testing the pipes were connected, effectively sealing the test cell from airborne contamination. The lubricating fluid was replaced every 1/3 MC and subsequently stored at -20 C° for future debris analysis. At this time point each cell was flushed with dilute detergent; soaked in disinfectant solution for min 20 minutes; rinsed with tap water and then rinsed with distilled water before refilling with lubricant.

The measurement time point was chosen to be 1 MC, at which point the test station cells were dismantled for a more thorough cleaning to remove potential bacterial contamination. The polyethylene components were removed and cleaned before being left for 48 h in a metrology lab prior to measurement. The Prodisc polyethylene inlay was removed from the inferior endplate by use of a thin metal sharpened spatula inserted between the metallic endplate and the PE disc inlay at the anterior end of the TDR. A small leverage applied to the spatula was sufficient to unlock the snap-lock mechanism and allow the inlay to be retrieved for measurement without damage; the Charité polyethylene core is unconstrained. To assist in non-abrasive cleaning of the components, they were submerged in an ultrasonic bath containing isopropanol for 10 minutes followed by drying with lint-free tissue. After the appropriate stabilising time was met, the mass was recorded (five measurements per disc). The ISO14242-2 standard was followed to calculate mass loss due to wear only. The six articulating discs were measured for gross mass loss, but to limit the effect of fluid absorption, the seventh soak control disc was used to subtract changes in mass due to soak effects only and therefore show net wear mass loss. The soak control disc was cyclically loaded to ensure that absorption was similar to the other articulating ones. Gravimetric results were presented in mg. The density of UHMWPE is  $0.934 \text{ mg/mm}^3$ : as an example, 10 mg of wear material by weight is equivalent to  $9.34 \text{ mm}^3$  of material by volume, hence whether reported by weight or volume the amount of wear material can be compared to volumetric wear rates in heavier materials with reasonable validity.

### **2.3.3.3 Statistical Analysis**

Analysis of variance (ANOVA) was used to analyse the gravimetric output data with  $\alpha=0.05$  for differences between data sets using SPSS for Windows (v18.0, SPSS Inc., Chicago, IL, USA). When analysing either Prodisc or Charité separately a one-way ANOVA was used. For comparison of data between Prodisc and Charité tests a two-way ANOVA was used due to the multiple factors of 1) test dynamics and 2) TDR design. Firstly a Levene's test was used to check for homogeneity of variance between the groups – the null hypothesis being that there was no difference between the variances from each set of results. If the Levene's test was not significant then a Tukey HSD post hoc analysis was used following the one-way ANOVA. If the Levene's test showed that there was a difference in the variances then a Tamhane T2



post hoc analysis was performed instead. The data sets discussed were obtained from the same samples for the period of experimentation therefore it could be argued that a repeated measures test should be performed. This however assumes that the pairing of samples was a) deliberate and b) had an effect on the outcomes. This was not the case and due to the short 'memory' of the UHMWPE samples it was decided that ANOVA be used without repeated measures.

### **2.3.3.4 Use of Perturbations of the Standard Testing Conditions**

This study compared the standard ISO test completed here and zero cross shear (CS) tests in the literature [Section 1.6.4.1]. Chapter 3 [In Vitro TDR Simulation] contains a detailed account of the testing parameters that were altered in order to isolate parametric effects. The basic altered parameters are summarised here.

#### *Low cross shear*

The standard ISO test uses out of phase LB and FE motions. For the low cross shear studies this was shifted from being 90° out of phase to in phase (i.e. zero degrees phase shift). This has the effect of producing a curvilinear wear track of low cross-shear ratio (as opposed to zero CS). The AR was retained so that finite element models could be more vigorously challenged with a low CS input motion rather than a zero CS one.

#### *Low Load*

The axial loading cycle of the standard ISO test was reduced by a factor of two from 600-2000 N, 2 Hz, waveform to 300 – 1000 N, 2 Hz, waveform. All other input parameters were kept. This challenged the existing Archard-based wear formula and helped in the development of a new wear formula.

#### *Reduced FE*

The FE motion cycle of the standard ISO test was reduced by a factor of two from +6°/-3° 1 Hz waveform to a +3°/-1.5° 1 Hz waveform. All other input parameters were kept. This study tested reduction in entrainment and attempted to replicate more realistic input parameters without changing all parameters.

## **2.4 Spine Simulator Verification**

The spine simulator experiments presented in this thesis were performed on the second of two virtually identically spine simulators, hereafter named A (first machine) and B (second machine). The first machine was delivered in 2008 and the second in 2009. Although the design was very similar, certain responses to the requirement specifications were altered to: a) improve reliability of the machine, e.g. oil lubricated gearboxes rather than grease lubricated; b) improve kinematic limits, e.g. increase LB capability to  $\pm 15^\circ$  and; c) improve reliability, which was a major issue with the first machine.

To verify that the simulator B would give comparable results to A, a standard ISO test was planned in order to compare the results of this with an identical test previously run on the simulator A. This configuration would also allow comparison with *in vitro* data available in the literature [97, 119, 120]. The test was run four MC and the results were compared for average wear rate, running in period and variability. They were also used to verify a computational model created by Curtis Goreham-Voss at the University of Iowa.

Prodisc-L components were used for the verification process. The Prodisc is a metal-on-UHMWPE device of a semi-constrained design. Six articulating discs were used in order to allow statistical comparison between results. A seventh disc was loaded cyclically with an identical ISO axial load as the other discs but without any motions in order to act as a soak control. Changes in the mass of the soak control could therefore be subtracted from the wear data and a true indication of mean wear calculated. It was expected that a statistically similar result from both simulators would be achieved and therefore allow comparison between simulators.

### **2.4.1 Results of Verification**

#### *Mean Wear Rates Comparison between Two Identical Simulators*

The average wear rate for the first simulator (sim A) was  $12.7 \pm 2.1$  mg/MC for a 5 MC length test [Table 2-4]. The second simulator (sim B) test produced  $16.1 \pm 1.4$

mg/MC but this test was terminated at 4 MC. The wear rate for the first 4 MC of the simulator A test period was  $13.0 \pm 3.0$  mg/MC. The simulator B result was 24 % greater than the original result obtained from simulator A and there was a significant difference (Student's t test,  $p=0.03$ ) between the 4 MC data (sim B) points and the 4 MC (sim A) points.

**Table 2-4 Comparison of mean wear rates for simulator A and simulator B**

Simulator	Wear (mg/MC)	0-1MC	1-2MC	2-3MC	3-4MC	4-5MC	Av/MC	SD
B	Mean	13.2	15.8	16.4	18.8	-	<b>16.1</b>	<b>1.4</b>
	SD	1.6	1.1	2.1	1.8	-	<b>1.6</b>	
A	Mean	9.5	13.3	23.7	5.5	11.3	<b>12.7</b>	<b>2.1</b>
	SD	2.4	4.8	3.3	1.6	1.4	<b>2.7</b>	

When comparing the final values at 4 MC (sim B) and 5 MC (sim A) the significance level increased to  $p=0.01$ . If the first 3 MC mean wear rates are compared the difference becomes insignificant ( $p=0.80$ ). Figure 2-20 shows the dip in wear rate and the following increase in wear rate for the two and three million cycle measurement points. This coincided with bacterial contamination of the simulator A test. All significances are recorded in Table 2-5. The mean wear rate at points 2 MC and 3 MC were not statistically different between simulators. The first and last million cycles were statistically different.

**Table 2-5 Inter-simulator statistical difference between accumulative mean wear rates**

Simulator	Wear (mg/MC)	0-1MC	1-2MC	2-3MC	3-4MC	4-5MC
A	Mean	9.5	11.4	15.5	13.0	12.7
B	Mean	13.2	14.5	15.1	16.1	-
	Significance value (p)	0.01	0.06	0.8	0.03	0.01*
	P < 0.05?	✓	✗	✗	✓	✓

\*Comparing 4 MC average with 5 MC average

The statistical difference between each million cycle measurement value, rather than the accumulated mean wear values, is shown in Table 2-6. The two million cycle measurement point changes from not statistically different to statistically different ( $p < 0.01$ ) but thereafter the differences are significant.

**Table 2-6 Inter-simulator statistical difference between each million cycle time point (per each MC rather than overall mean)**

Simulator	Wear (mg/MC)	0-1MC	1-2MC	2-3MC	3-4MC	4-5MC
A	Per MC	9.5	13.3	23.7	5.5	11.3
B	Per MC	13.2	15.8	16.4	18.8	-
Significance value (p)		0.01	0.24	0.00	0.00	-
P < 0.05?		✓	✗	✓	✓	

The difference between wear rates is emphasised by the difference in the standard deviation between samples under test (Table 2-4). The first simulator (sim A) shows a large average standard deviation of 2.7 compared to 1.6 for simulator B.

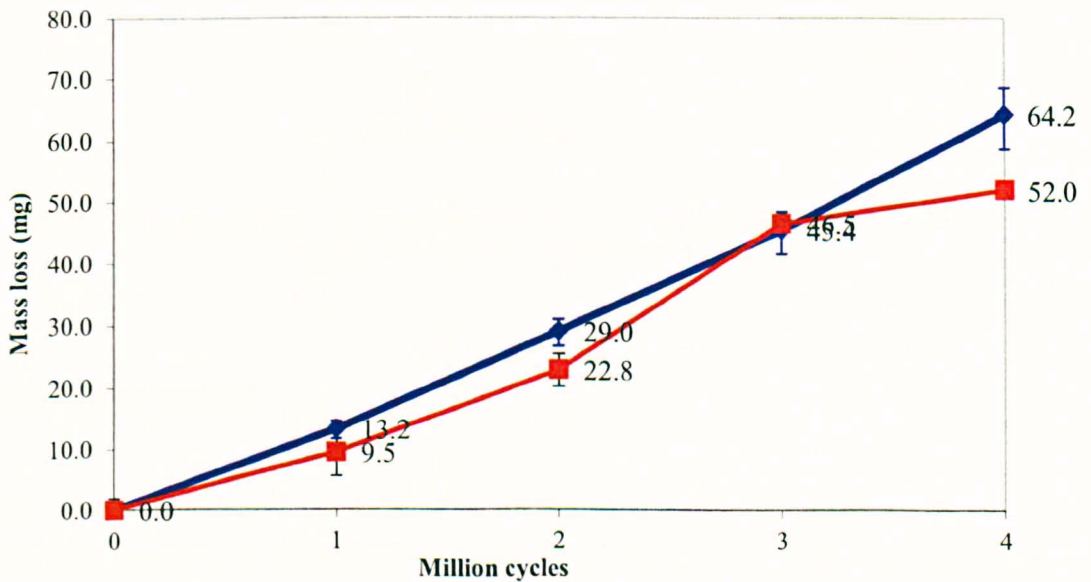


**Figure 2-20 Gravimetric data showing wear rates per MC (simulator B = blue, simulator A = red) ±95% confidence limits**

## 2.4.2 Feedback and Tolerance Limits

In order to verify that the simulator was producing loads in line with the prescribed ISO tolerances, a method of analysing the feedback waveforms was used. Feedback data from a standard test using dummy samples was used, with an average of three waveform results taken and plotted together with the tolerances allowed [Figure 2-21]. 'Index position' refers to the 128 data points recorded by the spine simulator software. After 100 cycles the axial load limits were within  $\pm 5\%$  at the minimum and maximum positions.

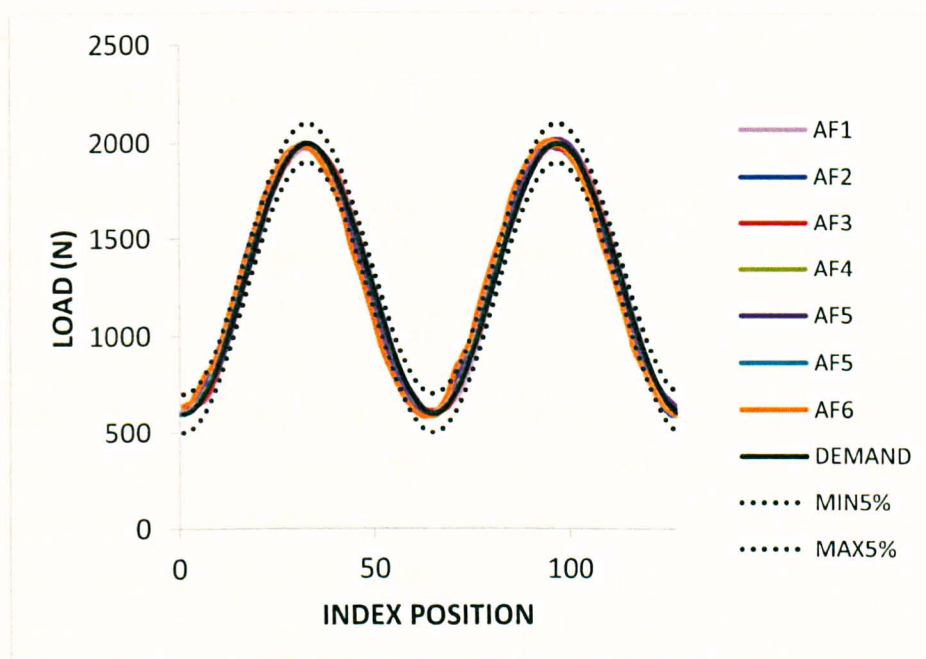


Figure 2-21 Feedback data averaged over three cycles is shown together with the tolerances allowed ( $\pm 5\%$ ) (AF1 = Axial Force 1 etc)

## 2.4.3 Discussion

The results were significantly different to the results from simulator A, however, that test encountered biological degradation of the serum at the two and three million cycle time points. The result of 16.1 mg/MC compared well with a previous ISO-based study by Nechtow et al. [119] with wear rates of 16.59 mg/MC. Nechtow et al applied a sinusoidal loading of 600-1750 N / 1 Hz for axial force as opposed to 600-2000 N / 2 Hz for the present study. The LB and FE waveforms, though not in

phase in the Nechtow study, were not 90° out of phase as in this test. Further, the bovine serum used was diluted to 50% rather than 25% in this test. The effect on the wear rates that these differences would have is difficult to predict.

Bushelow et al. [97] have compared MoP Prodisc and MoM Maverick wear in an ISO standard test and produced Prodisc wear results of 9.10 mg/MC which is less than the both simulator A and B tests or Nechtow et al. However, the exact nature of the waveforms were not shown or described. One notable difference between this test and Bushelow et al. and Nechtow et al. is that the serum lubricating fluid in this test has half the protein content of the ISO standard that they used. This may produce a more effective boundary lubricant that protects the PE surface more readily and hence reduce wear.

The bedding-in phenomena which is observed in some TJR *in vitro* tests was not present in the tests presented here. The difference between the mean wear rates for the entire tests and the initial 1 MC values was 3.2 mg and 2.9 mg for simulator A and B respectively. It should be noted that at the 3 MC and 4 MC time points for the simulator A test, there was bacterial contamination reported and a large fluctuation in wear rate from 23.7 mg/MC to 5.5 mg/MC. This was the first ever study completed on the Leeds design spine simulator and the learning process involved may have made the results inconsistent.

Though the final wear rate results were significantly different between simulator A and B, the results on simulator B were comparable to the range of Prodisc *in vitro* results reported and therefore the simulator was accepted for service.

## **3 In Vitro TDR Simulation**

### **3.1 Introduction**

To date, the effect of the input motion magnitude and phasing have not been fully characterised in terms of their impact on TDR wear [118] and the sensitivity to perturbations in these input parameters is unknown. The ISO standard has been shown to be a relatively high CS motion [147] and was chosen to represent a baseline high CS study which formed the basis of the following parametric investigations.

The aim of this study was to assess the wear rate of semi-constrained and unconstrained types of metal-on-UHMWPE TDRs under varying kinematic input conditions based upon the ISO 18192-1 standard. Modifications to the input parameters included altering the LB to FE motion phasing, the axial loading force and the FE rotation angle. The design of the Leeds spine simulator allows for translation in the transverse plane which may be of importance when testing unconstrained devices.

### **3.2 Method**

#### **3.2.1 Wear Simulation**

A description of the outline method, calibration and verification of the Leeds spine simulator was described in section 2.2. Comparative wear simulations were performed on using ISO18192-1 based motions for all tests. The Prodisc TDR represented a 'semi-constrained' type of TDR of ball-in-socket design with an inferior UHMWPE disc articulating against a superior cobalt-chromium-molybdenum (CoCrMo) cup [Figure 3-1].

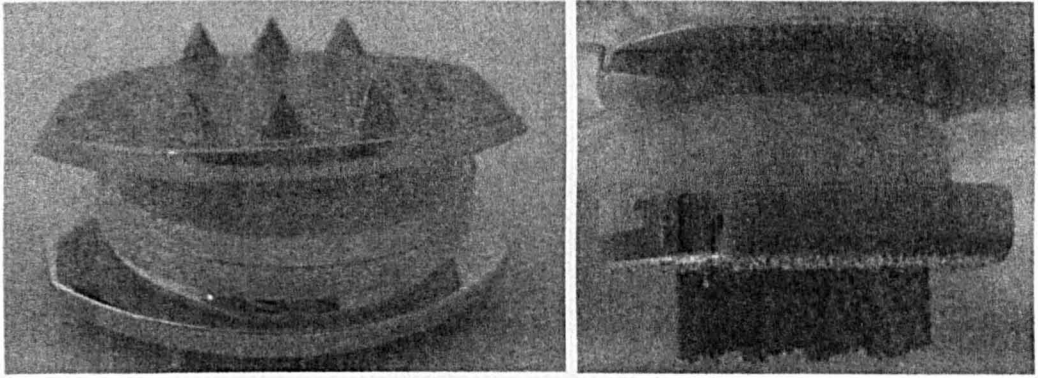


**Figure 3-1 Charité (left) and Prodisc (right) test components shown assembled**

The UHMWPE disc is attached to a CoCrMo base plate by means of a snap-lock mechanism. Theoretically this design provides a fixed centre of rotation (CoR) that is unlike a natural functional spinal unit in which a mobile instantaneous axis of rotation (IAR) is present [37]. The Charité TDR is an unconstrained design utilising a UHMWPE core which facilitates translation of the CoCrMo endplates relative to each other in the horizontal plane [Figure 3-2] and therefore allows multiple CoR positions.



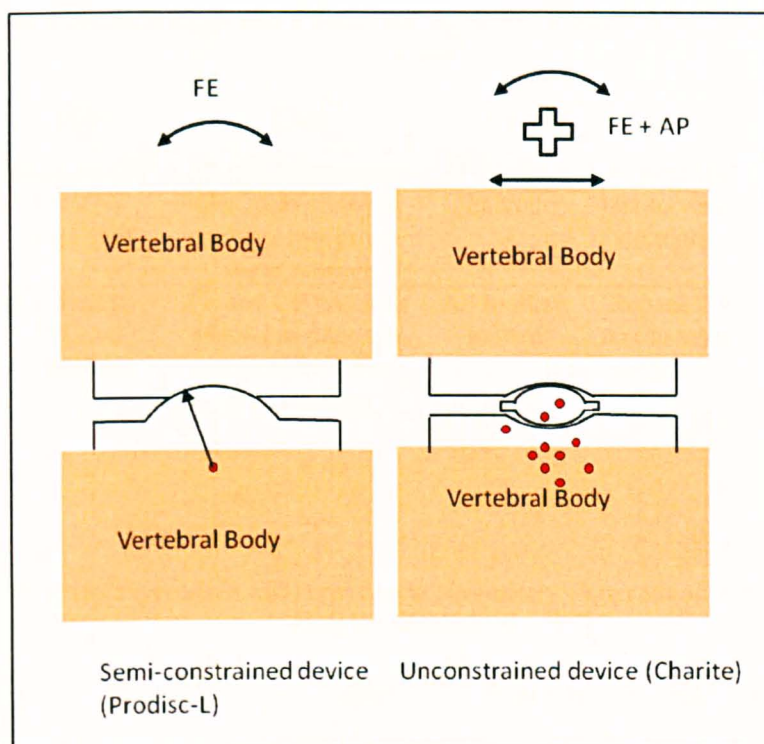


**Figure 3-2 Both TDR designs allow FE but the unconstrained Charité device allows translation in the transverse plane – red dots depict example CoR positions**

The simulations were split into a number of experimental studies [Table 3-1] of several million cycles. A summary of the standard and modified input cycles is shown in Table 3-2. The Prodisc and Charité devices underwent testing under ISO 18192-1 (standard ISO) conditions to establish baseline data [Figure 3-3]. In addition, the standard ISO test was repeated (designated ISO2) near the completion of both the Prodisc and Charité wear studies in order to verify that the simulator was still performing as expected. The second investigation used a modified standard ISO cycle with the phase of the LB changed to give 0 ° differences between LB and FE [Figure 3-4]. It was reasoned that this would produce a low cross-shear motion path that would be easily repeatable and allow comparison with the baseline test.

**Table 3-1 Experimental studies: four input cycles applied to Prodisc; three input cycles applied to Charité**

	<b>ISO</b>	<b>LXS</b>	<b>LL</b>	<b>ISO2</b>	<b>HF</b>
<b>Prodisc</b>	Standard ISO 18192-1 (baseline)	FE and LB motions placed in-phase to create a low cross-shear motion	AF loading halved	Repeat ISO test to verify simulation	FE motion halved
<b>Charité</b>	Standard ISO 18192-1 (baseline)	FE and LB motions placed in-phase to create a low cross-shear motion	AF loading halved	Repeat ISO test to verify simulation	N/A

**Table 3-2 ISO 18192-1 (standard ISO) input cycle parameters – alterations to the standard ISO cycle are highlighted**

<b>Input</b>	<b>Study</b>	<b>Input parameter</b>	<b>Input magnitude</b>	<b>Freq (Hz)</b>	<b>Phase wrt FE (°)</b>
<b>ISO and ISO2</b>	Baseline and repeated baseline	AF	600-2000 N	2	N/A
		AR	+2 °/-2°	1	+90
		FE	+6°/-3°	1	0
		LB	+2 °/-2°	1	-90
<b>LXS</b>		AF	600-2000 N	2	N/A
		AR	+2 °/-2°	1	+90
		FE	+6°/-3°	1	0
		LB	+2 °/-2°	1	0
<b>LL</b>		AF	300-1000 N	2	N/A
		AR	+2 °/-2°	1	+90
		FE	+6°/-3°	1	0
		LB	+2 °/-2°	1	-90
<b>HF</b>		AF	600-2000 N	2	N/A
		AR	+2 °/-2°	1	+90
		FE	+3°/-1.5°	1	0
		LB	+2 °/-2°	1	-90

The method of creation of the low CS test also meant that only one parameter was changed in the test, namely LB phase with respect to FE. A further rationale for the low CS comparison between Prodisc and Charité was that the amount of CS present on a unconstrained device is difficult to predict and calculate. This is due the unpredictable rotation that occurs at the mobile central core which influences the motion pattern at the bearing interface. Comparing results from this device with the semi-constrained Prodisc would aid with inference about the wear mechanism

difference between the different design rationales, and also allow an understanding of wear and effect of CS in comparison with other joints such as hip and knee TJR.

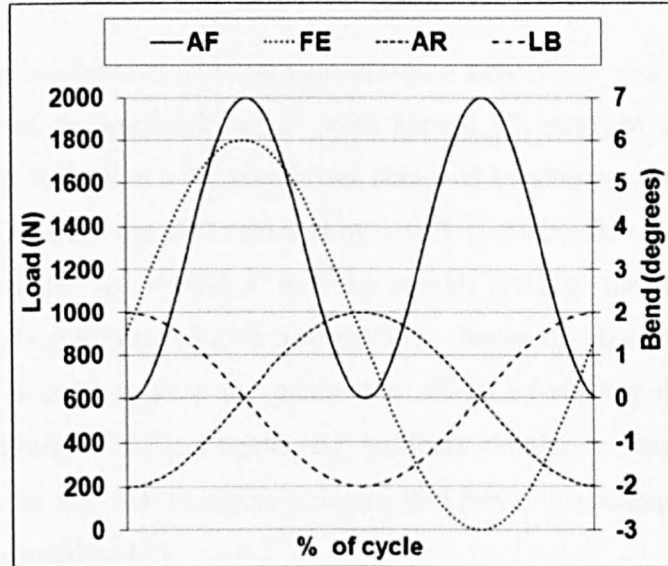


Figure 3-3 ISO 18192-1 lumbar TDR wear testing standard input motions and loads

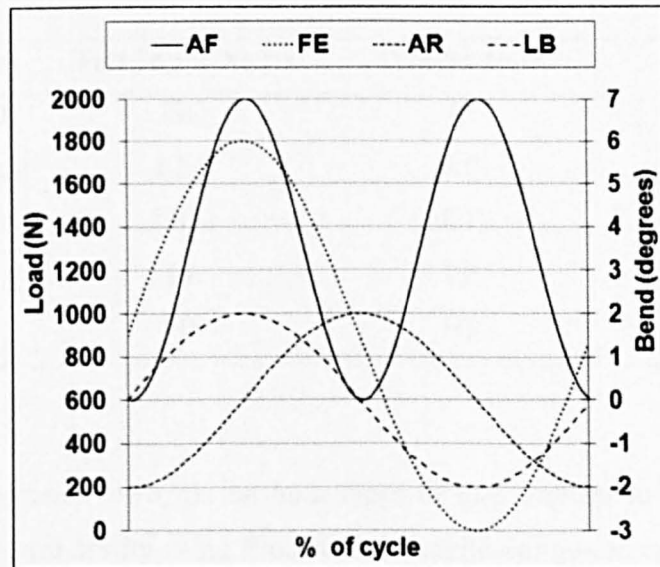


Figure 3-4 ISO 18192-1 lumbar TDR wear testing standard with FE and LB placed in-phase to produce a low cross-shear wear path

A further study was created to assess the effect of lower loads on the wear behaviour of the implants. This test used the ISO standard as a baseline and was followed with a modified 'low load' (LL) modified ISO input cycle. The axial force load input was scaled by a factor of 0.5 to give an exact halving of the load cycle. The frequency

was kept the same at 2 Hz. The effect of contact pressure on the wear rate could then be assessed. The factor of reduction of 0.5 was chosen as a convenient comparison with finite element models (FEM) of the wear behaviour.

For the Prodisc semi-constrained implant design a final study was designed to test the correlation of motion track length (with similar CS ratio) to the baseline ISO test. The change in motion track length was achieved by altering the rotational input of the FE motion from the ISO standard by a factor of 0.5. This meant that the FE angle was decreased to +4.5°/-1.5° and the overall distance that the disc bearing couple moved through was reduced. The methods chosen for all comparative studies were done so in order to keep the parametric effects of altering the standard ISO inputs to a minimum. The test inputs, cell numbers and the devices under test were coded as in Table 3-3. For example; standard ISO input, containing Prodisc device, cell number 3, would be IP3.

**Table 3-3 Test inputs were coded: I = ISO, X = low cross shear, I2 = repeat ISO, L = low load, H = half load; P = Prodisc, C = Charité**

<b>Input Cycle</b>	<b>Test Input Name</b>	<b>Prodisc tests</b>	<b>Charité tests</b>
Standard ISO	ISO	IP	IC
Low Cross Shear	LXS	XP	XC
Repeated ISO	ISO2	I2P	I2C
Low Load	LL	LP	LC
Half FE	HF	HP	-

Identical experiments were run on both types of disc implant to assess the inter-design-rationale variability using Prodisc and Charité designs as example implants. Mean wear rates were calculated from the total mass loss and compensated by a soak control measurement. Verification that the simulator meets ISO 18192-1 tolerances for both phasing and input magnitudes have been confirmed previously [148] for an identical machine and was repeated for the simulator used for these studies.

### 3.2.2 Profilometry and Imagery

A method of assessment of the tribological performance of the TDR bearing design under test was developed in order to monitor and compare bearing performance. This was done by using surface profilometry of both the polyethylene and metallic bearing surfaces. An attempt was made to segregate the modes of wear into three distinct regions of wear behaviour. A previous tribological report on Prodisc and Charité bearings [122] indicated that surface topography was more complicated than a simple profile trace could record. The wear scars present on these devices were inspected and observed to be burnished at the outer edges and roughened towards the pole region of the dome of the polyethylene components. In order to assess this quantitatively a method of surface profiling was developed. The results of the surface roughness values and clearance could then be used to add data to the wear processes taking place in the tribological regime. Knowledge of any anisotropic surface wear effects could be measured and described. Furthermore, an attempt to correlate a change in surface topography with the parametric changes in the input cycle waveforms could be undertaken. Average roughness was used in order to compare results with that already in the literature.

#### *Surface Profile*

A contacting surface profilometry instrument (120L or PGI800, Taylor-Hobson Ltd, Talysurf, UK) was used to record average roughness ( $R_a$ ) and average radius ( $R$ ). The use of contacting surface recording was used in order to gain both  $R_a$  and radius readings. The optical profiling alternative is unsuitable for non-reflecting materials or highly curved surfaces and only allows relatively small sections of area to be assessed at one time. The cut-off / bandwidth values used for the roughness filter in the profiler software were chosen based on Taylor-Hobson recommended values for non-periodic waveforms; 0.8 mm / 100:1 for the polyethylene components and 0.25 mm / 100:1 for the metallic components.

The traces were positioned in order to capture the greatest amount of data in a time-efficient manner [Figure 3-5]. The first trace from edge to edge was used for a general full area  $R_a$  value plus a truncated version of this trace was used to show the roughness at the pole area of the disc components. An example trace is shown in

Figure 3-6. The second trace was at the rim area of the wear scar where the edge of the cups articulates with the PE components.

The initial trace (trace 1, x-direction) was taken from as close the edge of the PE dome as was practicable for the Prodisc components and from flat to flat on the Charité components (a Charité trace is depicted in Figure 3-7). In order to ensure that the central (highest point) of the curved area was traversed, the trace stylus was moved across the pole area of the dome until the highest reading was observed. Then the stylus could be returned to a relevant start position. For the metallic cups the start/finish positions for the traces were placed on the flat edges of the cup rims. The trace itself was then truncated by 2 mm either side of the flats in order to eliminate data that was not part of the wear area. The initial trace (trace 1) was reported in full for the overall  $R_a$  (labelled ALL in results), then truncated [Figure 3-7] to yield roughness for the pole area of the dome (labelled POLE in results). Trace 2 (y-direction) was used to give roughness values for the burnished area at the edge of the wear area (labelled RIM in results). Measurements of the PE components were taken at the start and end of each experiment. Sample numbers were  $n=6$  for Prodisc and  $n=3$  for Charité (two surfaces analysed on Charité cores).

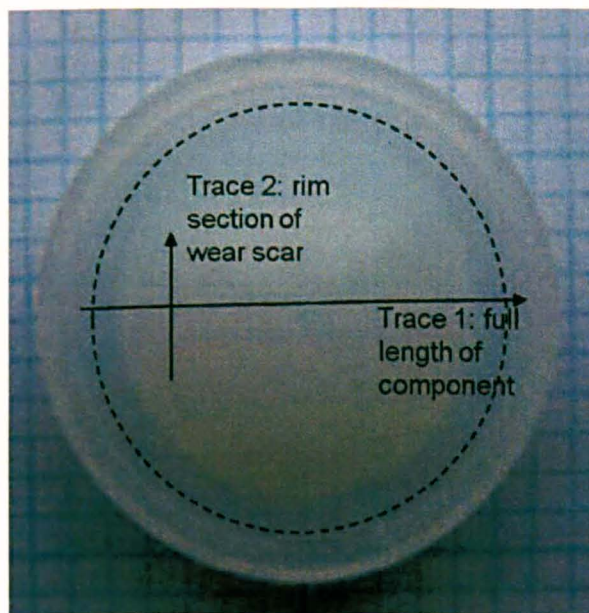
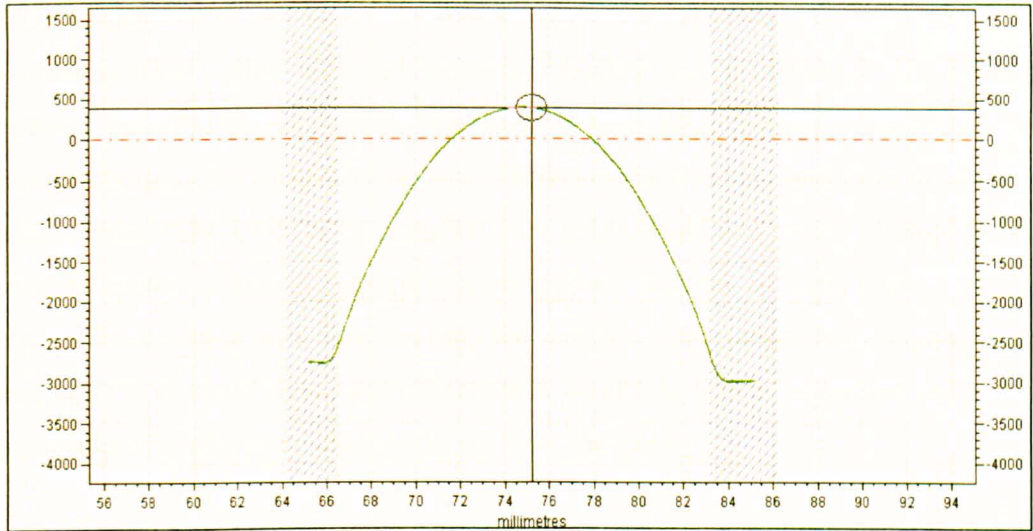
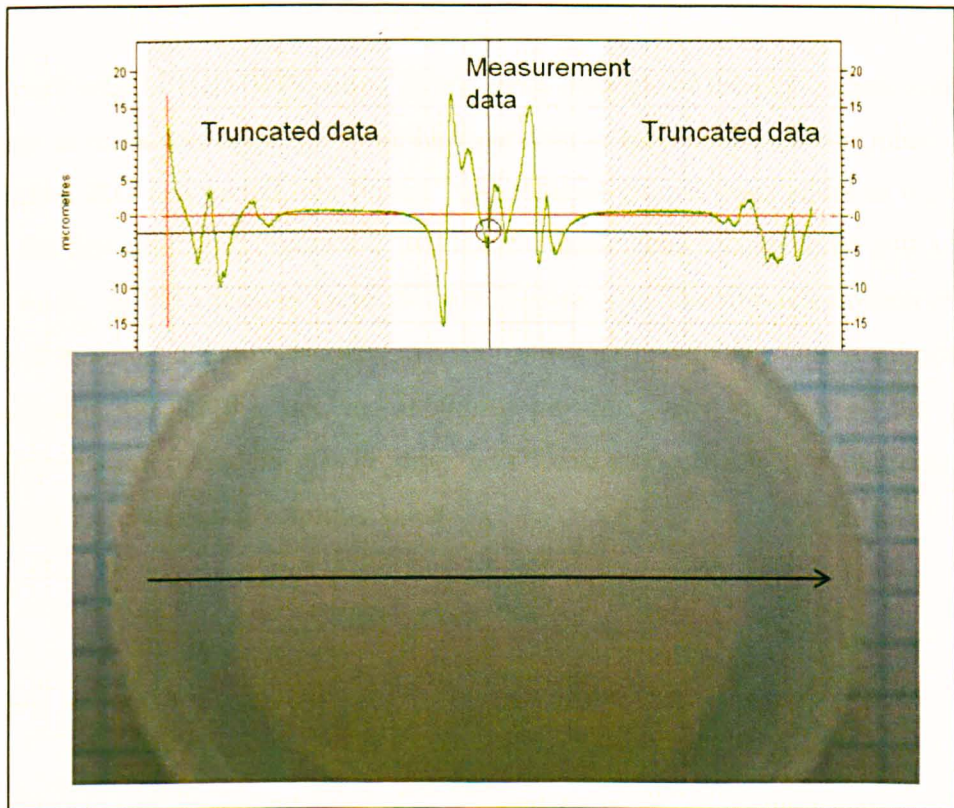


Figure 3-5 An example Charité core component with solid lines showing stylus trace positions and dotted line showing approximate position of the metallic cup contact area



**Figure 3-6 Example trace start/finish positions for the Charité PE component showing how the initial long trace was truncated for overall roughness measurement**



**Figure 3-7 An example Charité core (11 MC) showing profile trace and the truncating of the trace used to assess specific area profile phenomena (central roughened pole area shown)**

### *SEM images*

A Philips XL30 SEM with environmental facility was used for all SEM image capture. Initially the microscope was used in environmental mode but because of sample charging the images were poor. Therefore the machine was used in standard SEM mode. TDR UHMWPE samples were gold coated and mounted with carbon paint to ensure sufficient conductivity and reduce chances of static surface charge accumulation. Even with this method, the length of time under the electron beam was critical to avoid over exposure which results in a pale or burned out image especially over edges or valley in the surface topography.

## **3.3 Results (Wear)**

### **3.3.1 Standard ISO Input Motions**

The soak control UHMWPE discs gained mass throughout the experiment and this change in mass was deducted from the wear data at each measurement point. Over the initial ISO test period, the Prodisc soak control gained mass equal to 0.23 mg over the first four MC [Figure 3-8] while the Charité gained mass equal to 0.30 mg over 4 MC of the 5 million cycle ISO test [Figure 3-9]. The first few million cycles showed the most dramatic increase in soak control mass with the trend continuing at an average rate of 0.1 mg and 0.06 mg per MC for the rest of the wear experimentation period for the Prodisc and Charité respectively. It is interesting to note that there was no asymptotic value.



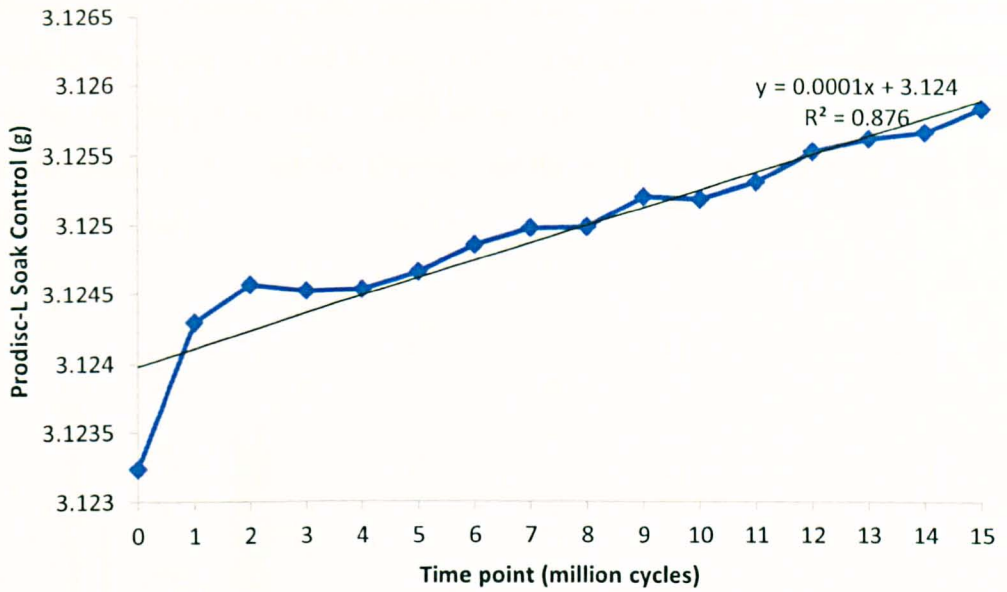


Figure 3-8 Soak control results for the entire spine simulator experimentation period for Prodisc (top) and Charité (bottom)

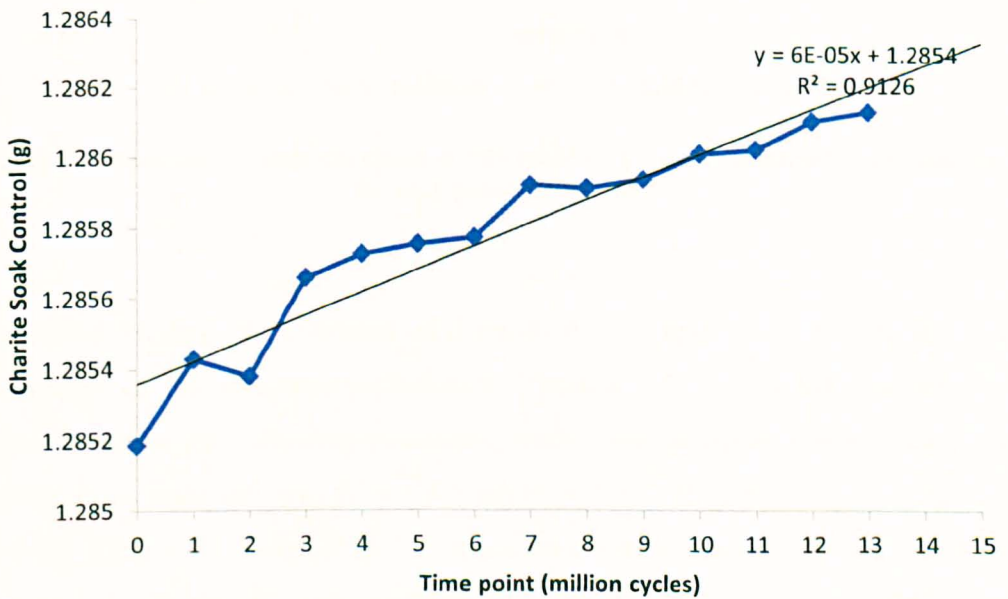
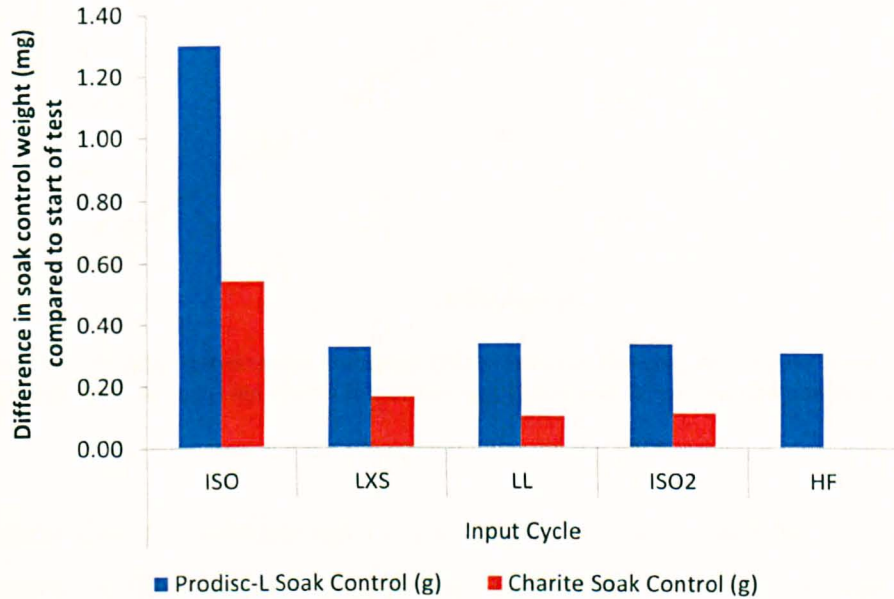


Figure 3-9 Soak control results for the entire spine simulator experimentation period for Prodisc (top) and Charité (bottom)

The trend in soak control activity is summarised by Figure 3-10 showing the plateauing of the soak control mass for both types of disc by the end of the first few

million cycles of standard ISO experimentation. However the Charité and Prodisc results differ in that the trend for the Prodisc is to absorb more fluid than the Charité over the full test period. This is difficult to explain, the Prodisc has increased mass (~three times) of the over the Charité, but the surface areas in contact with fluid should be similar.



**Figure 3-10 Soak control mass calculated as difference between end-point and start-point mass for each parametric study**

The initial Prodisc test consisted of a standard ISO input for 4 MC to act as an assessment of the simulator performance [Section 2.4] and a baseline result by which to assess the following parametric studies and compare previous data. The overall mean mass loss was  $62.4 \pm 5.5$  mg over 4 MC [Figure 3-11], ranging from 53.7 mg (IP3) to 71.2 mg (IP5). The mean wear rate averaged over the first 4 MC was  $16.1 \pm 1.4$  mg/MC, ranging from 13.9 mg/MC (IP3) to 17.8 mg/MC (IP5). Station number 5 was the highest wearing test cell position over the whole test and station 3 the lowest. Over the entire test the lowest and highest rates of mass loss did not remain at station 3 and 5 but varied between stations 1, 3, 5 and 6. The mean wear rate per MC remained approximately linear throughout the test with a gradient of 15.5 mg/MC.

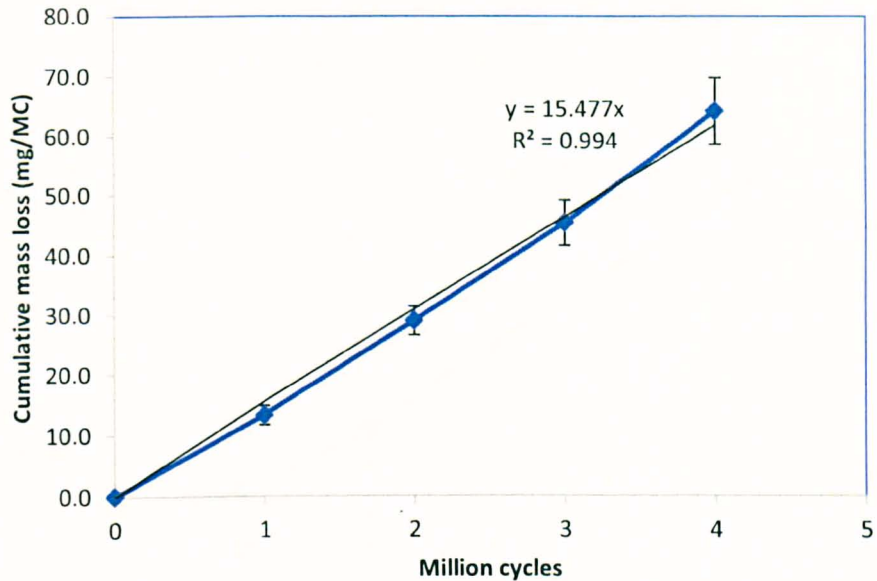


**Figure 3-11 Prodisc tested under standard ISO conditions showing cumulative wear rate  $\pm$  standard deviation (also shown is a linear regression and  $R^2$  correlation coefficient)**

The initial Charité test consisted of a standard ISO input for 5 MC to act as a verification of the simulator performance compared to results available in the literature and a baseline result by which to assess the following parametric studies. The length of this test was increased slightly to 5 MC over the Prodisc's 4 MC in order to mitigate some of the variability in the initial data. The overall mean mass loss was  $57.6 \pm 8.1$  mg over 5 MC [Figure 3-12], ranging from 49.9 mg (IC5) to 71.6 mg (IC1). The mean wear rate averaged over the first 5 MC was  $11.5 \pm 1.6$  mg/MC, ranging from 10.0 mg/MC (IC5) to 14.3 mg/MC (IC1). Over the entire test the lowest and highest rates of mass loss remained at station 5 and 1 except for the first 1 MC where the highest and lowest wearing test cells were 6 and 3. The mean wear rate per MC remained linear from the 1 million cycle point onwards, however, the first 0-1 MC showed a much lower wear rate.

Exclusion of the first 1 MC of wear established an increased average wear rate of  $13.4 \pm 2.0$  mg/MC, shown in Figure 3-12. The gradient of the regression line was 13.5 mg/MC when calculated for the 1-5 MC data points. Linear regression for the

1-5 MC data set revealed a similar  $R^2$  value to that obtained for the Prodisc. (The exclusion of the 1<sup>st</sup> MC was based on the statistical data presented in Table 3-5.)

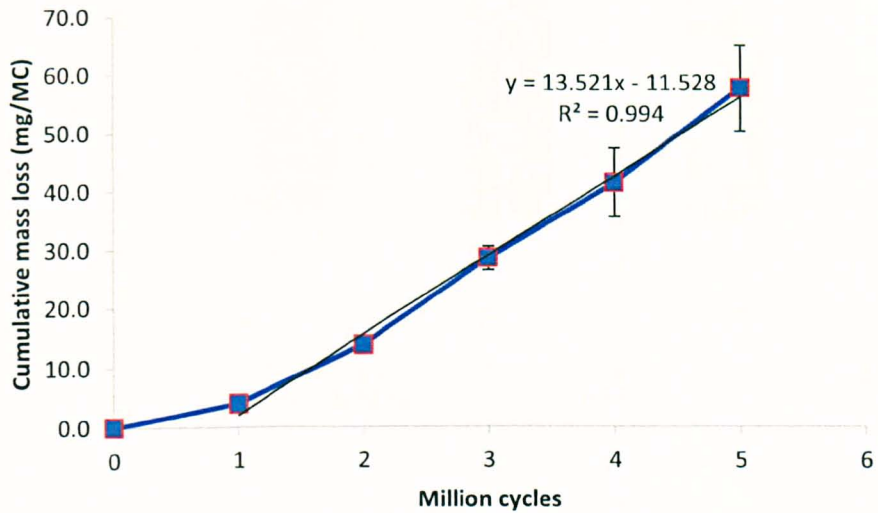


**Figure 3-12 Charité tested under standard ISO conditions showing cumulative wear rate  $\pm$  standard deviation (also shown is a linear regression and  $R^2$  correlation coefficient)**

There was a significant difference (two-way ANOVA,  $p = 0.03$ ) between the two disc design's average wear data when all million cycle measurement points were considered. Comparing the Prodisc data with the Charité data for only the 1-5 million cycle points of the Charité gave a non-significant difference (two-way ANOVA,  $p = 0.99$ ) [Figure 3-13].

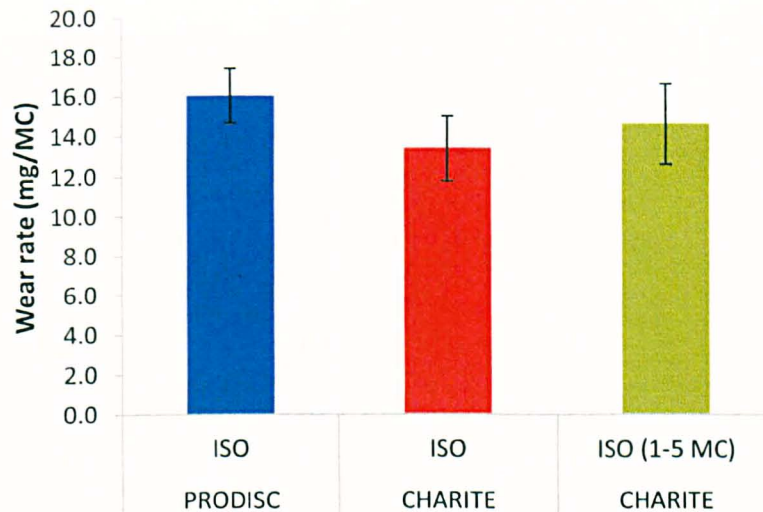


**Figure 3-13 Mean wear rates for the Prodisc and Charité disc designs (0-5 and 1-5 million cycle points shown for the Charité)**

Wear scars for all tests showed a large area of wear almost covering the entire dome of the UHMWPE components indicative of full contact over the cycle period between the bearing components. The worn surfaces had a polished appearance that was more pronounced towards the circumference of the worn area for both the Prodisc and Charité UHMWPE components [Figure 3-14]. Light optical microscopy (LOM) of the surface around the top of the dome area showed the build-up of debris at the pole (a close-up of the edge of this area is shown in Figure 3-15) and closer inspection of this debris revealed linear scratches that may have been caused by the entrapment and subsequent departure of wear particles from the dome area migrating to the outside fluid medium [Figure 3-16].

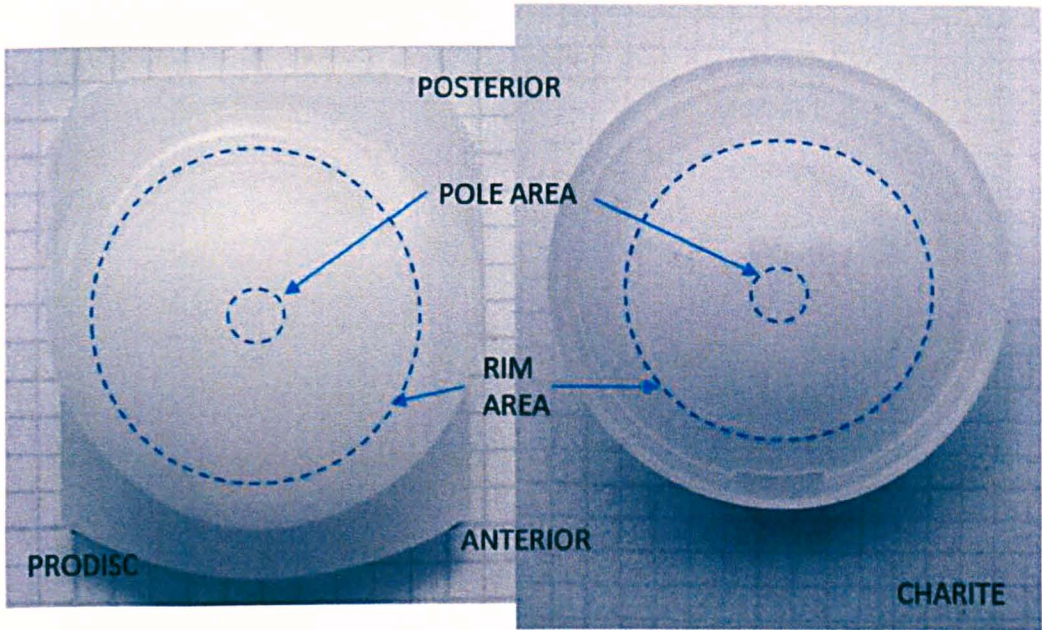


Figure 3-14 Prodisc and Charité wear scars particularly pronounced towards the circumference of the UHMWPE bearing and toward the anterior of the Prodisc (scale 2mm)

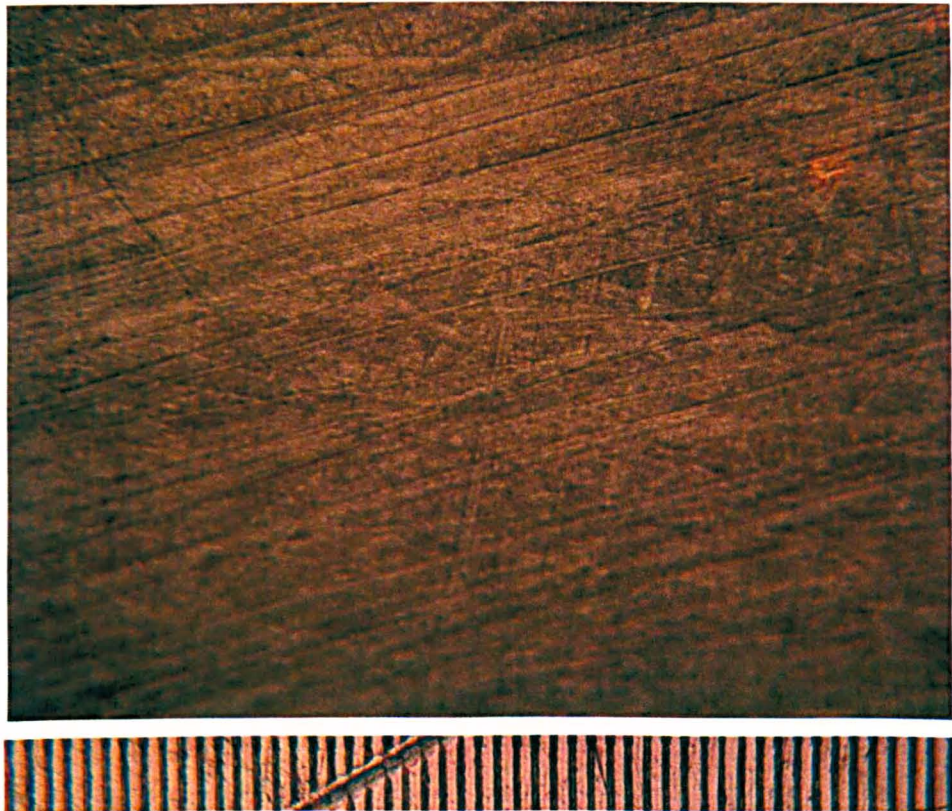


Figure 3-15 x25 magnification LOM image of the dome area of the Prodisc showing predominantly linear wear tracks (scale shown is 0.01 mm per division)

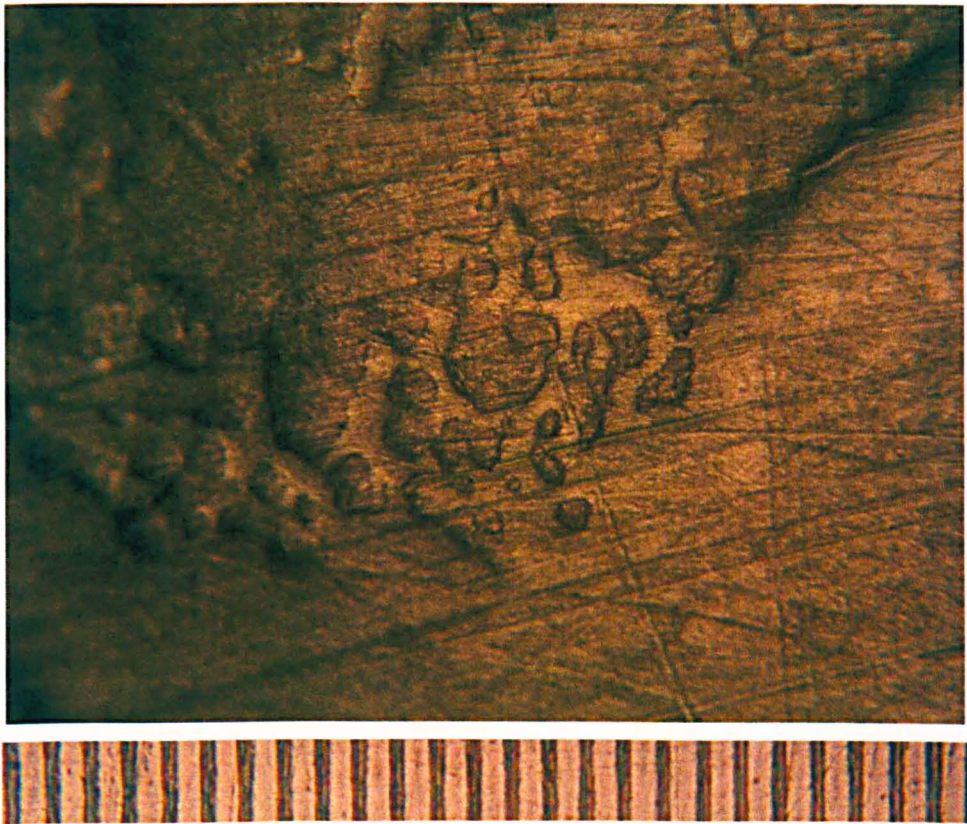


Figure 3-16 x50 magnification LOM image of the pole area at the edge of the roughened section of the Prodisc – the islands of debris have been reapplied the surface (scale shown is 0.01 mm per division)

The initial standard ISO results were followed by the following parametric studies:

- Low cross shear (LXS)
- Low Load (LL)
- Repeated ISO (ISO2)
- Half flexion-extension (HF)

The following sections outline the results for each of these modified input cycle studies.

### 3.3.1.1 Low Cross Shear Input Motions

#### *Prodisc versus Charité*

The baseline standard ISO tests using Prodisc and Charité samples were followed by a low cross-shear (modified ISO) study. The baseline tests produced wear rates of  $16.1 \pm 1.4$  mg/MC and  $13.5 \pm 2.0$  mg/MC for the full Prodisc study and the 1-5

million cycle data for the Charité respectively. The following reduced cross-shear studies produced wear rates of  $6.0 \pm 1.3$  mg/MC and  $8.2 \pm 1.3$  respectively [Figure 3-17].

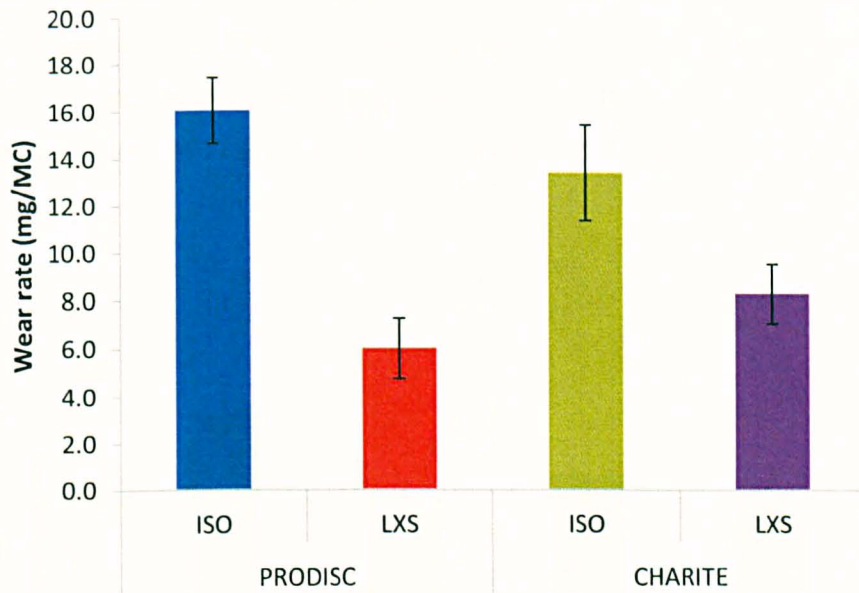


**Figure 3-17 Prodisc low CS average wear rate compared to the standard ISO ( $\pm$  standard deviation)**

The reduction in mean wear rate for the low cross-shear motion path using the Prodisc device was significant (one-way ANOVA,  $p < 0.01$ ) showing a drop to 37% of baseline. There was a significant difference (two-way ANOVA,  $p < 0.01$ ) in mean wear rate between the low cross-shear input for Prodisc and all other input/disc combinations with the exception of the Charité low CS test. The reduction in mean wear rate for the low cross-shear motion path using the Charité device was significant (one-way ANOVA,  $p < 0.01$ ) showing a drop to 56 % of baseline (using the 2-5 million cycle data) or 71 % (when using the entire data set). The Prodisc and Charité low CS input results were not significantly different (two-way ANOVA,  $p = 0.76$ ). The low CS cycle results for the Charité were 38 % higher than that for the Prodisc while the ISO results were lower: 17 % for the 1-5 MC data and 28 % for the full Charité data.



### 3.3.1.2 Low Load Input Motions

#### *Prodisc versus Charité*

The baseline standard ISO tests using Prodisc and Charité samples were followed by a low load (modified half load ISO) study. The baseline tests produced wear rates of  $16.1 \pm 1.4$  mg/MC and  $13.4 \pm 2.0$  mg/MC for the full Prodisc study and the 1-5 million cycle data for the Charité respectively. The following reduced load studies produced wear rates of  $11.8 \pm 1.0$  mg/MC and  $12.5 \pm 3.7$  respectively [Figure 3-18].

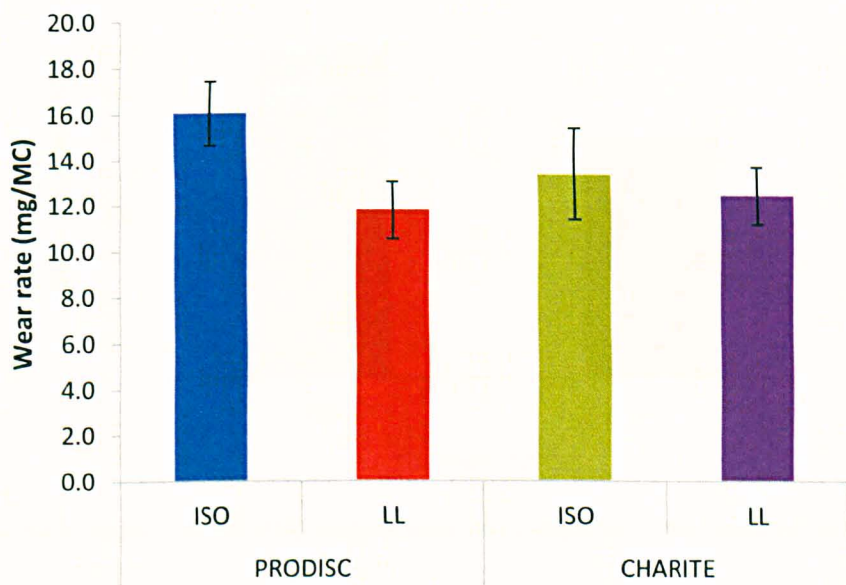


**Figure 3-18 Prodisc low CS average wear rate compared to the standard ISO (Charité results shown are 2-5 MC average)**

The reduction in mean wear rate for the low load cycle using the Prodisc device was significant (one-way ANOVA,  $p < 0.01$ ) showing a drop to 74% of baseline. The reduction in mean wear rate for the low cross-shear motion path using the Charité device was not significant (one-way ANOVA,  $p = 0.56$ ) showing a drop to 93 % of baseline (using the 1-5 million cycle data).

### 3.3.1.3 Half Flexion-Extension (Prodisc only)

#### *Prodisc only*

The baseline standard ISO tests using Prodisc samples was followed by a low load (modified half FE ISO) study. The baseline test produced wear rates of  $16.1 \pm 1.4$  mg/MC, with the following reduced FE experiment producing a wear rate of  $11.7 \pm 2.4$  mg/MC [Figure 3-19].

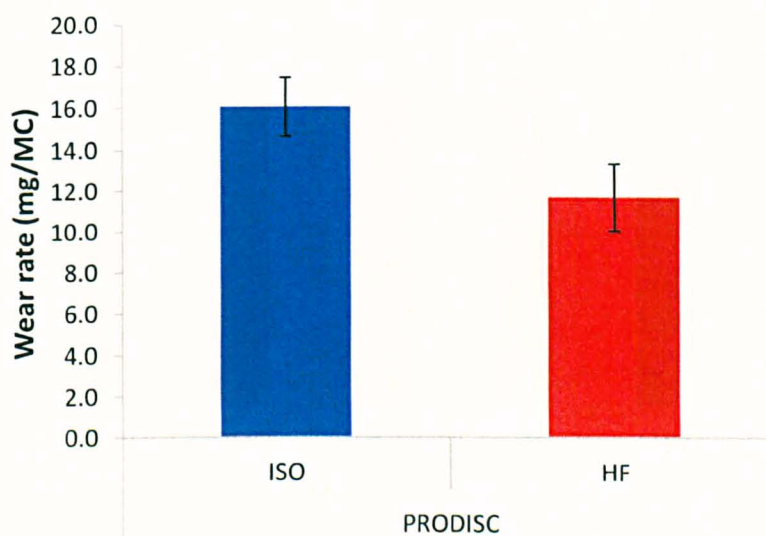


Figure 3-19 Prodisc half FE (HF) average wear rate compared to the standard ISO cycle

The reduction in mean wear rate for the half FE cycle using the Prodisc device was significant (one way ANOVA,  $p < 0.01$ ) showing a drop to 73% of baseline. The reduction in mean wear rate was significantly different (two way ANOVA,  $p < 0.01$ ) from all input cycle studies with the exception of the low load test ( $p = 1.00$ ).

### 3.3.1.4 Standard ISO Verification Study (Initial and final ISO studies compared)

#### *Prodisc*

The initial standard ISO studies for Prodisc devices were repeated after the intervening low CS and low load studies to ascertain if the spine simulator was still delivering correct baseline data before commencing with the final half FE study.

When comparing the entire data set for the ISO based results (first ISO run followed by the later repeated ISO run) the data showed little deviation from the initial 1 million cycle point [Figure 3-20]. However the data did show a widening of the variance at the latter measurement points compared to the start of the study, though this was not significant using Levene’s test for homogeneity of variance ( $p=0.13$ ).

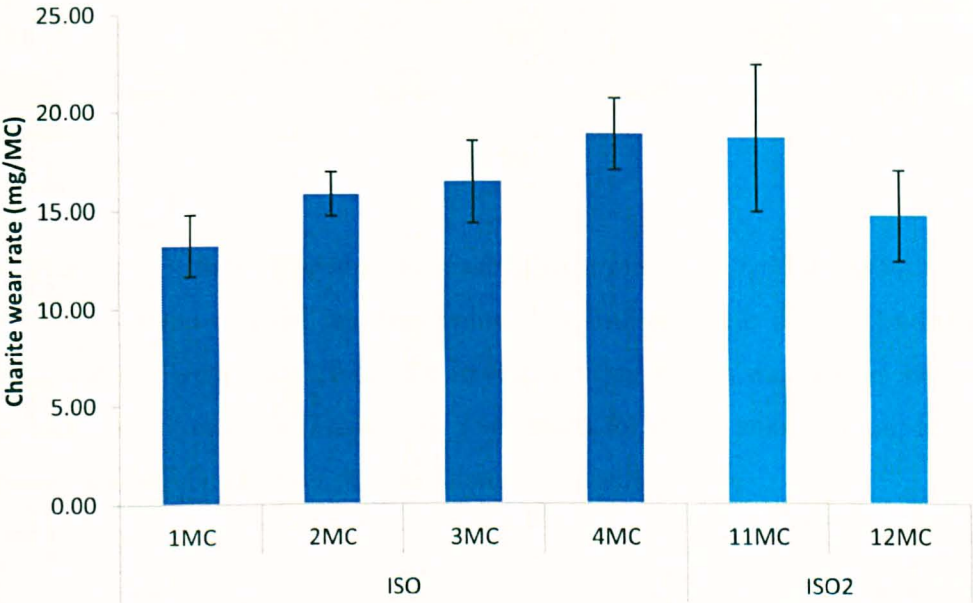


**Figure 3-20 ISO and repeated ISO (ISO2) wear rates for the Prodisc device (note that the repeated ISO test was completed after a gap of 6 MC)**

In order to check that steady state wear was achieved, a one-way ANOVA was performed on the entire Prodisc ISO wear data. The p values (one-way ANOVA) are summarised in Table 3-4. From the 1<sup>st</sup> million cycle measurement point the data was not significantly different for most comparison measurement points [Table 3-6]. For this data, homogeneity of variance could be assumed ( $p<0.05$ ) and the Tukey HSD post hoc test was used.

**Table 3-6 Table 3-4 Prodisc million cycle measurement points showing significance levels (using Tukey HSD test for homogenous variances)**

		ISO Cycle Measurement Point (MC)					
		1	2	3	4	11	12
ISO Cycle Measurement Point (MC)	1		0.37	0.17	<0.01	<0.01	0.87
	2			1.00	0.22	0.28	0.95
	3				0.44	0.53	0.77
	4					1.00	0.04
	11						0.05*
	12						
Indicates a non-significant difference between measurement points							

\* 0.050

The repeated ISO study showed an increase in wear rate to  $16.7 \pm 2.8$  mg/MC which was 104 % of the original baseline value (0-4 million cycle data). The highest wearing stations were variable but the lowest wearing station was always station 3 from 1 MC point onwards [Table 3-5]. The reason for this is unknown, but is more probably device related rather than simulator cell position.

**Table 3-5 Prodisc ISO studies showing minimum and maximum wearing test cells (mg/MC)**

Cell	ISO				ISO2	
	1MC	2MC	3MC	4MC	11MC	12MC
IC1	12.92	16.98	18.07	19.63	23.60	16.74
IC2	14.11	16.16	14.40	17.86	18.72	18.00
IC3	12.39	14.34	13.32	15.68	12.17	11.85
IC4	13.19	16.48	17.28	20.14	19.02	13.61
IC5	15.62	16.29	18.48	20.80	17.80	13.89
IC6	11.02	14.49	16.83	18.90	20.54	13.90

MIN

MAX

*Charité*

The initial standard ISO studies for Charité devices were repeated after the intervening parametric studies to ascertain if the spine simulator was still delivering correct baseline data. When comparing the entire data set for the ISO based results (first ISO run followed by the later repeated ISO run) the results show a clear steady

state wear rate emerging at around the 2 million cycle measurement point [Figure 3-21]. The data also shows a wide variance at the latter measurement points compared to the start of the study.

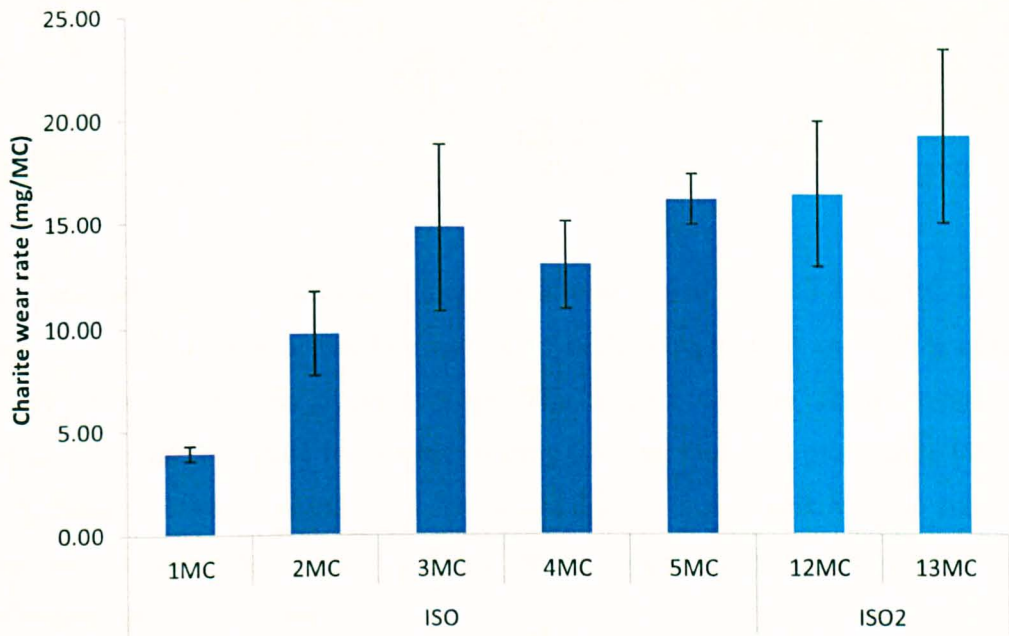


**Figure 3-21 ISO and repeated ISO (ISO2) wear rates for the Charité device (note that the repeated ISO test was completed after a gap of 8 MC )**

In order to check at what point the steady state wear began, a one-way ANOVA was performed on the entire Charité ISO wear data. The p values summarised in Table 3-6 show that from the 2 million cycle measurement point the data is not significantly different. For this data the homogeneity of variance could not be assumed ( $p < 0.05$ ) and the Tukey HSD post hoc test was changed to a Tamhane T2 post hoc test.

**Table 3-6 Charité million cycle measurement points showing significance levels (using Tamhane’s test for non-homogenous variances)**

		ISO Cycle Measurement Point (MC)						
		1	2	3	4	5	12	13
ISO Cycle Measurement Point (MC)	1		0.01	0.02	<0.01	<0.01	0.01	<0.01
	2			0.43	0.35	<0.01	0.08	0.03
	3				1.00	1.00	1.00	0.87
	4					0.22	0.81	0.25
	5						1.00	0.96
	12							1.00
	13							
Indicates a non-significant difference between measurement points								

The repeated ISO study showed an increase in wear rate to  $17.8 \pm 3.7$  mg/MC which was 154 % of the original baseline value (0-5 million cycle data) and 121 % of the steady state 1-5 million cycle average. The highest wearing station remained constant at station 1 while the lowest wearing stations were less predictable [Table 3-7]. Again the reason is unknown, but as the highest and lowest wearing stations changed between tests, it is less probable that this phenomenon was connected with particular simulator stations.

**Table 3-7 Charité ISO studies showing minimum and maximum wearing test cells (mg/MC)**

Test Cell	ISO					ISO2	
	1MC	2MC	3MC	4MC	5MC	12MC	13MC
IC1	4.13	13.30	19.09	16.66	18.40	21.39	24.62
IC2	3.90	9.10	12.26	12.58	16.56	19.67	21.91
IC3	3.26	10.05	16.34	10.47	16.04	11.96	16.78
IC4	4.14	7.93	11.42	12.29	15.57	13.91	12.42
IC5	3.86	7.97	10.28	12.17	15.67	16.13	20.06
IC6	4.27	10.12	19.39	13.77	14.82	15.32	19.48

MIN  
MAX

### 3.3.1.4.1 Wear Data Summary

There was only one outlier present in the entire Prodisc and Charité gravimetric data sets. The box plot [Figure 3-22] demonstrates the spread of data and the absence of outliers. Beyond the low load study (LP) the spread of the data increases and this

was reflected in increased levels of variance in the statistical data. The Prodisc experimental studies were performed on the spine simulator before the Charité test. Data from the Charité studies showed that from the second study (low load) the range of data was larger than the Prodisc experiments. This resulted in a large variance and suspected outliers. Levene's test was influenced by this wide data range homogeneity of variance could not be assumed when comparing the Prodisc and Charité data. The spread of data increased in the Charité experiments.

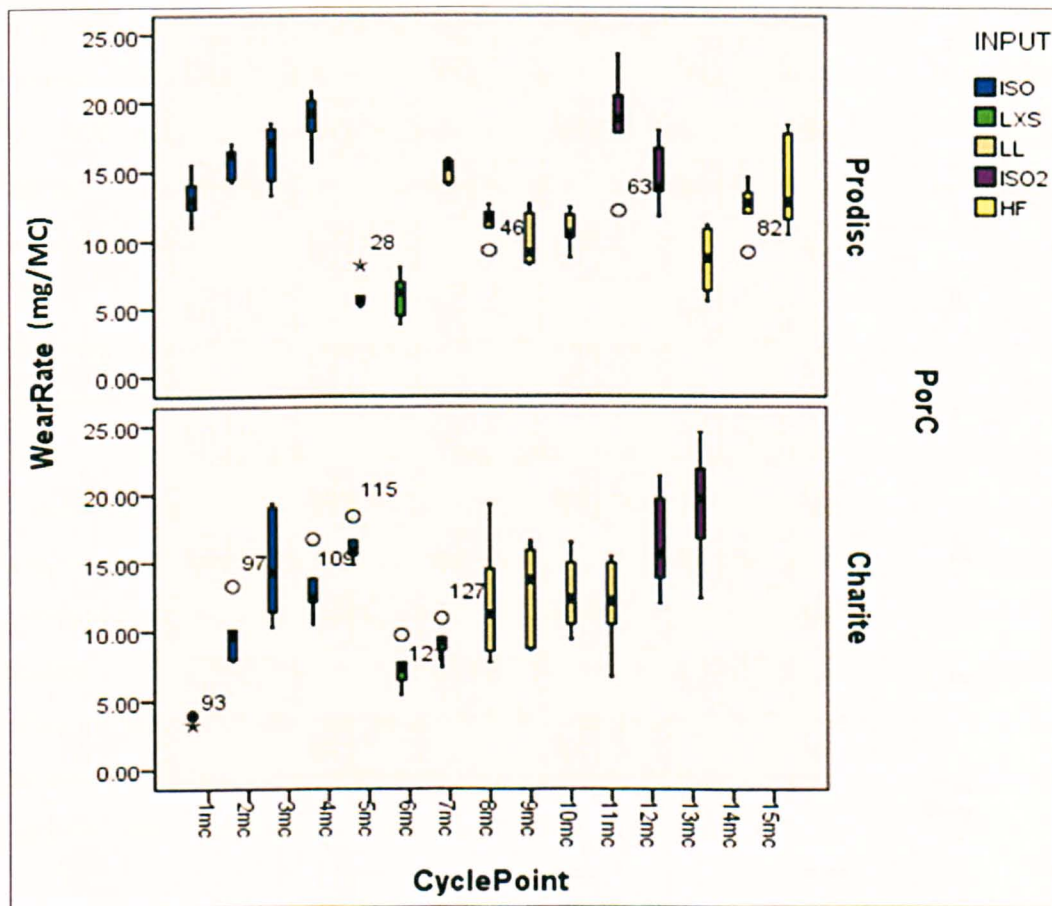


Figure 3-22 Spread of data of entire spine simulator experiments showing widening of spread for the secondary Charité studies (bottom) compared to the Prodisc (top)

The standard ISO test results were of the same magnitude for the Prodisc and Charité devices with the Prodisc wearing higher than the Charité by 28% when comparing the full Charité data but by only 17 % when the first million cycles was excluded from the Charité data set. This noticeable difference in the wear behaviour was due to the initial low bedding-in wear exhibited by the Charité TDR. This device showed low wear (approximately half) for the first 1 MC. Comparing the

wear rate indicated by the linear regression line and the average mean wear rate showed a large difference, therefore the first 1 MC were excluded. In the reporting of wear rates the mean average was used throughout the testing as this was a simple way of ensuring correct comparisons rather than using linear regression.

When considering average data results for each experimental input cycle study extreme data points and outliers were not common within the experimental studies in this series of tests. The mean data of Prodisc based results didn't show any extreme values of concern. The Charité average wear data showed only one possible anomaly in the low CS data. However, when the full data set was disseminated into per-million data sets there were more possible anomalies but these were included in all the data analyses as the values were not far enough from the mean to be classed as definite outliers.

An issue of concern with the simulator performance was the high and low wearing stations. The highest wearing Prodisc stations were variable which is as expected with a level of random experimental error. But the lowest wearing station was consistently station 3 (IP3 for Prodisc). This has therefore introduced a certain amount of non-random experimental error. The Charité tests on the same simulator produced an opposite trend, where the highest wearing station was consistently station 1 (IC1) but the lowest wearing stations were variable. Since these studies were completed on the same simulator and which had regular re-calibration it is not possible to isolate a reason for consistent high or low wearing stations, however, it is more probable that specimen difference rather than station issue was the cause.

The mechanism of wear of the TDRs under test appears to have been similar to existing hip and knee UHMWPE devices, except that the pole areas exhibited a roughening effect due to a new bio-tribological effect. Third body damage resulted in linear wear tracks or scratches and may be due to larger polyethylene wear debris making its way from a central region of bearing contact to the outer rim and into the lubricating medium – this may also be linked to the build-up of re-attached debris at the pole regions. The roughening at the pole vicinities seems to have been caused by re-attachment of debris to the polyethylene surface. The burnishing exhibited on the



polished rim regions is indicative of micro-polishing abrasion or perhaps viscous flow due to elevated contact stress [149].

The repeated ISO verification of the Prodisc and Charité TDR tests demonstrated that the spine simulator was capable of maintaining correct wear behaviour even after several millions of cycles of running time. For the initial standard ISO study both TDR designs showed wear rates rise steadily (much more so in the first million cycles of the Charité test) and this phenomena has been observed in a previous simulator test using the same design of components and virtually identical design of simulator [122]. However the following repeated ISO study showed a reverse trend whereby the wear rate steadily decreased. The tribological explanation for this is difficult to establish but a possible hypothesis for the initial wear rate trend was that the bedding-in of the polyethylene components initially resulted in a smaller area of real contact which lowered the wear rate. A cause of this would be the spiral machining marks which as well as roughening the new surface (approximately 0.5-1  $\mu\text{m}$ ) also increase the ‘valley’ space between these regular marks [Figure 3-23]. This may explain why the Charité device showed a much lower initial million cycle wear rate because the device has two UHMWPE surfaces and any surface machining effects would be greater in this case. However, analysis of the 0, 1, 2 MC of data for a relationship between clearance,  $R_a$ , or  $R_{sk}$  (valley to peak ratio) provided no link to the observed wear rate. It should be noted that polyethylene components will deform considerably under load and this is very difficult to analyse dynamically.

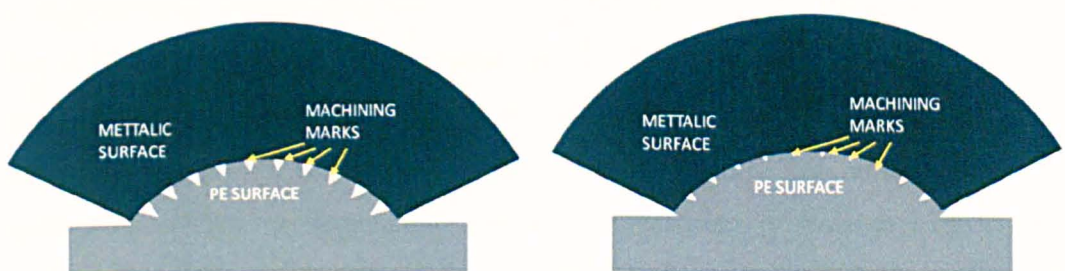
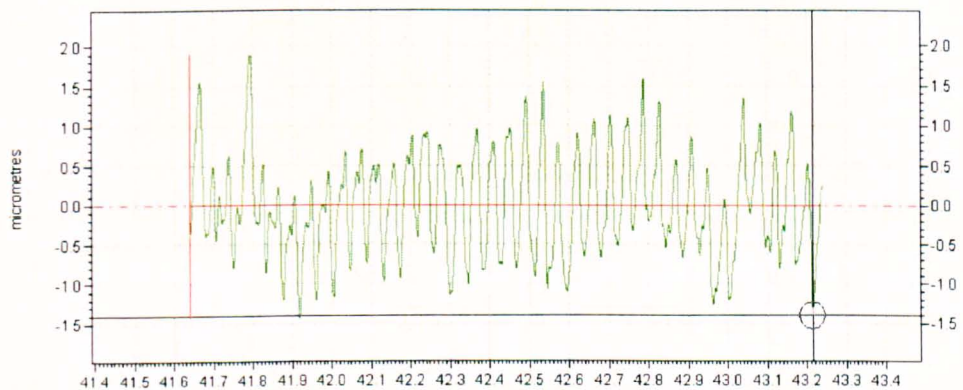


Figure 3-23 Schematic depicting (exaggerated) machining marks on the surface of a TDR bearing surface and the postulated increased contact area after bedding-in

### 3.3.2 Profilometry and Imagery

#### 3.3.2.1 Prodisc

Before the start of the first study, the Prodisc PE components had an  $R_a$  value of  $1.022 \pm 0.17 \mu\text{m}$  measured over the entire dome length. The metallic cups had an  $R_a$  value of  $0.010 \pm 0.001 \mu\text{m}$  measured from the central 12 mm of concave surface. The PE components exhibited a periodic surface topography consistent with having been machine turned (Figure 3-24).



**Figure 3-24 Close up of surface profile demonstrating periodic profile resulting from machining of the Charité core (1.6 mm length shown)**

After the first 4 MC of standard ISO testing the PE domes were assessed with the same method. The full area  $R_a$  value (labelled ALL in Table 3-8) had changed slightly to  $0.837 \pm 0.37 \mu\text{m}$  (82 % of start value). However, closer inspection of the surface revealed a range of values from  $0.165 \pm 0.141 \mu\text{m}$  (16% of start value) at the rim to  $2.245 \pm 0.927 \mu\text{m}$  (220 % of start value) at the pole area of the dome. The rim displayed signs of burnishing, cold flow and increased wear. The pole area of the dome was roughened by a layer of debris [Figure 3-25]. The image shows the application of ink to demonstrate partial re-attachment of polyethylene to the surface. Where the ink is pale, there was seepage of ink underneath the roughened area. The thickness of the debris roughened area measured at 4 MC of ISO testing was  $123 \pm 15 \mu\text{m}$  ( $n=5$ ). The following parametric studies produced changes in surface  $R_a$  summarised in Table 3-8 and graphically in Figure 3-26.

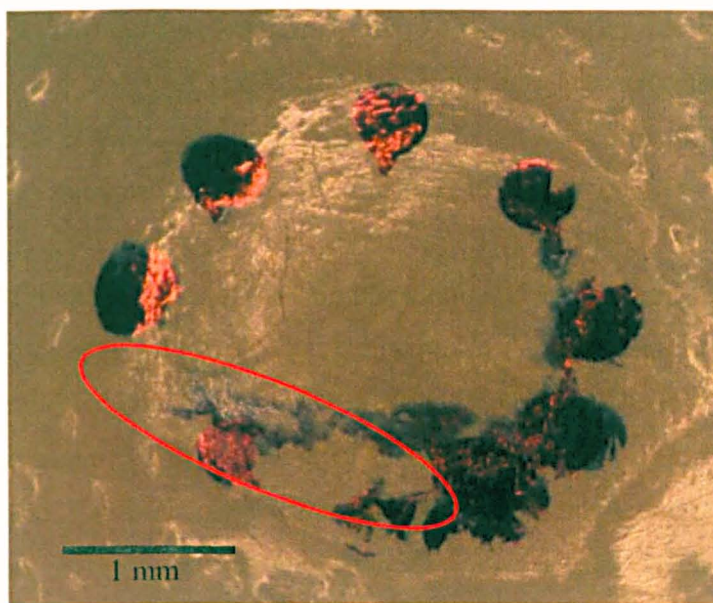


Figure 3-25 Image of the pole area of the dome of a Prodisc (ISO test) showing the roughened area of the disc and penetration of ink (circled) under some of the debris

Table 3-8 Full  $R_a$  results for the Prodisc PE components (average and standard deviation)

	( $\mu\text{m}$ )	ALL	RIM	POLE	APPEARANCE
0 MC	Ave	<b>1.022</b>	<b>1.022</b>	<b>1.022</b>	matt, barely visible machining marks
	SD	0.175	0.175	0.175	
ISO(4mc)	Ave	<b>0.837</b>	<b>0.165</b>	<b>2.245</b>	some burnishing, obvious roughening of pole area
	SD	0.371	0.141	0.927	
LXS(2mc)	Ave	<b>0.671</b>	<b>0.177</b>	<b>0.613</b>	some burnishing, little roughening at pole
	SD	0.339	0.048	0.272	
LL(4mc)	Ave	<b>0.255</b>	<b>0.085</b>	<b>0.084</b>	some burnishing, no roughening at pole
	SD	0.116	0.073	0.033	
ISO2(2mc)	Ave	<b>0.467</b>	<b>0.32</b>	<b>1.175</b>	some burnishing, some roughening at pole
	SD	0.216	0.22	0.691	
HF(3mc)	Ave	<b>0.317</b>	<b>0.352</b>	<b>0.795</b>	some burnishing, little roughening at pole
	SD	0.363	0.179	1.129	
SK(15mc)	Ave	<b>0.99</b>	<b>0.33</b>	<b>0.49</b>	matt, barely visible machining marks, some staining from serum, faint rim contact outline

Note: LXS=low cross shear, LL=low load, ISO2=repeated ISO, HF=half FE, SK=soak

The low CS results suggested that the full surface  $R_a$  (ALL, Table 3-8) and rim  $R_a$  (RIM, Table 3-8) remained similar to the first ISO experimental results at 80 % and

107 % of the ISO experiment values. However the pole roughness (POLE, Table 3-8) decreased substantially to 27 % of the ISO value. Visual inspection also confirmed that the trend for debris reattachment ceased during the low CS testing. For the following low load test (LL) the average roughness for the entire dome lowered to 30 % of the ISO value. The rim roughness also lowered, to 52 % of the ISO value. The pole area  $R_a$  lowered considerably to 4 % of the ISO value.

The repeated ISO test was used to ensure the simulator was delivering accurate wear data. The  $R_a$  values gained here were indicative of the repeatability of the surface tribology when tested under consecutive wear patterns. This second ISO test showed a full area  $R_a$  value of 56 %, rim  $R_a$  of 194 % and pole area  $R_a$  of 52 % of the of the original ISO test. Caution in interpretation is advised as this test was run for 2 MC whereas the original ISO test was for 4 MC. However, as can be seen in Figure 3-26 the trend for each area  $R_a$  value was similar to the first ISO study. After the ISO2 simulator check, the following study was to assess halving the FE. The full area and pole  $R_a$  decreased to 38 % and 35 % of the original ISO study respectively, but the rim increased to 213 %.

To assess the effect of the axial loading alone on the surface topography, the soak control disc was profiled. When compared to the initial 0 MC value, the overall full area  $R_a$  stayed approximately equal at 97 %. However the rim and dome changed to 32 % and 48% respectively. The metallic cups of the Prodisc were profiled before and at the finish of testing. The 0 MC  $R_a$  value was  $10 \pm 1$  nm and this increased to  $28 \pm 18$  nm by the end of 15 MC of various paramedic testing [Figure 3-27]. Although this was an increase to 280 % of original, the standard deviation was high and therefore there was no statistical difference (one-way ANOVA,  $p=0.057$ ) between the two values.

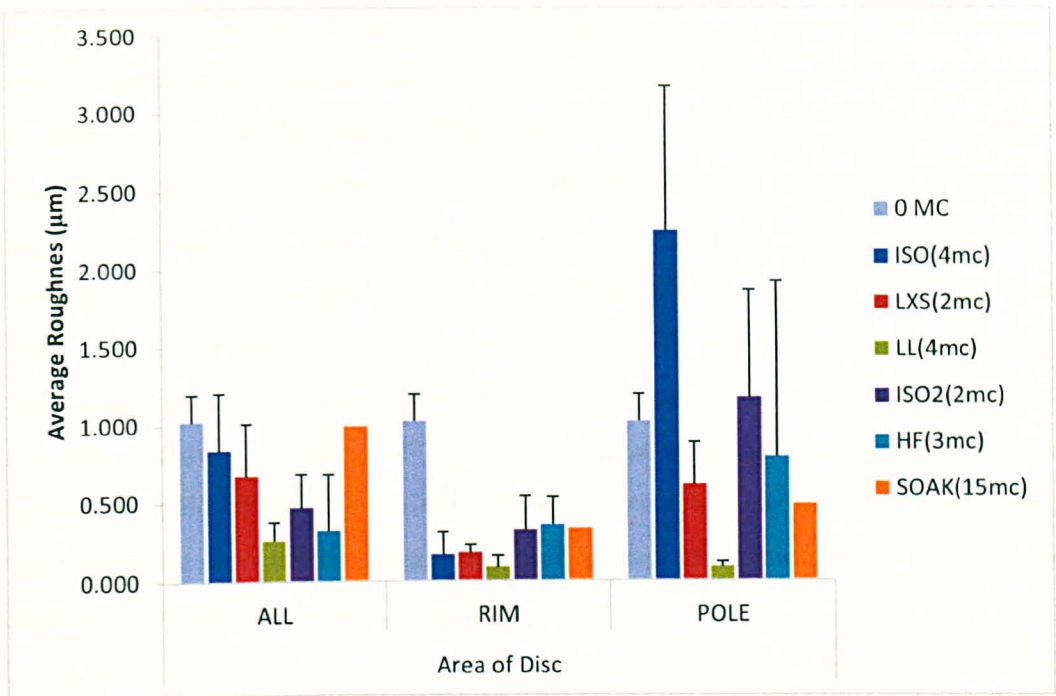


Figure 3-26 Prodisc disc  $R_a$  trace results separated into entire disc length (ALL), edge wear (RIM) and roughened area on the pole of the dome (POLE)

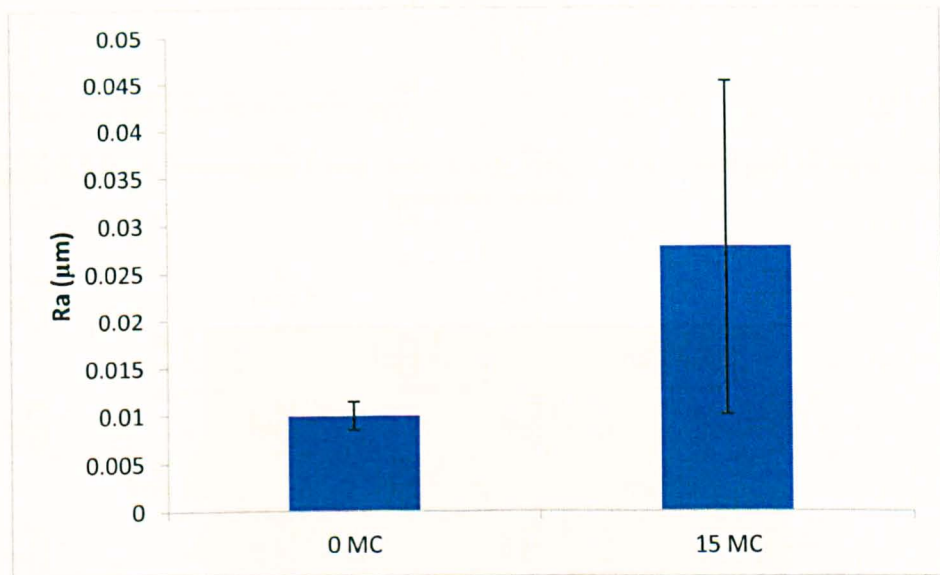


Figure 3-27 Prodisc metallic cups before and after wear testing for 15 MC of various parametric tests

### *Wear scar symmetry*

The wear scars of the Prodisc device were more heterogenous as compared the largely isotropic Charite features. As an example, the Prodisc profile was assessed

for symmetry after the second ISO test. The height loss of the wear scar at the rim was compared to that on the unworn material. To do so, the profiles were exported to analysis software (Mountains, Form Talysurf, Leicester, UK). The profiles were removed of form (using a curve filter), resulting in an approximately flat profile that showed only the wear scar minus the original surface form. From this clear view samples ( $n=3$ ) were assessed and the posterior height loss was  $1.56 \pm 4.9$  mm and the anterior height loss  $0.48 \pm 0.03$  mm, a ratio of  $\sim 3:1$ , an example measurement is shown in Figure 3-28. The lateral traces displayed more symmetrical wear, an example is shown in Figure 3-29. A possible cause of the lack of anterior-posterior symmetry could be that the motion path at the posterior was of larger aspect ratio than at the anterior. In comparison, the motion track dimensions were identical for mirrored positions about the AP centre line.

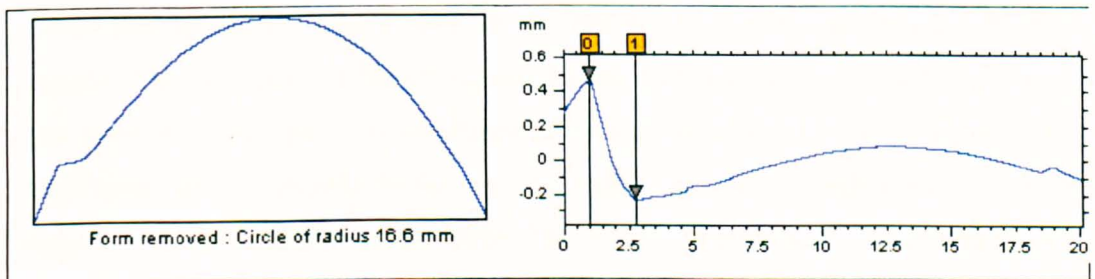


Figure 3-28 Left: Prodisc wear scar (2MC ISO2) Right: Measurement after form removal (posterior to left)

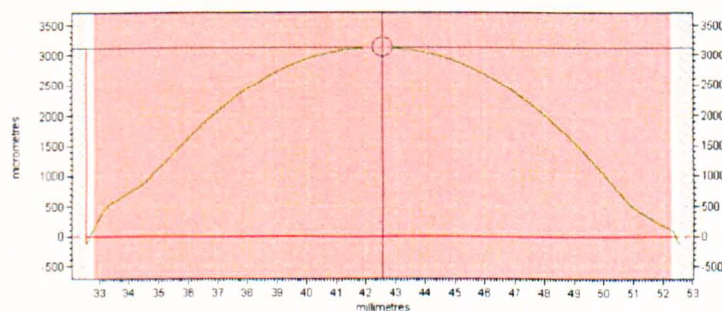


Figure 3-29 Increased symmetry of wear for the lateral profile across a Prodisc (ISO2)

### 3.3.2.2 Charité

Results are reported as two values, the first is the superior value followed by the inferior value. Before the start of the first study, the Charité PE components had  $R_a$

values of  $0.657 \pm 0.055$  and  $0.660 \pm 0.036$   $\mu\text{m}$  for superior and inferior surfaces of the PE core measured over the entire core length. The metallic superior and inferior cups had  $R_a$  values of  $0.016 \pm 0.002$   $\mu\text{m}$  and  $0.017 \pm 0.001$   $\mu\text{m}$  respectively, measured from the central 10 mm of concave surface at the start of the study.

The ISO test was increased to 5 MC for the Charité due to bedding-in effects at the start of the test. After 5 MC the same analysis method was used to check the surface topography on the superior and inferior surfaces of the Charité cores and end plates. The full area  $R_a$  value (labelled ALL in Table 3-9) changed significantly to  $0.2407 \pm 0.991$   $\mu\text{m}$  and  $1.390 \pm 0.646$   $\mu\text{m}$  respectively (366 % and 211 % of start values). Closer inspection of the surface revealed a range of values from  $0.092 \pm 0.027$   $\mu\text{m}$  (14% of start value) at the superior rim to  $3.380 \pm 1.553$   $\mu\text{m}$  (515 % of start value) at the pole area of the superior dome. The rim displayed signs of burnishing, cold flow and increased wear. The pole area of the superior dome was roughened by a layer of debris that appeared to have been re-attached to the surface as with the Prodisc sample. The thickness of the debris-roughened area was approximately 0.05 mm. The inferior surface was also roughened at the pole area but to a lesser degree. Very large error bars are present for the superior surface pole area roughness due to large sample variation and low sample size. The following parametric studies produced changes in surface  $R_a$  summarised Table 3-9 and graphically in Figure 3-30 and Figure 3-31.

**Table 3-9 Superior and inferior surface  $R_a$  results for the Charité PE components (average and standard deviation)**

Superior	( $\mu\text{m}$ )	ALL	RIM	POLE	APPEARANCE
0 MC	Ave	<b>0.657</b>	<b>0.657</b>	<b>0.657</b>	matt, barely visible machining marks
	SD	0.055	0.055	0.055	
ISO(4mc)	Ave	<b>2.407</b>	<b>0.092</b>	<b>3.38</b>	some burnishing, obvious roughening of pole area
	SD	0.991	0.027	1.553	
LXS(2mc)	Ave	<b>5.587</b>	<b>0.053</b>	<b>2.48</b>	some burnishing, obvious roughening of pole area
	SD	6.513	0.005	1.07	
LL(4mc)	Ave	<b>2.937</b>	<b>0.11</b>	<b>6.407</b>	some burnishing, obvious roughening of pole area
	SD	1.147	0.017	2.939	
ISO2(2mc)	Ave	<b>2.963</b>	<b>0.33</b>	<b>5.78</b>	some burnishing, obvious roughening of pole area
	SD	0.902	0.046	1.581	
SOAK(15mc)	Ave	<b>0.99</b>	<b>0.33</b>	<b>0.49</b>	matt, barely visible machining marks, some staining from serum, faint rim contact outline
<b>Inferior</b>					
Inferior	( $\mu\text{m}$ )	ALL	RIM	POLE	APPEARANCE
0 MC	Ave	<b>0.66</b>	<b>0.66</b>	<b>0.66</b>	matt, barely visible machining marks
	SD	0.036	0.036	0.036	
ISO(4mc)	Ave	<b>1.39</b>	<b>0.114</b>	<b>0.983</b>	some burnishing, lesser roughening of pole area
	SD	0.646	0.015	1.487	
LXS(2mc)	Ave	<b>1.093</b>	<b>0.066</b>	<b>0.72</b>	some burnishing, reduced roughening of pole area
	SD	0.254	0.027	0.462	
LL(4mc)	Ave	<b>1.48</b>	<b>0.119</b>	<b>2.07</b>	some burnishing, lesser roughening of pole area
	SD	0.38	0.046	1.704	
ISO2(2mc)	Ave	<b>1.857</b>	<b>0.293</b>	<b>3.16</b>	some burnishing, lesser roughening of pole area
	SD	0.457	0.101	2.133	
SOAK(15mc)	Ave	<b>0.99</b>	<b>0.33</b>	<b>0.49</b>	matt, barely visible machining marks, some staining from serum, faint rim contact outline

Note: LXS=low cross shear, LL=low load, ISO2=repeated ISO, HF=half FE, SK=soak

The inferior roughness was generally smoother for than the superior roughness for all test states. Under low CS testing, the rim and pole areas demonstrated an identical change in  $R_a$  from the ISO results at 58 % and 73 % respectively for both superior and inferior surfaces. However, the overall roughness for the entire surfaces was 232 % and 79 %. This was due to the very high roughness result for the superior surface under ISO conditions. For the low load experiment the rim and pole area  $R_a$  values also showed similarity between superior and inferior surfaces. Under this test the full area  $R_a$  remained approximately static at 122 % and 106 %. A repeated ISO



standard input test revealed a similar full area  $R_a$  to the first ISO results, but the rim and pole area roughness had changed by 357 % and 171 % respectively for the superior core surface with similar results for the inferior surface.

At the end of all testing the soak control core was measured and compared to the unused PE surface results. The superior and inferior surfaces displayed near identical changes in  $R_a$  value of 151 % and 150 % for the complete assessment length, 75 % and 74 % for the pole of the dome area and identical 50 % of start value for the rim measurement. The end plate cups were re-assessed at 13 MC and as can be seen from Figure 3-32, there was no significant (one-way ANOVA,  $p > 0.05$ ) change in surface roughness on either superior or inferior end plates.

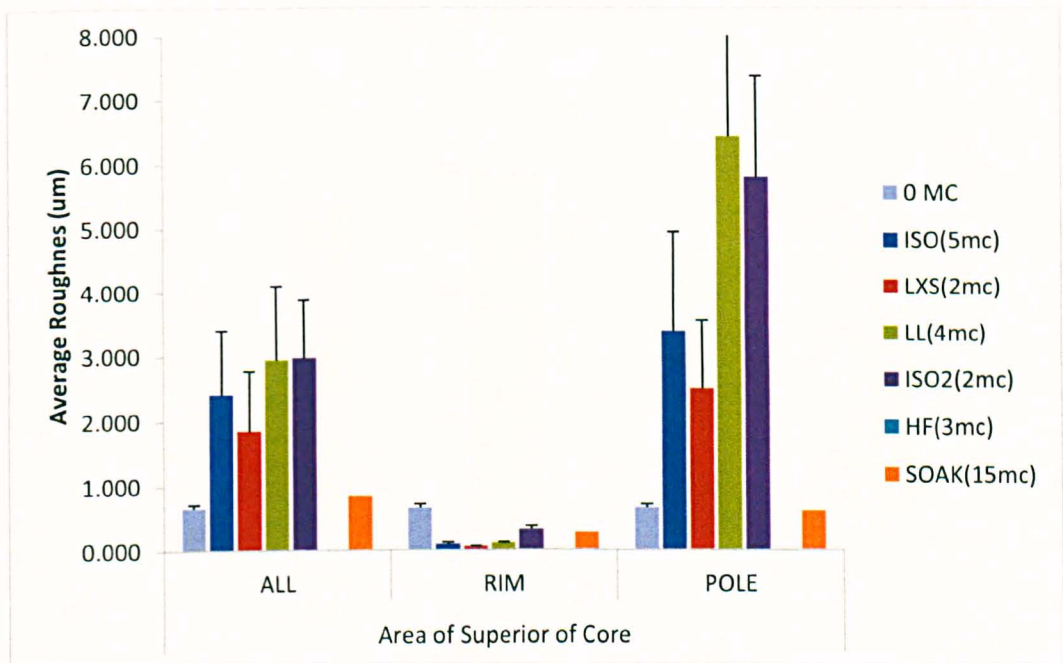


Figure 3-30 Charité superior core  $R_a$  trace results separated into entire disc length (ALL), edge wear (RIM) and roughened area on the pole of the dome (POLE)

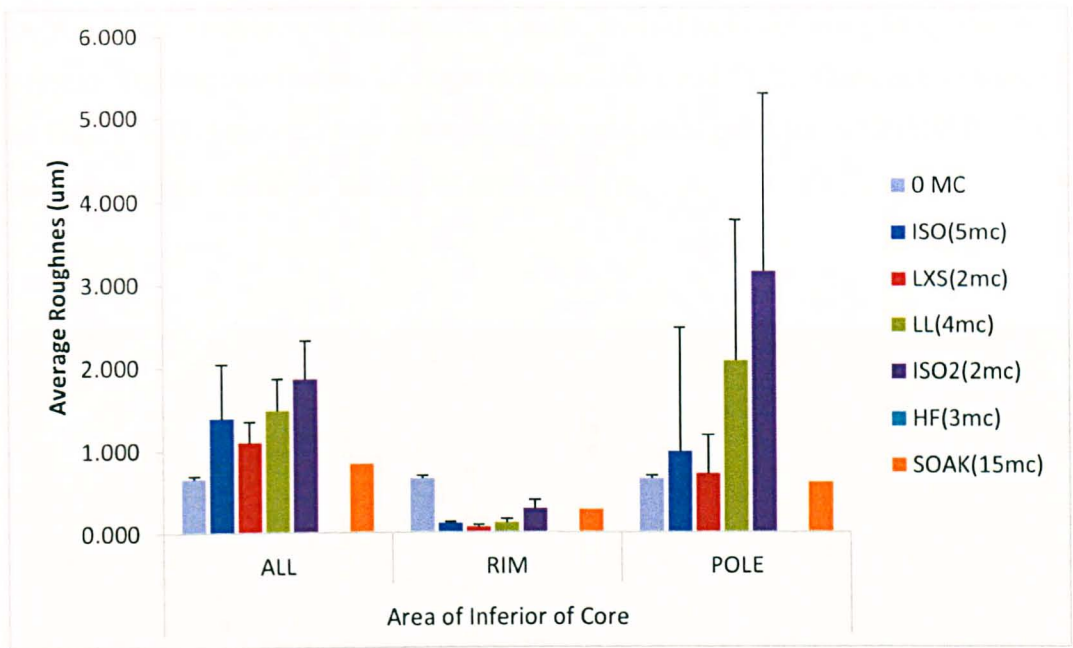


Figure 3-31 Charité inferior core  $R_a$  trace results separated into entire disc length (ALL), edge wear (RIM) and roughened area on the pole of the dome (POLE)

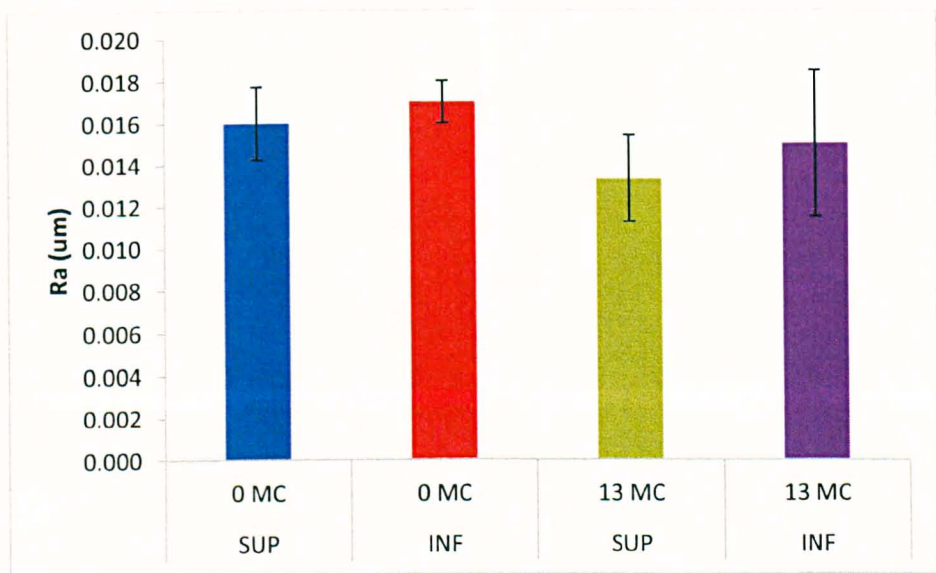


Figure 3-32 Charité superior (SUP) and infer (INF) cups surface profiled before and after 13 MC of wear testing

### 3.3.2.3 SEM Analysis

Gold coating was employed to make the samples conductive to the electron beam. This is a destructive process and so samples from a previous study [122], with 5MC ISO testing completed, were plated and mounted with carbon paint. Example images are shown in Figure 3-33. The images appear to show layered areas where this could

be the result of debris re-attachment. Linear, multidirectional scratching was also present. The last two images of magnification 2588x and 5172x (bottom two images of Figure 3-33) begin to show what could be individual particles of UHMWPE. The appearance is a 'smeared' surface of several layers.

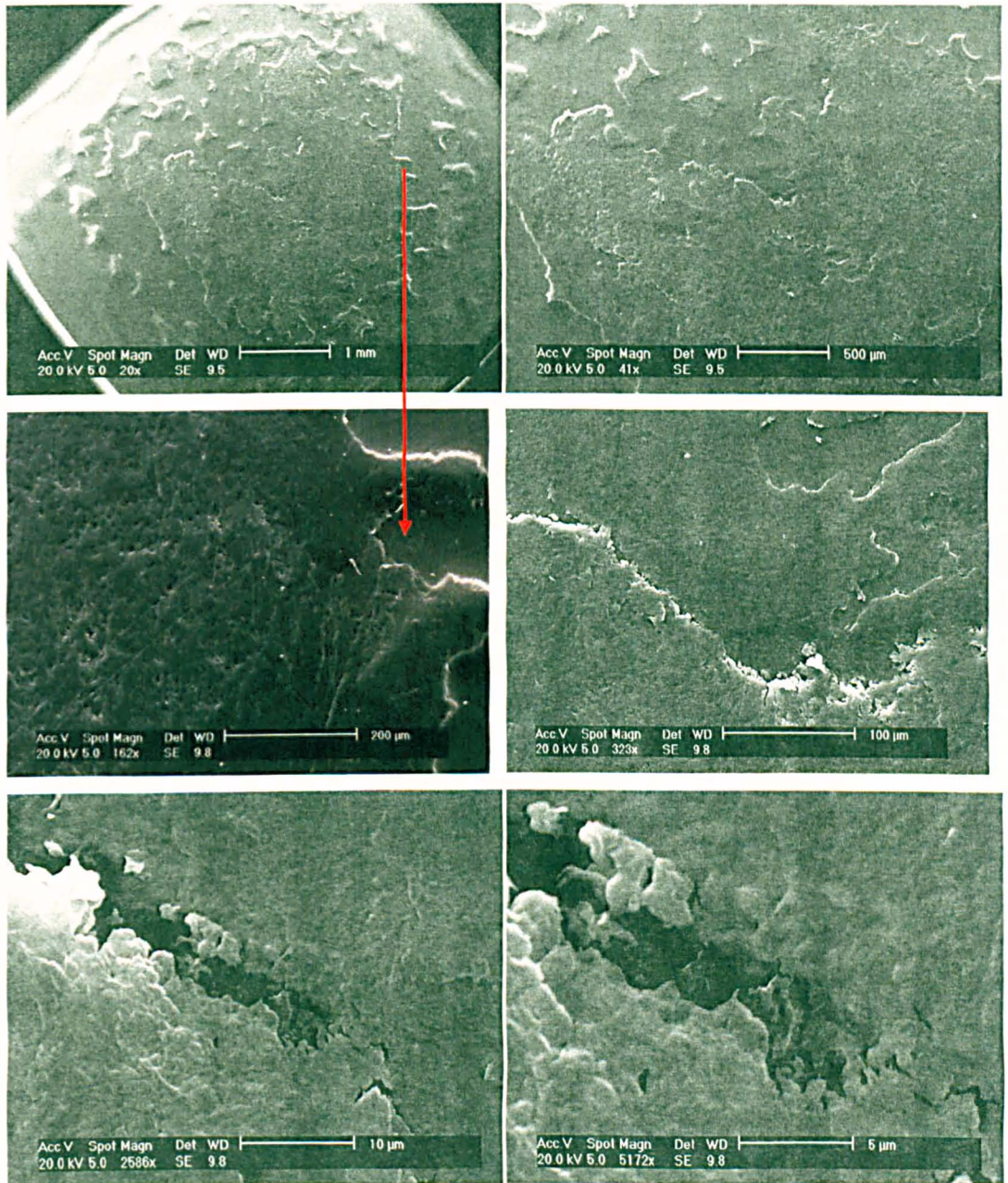


Figure 3-33 Charité SEM images of roughened area around the pole (descending increase in magnification), showing appearance of built up layers of particles

### *Prodisc Summary*

General  $R_a$  value for ISO tested discs was similar to the original unworn material but the use of specific area topographical analysis demonstrates different wear characteristics dependant on the position on the disc. Rim roughness in the y direction was much reduced and tallied with observed burnishing of the rim. Rim roughness in the x-direction (observed in trace 1) was recorded as part of the 'ALL' results. Pole roughness seems was caused by re-attached debris and was confirmed using dye which was observed to penetrate under the debris. For the LXS study, RIM and ALL results were similar to the first ISO test, but the pole area of the dome was much smoother (27 % of ISO). The pole area may have been releasing wear debris more efficiently under this type of motion therefore resulting in less re-attachment and smoother surfaces. The LL study produced a much reduced surface roughness both lower than the original ISO (30 %) and original unworn material. The pole area reduced in roughness to 4 % of the ISO equivalent value. The lower contact stress promoted release of wear particles from the pole area and resulted in a polishing effect. The HF surface characteristics were similar to the ISO2 results. However, due to the shorter test length of the ISO2 study, there was less time for the trend for debris deposits to build up on the pole. Interestingly, the dynamically loaded soak also showed a smoothing of the rim area indicating that contact pressure here was high enough to deform the surface asperities and lower the  $R_a$  value.

### *Charité*

The surface profile results for the Charité depicted much greater variance and are harder to draw conclusions from. Overall, the trend was similar to the Prodisc described above, but there were some characteristics that were opposite to the Prodisc. The LL results did not demonstrate the same fall in average roughness and the pole area stayed relatively rough indicating that for this device the wear/lubrication regime did not change when the surface stress was reduced. SEM images have highlighted the wear debris re-attachment effect and shown this to result in a layered surface of what could be compacted particles of UHMWPE.

### **3.4 Discussion**

#### **3.4.1 Rates of Wear**

The observed differences between the wear rates in the present study have highlighted differing effects of altered phasing, loading and sliding distance and add to a body of evidence begun by a previous experimental study which highlighted the difference in wear behaviour between standard ISO and additional anterior-posterior input conditions [122]. The tests conducted have been of a shorter length than that advised by ISO or ASTM (both 10 MC). However, these standards and guidance documents are primarily for manufacturers to benchmark their designs. *In vitro* studies by Grupp et al. and Nechtow et al. and both showed roughly linear wear over an 8 and 10 MC period respectively [119, 120]. Therefore the rationale for altering the ISO tests and experimenting with different parametric effects does not warrant a full 10 MC study.

Previous ISO-based studies of polyethylene-on-metal TDRs have shown a wide variation in wear rates in the range of 2-20 mg/MC [97, 119, 120, 128, 150] A full list of lumbar TDR *in vitro* test data is presented in Table 3-10. The lowest wearing metal-on-polyethylene disc using out-of-phase motions is the Activ-L (2 mg/MC ) [120] and the highest wearing was a Charité sample subject to a modified ISO plus anterior-posterior displacement cycle [122]. For out-of-phase input conditions, the Prodisc TDR have wear rates reported between 10-16 mg/MC [97, 119, 128] and Charité devices have been reported to wear at 12 mg/MC [122]. The latter wear rate was an average of five MC including an initial lower wearing period at the first 1 million cycle measurement point. Therefore the wear rates reported in this study of Prodisc and Charité devices forms a reasonable representation of what is expected for *in vitro* testing.

**Table 3-10 Summary of wear results for both in vitro and computational**

<b>Investigating authors and year of study</b>	<b>Wear rate (mg/MC)</b>	<b>TDR</b>	<b>Comments</b>
Present study	16.1±1.4	Prodisc-L	ISO
	6.0±1.3	Prodisc-L	In-phase*
	11.8±1.0	Prodisc-L	Low load
	11.7±2.4	Prodisc-L	Half FE
	13.4±2.0	Charité	ISO
	8.2±1.3	Charité	In-phase*
	12.5±3.7	Charité	Low load
Vicars (2009) [122]	12.7±2.1	Prodisc-L	4DoF, ISO
	12.2±1.0	Charité	
Nechtow (2006) [119]	16.59±0.96	ProDisc-L	4DoF, ISO (frequency shifted)**
	19.35±1.16	Charité	
Bushelow et al. (2008) [97]	9.19	ProDisc-L	4DoF
Grupp et al. (2009) [120]	2.70±0.30	Activ-L	4DoF
Nechtow et al. (2006) [119]	0.35±0.01	ProDisc	4DoF, in-phase motions*
	-0.87±0.76	Charité	
Grupp et al. (2009) [120]	0.14±0.06	Activ-L	4DoF, In-phase motions*
Vicars (2009) [122]	11.6±1.2	ProDisc-L	5DoF, ISO + AP shear load
	22.3±2.0	Charité	ISO + AP shear displacement
Serhan et al. (2006) [123]	0.13	Charité	ASTM (in-phase)

\*In-phase motions described as '4DoF' could also be described as 3DoF by other authors, given that the FE and LB motions effectively produce a single resultant motion

\*\*\*Frequency shifted' refers to non-unity values of Hz

Very low wearing results from the literature are indicative of zero CS kinematics based on either ISO [119] or ASTM recommendations but with two only two rotations operating in-phase [120, 123]. These zero CS motions allow authors to demonstrate exceedingly low wear or zero wear [123] which could be misconceived as evidence of the potential longevity of TDR. Computational experimental results have failed to replicate *in vitro* wear without the application of scalar factors to the data in order to fit laboratory experience or are based on 're-engineered' wear factors accrued from the experiments themselves.

Overall wear rates for ISO standard conditions in the vicinity of ~15 mg/MC compares equivalently to modern metal-on-UHMWPE hips [151] (cross-linked) and less than or equal to older conventional UHMWPE hips (15-40 mg/MC ) [151-154]. Total knee replacement wear from *in vitro* simulator tests typically show wear rates of approximately 10 mg/MC [155-159]. Considering the relative size of TDR and TKR the equivalence shown between wear rates could be considered surprising given that TKRs operate at higher loads, larger flexions, and according to experimental data from Galvin et al. a contact area of 423.33 mm<sup>2</sup> (pre-test) [160] which is ~2x the contact area under ISO motions. However, the TDR designs have to undergo two compressive cycles per stride compared to hips and knees that only have one compression cycle followed by a swing phase load. The swing phase allows lubricant to penetrate the wear patch contact area and (in metal-on-metal hips) has been proven to lower friction and wear [132], although its effect for MoP devices is unknown. The increased cyclical loading rate of the TDR may increase the wear factor as has been reported *in vitro* for MoP hips [161]. The lack of lubricant due to a high 'swing phase' and the higher cyclical axial loading may increase the TDR wear above what would be expected of this size of device. This is of course ignoring the Archard equation in which wear is independent of contact area - the applied nominal contact pressure has been shown to influence wear factor [160, 162, 163].

The wear scar produced on the Prodisc device was heterogeneous, with more pronounced volume loss towards the posterior, whereas the Charité device exhibited more equal wear distribution over the entire surface. Analysis of the level of CS at the Prodisc surface shows that the aspect ratio of the slide track was greater at the posterior due to the kinematics of the combined inputs [Figure 3-36]. In comparison, the surface profile traces for the Charité showed a symmetrical wear path between anterior and posterior sections. The discs were subject to exactly the same kinematics and load, therefore the logical explanation lies in the mobile nature of the Charité core. Video analysis of the core showed it rotated at 3.6°/cycle. This rotation would in effect spread the differing wear characteristic over an entire revolution of the disc and so produce the even wear observed in this study and in some retrievals [164]. The level of core motion has been assessed in a cadaveric *in vivo* study and was found to be relatively locked in place to the inferior plate in 50% of the samples

tested by O'Leary et al. [165]. Gorham-Voss et al. also demonstrated (in a computational wear study) that the Charité device displayed preferential wear in the superior bearing couple [150]. The symmetry of the wear did not become equal until the friction factor of the inferior component was lowered to 12.5 % of the superior one. Further, the CoR was moved from the centre of the mobile core (0 mm) to 12 mm below this point and no evidence of the CoR position affecting a change in rotation behaviour was found.

The effect of the level of CS on wear rate was less pronounced for the Charité device which showed a drop in wear rate to 61 % of baseline standard ISO when subject to low CS input kinematics. In comparison the Prodisc dropped to 37 % of baseline. The reduced sensitivity of the Charité to changes in input phasing may be due to the core rotation, however, analysis of the motion tracks showed a similar aspect ratio for both Charité and Prodisc devices. The principle of separating motions into linear or curvilinear motions has been used in knee replacement design to produce the mobile bearing TKR. This design has been shown to wear less than a fixed bearing *in vitro* [155, 158, 159]. But *in vivo* results have only shown equivalence to fixed bearing designs [166], perhaps due to the sensitivity of wear rate to accuracy of surgical alignment and a lack of rotation of the platform in real-life use. Therefore any possible advantage of the rotating core in the Charité design may be of limited use *in vivo*.

Under half load kinetics the behaviour of the two devices under test was similar. The Prodisc wear fell to 74% of baseline and the Charité to 93 % of baseline [Sec 3.3.1.2]. The fall in wear rate was much less than the 50% that could be expected if predicting wear using classical wear theory - where the wear volume is proportional to the distance of sliding motion and load applied [80]. In this case the distance of slide remained constant and so only the 50% reduction in load is relevant. The fact that this did not reduce the wear by half confirms the known non-linear wear behaviour of UHMWPE when articulating against metallic bearing surfaces [161, 167] in the context of TDR design. A new formulation of wear law has been developed at the University of Leeds and is given by Equation 3-1:



$$V=CAS$$

**Equation 3-1**

Where  $V$  is volume of wear,  $A$  is real contact area and  $S$  is sliding length. The constant  $C$  is a wear coefficient (as opposed to a wear factor in the Archard formula) and is computed from experimental data. The value  $C$  is based on experimental data and is changed depending on the load applied. However, for finite element based wear prediction the value of  $C$  is predicted using the real area of contact rather than the nominal one used in experimentation. In comparison,  $K$  has been found to decrease with increasing load thereby directly contravening classical wear theory [161]. It is thought that the real area of contact for UHMWPE-on-metal bearings changes under increasing contact pressure. The full mechanism is not fully understood but is related to the change in contact area at the UHMWPE asperity and metal bearing interface. Accordingly, the TDR area of contact changed during a halving of loading and a tribological mechanism has prevented the wear rate from halving.

Using a finite element dynamic wear model of the Prodisc TDR, a better representation of the wear change (compared to classical wear theory) has been achieved by Dr Feng Liu (University of Leeds) using this new formula. The results showed that the new wear formula accurately predicts the trend in wear rate (i.e. a non-linear change) [Figure 3-35] but did not produce a correct absolute wear rate [Figure 3-34] demonstrating that although the new wear formula is an improvement over scaled, Archard-based FEM models, it is not yet generalisable without also using a scaling factor to correct the absolute values. However, only one correction value needs to be applied.

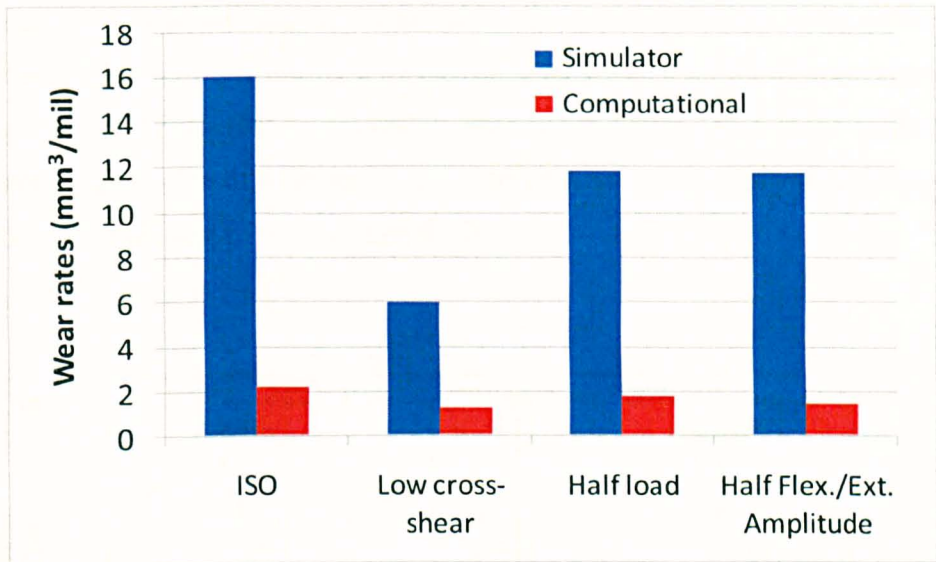


Figure 3-34 Comparing absolute results from Prodisc in vitro simulation and Prodisc finite element wear prediction (Dr Feng Liu)

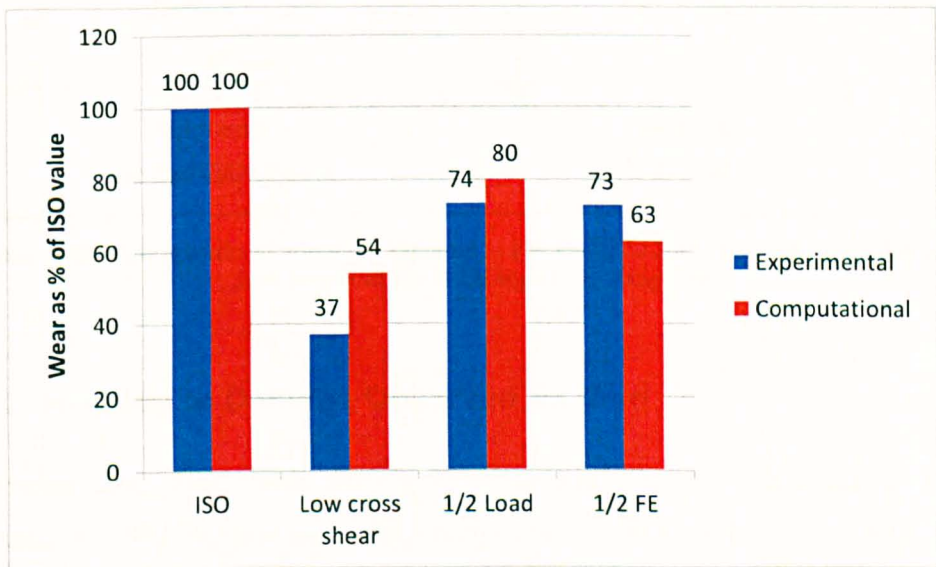


Figure 3-35 Normalised comparison of Prodisc wear rate between different kinetic inputs showing the relative changes of the computation closely following the simulation

The half flexion experiment (applied to the Prodisc only) resulted in a reduction in wear to 73 % of baseline. In comparison the reduction in average motion path distance from standard ISO to half FE was to 65 %. A slight increase of CS from 0.23 to 0.25 also resulted [Figure 3-36, Dr Feng Liu, University of Leeds]. If the motion tracks length result is used to produce a data set of average wear rate for the half FE input cycle (i.e. 65 % of the ISO data rather than 73 %) and then compared to the simulator-gained result of 73 % of ISO baseline, a statistical comparison

between the two results can be computed by t test. This showed a non-significant difference ( $p=0.35$ ). Therefore it could be concluded that for purely kinematic changes in input cycle that do not unduly change the degree of CS at the surface, the traditional calculation of wear formula (based on Archard classical wear theory) can still be a valid process of wear rate prediction.

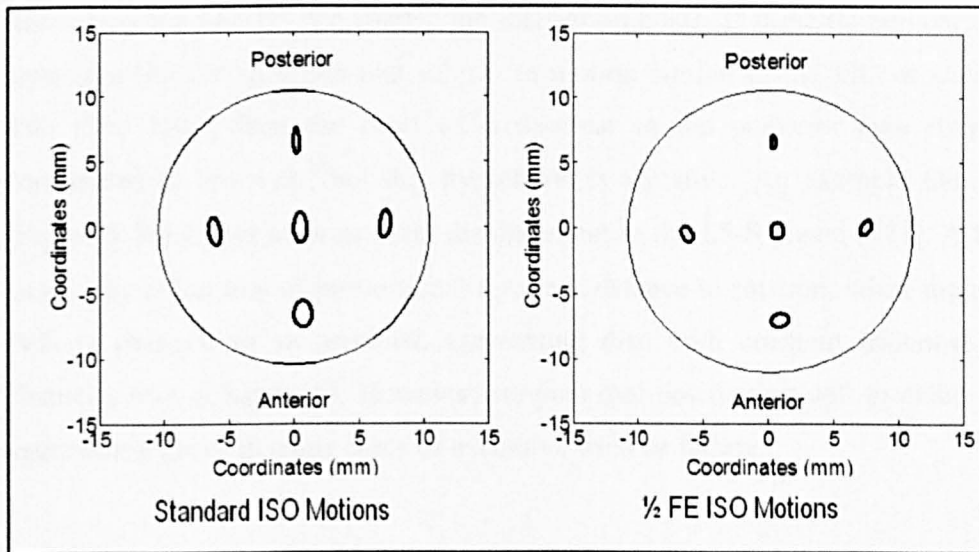


Figure 3-36 Motion paths of standard ISO and  $\frac{1}{2}$  FE modified ISO demonstrating shortened path length of the  $\frac{1}{2}$  FE input [Dr Feng Lui]

### 3.4.2 Relation to Damage Observed Ex Vivo

Following simulation, both devices (Prodisc and Charité) had areas of highly polished polyethylene and also large matt sections. Changes in surface topography were confirmed as the cause of the optical appearance of the wear scar areas. The burnished sections (a ring of polishing around the circumference) on both devices was a factor of 3-5 smoother than the more central matt areas for all input conditions. The burnished ring of polyethylene coincides with the edge of the contact with the metallic cup endplate (endplates in the case of the Charité) which seems to elicit an edge loading effect [168]. Cornwall et al. [149] have classified burnishing as being due to micro-polishing or viscous plastic flow from adhesive wear. Since the edge loading of the metal-on-PE bearing was high, this latter mode of wear seems probable. Although, a known source of polishing effect is the elliptical rotation of a metallic bearing in relation to a PE component.

The range of conditions of explanted Charité discs tends to be large and the *in vitro* tested discs have not represented commonly seen artefacts such as rim impingement [Figure 3-37] [131, 136, 169, 170]. The exact cause of rim impingement is unknown, though it could be related to surgical positioning. Another possibility is that the anterior component of the torso weight pushes the superior cup forward over the inferior cup and in doing so tilts the mobile core so that further shear is only resisted by the thin PE rim against the inferior endplate. If these mobile cores have been in a ‘locked’ position and subject to motion similar to the ISO or Callaghan data [Sec 1.4.1] then the level of cross-shear at the posterior area may have contributed to the wear, but this hypothesis is tentative. An example radiograph [Figure 3-38] shows anterior shear displacement in the L5-S1 level [171]. A further possibility is the loss of proportional torque resistance to rotation, when the natural IVD is changed to an artificial, articulating disc with constant frictional torque characteristics [Chapter 6]. However, surgical mal-positioning will probably be an aggravating factor in some cases of excessive wear or failure.

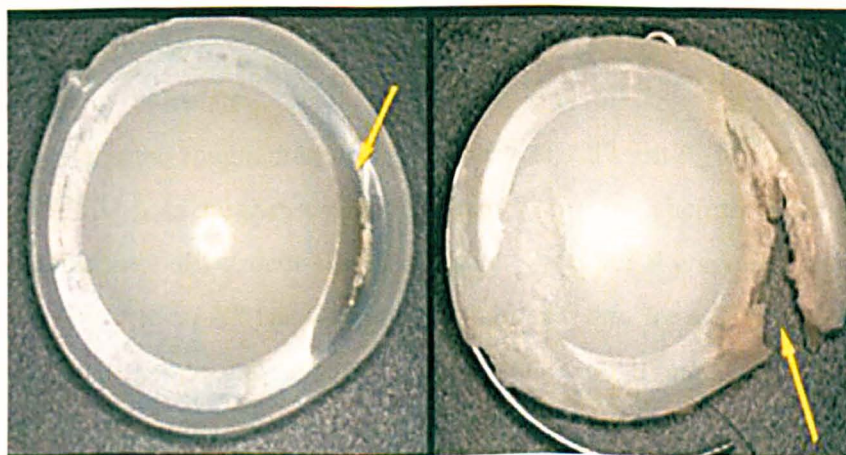


Figure 3-37 Rim entrapment of Charité explants [131]

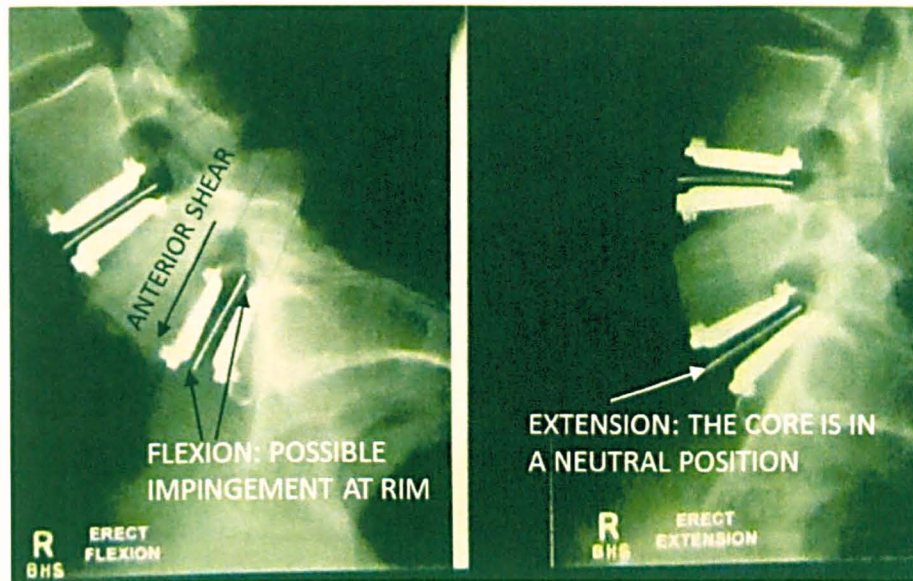


Figure 3-38 Radiograph image showing the anterior shear present at L5-S1 (left) when subject to flexion [171] - tilt of core appears to be caused by anterior shear

A previous study by Vicars et al. [128] has examined the effect of an additional anterior-posterior shear displacement on the Charité. Although this did increase the wear rate by nearly two-fold, rim damage was not found and so cyclical AP shear does not appear to be a cause of rim damage either. The loading applied in the Vicars et al. study was +175 N / -140 N for a Prodisc and these values were adapted from an *in vivo* calculation made by Callaghan et al. [1]. The samples tested displayed preferential roughening of the pole area to  $1.87 \mu\text{m} R_a$  which is very close to the purely ISO pole roughening reported here ( $2.3 \mu\text{m}$ ). Therefore it appears that AP loading does not affect debris re-attachment. Vicars et al converted the AP load of the Prodisc test to an AP translation of +2 mm/-1.5 mm for a Charité study (done so as to avoid possible dislocation of the mobile core if under an AP loading). Surface roughness in this experiment was not recorded and no evidence of rim damage was noted. It may be that the dynamic translation chosen was not suitable to replicate rim damage observed in ex-vivo samples.

O'Leary et al. [165] studied the *in vitro* biomechanical motions of the Charité device using cadaveric spines (mean age  $52 \pm 9.3$ ) designed to simulate *in vivo* effects. Force rather than rotational displacement was used (8 Nm flexion, 6 Nm extension) plus a follower preload of either zero or 400 N. Motion patterns were described from the perspective of the sagittal view. There was a tendency for the superior bearing

surface to show preferential motion over the inferior surface and during flexion some anterior shear was present [Figure 3-39]. This was observed in 9/10 of unloaded segments and in 5/10 of the 400 N preloaded spines. Video analysis of the experimental motion traces [discussed more fully in Chapter 4] has also shown a preference for superior motion and this has been computationally modelled by Gorham-Voss et al. [150].

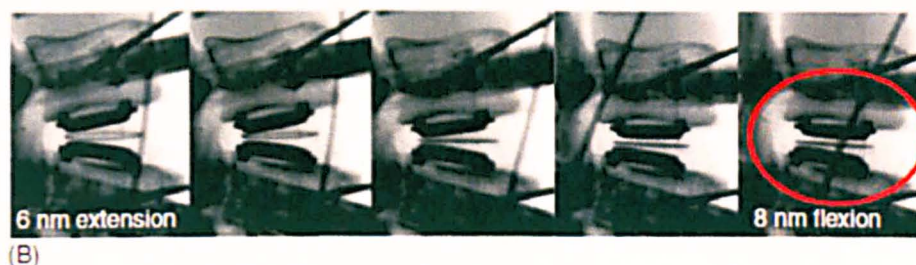


Figure 3-39 Image modified from O’Leary with anterior shear displacement visible when in flexion (circled)

Choma et al. reported on the condition of an explanted Prodisc (n=1) after 16 months service due to continued back pain [172]. They described a burnished appearance of the dome (i.e. the pole area) of the disc with no roughening present (i.e. the opposite result of *in vitro* testing reported here). Burnishing was also present on the outer (non-bearing) anterior section of the disc under flexion due to dislocation of the disc. The Prodiscs tested under low load conditions did show a much reduced pole area roughness, but the overall *in vitro* results do not correlate well with Choma et al. Without knowledge of the weight of the patient described by Choma et al. it is impossible to make a connection between loading and pole area surface morphology.

Both TDR designs seem susceptible to significant scratching on ex-vivo samples. Microscopic scratches were present on the PE surfaces but macroscopic scratches observed in explant reports [93, 138, 172] were not replicated. Studies from hip implants have shown that third-body wear resulting from bone or cement particles is possible. In TDR procedures, bone cement is not used (except rarely in prophylactic vertebroplasty-TDR hybrids) but bone debris may be a risk since the surgeon needs

to remove bone from the vertebral end plates before TDR positioning, therefore bone particles may become drawn into the bearing surfaces and cause scratching.

Microscopic scratches were present on the *in vitro* tested components and these have also been observed during explant analysis by Anderson et al. [Figure 3-40] using secondary electron microscopy (SEM) [136]. Pictured in Figure 3-41 is a light optical microscopy (LOM) image of a Charité core for comparison, tested in the present study. The linear scratching appearance is common between them and is somewhat surprising given that the *in vitro* test cycle produces high CS elliptical inputs and *in vivo* condition are also expected to be highly non uniform. A problem with this direct comparison is the difference in magnification between LOM and SEM images and the two different methods of image capture. Outwardly the images appear similar, but the scale of the visual inspection is approximately two times different, however, evidence of similar appearance linear scratching is clear.

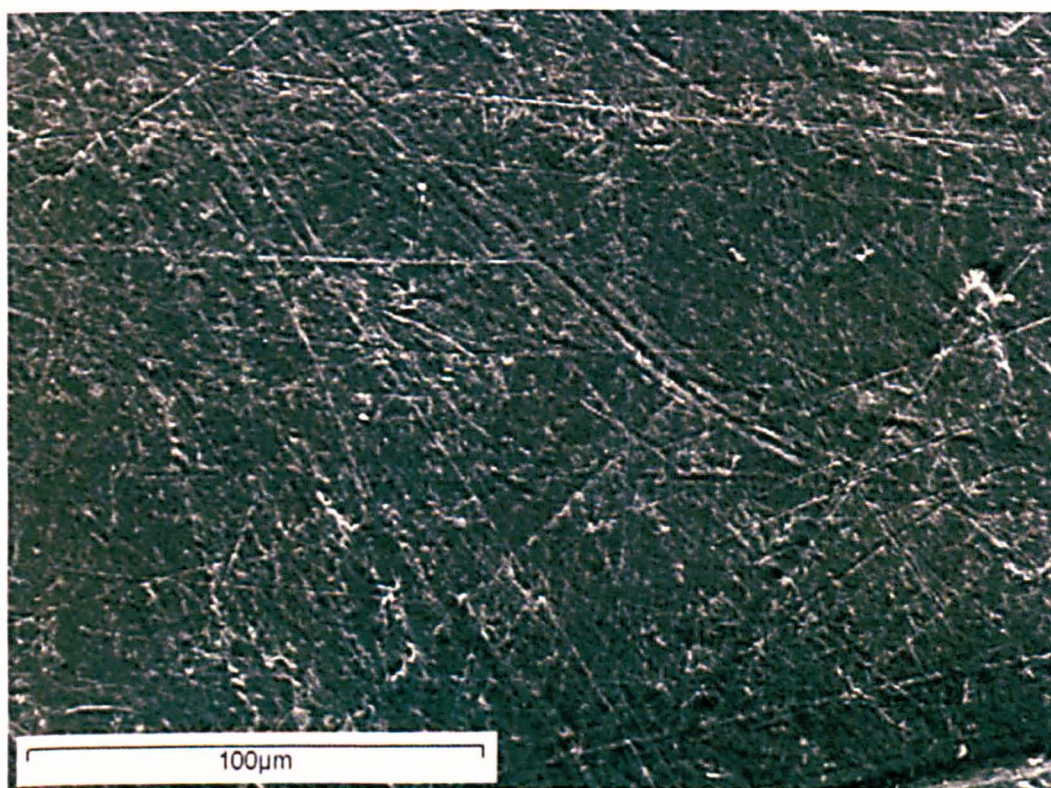


Figure 3-40 SEM of ex vivo Charité PE core ([170])

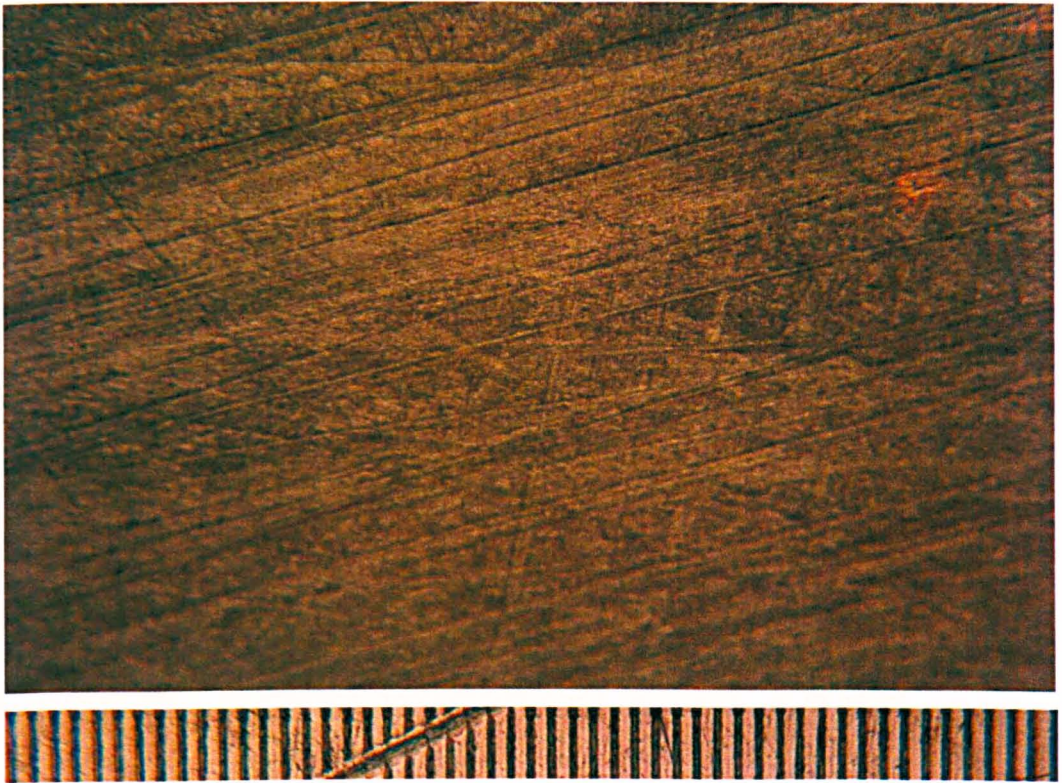


Figure 3-41 LOM image of a Charité PE core surface (0.1 mm per division).

In Section 3.3.2.3, the SEM image [Figure 3-33] of the Charité core was described as exhibiting a ‘smeared’ appearance postulated to be re-attachment of debris together with linear micro scratches. No explant retrieval analysis is known to the author that corroborates this tribological phenomenon. However, images contained in Choma et al. [172] [Figure 3-42, no scale given] do show a similar appearance. The authors described this surface as “demonstrating microscopic evidence of adhesive/abrasive wear”. From this single image it is hard to extrapolate full wear behaviour, but the image does contain similar surface features to the SEM image from *in vitro* testing presented here [Figure 3-43]. However, previous experience gained by the author using SEM methodology suggests that this image was taken using environmental SEM and hence the image appears to show ‘charging’ of the surface and hence poor resolution/contrast.



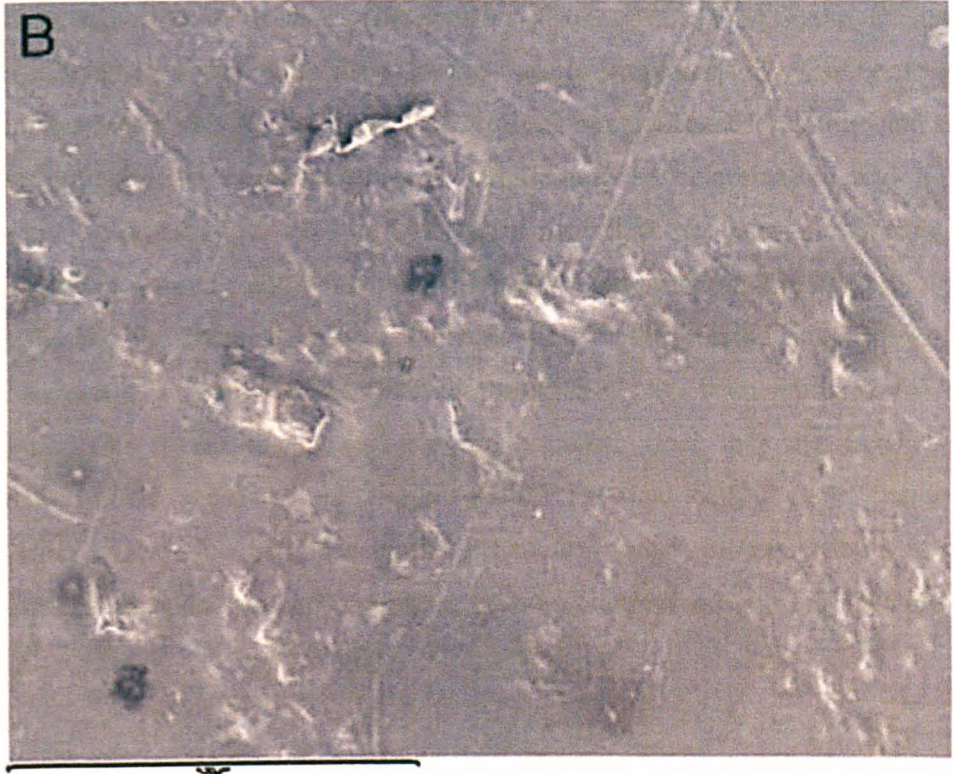


Figure 3-42 SEM image from Choma et al. [172] taken from the pole area of a Prodisc explant (scale not visible in original paper) – shows similarity to the SEM image of Figure 3-43 from the in vitro test

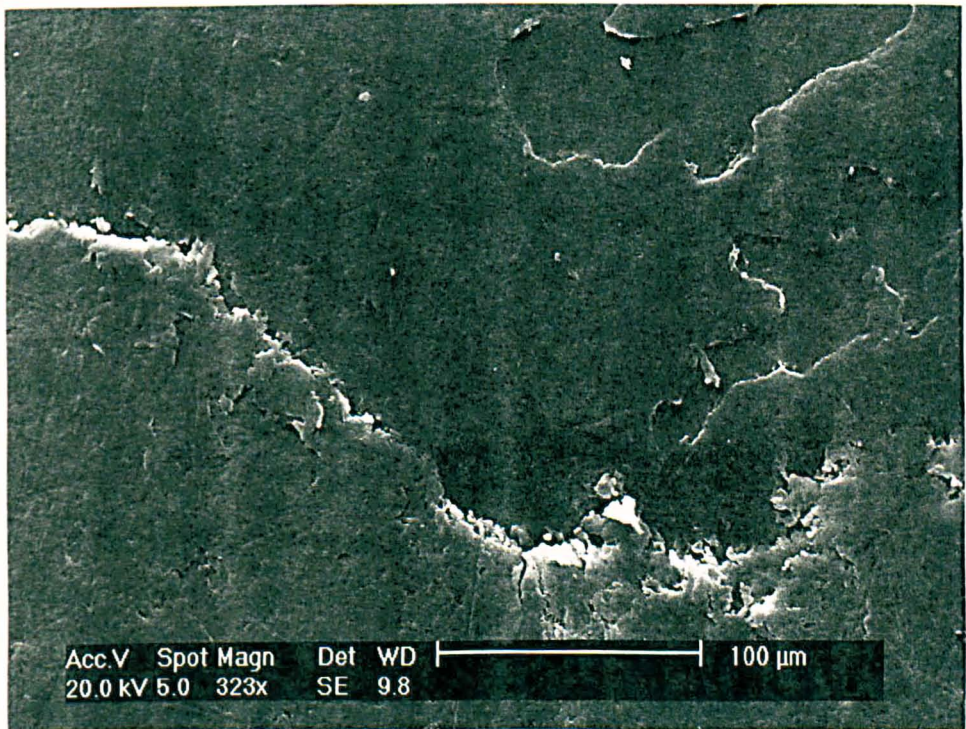


Figure 3-43 SEM image of a Charité (ISO tested) core showing overlapping re-attached debris plus linear multidirectional scratching

A related failure mode in TKR, described by Fisher et al. [173], is the mechanism of wear in knee replacement polyethylene inserts. Implants with less conforming dimensions result in higher surface contact stress, which if exceeding the yield stress of the polyethylene can lead to early fatigue-induced delamination and failure. Excessive 'gliding' of the tibia on UHMWPE insert has also been shown to induce high levels of fatigue stress which can also lead to malfunction. The combination of short FE and the 'reverse bearing' configuration of the bearing couple (i.e. PoM rather than MoP) meant that the effect of gliding may have been similar in the TDR bearings. The medial-lateral and anterior-posterior float that the Leeds spine simulator allows, combined with the untypical 2 Hz axial loading cycle (that inputs maximum load at the extremes of the FE motion cycle) also contribute to edge loading effects where the rim perimeter became compressed and highly burnished [168].

### **3.4.3 Biological Implications**

The osteolytic potential from wear debris generated by Leeds spine simulator studies has been assessed for the Prodisc by Tipper et al. and the debris produced by the standard ISO wear test was shown to be as reactive as hip and knee debris under their respective ISO standard testing conditions [174]. As of the year 2003 there were no known reported cases of osteolysis, but since then a small number of clinical cases have emerged showing a detrimental reaction to UHMWPE wear particles *in vivo* [138-140, 142]. Giant cells, macrophages and inflammation have been seen in Acti-L patients (but not full osteolysis) [175].

Although not part of the present study, MoM discs have also resulted in some failure related to pseudo-tumours or granulomas [176, 177]. It is worth noting that Bushelow et al. [97] found that the MoM Maverick TDRs they tested (precise inputs unknown, believed to be coupled motions) showed wear rates 10-50 times that expected in THR. In comparison, Mathews et al. [135] compared the 1.2 mm<sup>3</sup> of debris resulting from Maverick MoM discs they tested, to THR that had <5 mm<sup>3</sup> wear rate before explants. Details of test methodology were not reported. They stated:

*“in the total hip arthroplasty literature, retrieval studies reporting <5 mm<sup>3</sup> of debris generated per year for metal-on-metal hips did not have any significant effect on osteolysis...”*

This could be misleading, as osteolysis is not the most common form of adverse reaction in MoM THR. Other failure modes such as pseudo-tumours, soft tissue necrosis and aseptic lymphocytic vascular and associated lesions (ALVAL) must be considered. Also, retrieval analysis studies by Morlock et al. [178] have noted the relationship between increased wear rates (for example, from rim loading) and early failure. This *ex vivo* wear evidence was simulated *in vitro* by Leslie et al. [133], finding large increases in wear under adverse rim-loaded conditions. These wear rates were 8.9 mm<sup>3</sup> and this is of the same order of magnitude as that reported by Bushelow et al. [97]. The debris or ion concentration in the IVD area will probably be contained in a smaller volume of tissue than in the hip. A review of reported MoM TDR adverse reaction by Golish et al. [179] found a total of 10 (lumbar and cervical) reports of adverse tissue reaction and concluded that a high degree of suspicion of this bearing combination should be maintained until proved safe.

In the first generation of hip arthroplasties, the instances of adverse reactions to particulate debris did not initiate problems until approximately a decade after the implantations began [180]. Even then, the role of debris in loosening was not clear. There are a relatively small number of particle-reactive TDR patients reported in the literature. However, whether that cascades into the volume of revisions that appeared after the first decade of Charnley THR prostheses remains to be seen. Rates of wear in MoP TDR appear comparable to present-day hips and knees but it is confined to a smaller biological vestibule - the risks associated with this in the spinal domain are not clear.

A study by Paré et al [181] compared the performance *in vitro* of Maverick MoM devices to a maverick explant that was removed at 12 months from a low activity patient. The performance was evaluated in terms of pre and post-test average roughness. The experimental testing was based on an older ASTM guide of 1200 N and  $\pm 10^\circ$  FE/LB with motions applied sequentially and run at 2 Hz for 1 MC in diluted bovine serum. The *in vitro* tested discs (n=6) had initial R<sub>a</sub> values of  $9 \pm 2$

nm and post-test values of  $322 \pm 87 \mu\text{m}$ , an increase on 3600 %. In comparison the explant (n=1) showed an  $R_a$  value of  $21 \pm 11 \text{ nm}$ . Assuming the original surface was of similar roughness to the *in vitro* discs, the very small increase in  $R_a$  is an indicator of a good tribological regime. However, the patient was not typical and the disc would not have been subject to a full range of motion. The high  $R_a$  for the *in vitro* tested discs is an indication of poor tribological performance and a signifier of a high degree of abrasion. However, although UHMWPE is known to wear at much lower rates under rectilinear motion, metal on metal bearings perform better with crossing path motion which tends to polish the surfaces [182, 183]. Therefore the unidirectional motion used in the test may only have been representative of a worst case scenario. In the same publication the authors tested an unspecified MoM TDR and found no different in  $R_a$  change between ISO and uni-directional ASTM motions, but this was only one sample so the results are not conclusive.

In an extensive explant surface analysis report by Kurtz et al. [184] sixteen implants from 14 patients were examined, with a range of implantation periods of 2.9-16.0 years. The implants were split so that gamma sterilised in air implants could be identified (8 pre 1997 and 8 post 1997). Intractable pain and facet degeneration was the primary cause of revision surgery in all cases. The retrieved polyethylene Charité cores had median  $R_a$  values of  $0.101 \mu\text{m}$  and this was compared to a single Charité unused core with an average median  $R_a$  of  $0.366 \mu\text{m}$ . The  $R_a$  of the cores was compared to that of explanted UHMWPE hip acetabular cups which were found to be  $0.193 \mu\text{m}$ . The metallic endplate roughness was measured to be  $0.021 \mu\text{m}$  and compared to equivalent acetabula head roughness of  $0.010 \mu\text{m}$ . The new Charité and new heads were quoted as having  $R_a$  values of  $0.019$  and  $0.003$  respectively.

In the simulator experiments it was found that the pre-test roughness generally increased when considering a trace of the full disc area, but the interpretation of results was highly dependent of the surface area of interest. For example, the periphery areas where the endplate edges articulate with the PE core displayed a much reduced  $R_a$  value, but the central or pole area most often showed increased roughening obvious to the naked eye – these effects were not reported by Kurtz et al.

The roughness of the unused core was higher in measurements presented in this study as compared to Kurtz et al. [184]. This could be because the cores were different due to a change in machining process (e.g. the lathe turning speed was higher, or the tool traverse speed was lower) or the difference in method of measurement was the cause. This latter cause may be more likely when the results from Kurtz are examined in more detail. Kurtz et al. also used a 3D white light interferometer surface profiler. This has two important limitations for ball-in-socket joint replacement assessment:

1. Due to the concavity of the metallic components and convexity of the polyethylene cores the light is not reflected directly parallel back into the sensor therefore only a very small portion of the component can be assessed. In this author's experimentation with this type of equipment, a maximum of  $\sim 1 \text{ mm}^2$  could be measured. Since the component's length of bearing surface is over 15 mm this is a very narrow window of measurement and probability dictates that features of higher roughness will be effectively 'filtered out'.
2. The surface reflectivity required to maintain a level of intensity necessary to allow light interference patterns is high. Polyethylene components have very low reflectivity and unless coated with gold will not reflect enough light. This will result in high levels of noise and hence the roughness signal is attenuated.

Kurtz et al. reported surface  $R_a$  values for unworn acetabular cups of  $0.003 \mu\text{m}$  (3 nm). This is a very low value and well below typical values reported elsewhere. The method of measurement may have had an impact of these values. They analysed patches of bearing of  $0.3 \times 0.4 \text{ mm}$ . When one considers the usual cut-off parameters chosen for surface roughness measurement (typically  $0.25 - 0.8 \text{ mm}$ ) it is obvious that these lengths cannot be utilised in such a small measurement area. In order to achieve the mandatory ISO standard of 4 lengths per measurement the authors would have had to use cut off values  $< 0.1 \text{ mm}$ . This would result in excessive filtering and lead to lower  $R_a$  values. The contacting methods of roughness profiling chosen in the studies presented in this thesis are therefore probably more accurate than non-contacting ones. The limitation of the contacting method is that severe roughening (i.e. damage) may be unsuitable for the contact stylus being used.

The surface roughness reported here for the Charité disc is consistent with a recent paper by Prokopovich et al. [185] who reported a standard ISO cycle point pole roughness of 3-4  $\mu\text{m}$  for both superior and inferior surfaces which compares well to the values of 2.4  $\mu\text{m}$  and 1.4  $\mu\text{m}$  found in this study for the same surfaces. Prokopovich et al. found that the rim of the components (“surface 2”) did reduce in roughness throughout the test but this phenomenon was not expounded upon. The results of the present test confirm the presence of edge effects due to rim loading and burnishing. The same effect was also seen on the Prodisc components where  $R_a$  changed from 1  $\mu\text{m}$  (unworn) to 0.84  $\mu\text{m}$  for the whole disc, 0.17  $\mu\text{m}$  for the burnished rim and 2.25  $\mu\text{m}$  for the roughened dome. It has been observed that PE debris is hindered from leaving the wear zone under certain kinetic inputs. A hypothesis for this is that the deformation at the PE edges, due to the metallic cups, hinders particulate debris movement out of the wear zone.

#### **3.4.4 Summary**

The pattern of wear and trend in surface roughness changes has been found to be similar to that of other *in vitro* tests and has been described numerically to a more detailed level in terms of relationship to wear behaviour. Unfortunately, *ex-vivo* results do not display the same ‘pole roughening’ that has been observed and therefore even though the ISO wear test may replicate *in vivo* behaviour in terms of material loss [186] it does not appear to replicate the true tribological wear mechanisms.

A commonly reported surface feature *ex-vivo* is rim damage in Charité and rim impingement of Prodisc. In the studies presented here, no evidence of abnormal rim damage was observed. However, at the end of testing, the outer-rim depth increased by 5 % over the depth of the soak control and this change was significant (t test,  $p=0.02$ ). This change was not expected and not noticed until the end of testing and so a chronological record of change is not available. The rim appeared to splay in the axial direction and this behaviour may add to the risk of fracture at the rim as observed in some explants [93, 169, 170]. This behaviour was also recorded after *in vitro* experimentation by R Vicars [122]. The wire marker was removed from the test specimens before the study, therefore the behaviour of the wire marking under simulation conditions is not known.

Due to a lack of explant samples and a direct topographical comparison, it is difficult to correlate with any degree of certainty *in vitro* results from spine simulators with *in vivo* performance. However, certain clues as to the behaviour have been gained, such as rim deformation, patterns of roughening on the polyethylene surfaces and comparative performance with other TJRs. Further work to improve the link between *in vivo* and *in vitro* results is still an ideal if improvement in design and longevity are to be forthcoming.

## 4 Tracking of Motion Paths

### 4.1 Introduction

The motion track shape on the surface of a bearing refers to the dimensions of the track that would be produced if one bearing was kept stationary and the other articulating with motions dictated by the kinematics and phasing of the input cycle used. A single degree of freedom input such as FE would produce a rectilinear motion shape of one dimension (viewed vertically) or a curvilinear shape when the radii of the bearing itself is considered. Both MoM and MoP bearing couples have been demonstrated to be sensitive to motion track shape. MoM bearings display higher wear for rectilinear/curvilinear motions and lower wear for multidirectional sliding [187] (which produces polishing). Conversely MoP components have been shown to produce very low wear rates under curvilinear input cycles and higher wear rates under multidirectional inputs [126, 188]. The exact shape of the sliding motion track is dependent on the input motion cycle, the phasing of the inputs and the design of the bearing. Paré et al. [147] have compared ASTM and ISO motion on a fixed CoR device but there are still uncertainties regarding the amount of bearing constraint and its potential effect. When testing TDR devices, the kinematic phasing of the motion inputs has been demonstrated to have a large effect on wear, producing very low wear for zero CS motions [119, 123] and moderate wear under low CS motions [Section 3.3.1.1]. To gain greater understanding of how these phenomena may alter between semi- and un-constrained TDRs, an experimental methodology was developed in order to understand the type of motion paths that were occurring at the bearing surface. Bespoke motion path components were designed in order to replicate the dimensions of Prodisc and Charité prostheses. Motion paths calculated computationally through use of Euler angles cannot replicate AP and ML motion present in mobile-bearing devices.

The experimental questions were:

- What are the differences in operational character in terms of motion paths of semi-constrained and unconstrained bearings?
- How does the standard ISO input cycle relate to real *in vivo* Callaghan-based [1] input kinematics?



- What effects do phasing and AP shear dynamics elicit?

## **4.2 Methods**

### *Materials*

In this study Prodisc and Charité devices were simulated using custom-designed TDR replicates that included scribes built into one bearing surface. Tracking was achieved by scratching off a thin layer of ink from the opposite bearing surface. The dimensions of the original components were followed as closely as possible in order to compare the effects of semi-constrained (Prodisc) and unconstrained (Charité) designs. The Charité device was modelled as two concave dishes representing the end plates which housed polyoxymethelene (trade name: Delrin) scribes inserted from the underside and retained by springs and grub screws. Between the two concave components was a mobile core. Holes containing the scribes were threaded part way to allow the grub screws to be adjusted to the correct amount of scribe contact force. The Prodisc components operated in a similar way but with only one endplate containing scribes. Holders used to contain the motion tracking components were similar to those used in the wear testing studies.

The Prodisc and Charité TDR dimensions were measured using a surface profilometry instrument (PGI 800, Form Talysurf, Leicester, UK) and the primary dimensions used were the radius of curvature of the bearing surfaces and the fillet radii at the edge of the bearing surface. Prodisc components used the same dimensions as the original discs but the UHMWPE convex components were replaced with a metallic component. As this test was not reliant on the frictional characteristics of the device this was unimportant. Initial experimentation showed that the original Charité UHMWPE core was too soft to interact with the scribes used. Delrin cores (a hard polymer material) were therefore designed in order to eliminate scratching at the surface. Due to manufacturing limitations the core dimensions needed to be changed from those used in the wear testing experiments. The original cores were 'size 2', 7.5 mm in height. The thickness of the material at the rim was <1 mm, which was impossible to manufacture. Therefore the rim thickness was increased to 3 mm to aid in ease of replication. To preserve range of

motion of the device both the rim thickness and the height of the central dome area was increased by the same amount. Charité cores are commercially available up to a height of 11.5 mm therefore this design adjustment was acceptable. The concave end plates were replicated in stainless steel and had recessed holes arranged centrally and radially to allow scribes to be fitted to both superior and inferior components [Figure 4-1]. The tolerance between the scribes and the recesses was 0.05 mm. A limitation of using scribes was that the Charité mobile core could be subject to extra tangential frictional loading and hence changes in kinematic behaviour due to the surface drag of the scriber-core contact. Full technical details of the motion tracking equipment are shown in Appendix B.

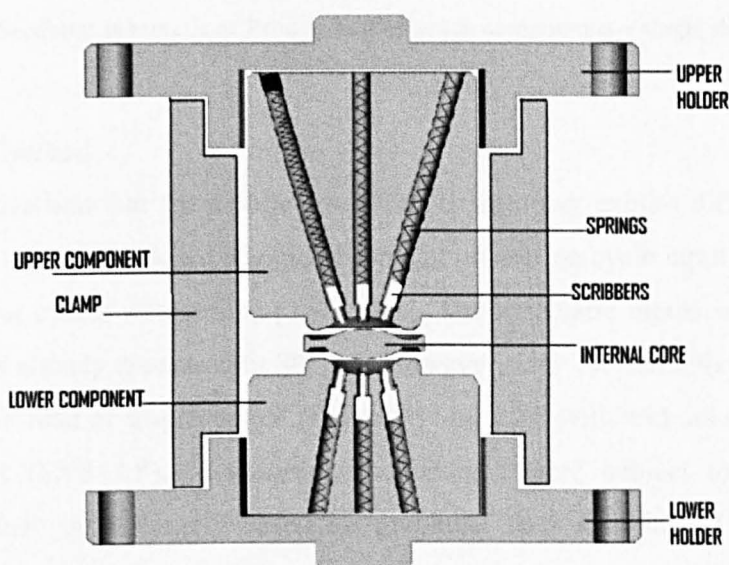


Figure 4-1 Sectional schematic of Charité motion track components

The replicate Prodisc motion tracking devices only required the fitment of scribes to one bearing surface. The superior surface was designed with multiple recesses to allow fitment of scribes. The inferior surface was a Delrin dome with no scribes [Figure 4-2].

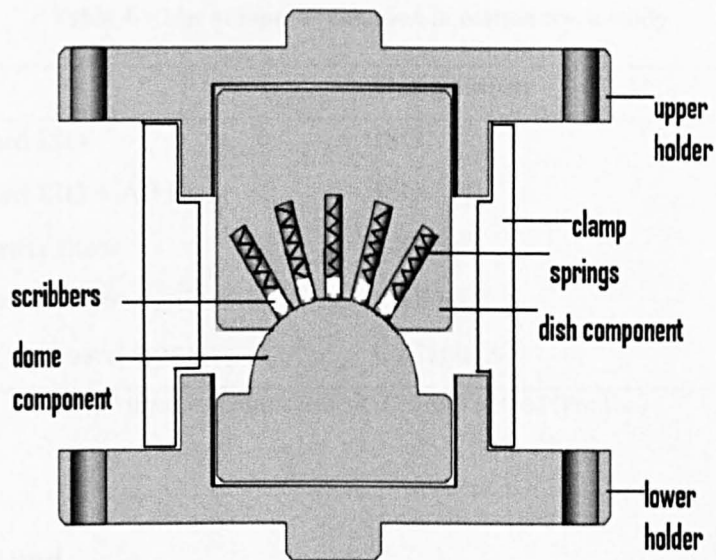


Figure 4-2 Sectional schematic of Prodisc motion track components – single sided scribers

#### *Input Cycle Method*

It was hypothesised that the mobile-core TDR design may exhibit different motion tracks to the semi-constrained design, dependent on motion cycle input. Therefore, a range of input cycles were tested [Table 4-1]. The kinematic inputs were all based on the cycles already discussed in Sec 3.2. However, new cycles included: ISO with additional AP load or displacement (ISO+AP) and LXS with additional AP load or displacement (LXS+AP). In addition, the designs were subject to a clinically relevant kinetic input largely based on graphical data for ‘normal’ walking by Callaghan et al. [1]. This cycle was converted from the original plot to an MS Excel spread-sheet using image processing software (DataThief III, 2006, by B. Tummers). The ‘normal walking’ kinematics and ‘L4/5 joint compression forces’ were traced using 128 points and finally converted to .txt format for use in the spine simulator. Details of the ISO+AP motions are described by Vicars et al. for the Prodisc [128] and Charité [130] respectively.

**Table 4-1 List of input cycles used in motion track study**

<b>Input</b>	<b>Designation</b>
Standard ISO	ISO
Standard ISO + AP shear*	ISO+AP
Low cross shear	LXS
Low cross shear + AP*	LXS+AP
Callaghan based input	Callaghan

\*AP input was displacement (Charité) or load (Prodisc)

### *Simulator Method*

In order to stabilise the assembly and fitment of the test components, two hemi-cylindrical clamps were used to tightly fit the holders and prevent motion [labelled 'clamp' in Figure 4-2]. These were secured temporarily with cable ties to keep the two cylinder halves together until the assembly was inside the simulator. Components using the Charité design were labelled so that the inferior and superior sides of the mobile core were recorded correctly. Before assembly the convex surfaces were coated in non-permanent ink. Once mounted, the cable ties were cut and the stabilising clamps removed. The spine simulator was then run with two cycles (minimum cycle count allowed by the simulator design) of the desired input motion after which the machine was stopped and the stabilisers reattached until the motion track components could be removed from the machine and inspected. Images were orientated with respect to the simulation direction and recorded digitally.

### *Extended motion testing (Charité)*

As previously mentioned [Section 4.2], the original Charité core material was too soft for motion path use; however, this material was useful one on type of test: continued application of the input cycle. This allowed inspection of the surface by use of engineers blue dye which penetrated the scribe indents and showed the pattern of wear for a continued test. This demonstrated the difference between the single-cycle motion track test and the continued application of the input dynamics. The Prodisc design did not need to be tested in this way as the design of the bearing meant that the motion due to continued application of the cycle is identical to a

single motion, whereas the Charité design with its mobile core is much more difficult to predict.

### *Analysis*

Images of the surfaces contained five sets of paths and were analysed for length and width. Each image was first calibrated by setting the image software (Image Pro Plus, Media Cybernetics, Inc., Bethesda, MD) to measure a length from a steel rule in the image frame. The number of pixels corresponding to the calibrated length then acted as a measurement for the motion tracks. Details of the mathematical correction for the curvature of the surface are in Appendix C.

## **4.3 Results**

The results of the Prodisc length and width measurements are shown in Figure 4-3 below. There was no significant difference between the Callaghan-based cycle and the ISO cycle (t test,  $p > 0.05$ ) for either length or width of track. Addition of AP force lengthened the length track to 108 % of ISO, though this difference was not significant ( $p = 0.24$ , ANOVA). This addition also appeared to narrow the width of the track but this may have been an artefact of the measurement technique (the error bars were large and the difference not significant,  $p = 0.17$ , ANOVA). The LXS motion resulted in very narrow paths and as a result the width was difficult to discern from the pattern, therefore only the length was reported; as expected this was the same as the ISO input. Addition of AP shear to the LXS cycle increased the width of the motion path to a point where it was measurable, but this was less than the width recorded for ISO+AP ( $p < 0.05$ , ANOVA). An example motion path image is shown in Figure 4-4.

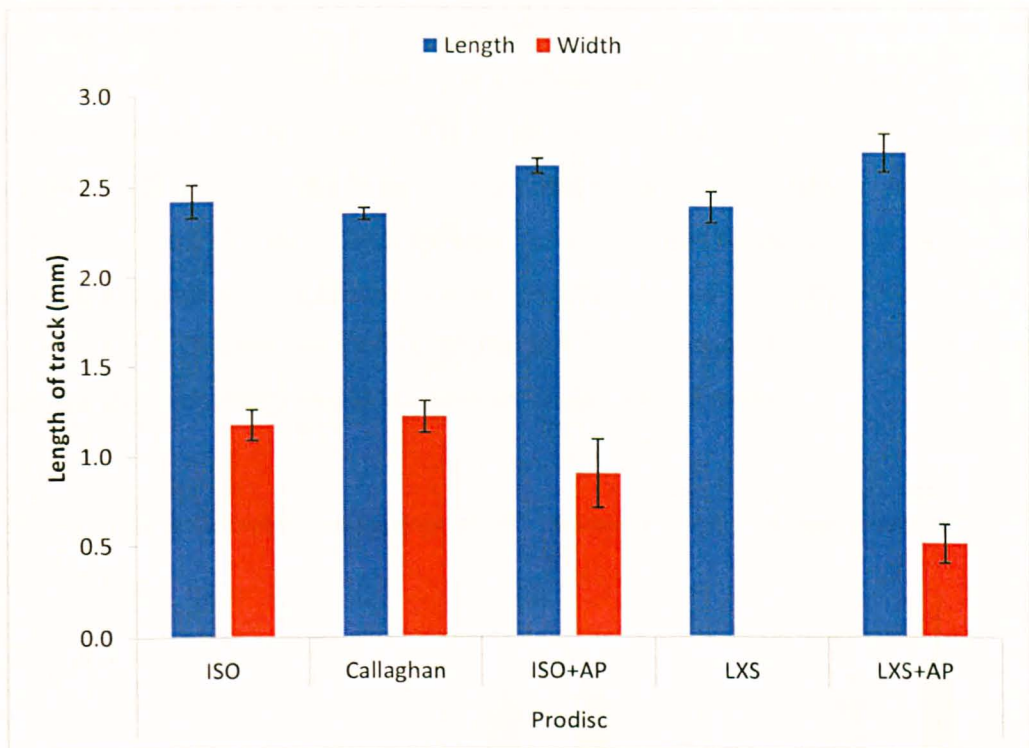


Figure 4-3 Prodisc motion track measurements for all input cycles ( $\pm$  standard deviation)

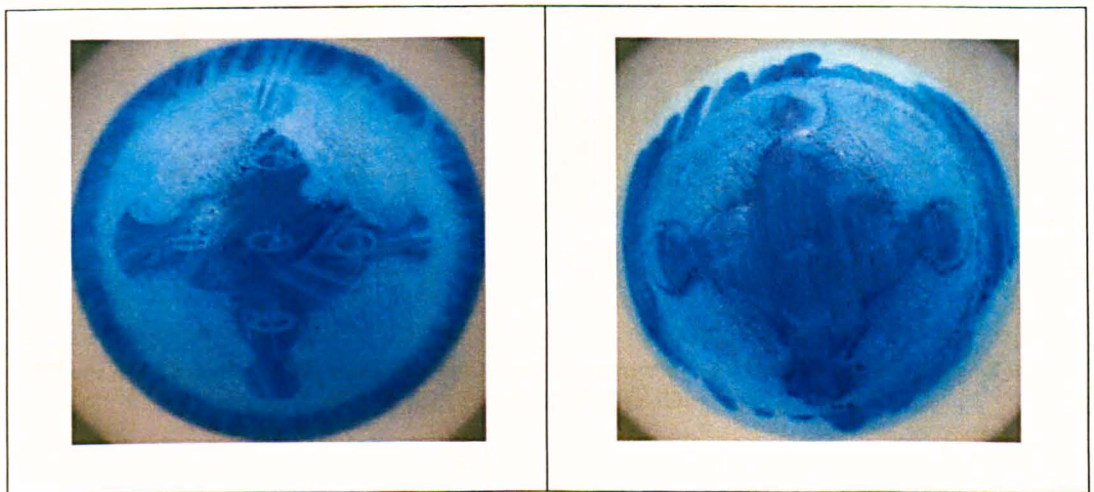
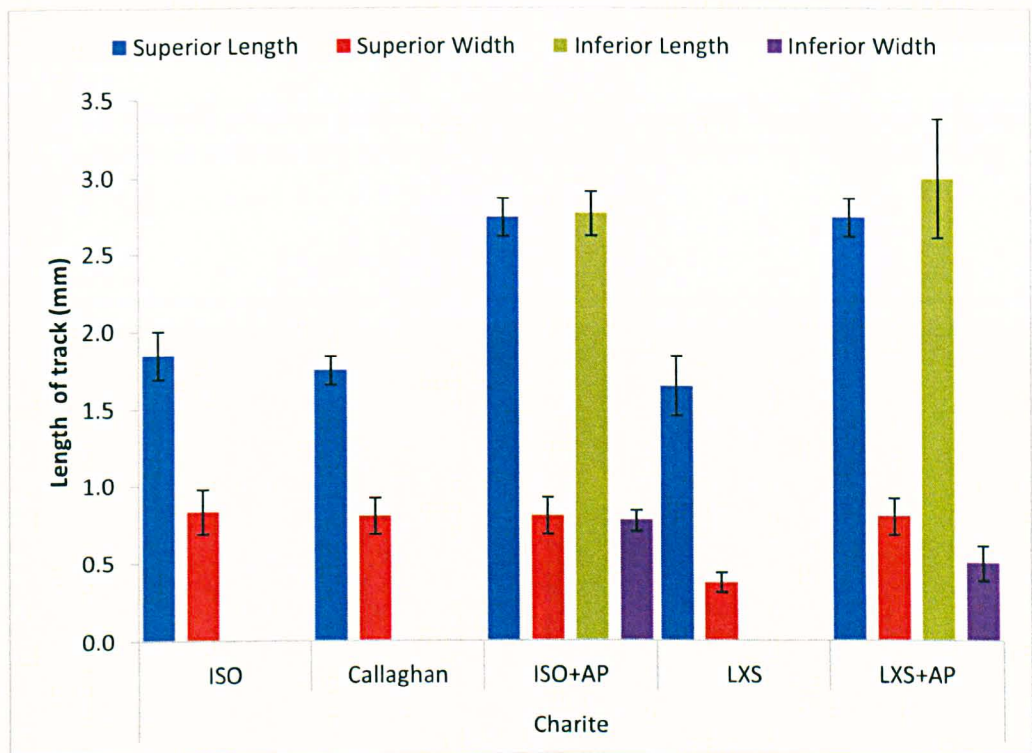


Figure 4-4 Prodisc motion tracks images, ISO (left) and LXS (right)

The second stage of the experimentation investigated motion on the unconstrained Charité bearing [full results are summarised in Figure 4-5]. The ISO input cycle showed that there was minimal motion of the inferior bearing. Due to marking from start-up of the simulator it was impossible to measure the small motion tracks on the inferior surfaces, however this did not mean that the movement was zero. Average track measurements from Callaghan input motions appeared identical to the ISO

cycle measurements (t test,  $p=0.35$ ). Addition of AP shear displacement to the ISO cycle resulted in significant superior and inferior motion of similar magnitude. This was in contrast to the purely ISO motion in which superior motion was more prominent. The width of the track did not change, however, the length was increased to 148% of the ISO value. The LXS input resulted in similar length tracks to the ISO input, but significantly narrower widths ( $p<0.05$ ) [Figure 4-7]. The addition of AP shear to the LXS input resulted in similar behaviour to the ISO+AP cycle, but with significantly reduced ( $p<0.05$ ) ML motion on the inferior surface.



**Figure 4-5 Charité motion track measurements for superior and inferior surfaces for all input cycles ( $\pm$  standard deviation)**

The ISO motions and Callaghan cycle both displayed rotation of the mobile core. The spiral pattern of motion track on the bearing surface is highlighted in Figure 4-6, where the image shows engineers blue that has soaked into the deformed plastic.

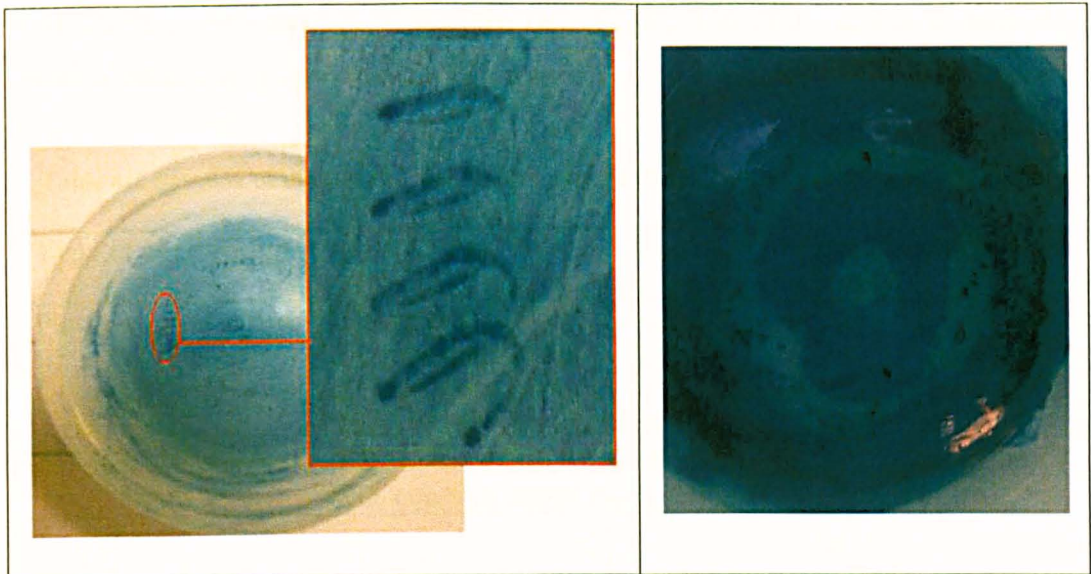


Figure 4-6 Continuous motion paths on an actual Charité core (left) showing the spiral motion path (indent from scribers) and replicate PE core (right) as a result of scratching ink off the surface

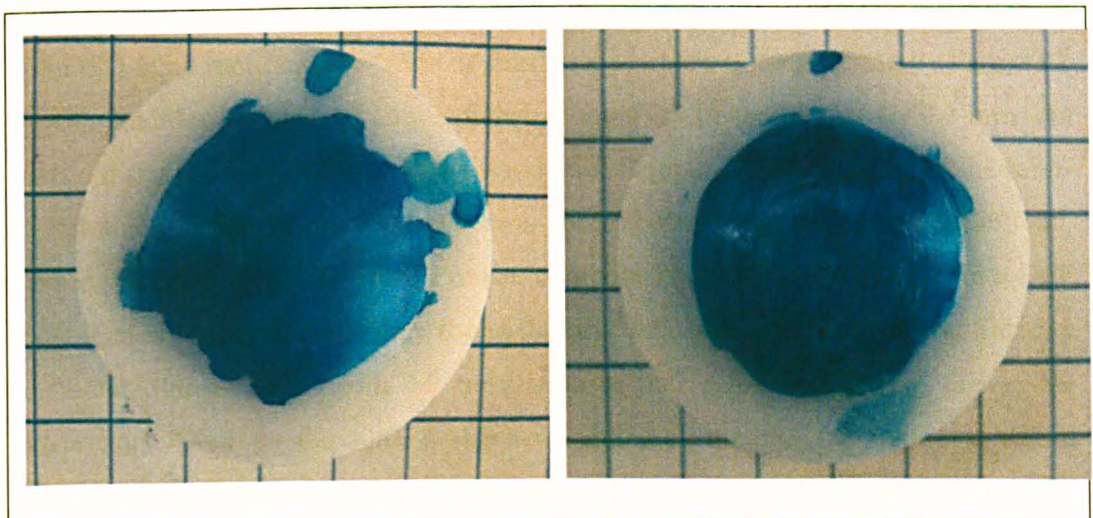


Figure 4-7 Comparison between motion tracks of low CS (LXS) input (left) and pure ISO (right)

The Charité mobile core had a propensity to rotate under ISO motions [150]. This rotation has been recorded here under differing motions and with two types of core: 1) original Charité core, 2) copy Delrin core. The results are shown in Table 4-2. Increasing the axial load increased the rotation speed. Using a cyclical axial load (600–2000 N) increased the speed further. The original cores were compared to the specially designed copies to compare different frictional characteristics. Original



UHMWPE cores rotated faster than the Delrin cores. Use of the scriber to mark the motion tracks also increased the rotation speed.

**Table 4-2 Rotation of the Charité mobile core under differing inputs and of two design types**

Type of core design	Input Cycle	Rotational velocity (°/cycle)
Plastic copy (Delrin)	ISO, constant 300 N	0.24
	ISO, constant 600 N	0.34
	ISO, constant 2000 N	0.93
	Standard ISO (600-2000 N)	3.60
Original UHMWPE	ISO, constant 300 N (no scribes)	1.20
	ISO, constant 300 N (with scribes)	3.36

#### **4.4 Discussion**

##### *Prodisc*

The ISO input motion tracks were of similar appearance to those found by Pare et al. [147]. Addition of AP load only lengthened the track of the Prodisc by 0.2 mm, but was not significantly different to the standard ISO input. This is because of the semi-constrained design of the Prodisc resists shear forces when under transverse load. When Vicars et al. [128] tested Prodisc components under four DoF and five DoF (AP loaded) configurations they found that the wear rate was also not significantly different. For an increase in AP translation in the region of 0.2 mm, this is not surprising. However, the authors also commented on the changed wear scar which was observed to include greater deformation of the rim of the disc. In this case, the addition of an extra 0.2 mm of translation did affect the wear characteristic and therefore the long-term behaviour, perhaps in terms of fatigue effects, may be of concern when anterior torso-related load components are applied. The similarity between ISO and Callaghan motion data is interesting, as the Callaghan-based input is non-sinusoidal ‘real’ *in vivo* data from low back measurements. Even with the differing phasing of the motions, the net result was that the ISO standard reasonably replicates this *in vivo* data, at least in terms of aspect ratio of the motion tracks and hence probably has a not-dissimilar CS ratio.

### *Charité*

Adding AP shear (displacement rather than load) to the Charité LXS test seemed to increase the width of lateral motion track. All the Charité tracks were greatest at the superior surface, with some tracks on the inferior surface unreadable due to difficulty in discerning between simulator start-up marking and actual marks from the input cycle. The addition of AP shear was much more apparent on the unconstrained Charité than on the Prodisc, with the length of track increasing significantly. The effect of AP shear has been studied *in vitro* by Vicars et al. [130] who found significant increases in wear when the longitudinal motion increased. Where inferior surface measurements could be taken, the length and width of the tracks was identical to the superior ones, except for the LXS+AP width track. Shorter overall tracks on the Charité were due to two-surface motion and slightly smaller radii of the bearing surfaces (13 mm versus 14.5 mm for Charité and Prodisc respectively). The ISO and Callaghan results were very similar, even though the type of bearing design had changed from semi-constrained to unconstrained.

Rotation of the mobile Charité core has been observed previously [122] but this is the first time the resultant spiral motion tracks have been recorded. The rotation speed increased with increasing load and with the use of different materials. This suggests that increasing the frictional torque at the surface further amplified the difference in friction between superior and inferior bearing surfaces.

#### **4.4.1 Summary**

Addition of AP loading to the Prodisc design lengthened the motion tracks by a small amount that would not appreciably affect the cross shear ratio but would have other effects such as increasing surface stresses at the rim of the PE dome. However, the Charité disc did show a large increase in longitudinal motion, due to the unconstrained mobile core having little resistance to shear displacement. The AP displacement and AP load applied to the two discs are not directly equivalent and therefore caution should be exercised in concluding differences in TDR behaviour. The *in vivo* Callaghan data applied to the *in vitro* test studied here resulted in similar lengths and widths of tracks to the ISO standard. Although this is interesting, it should be noted that the Callaghan data itself was gained from one sample and

calculated from an entire lumbar section. Rotation of the Charité core was observed and it is postulated that this effect produced the isotropic wear described in Section 3.3.2.

## **5 Investigation of Short Stroke Effects**

### ***5.1 Introduction***

The results of the TDR spine simulator wear investigations demonstrated a recurring phenomenon, where the polar region of the PE components would become rougher than the outer circumferential areas [Sec 3.3.2]. This area became burnished but the outer regions between the pole and the rim remaining at approximately the same level of roughness. This occurrence of roughening and height increase at the pole area may provide an indication of the wear processes that occur at this point. For the ISO TDR wear standard the rotational inputs are much smaller than the equivalent hip and knee standards. For example, the largest rotational input for TDR testing is the FE of 9° in total (+6° flexion/-3° extension). The equivalent hip input is ±25° making 50° total rotation, whilst for a total knee replacement the total flexion/extension rotation is ±30°.

The debris at the pole was observed to sit proud of the radial surface [Sec 3.3.2] and was shown to absorb ink indicating it was a build-up of semi-attached UHMWPE material. Re-attachment of wear debris observed in spine simulator tests prompted further research into the mechanism and what experimental conditions promoted this phenomenon. The maximum rotational motion of the ISO test results in a curvilinear motion of 2.3 mm (9° over a 14.5 mm radius), which may not be sufficient movement to release debris generated at the pole. It was postulated that the short overlapping nature of the bearing motion may be responsible for entrapment of wear debris, described schematically in Figure 5-1.

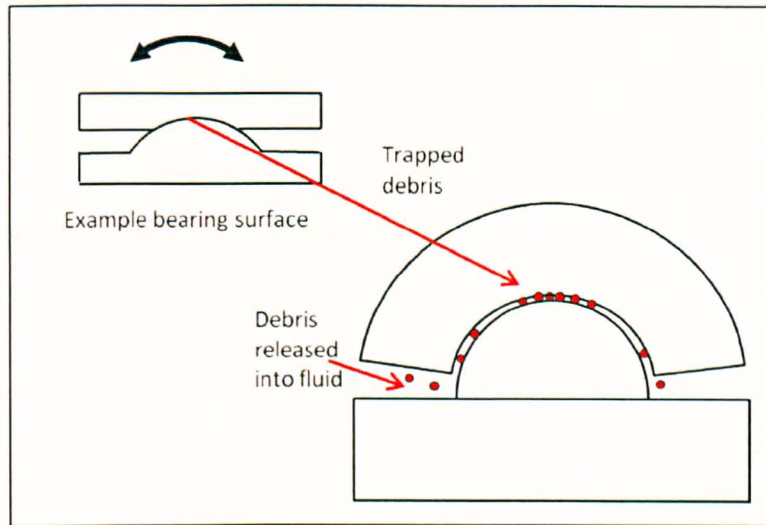


**Figure 5-1 Example TDR (left) shown in close up section (right) with wear particles (red) shown accumulating at the pole and escaping at the edges**

In order to isolate the cause of debris entrapment, a study of the effect of long versus short strokes was undertaken (using the same value of cross-shear for both tests) using a pin-on-plate (PoP) apparatus. A long stroke wear patch (that cleared the wear path area) was compared to a short stroke motion path which resulted in an overlapping patch of wear where lubricant starvation or debris entrapment could occur [Figure 5-2].

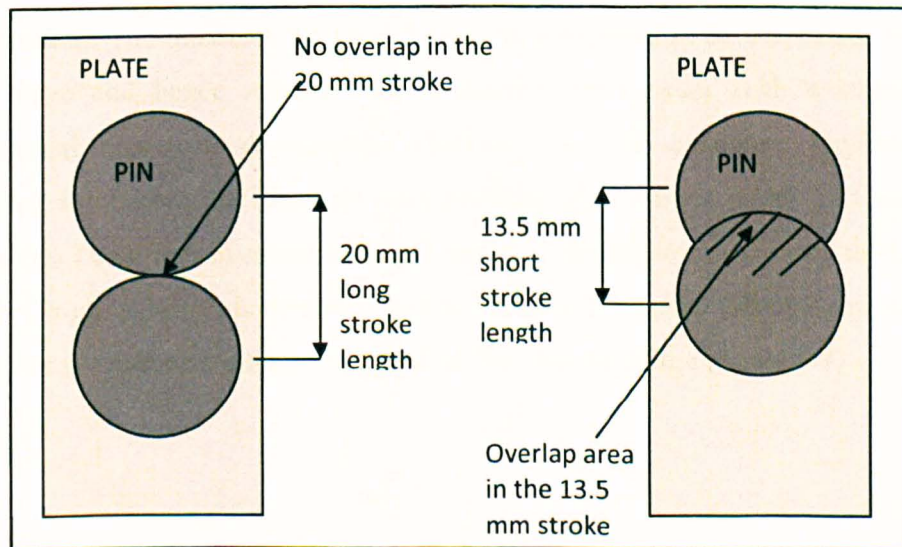


**Figure 5-2 Plan view schematic of the PoP system showing two tests, (a) is 20 mm stroke length and (b) is 13.5 mm stroke length, the pin moves cyclically**

In order to use correct contact pressure values for the PoP tests, it was necessary to establish the correct contact pressure present at the surface of both TDR designs used in the study. Theoretical predictions were first used to gain Hertzian contact pressures, these were followed by compressive tests using pressure sensitive film that captured the contact pressure directly. The films also gave a clear indication of contact area.

It was hypothesised that the shorter rotational motion of the TDR inputs may have resulted in wear debris not having opportunity to exit the bearing interface without first being reattached onto the polyethylene surface and hence roughening that face. The Charité UHMWPE components exhibited this behaviour on both superior and inferior surfaces. The aim of the following experiments was to study this effect in terms of short and long stroke behaviour, and in addition, quantify the contact pressures present in TDR bearings so that PoP experiments could be devised.

### **5.1.1 Theoretical Prediction of Contact Pressure**

A pictorial explanation of Hertzian contact and the variables used is shown in Figure 5-3. Basic values for material properties used for Hertzian analysis are listed in Table 5-1. To gain an initial understanding of contact pressure, a simple Hertzian contact analysis was undertaken to assess probable contact pressure. Unfortunately, the clearance (difference in radii) of the TDR bearings is impossible to know while in operation. The tolerance for manufacture was believed to be 0-0.4 mm, which is very large and hence assumes that bedding-in will occur with a steady state operational clearance developing. Therefore, several clearance regimes were analysed to observe the effect on peak pressure ( $P_o$ ), contact width ( $2a$ ) and shear stress ( $\tau$ ). The effect of moving from a minimal clearance of 0.01 mm to 0.66 mm for the Prodisc design is demonstrated in Table 5-2. Similar calculations show the effect for the different dimensions used on the Charité design [Table 5-3].

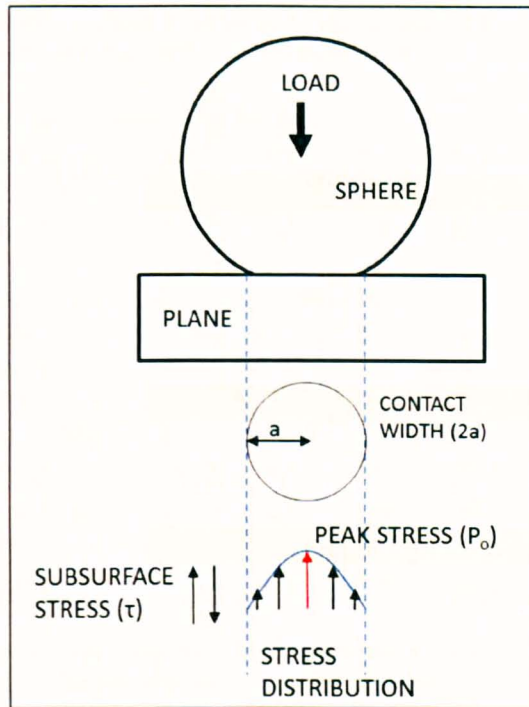


Figure 5-3 Hertzian contact theory showing stress distribution, peak stress ( $P_o$ ), shear stress ( $\tau$ ) and width of contact ( $2a$ ) for a sphere on an infinite flat plane

Table 5-1 Prostheses material properties

Material	Poisson's ratio	Elastic modulus (MPa)
CoCr	0.3	230 000
UHMWPE	0.4	1 000

**Table 5-2 Prodisc results obtained from using Hertzian contact theory (highlighted are peak pressure,  $P_o$ , width of contact,  $2a$ , and shear stress,  $\tau$ )**

Theoretical output parameters					
Clearance	0.01	0.05	0.25	0.44	0.66
$P_o$ (2KN)	1.07	3.13	9.05	13.09	16.98
$P_o$ (0.6KN)	0.72	2.09	6.06	8.76	11.37
$a$ (2K)	29.86	17.48	10.27	8.54	7.50
$a$ (0.6KN)	19.99	11.70	6.87	5.72	5.02
Contact width					
$2a$ (2KN)	59.73	34.96	20.54	17.08	15.00
$2a$ (0.6KN)	39.98	23.40	13.75	11.44	10.04
Area (2KN)	2802	960	331	229	177
Area (0.6KN)	1256	430	148	103	79
$\tau$ (2KN)	0.32	0.94	2.72	3.93	5.09
$\tau$ (0.6K)	0.22	0.63	1.82	2.63	3.41

$P_o$  (2KN): peak pressure at 2KN,  $a$  (2KN): contact half width at 2KN,  $\tau$  (2KN): shear stress at 2KN, Area: area of theoretical contact if the pressure distribution was Hertzian

**Table 5-3 Charité results obtained from using Hertzian contact theory (highlighted are peak pressure,  $P_o$ , width of contact,  $2a$ , and shear stress,  $\tau$ )**

Theoretical output parameters					
Clearance	0.01	0.07	0.25	0.38	0.66
$P_o$ (2KN)	1.24	4.52	10.46	13.74	16.98
$P_o$ (0.6KN)	0.83	3.02	7.00	9.20	11.37
$a$ (2K)	27.77	14.54	9.55	8.34	7.50
$a$ (0.6KN)	18.59	9.73	6.40	5.58	5.02
Contact width					
$2a$ (2KN)	55.53	29.08	19.11	16.67	15.00
$2a$ (0.6KN)	37.18	19.46	12.79	11.16	10.04
Area (2KN)	2422	664	287	218	177
Area (0.6KN)	1085	298	129	98	79
$\tau$ (2KN)	0.37	1.36	3.14	4.12	5.09
$\tau$ (0.6K)	0.25	0.91	2.10	2.76	3.41

It can be seen that the theoretical value of contact pressure is very dependent on the chosen clearance value. Also, the maximum width of contact was very sensitive to the clearance value used. It should be noted that the Hertzian transformation is based on a sphere-on-plate equivalence and the width of contact relates to this model. However, given that the maximum width of contact for the TDRs was ~17 mm across, it is of potential concern that this value was not reached until a clearance of



0.44 mm was used – a value improbable in actual operation. The results of the theoretical assumptions are shown in Figure 5-4.

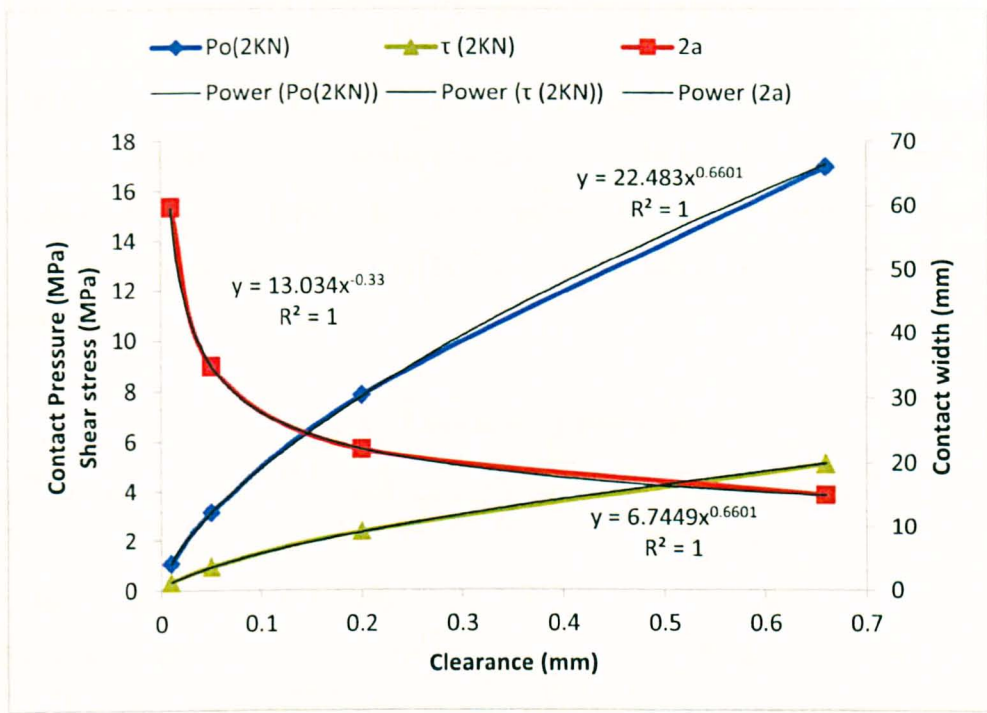


Figure 5-4 Hertzian analysis showing maximum contact pressure ( $P_o$ ), shear stress ( $\tau$ ) and contact width ( $2a$ )

From the graph [Figure 5-4] it can be seen that both the peak pressure ( $P_o$ ) and shear stress ( $\tau$ ) are a power-function of clearance raised to index value 0.66. This means that as clearance is increased, the effect on contact pressure diminishes. In contrast, the contact width of the bearing ( $2a$ ) is a power function of index 0.33. The effect of this is to dramatically widen the theorised contact width for small clearance values. Since the maximum practicable contact width for the TDR devices under test is finite and approximately 15-20 mm, the Hertzian theory suggests that edge loading of the bearing may occur because the theoretical contact width ( $2a$ ) is usually outside this finite range.

It is clear from this simple model that the lack of knowledge about in-operation contact clearance means that theoretical models rely too heavily on clearance assumptions and as such a practical experimental method of contact pressure

measurement was undertaken in order to facilitate appropriate design of the PoP experiments.

### 5.1.2 Experimental Contact Pressure Measurement

The TDR under test was mounted in a holder also used for friction testing (described in Sec 6.2). An initial experiment using engineers dye mixed with petroleum jelly gave inconsistent results and was abandoned in favour of a pressure sensitive film (Fujifilm, Fuji Prescale, FujiFilm NDT Systems Inc., USA) of three different grades [Table 5-4].

**Table 5-4 Grades of Fujifilm used**

Fujifilm type*	Load used (N)	Bearing used
SLP (double sheet)	600	Charité
LP (double sheet)	2000	Prodisc
MP (mono sheet)	2000	Prodisc, Charité

\*SLP=super low pressure, LP=low pressure, MP=medium pressure

Fujifilm recording uses impregnated bubbles of die in the film which burst under certain pressures. The level of sensitivity required is based on trial and error selection. A potential flaw in the use of film is the inherent alteration of contact clearance. The thickness of the Fujifilm was  $109 \pm 3 \mu\text{m}$  for the mono sheet (MP) and  $88 \pm 5 \mu\text{m}$  for the double sheet (SLP and LP), but was unknown when under pressure. The load was applied by a tensile test instrument (Instron Ltd., High Wycombe, U.K.) and ramped up over a period of 30s to a maximum and then held for 30s to achieve steady state loading. The resultant contact patches were then recorded. Example before-and-after images of a contact film are shown in Figure 5-5 and Figure 5-6.

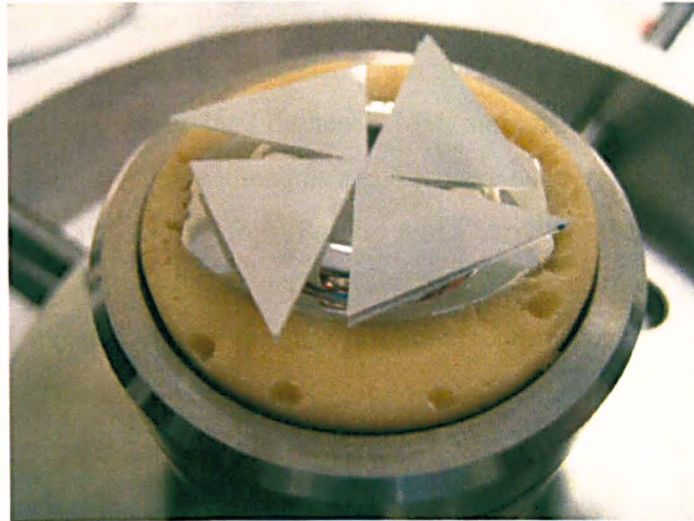


Figure 5-5 A Charité device with Fujifilm in place before compression

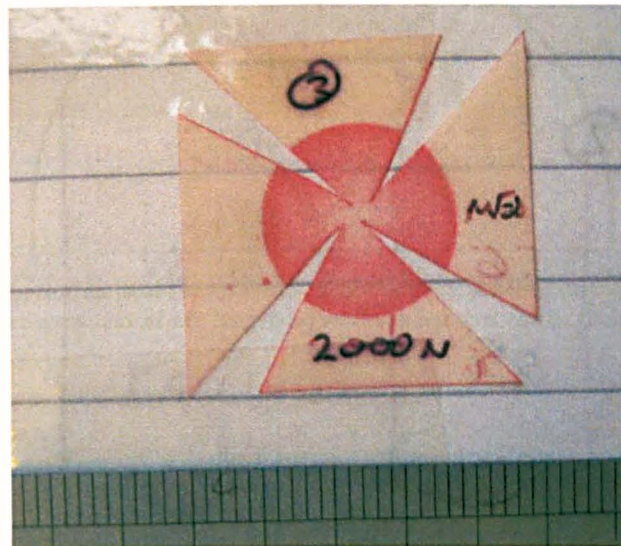
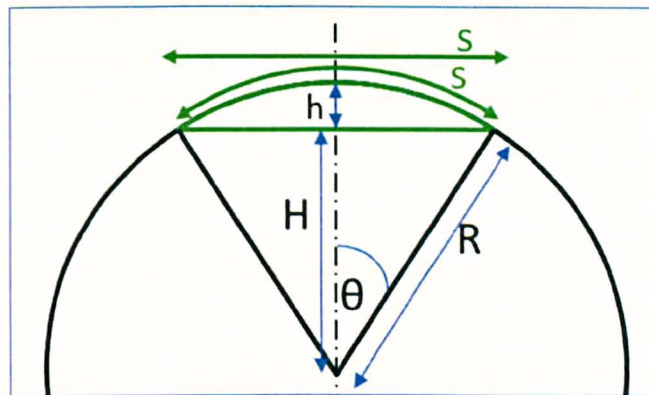


Figure 5-6 The resultant contact pattern was recorded on the petal-patterned Fujifilm next to a scale and analysed in measurement software

All measurements were repeated three times using identical Fujifilm patterns that did not leave gaps between the ‘petals’ or allow overlap. Once the loading profile was complete, the sample and film was removed from the machine and inspected and photographed for future measurement. The load on the test sample and the recorded area were used to calculate contact pressure. In previous works, the area calculation has been done by drawing around the petals of the contact patch. However, this is both subjective (if the pattern is not clear and repeatable) and is highly dependent on the accuracy of the initial cutting of the film. In order to address this issue, a mathematical method of calculation using only the measured

circular area was developed. Referring to Figure 5-7, the arc length ( $s$ ) was inferred from a measurement of the area of contact from the image analysis software (Image-Pro Plus, Media Cybernetics, Inc., Bethesda, MD) and represented the contact width of the TDR bearing. The known lengths  $s$  and  $R$  were used to find  $\theta$ . From length  $R$  (known to be 14.5 and 13 mm from Prodisc and Charité respectively) the length  $H$  was determined from  $R\cos\theta$ . The depth of the cord ( $h$ ) is equal to  $R-H$ . Hence, from the formula for the area of a sphere section ( $2\pi Rh$ ), the actual area of contact during compression was found.



**Figure 5-7 Diagrammatic representation of a convex bearing surface, showing the measurement of arc length ( $s$ ) as the measured contact width**

Three loads were evaluated for their impact on contact pressure and contact area. These were 600 N (lowest load of ISO waveform), 2000 N (highest load of ISO waveform) and 3000 N (chosen to represent an extreme loading). In addition to the axial loading, the Charité device was also tested with the mobile core rotated and translated to the maximum position permitted by its design [Figure 5-8]. This was done to investigate a possible loading condition that may produce extreme or concentrated stresses.

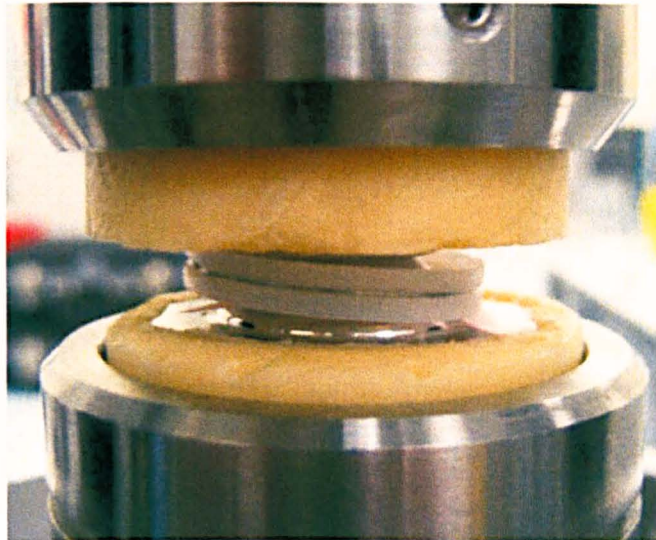


**Figure 5-8 Charité mobile core translated and tilted between its endplates (mounted in cement)**

### **5.1.3 Experimental Contact Pressure Results**

Contact pressure and contact area results showed a significant difference between Prodisc and Charité values (t test,  $p < 0.01$ ) for all load points. The behaviour of the Prodisc sample under various loads is recorded in Figure 5-9. The results indicated a contact stress of between 3.2 and 8.9 MPa for 600 and 2000 N respectively. Using a clearance value of 0.25 mm, the theoretical results compared well for the 2000 N load but not so for the lower load. In reality, the clearance of the device may change as contact pressure increases, due to deformation of the PE component. A significant difference between the Hertzian theory and practical evidence was that the density of pressure distribution was not parabolic but uniform with a sharp contrast between contact and zero contact [Figure 5-10] and was therefore plug-shaped in appearance. Compared to Table 5-2 it can be seen that the experimentally measured area of contact for the Prodisc rose more slowly as load was applied.

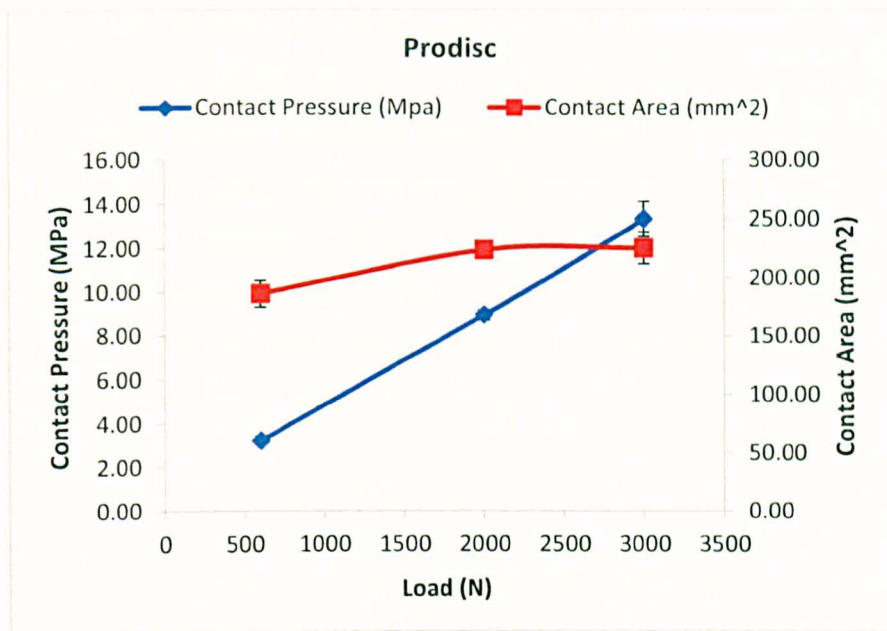


Figure 5-9 Compressive contact pressure and contact area results for the Prodisc TDR bearing

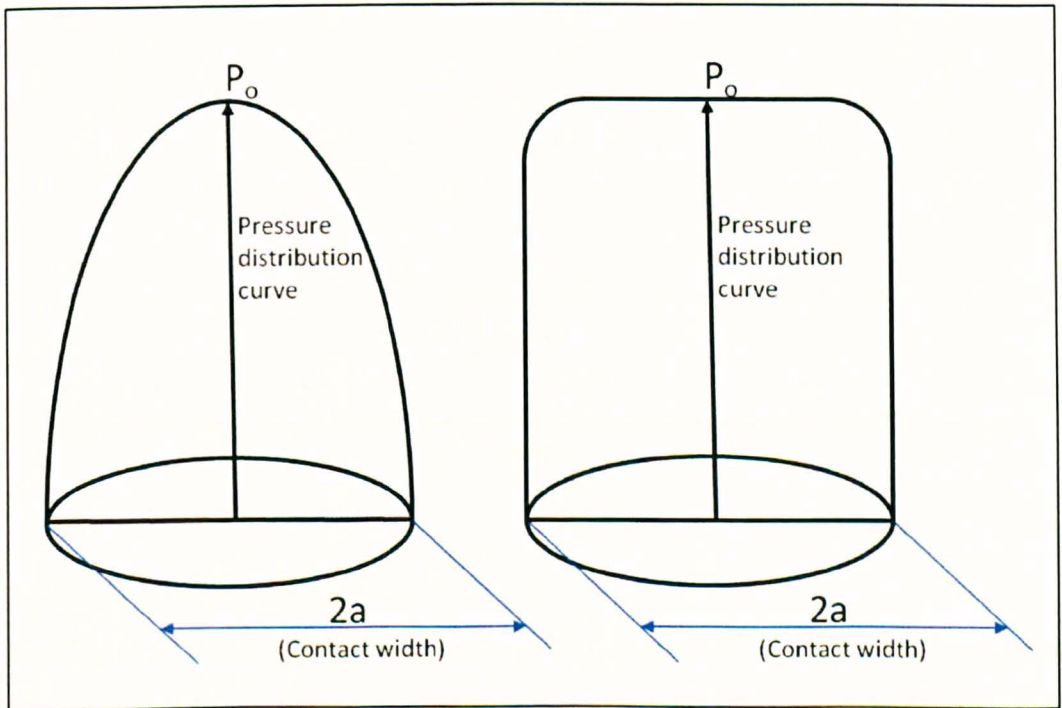


Figure 5-10 Theoretical pressure distribution (left) and actual plug shaped distribution (right)

The behaviour of the Charité sample under load is shown in Figure 5-11. The results indicated a contact stress of between 4.3 and 13.8 MPa for 600 and 2000 N respectively. Using a clearance value of 0.38 mm, the theoretical results compare

well for the 2000 N load but not so for the lower load which was approximately two times that of the experiment. In practice it is probable the clearance of the device changed as contact pressure increased, due to deformation of the PE component. The Charité TDR also displayed the same contact pressure distribution as described for the Prodisc above. Compared to Table 5-3 it can be seen that the experimentally measured area of contact for the Charité rose more slowly as load was applied. The contact pressure for the tilted disc (average 5.2° from the horizontal) was not significantly different from the flat disc result.

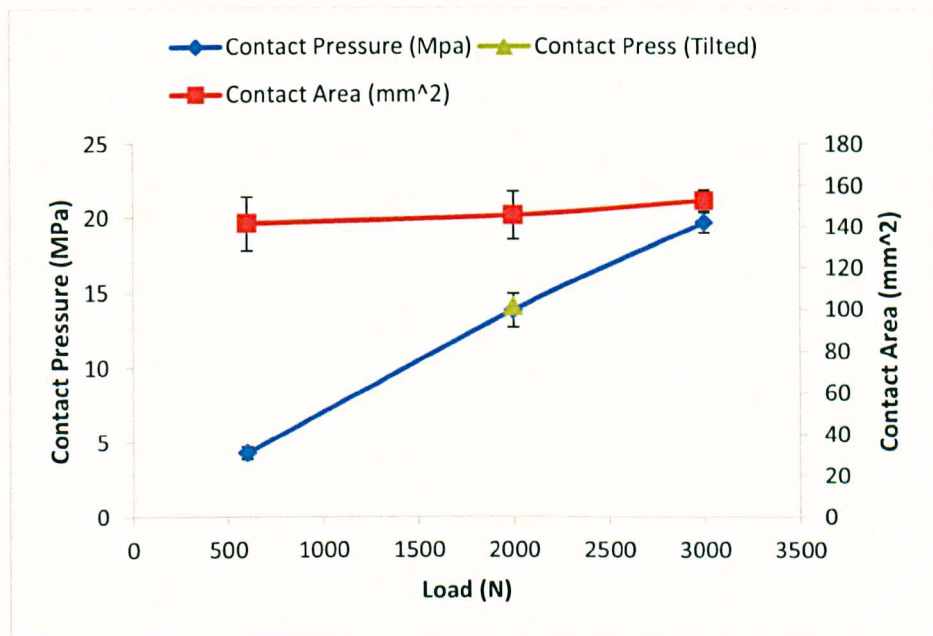


Figure 5-11 Compressive contact pressure and contact area results for the Charité TDR bearing

#### *Implications for PoP Experiment*

In order to select an appropriate contact pressure and load for the PoP experiment it was necessary to compute and experimentally verify the existing contact pressure in TDRs. The range of pressure that corresponded to the ISO input was between 3.2 and 13.8 MPa for the Prodisc and 4.26 to 13.32 MPa for the Charité. The PoP tests required a large surface area and reasonable stroke length in order to a) allow a change in stroke length without a change in CS ratio and b) to increase the chance of debris entrapment. To achieve the minimum 3.2 MPa nominal contact pressure from a pin on a plate would require a 10 mm diameter pin (using a maximum allowable

load of 240 N). However, this width would not have allowed for sufficient overlap of the pin in the motion path area. Therefore, a maximum value of contact area was used and the contact pressure was allowed to fall below that required in theory.

## 5.2 Pin on Plate Methodology

A six station PoP simulator was used for the stroke length investigations. The UHMWPE pins used were a custom-design of 20 mm diameter giving a contact face of 314 mm<sup>2</sup> [Figure 5-12], designed to maximise the chance of debris entrapment during short stroke motion. CoCr plates of a standard design were polished to  $R_a \sim 0.010 \mu\text{m}$  and re-polished between wear tests using an identical method to achieve the same  $R_a$  value. Bovine serum diluted to 25 % was added at a volume of 55 ml per cell. Non-irradiated GUR1020 polyethylene dowel was used to make the pins with a turned finish on the bearing face.

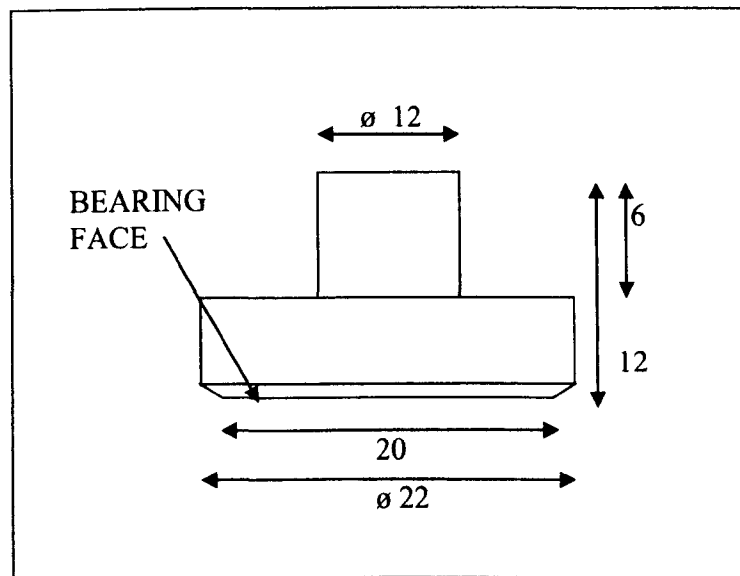


Figure 5-12 PoP pin design for a wide contact area bearing face (all units in mm, material GUR 1020)

The load applied was 240 N which was the maximum permissible. This resulted in a contact pressure of 0.76 MPa which was 12 times lower than the peak stress experienced on the Prodisc TDR for a 2000 N load. This relatively low value was



not ideal, but unavoidable given the limitations of the equipment. However, from Hertzian contact analysis, it can be shown that the peak pressure was 1.15 MPa at the centre. The long stroke test was 20 mm in length which meant that the 20 mm diameter UHMWPE pin had a stroke length equal to a full width of the pin surface on the CoCr flat surface before returning to the start position. In contrast, the short stroke test was 13.5 mm in length. This allowed a distance of 6.5 mm to be left permanently covered by the pin contact and hence be a potential source of a) lubricant starvation and b) an area where wear debris may become 'trapped' to some extent.

In order to ensure that only one parameter was changed (path distance) rather than two (path distance and CS ratio) a method of keeping the same CS ratio for both tests was used. A spread-sheet calculation of CS ratio (Dr Abdellatif Abdelgaied, University of Leeds) was used to compute the optimal stroke length for two different pinion gears. These two pinion and stroke length combinations resulted in the same CS ratio for both investigations so that only the effects previously described would be tested [Figure 5-13]. For the long stroke test a large pinion (56 mm) provided a CS ratio of 0.03 and for the short stroke test a smaller pinion was used (38 mm) to create the same CS ratio value. The ISO standard for spine simulation results in a significantly higher CS ratio of 0.2. The PoP equipment was unable to replicate such high values.

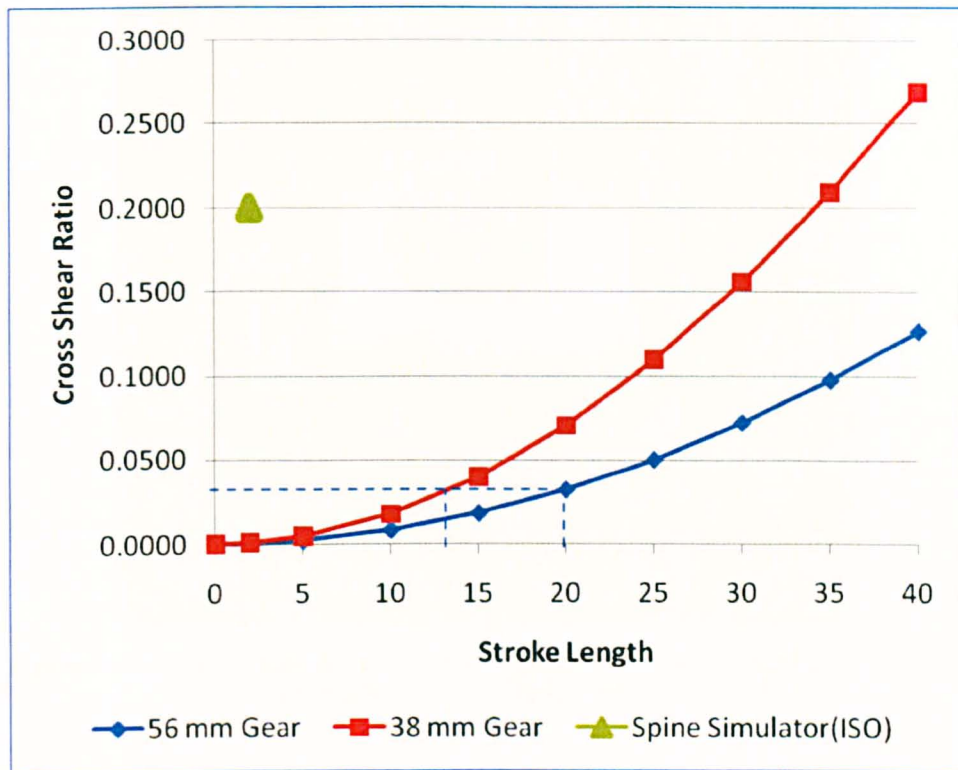
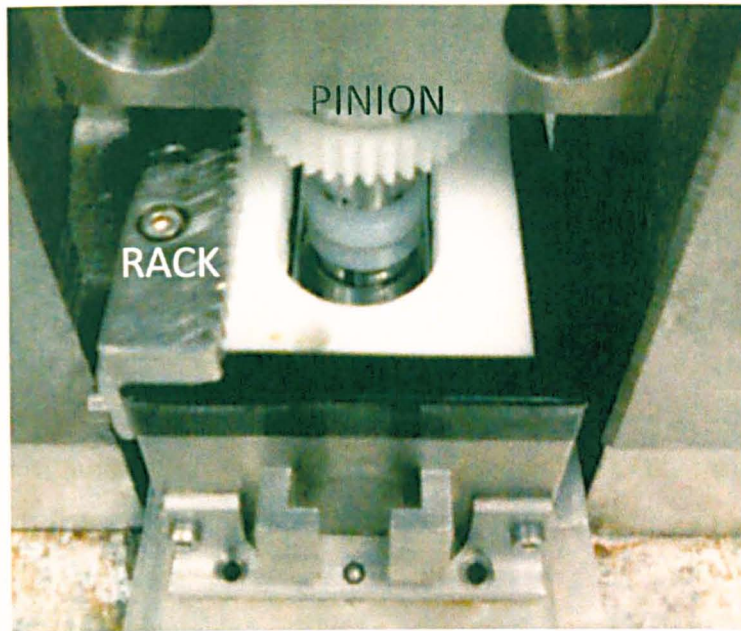


Figure 5-13 PoP theoretical CS ratios based on two pinion gear sizes used on the PoP machine for a 20 mm and 13.5 mm stroke length producing the same CS value

Six pins and six plates were produced and subject to reciprocating loaded contact. The machine used a scotch yoke mechanism to produce a sinusoidal reciprocation motion at the plate surface. The pins were held stationary in the plane of the plates and were constantly loaded by a cantilever beam with a calibrated lead weight. A choice of two gear sizes allowed for selection of a suitable CS ratio for the test components. The pins were rotated about their vertical axial by use of a rack and pinion drive [Figure 5-14]. The rack was mounted on the plate holder and drive was transferred to the test pin by a gear wheel mounted above the pin.



**Figure 5-14 A single station from a six station rack and pinion system of a PoP wear rig showing UHMWPE pin in contact with a CoCr plate**

In addition to the six wearing pins, three soak controls were used to counteract fluid absorption in the volume loss measurements. Both the pins and plates operated with flat-on-flat counterfaces with the pins having a small edge chamfer. The soak control pins were unloaded and remained in soak or in a controlled atmosphere for the duration of the test period.

Before starting a test the sample pins to be used were soaked in sterile water for a minimum of 14 days to allow for full water absorption. Frequency of the machine was checked and set at 1 Hz. The wear studies were run continuously for 4 days and approximately 300 000 cycles then stopped so that the samples could be cleaned and the wear assessed. A microbalance with accuracy of 1  $\mu\text{g}$  was used to weigh the pins after stabilising for 72 h in a controlled environment. Three soak control pins were used for all tests and any difference between the soak control weight and that of the wear pins was compensated. After gravimetric assessment and calculation of the distance travelled by the pin motion path, the wear rate and wear factor was computed [Equation 5-1], where  $V$  is volume loss,  $L$  is load and  $S$  is sliding distance. In addition, profile traces were taken from both the pins and plates (Talyor-Hobson, PGI800, UK). The study was then re-started for a further 300 000 cycles sequence continued for 3 weeks in total, equating to roughly 1 MC of sequential

testing. After each inspection, pins were re-mounted in the same station and orientation. The time between stopping the machine and re-starting was 3 days.

$$\text{(Wear factor) } K = \frac{V}{LS}$$

**Equation 5-1**

### *Surface profiling*

The pre-wear surface of the pins had a surface roughness period of 0.18 mm, which required a maximum cut-off value of 0.8 mm to be applied to the surface data. The plates did not show appreciable waviness and a cut-off value of 0.25 mm was used. These cut-off values corresponded to those used in the TDR profiling assessment and were therefore comparable.

Summary of PoP methods:

1. Stroke length of 20 mm to expose entire contact area (56 mm pinion)
2. Stroke length of 13.5 mm to give contact area overlap of 6.5 mm (38 mm pinion)
  - CS ratio = 0.03 for both tests
  - Test for ~1 MC (3 weeks)
  - Compare wear factor of these two identical CS ratio tests
  - Check surface profile for signs of re-attachment of wear debris

## **5.3 Results**

The fluid absorption rate for the three week (1 MC) test was 40 µg (long stroke) and 63 µg (short stroke) which was approximately 1.7 % and 1.8 % of the total wear value respectively. The wear rate was affected by one high wearing station throughout the study, shown in Figure 5-15 and Figure 5-16.

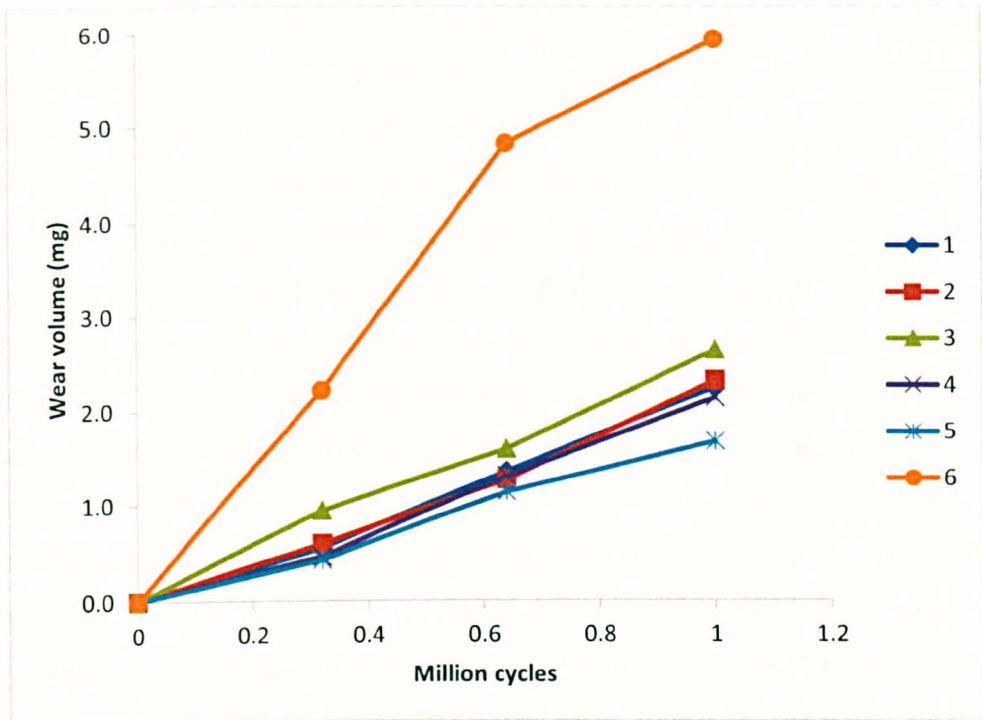


Figure 5-15 Long stroke study: per measurement time point wear removal from pins 1-6 showing the high wearing pin

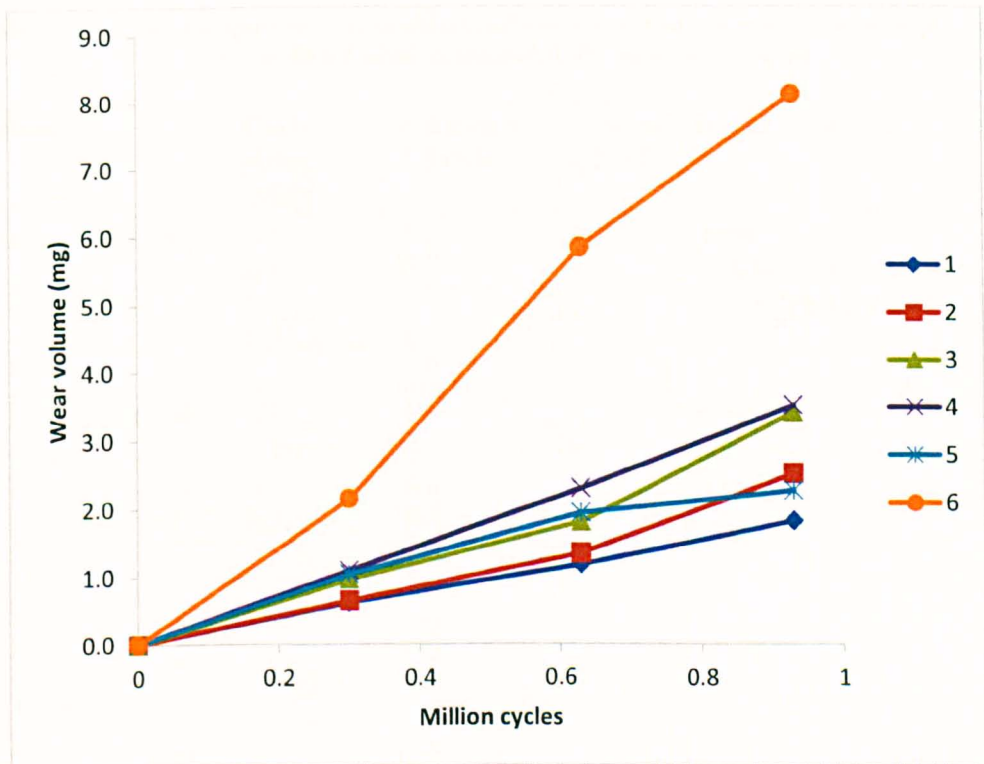


Figure 5-16 Short stroke study: per measurement time point wear volume removal from pins 1-6 showing the high wearing pin

From the individual wear rate plots, it was apparent that one station was consistently high wearing. In order to separate this station from the others, a quantitative method was used based on the amount of standard deviation from the mean wear rate. The mean wear  $\pm 2$  standard deviations (SD) was checked throughout the test period and station 6 wear rate exceeded these parameters twice [Table 5-5]. When a narrower range of acceptable values was used ( $\pm 1.5$  SD) it was clear that station 6 had a propensity to over wear for all measurement points bar one (0.9 MC of 20 mm stroke test). The reason for this is not clear from the record of simulator activity. Station 6 did not run dry of lubricant but other unfavourable issues such as low lubricant level were recorded. The design of the PoP equipment is such that the main drive motor sits beneath station 5 and 6 and this may have had a heating effect. Further investigation using SPSS statistical software (SPSS, IBM, USA) confirmed the presence of two outliers for the average wear factors over the full test; these are shown in the box plot of Figure 5-17. The wear results are therefore presented without station 6 data (i.e. n=5 only).

**Table 5-5 A check for spurious results obtained from test station pin wear – based on pin wear factor at each 1/3 MC compared to the mean wear factor**

<b>Study</b>	<b>Cycle point (MC)</b>	<b>&gt; mean <math>\pm</math> 1.5xSD</b>	<b>&gt; mean <math>\pm</math> 2xSD</b>	<b>Issues reported</b>
20 mm stroke	1/3	6		none
	2/3	6	6	ST6 lubricant very low
	1			ST5/6 lub very low
	Full cycle	6		N/A
13.5 mm stroke	1/3	6		none
	2/3	6	6	none
	1	6		none
	Full cycle	6		N/A

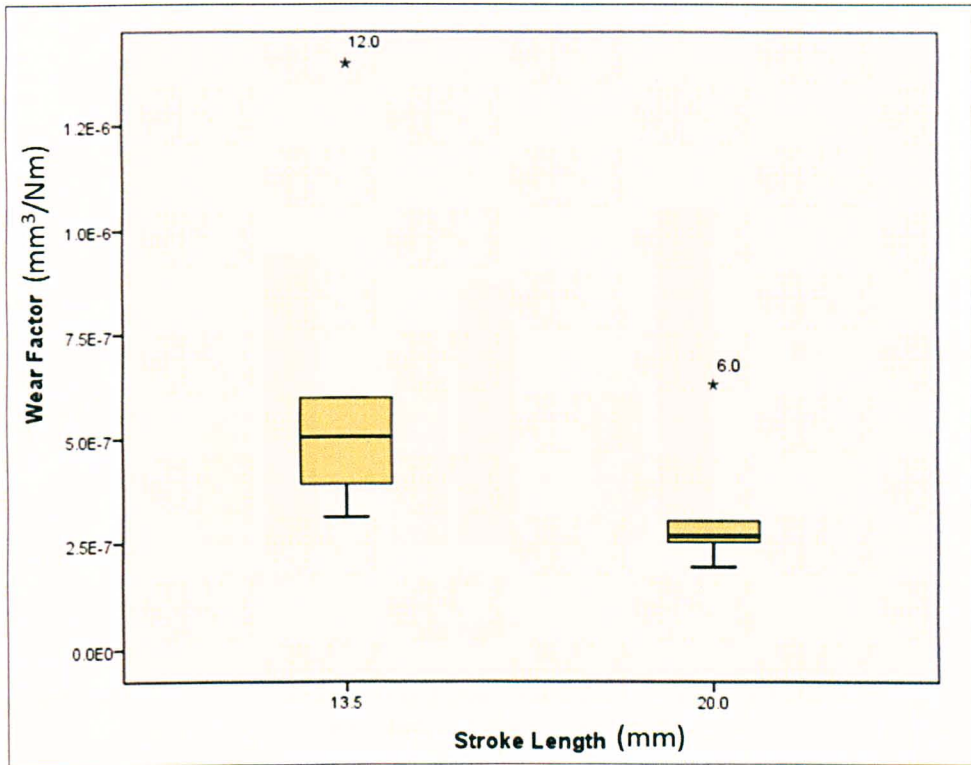


Figure 5-17 Box plot showing the average wear factor for both tests and the outliers (both pin number 6, \* indicates possible outlier in SPSS)

The average wear was  $2.4 \pm 0.4 \text{ mm}^3/\text{MC}$  and  $2.9 \pm 0.8 \text{ mm}^3/\text{MC}$  for the long and short stroke studies respectively. The wear rates were not statistically different (independent samples t test, equal variance assumed,  $p=0.22$ ). The wear factor for the long stroke study was  $2.5 \times 10^{-7} \text{ mm}^3/\text{Nm}$ , however, for the short stroke test of the same CS value this value was  $4.5 \times 10^{-7} \text{ mm}^3/\text{Nm}$  due mainly to the reduced sliding distance which altered the result of Equation 5-1. The wear factors were statistically different ( $p=0.017$ ). Every 300 000 cycle point the wear factor data was steady state [Figure 5-18] demonstrating no appreciable bedding-in wear.

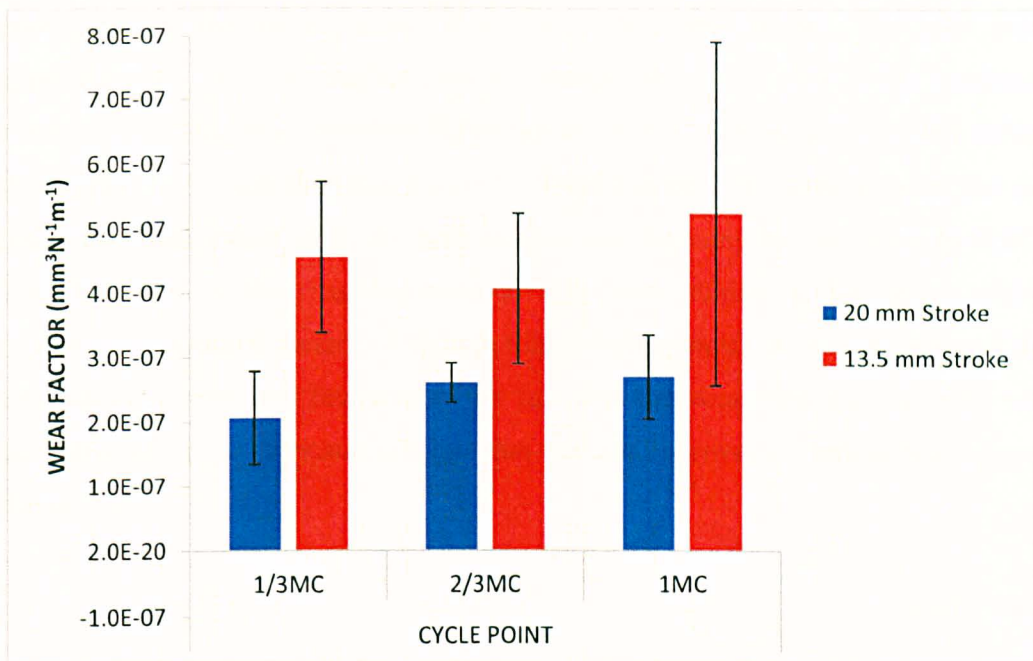


Figure 5-18 Per million cycle point wear factor values as an average (n=5) for a 20 mm stroke length and 13.5 mm stroke length

The wear factor for the short stroke test increased to 181 % of the initial long stroke value [Table 5-6]. In comparison, the spine simulator Prodisc studies showed an increase in wear factor to 112% of baseline between ISO and half FE input cycles. The wear factor calculation for the spine simulator was done by averaging the loading cycle of 600-2000 N to 1300 N.

Table 5-6 Comparison of spine simulator and PoP wear values and wear factors (HF: half FE, LS: long stroke, SS: short stroke)

PRODISC SPINE SIMULATION Measurement	PRODISC SPINE SIMULATION			PoP TEST	
	ISO	HF		LS	SS
Wear rate (per MC)	16.1	11.7		2.4	2.9
% of baseline wear	100%	73%		100%	122%
Ave path distance (mm)*	4.9	3.2		40.0	27.0
average load (N)	1300	1300		240	240
wear factor (mm³/Nm)	2.4E-06	2.6E-06		2.5E-07	4.5E-07
% of ISO wear factor	100%	112%		100%	181%

\* Calculated by Dr Feng Lui, University of Leeds

### Surface profile data

In addition to gravimetric data, surface profile analysis provided additional detail as to the tribological performance. For both studies the pins and plates were finished to



approximately the same values of  $R_a$  (at 0 MC data point). The pins were approximately 100-fold rougher than the plates, which was due to the machined surface of the pins and a polished (lapped) plate surface. Before and after test values (0 MC and 1 MC) are shown in Figure 5-19 and Figure 5-20. It can be seen that the initial and final values of  $R_a$  for both studies was the same for the plates ( $p < 0.01$ ). The  $R_a$  values of the pins decreased as they were subject to burnishing which resulted in a polished surface. Although this polishing would be advantageous if the lubrication regime was favourable, the fact that the wear rate did not alter was indicative of a poor lubrication regime that was not improved by further polishing of the samples.

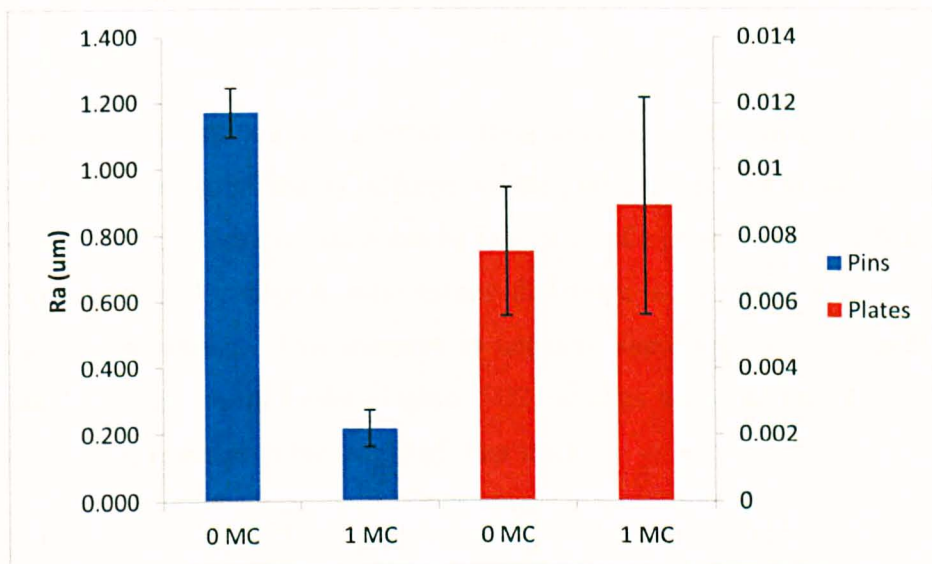


**Figure 5-19 Long stroke: Average roughness for the pins and plates before and after testing to approximately 1 MC showing no change for the plates but a polishing of the pins**

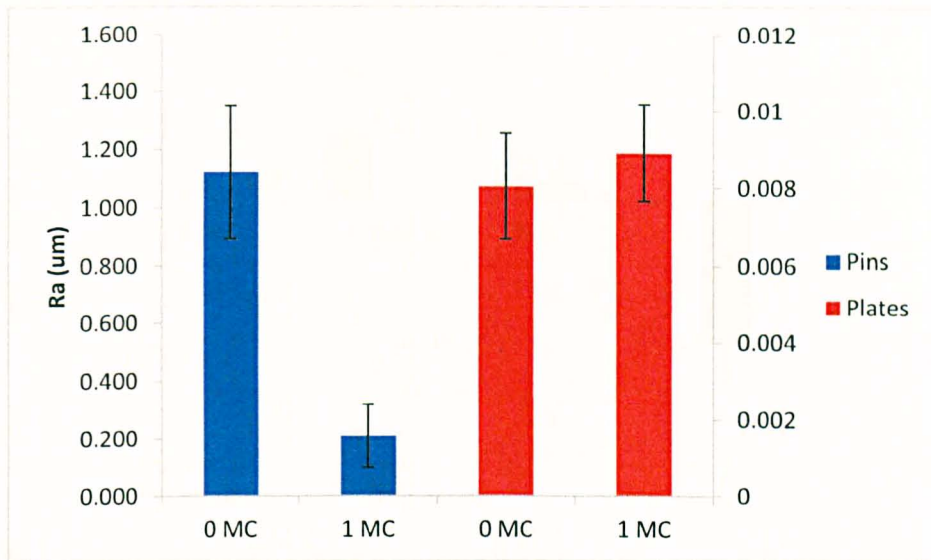


**Figure 5-20 Short stroke: Average roughness for the pins and plates before and after testing to approximately 1 MC showing no change for the plates but a polishing of the pins**

The pins and plates started with a positive roughness skew value ( $R_{sk}$ ). At the end of testing this was not significantly different for the pins but was significantly lower for the plates ( $p < 0.05$ ). Negative skew can be indicative of a good bearing surface, since the increase in valley-to-peak ratio means that there is increased ability to keep lubricant at the surface. This increase in negative skew happened for both long [Figure 5-21] and short stroke [Figure 5-22] studies and was therefore a wear phenomenon not related to the length of wear track.

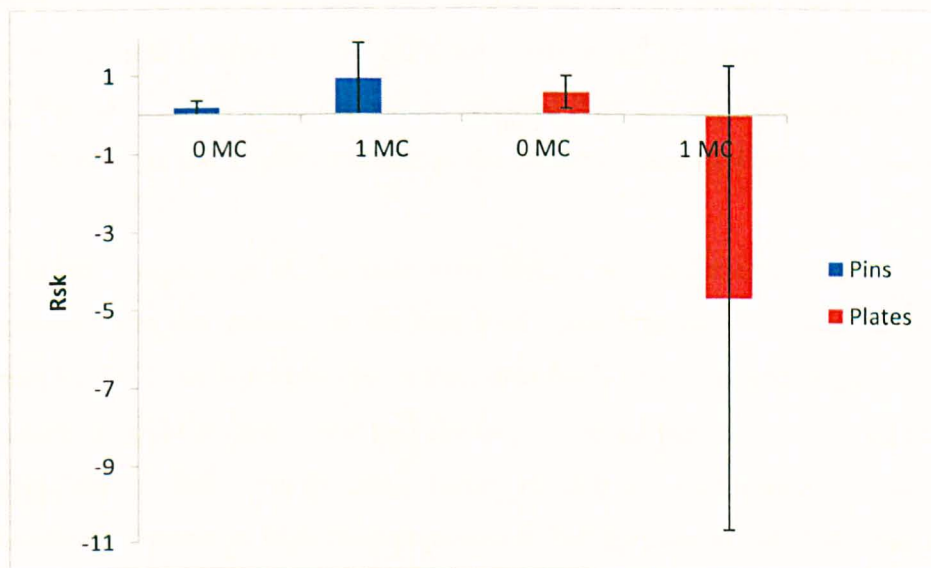


**Figure 5-21 Long stroke: Average skewness for the pins and plates before and after testing**

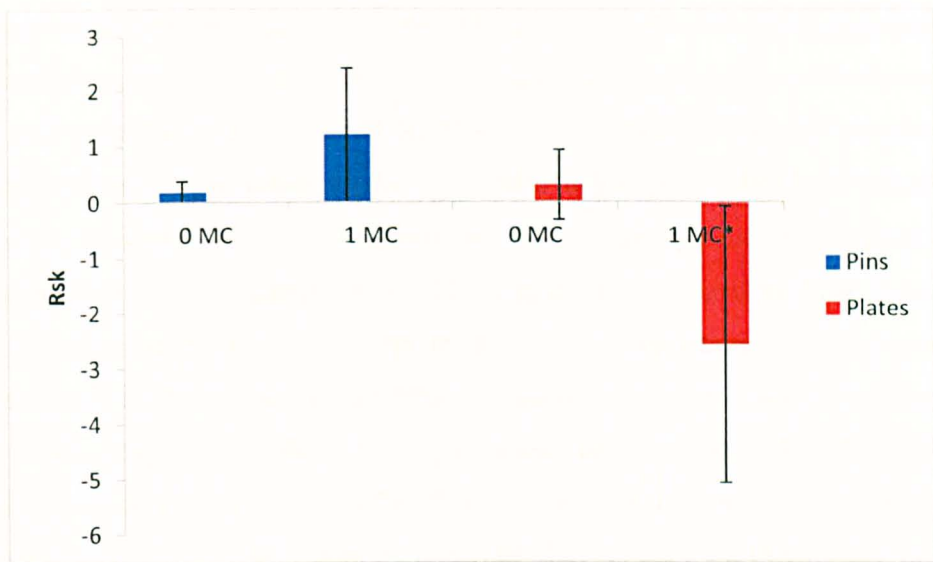


Figure 5-22 Short stroke: Average skewness for the pins and plates before and after testing (\*an outlier value was found and deleted from the skew analysis for the plates 1 MC data set)

## 5.4 Discussion

### 5.4.1 TDR Surface Contact Pressure

Pressure sensitive film has been used as a contact area and contact pressure study tool for both hips (C. Brockett [189]) and knees (Zdero et al. [190]) with reasonable success, although both authors urged caution with regard to sensitivity of film used and the potential effect on contact clearance. MoP hips have been reported to experience contact pressures of approximately 3-6 MPa [191] or perhaps as high as 20 MPa [192] (although this may have been a contact mechanics calculation on an unworn hip) and between 15-50 MPa for conforming and non-conforming knees [193]. For the 2000 N load, the values reported here are approximately two times that for MoP hips and slightly lower than the minimum reported for MoP knees.

The surface roughening at the pole area (debris re-attachment) of the PE TDR components was not present in the half load spine simulator studies (reported in Section 3.3.2). Total hip replacement tests also don't report roughening in this way. Therefore, it could be postulated that the larger contact pressures observed in TDR bearings are a major contributing factor to debris re-attachment. Total knee replacements experience high contact pressures, but they are of very low conforming design and therefore are perhaps not directly comparable to TDR.

A theoretical Hertzian study of Lumbar TDRs by Wenzel et al. [194] suggested that contact pressures between 3-6 MPa were expected for clearances of between 0.05 and 0.15 mm for a load of 1500 N. However, the authors did not validate their results with any experimental evidence, nor did they explore other load magnitudes. A further drawback was that Wenzel et al. did not consider the implications of the reversed bearing combination of the TDRs studied (compared to THR) and how this affects contact behaviour. The results of the experimental contact analysis performed here show that the distribution of surface pressure is not Hertzian, and in fact is plug shaped. At 1500 N the experimental pressures were 7 and 10 MPa for the Prodisc and Charité respectively. This is approximately double that predicted by Wenzel et al. [194]. The results demonstrate that reliance on theoretical values is unwise. Also of interest is the wide contact width predicted by Hertzian analysis. In practice this means that the pressure is amplified in the outer regions (and attenuated at the centre) and hence the Hertzian distribution of pressure is incorrect for this type of TDR analysis.

#### **5.4.2 PoP Experiment**

The use of reciprocating multi-directional PoP testing is often used as a pre-cursor to more complex simulator studies. This experiment compared the wear behaviour of long and short stroke motions while keeping the CS ratio constant. It was postulated that the overlapping motion of the short stroke experiment would highlight the effect of decreased motion paths on the wear characteristics in terms of debris entrapment and lubrication changes. In the TDR ISO-based studies there was a trend towards a build-up of debris and consequent roughening of the pole area of the PE domes [Sec 3.3.2]. Evidence for this came from the significant increase in height at the poles and the evidence that ink could penetrate the roughened material. In order to assess what parameters caused this, the long versus short stroke (overlapping) PoP test was devised. The original postulation was that the short stroke set-up would be favourable to debris entrapment. However, no evidence of this was found in terms re-attachment of debris. However, both the spine simulation and PoP experiments showed an increase in wear factor for a reduced sliding distance test.

A previous PoP study by Kang et al. [124] contained details of a constant CS comparison between two UHMWPE PoP studies using 8 mm diameter pins with

two stroke lengths of 20 mm and 12 mm. However, the test did not involve overlap between the bearing surface slide tracks, due to the small diameter pins used, and therefore is not an ideal comparison with the present test for debris entrapment or lubricant starvation (nor was it intended to be so). But when this data is plotted next to the wear factors found here [Figure 5-23], the wear factors also demonstrate that shorter stroke lengths can create larger wear factors, although the difference between Kang et al.'s 12 mm (Kang20) and 20 mm data (Kang20) was not statistically significant. The wear factors for the PoP studies are comparable to literature, however, the spine simulator wear factors were higher than equivalent non-cross linked hip wear from both simulation and explants [192, 195, 196].

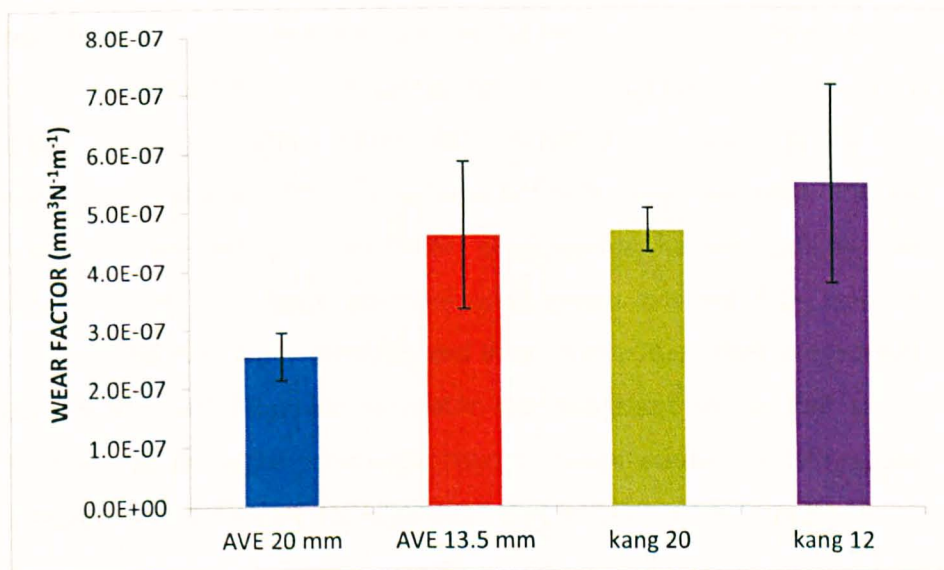


**Figure 5-23 Results of 20 mm long stroke and 13.5 mm short stroke compared to a study by Kang et al: Kang20 = 20 mm stroke length and Kang12 = 12 mm stroke length (note Kang et al used 8 mm diameter pins and 3.18 MPa contact stress)**

The 20 mm long stroke study had the same 1 Hz frequency as the short stroke test therefore an increased speed was necessary to cover the greater distance in the same time period. This would have two potential effects: 1) the lubrication may be improved by the increased entrainment velocity 2) the rate of frictional heating could be higher. The increase in wear factor for the short stroke PoP test suggests that the lubrication regime becomes less favourable due the slower reciprocation speed and the perhaps because of the overlapping bearing contact patch.

It is known that a cyclically loaded wear test will exhibit a higher wear factor than a statically loaded one [161]. Future investigators should consider using a PoP test using a higher baseline CS ratio (~0.2 would be equivalent to the spine simulator ISO study), shorter strokes and cyclical loading of the bearings. Such a study may be able to differentiate between the parameters that instigate debris re-attachment and the associated roughening of the polyethylene bearing surfaces.

### **5.4.3 Summary**

This series of experiments has shown that decreased entrainment velocity and wear scar area overlap depletes the lubrication regime quality and increases the wear factor substantially. In comparison, the spine simulator study (½ FE ISO based motion, Section 3.3.1.3) demonstrated only a small increase in wear factor. In that test it was probable that the lubrication regime was already at a poor level and so a reduction in bearing surface motion did not reduce the quality of the lubrication regime greatly and hence the wear volume fell rather than increased. The PoP study presented in this section provides further confirmation that the resultant wear factor is an output from a complex bio-tribological system controlled by many different (and often unknown) input variables and their interactions. Both polyethylene wear factors for the half FE spine simulator test and short stroke PoP studies have implications for the input parameters used in computational modelling, and offers some insight into the reason for high wear seen in TDR *in vitro* studies compared to MoP hip studies.

The contact pressures measured were approximately double that expected in MoP THR. The half load TDR tests showed much reduced debris re-attachment at the poles. Therefore, it is postulated that high contact pressures in TDR are a contributory cause of debris re-attachment and roughening on the PE components.

## 6 Frictional Characteristics of TDR

### 6.1 Introduction

To date, little data on the frictional characteristics of MoP TDRs is available. It is reasonably clear what loads can be expected *in vivo* [1], but the level of protein concentration in the lubricating fluid is unknown. There could be a complete lack of any synovial-type fluid and the bearing may be only wetted by interstitial fluids of unknown viscosity. Further to this, the values of rotational velocity and frequency of operation will probably encompass a wide range of values. The behaviour of THR has been extensively studied and forms a body of knowledge that helps to explain some tribological behaviour and highlight differences between designs. Total disc replacements often share similar materials and dimensions to THRs, however, the bearing materials are reversed (PoM rather than MoP) and unexpected wear phenomena such as edge-loading and debris re-attachment [Sec 3.3.2] have highlighted the differences between TDR and THR tribology. It is also difficult to predict the effect that unconstrained TDR bearings will have on frictional torques. In addition, the replacement of a natural-tissue (visco-elastic) IVD with an artificial (articulating) TDR replacement is a fundamental change in design rationale when compared to hip and knee replacement theory.

Frictional properties of articulating joint replacements are an important indicator of tribological performance. Since it is difficult to predict precisely what operational envelope TDRs *in vivo* are subject to, it was necessary to design an investigational study of both friction and lubrication. The studies were based on the standard ISO input and used parametric changes to the testing inputs to assess the effect of load, lubricant dilution, velocity and frequency. Data in the form of frictional torques and friction factors was processed and interpreted in context to other TJRs and the effects that these parameters may have *in vivo*.

### 6.2 Methods

TDR components were investigated for their frictional properties by use of a single station pendulum friction simulator (Simulation Solutions Ltd, Manchester, UK),

capable of applying axial loading (both static and dynamic) to 3 kN maximum and FE of  $\pm 30^\circ$  maximum. Computer control allowed the use of a selection of input kinetics based around those used on the spine simulator but without the LB and AR inputs. The friction carriage is mounted on hydrostatic bearings which produce two orders of magnitude less friction than that typically being measured, therefore the frictional torque of the bearing under test can be calculated ignoring the friction of the supporting carriage. By measuring the force on the piezoelectric transducer, the frictional torque and hence friction factor can be calculated [Figure 6-1].

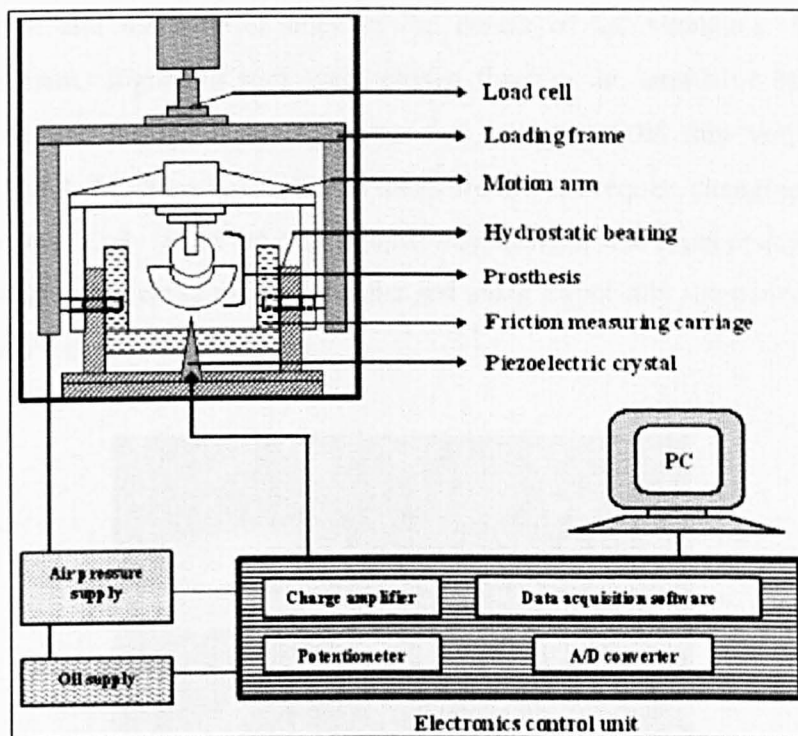


Figure 6-1 Friction simulator schematic showing set-up of MoP hip control [197]

### 6.2.1 Component Alignment

Alignment of CoR in friction simulation is of paramount importance as slight misalignment of components can introduce error to the torque transducer measurement (explanatory details in Appendix D). Custom designed holders were used to mount both Prodisc and Charité TDRs. This was achieved by using a screw-in inferior holder that could be attached to either of two holders designed for the separate CoRs of the TDRs under investigation (technical drawings of equipment used are in Appendix E). The TDR inferior and superior components were cemented into



cylindrical moulds that exactly fitted the new holder design and were mounted anatomically [Figure 6-2]. An open bath for the lubricant was attached to the inferior holder by an interference fit using an o-ring seal. This allowed serum to surround the components when positioned for test. The exact positioning of the components was done using dial and slip gauges to set the height of the components. The fixture base contained a grub screw that allowed small incremental movement of the TDR endplates until the correct height (and hence CoR) was reached. Two transverse and diametrically opposite grub screws were then used to clamp the TDR fixture cement to prevent rotation. The superior cup components were attached to the pendulum loading arm and the inferior ones in the centre of the simulator. Before test commencement, alignment rods were passed through the simulator bearings and would not pass through if the CoR was not within  $\pm 0.05$  mm vertically. The lubricant bath held 150 ml of fluid and therefore did not require changing after each parametric test. Only when the disc sample was changed was it necessary to replace the serum. The Prodisc samples were changed using a specially sharpened spatula to unlock the PE dome from the base.

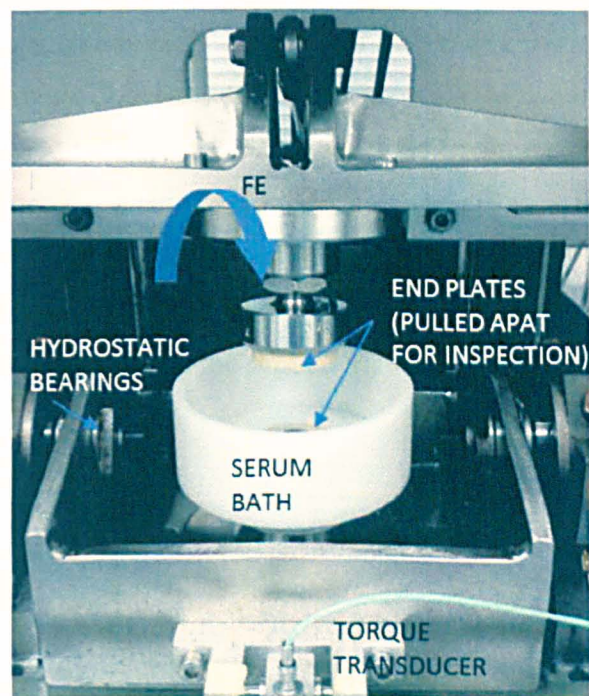


Figure 6-2 Charité endplates mounted in cement and the bath used to contain the lubricant

## 6.2.2 Input Kinetics

All kinematic inputs were based on a sinusoidal waveform; either the ISO hip input or the ISO TDR cycle. Frequencies between 0.5 and 2 Hz were used throughout. The loading waveform was either a single peak waveform as used in hip experiments, a double peak TDR waveform, or a constant load. FE and axial load were applied at the pendulum. Test cycles were completed in forward and reverse directions and the average results of these were used to cancel out error effects due to possible offset axial loading [Appendix D]. During forward or reverse cycle inputs, the frictional torques read by the load transducer were used to calculate the true frictional torque [Equation 6-1], where  $T_f$  and  $T_r$  are the forward and reverse torque values of the loading phase and  $T_t$  is the calculated true torque.

$$T_t = \frac{(T_f - T_r)}{2}$$

**Equation 6-1**

Axial load ( $W$ ) and radius of bearing ( $R_f$ ) were used to calculate friction factor ( $f$ ) from torque ( $T_t$ ) as shown in Equation 6-2. For the Prodisc device  $R_f$  was simply the radius of the bearing (14.5 mm), however, the Charité sample has two bearing surfaces of 13 mm radius. Since the bearing was set-up to match the spine simulator (i.e. with the CoR at the mobile bearing centre) the distance from the CoR to the bearing surface was half the height of the bearing (3.75 mm). This value of radius was used in the friction factor calculation as it most closely approximated the true moment arm (radius) over which the surface frictional force ( $F$ ) was applied.

$$f = \frac{T_t}{R_f W}$$

**Equation 6-2**

For both devices the constant load tests were not done in sequence but rather were applied in a pseudo-random order to avoid bias caused by the preceding test [Table 6-1]. Tests using ISO hip inputs were scaled from  $\pm 25^\circ$  to  $\pm 10^\circ$  so that impingement was avoided. Friction tests based on the ISO standard used input data identical to the

ISO standard except LB and AR were excluded. The constant load experiments used FE inputs of  $\pm 4.5^\circ$  which is  $\pm$  half of the full  $9^\circ$  FE used in the TDR ISO standard.

**Table 6-1 Order of application of constant load tests in order to limit the influence of one test affecting another**

Load (N)	500	1000	1500	2000	2500	2750/3000
Test order	2	4	1	6	5	3

Experiments using varying angular velocities were conducted by calculating slew rate of the bearing couple (slew rate = rate of change of waveform) where the FE reading crossed the x-axis. The formula that describes the input waveform is shown in Equation 6-3, where A is amplitude of wave,  $\omega$  is angular velocity ( $2\pi f$ , where f is frequency), t is time and  $f(\omega t)$  is the wave function. In order to find the velocity of the wave (gradient) it is necessary to take the differential of the function and set  $\omega t$  equal to  $\pi$  (where the wave crosses the x-axis at  $180^\circ$ ). Equation 6-4 is the differential of the wave. Equation 6-5 shows the slew rate formula (SL) after the angle of interest is set to  $\pi$ . An example calculation is shown in Equation 6-6 for a Prodisc bearing for an input angle of  $10^\circ$  at 1 Hz (where  $10^\circ$  is 0.175 radians, f is 1 Hz, bearing radius is 14.5 mm). This method of velocity calculation is more accurate than velocity taken as the average speed of the rotation (e.g.  $10^\circ$  per second).

$$f(\omega t) = A \sin \omega t$$

**Equation 6-3**

$$\frac{d}{dx} f(\omega t) = A \omega \cos \omega t$$

**Equation 6-4**

$$|SL| = A \omega$$

**Equation 6-5**

$$|SL| = 0.175 \times 2\pi \times 1 \times 14.5 = 15.9 \text{ mm/s (where } 10^\circ \text{ is 0.175 radians, f is 1 Hz, bearing radius is 14.5 mm)}$$

**Equation 6-6**

### 6.2.3 Output Data

Data was logged for three cycles every 30 with 256 data points per cycle. An example of the position of the values of  $f$  taken from the friction results is shown in Figure 6-3 for a forward-cycle TDR ISO input. The experiments were usually 95 cycles in length and the data from the 91<sup>st</sup>-93<sup>rd</sup> cycle was averaged in order to reduce erratic values. A previous study using the Leeds friction simulator also found that 90-120 cycles was sufficient for steady state results [189]. In addition, the friction results were taken from an average of 10 data points where the FE motion plot crossed the x-axis. This was repeated for three samples using forward and reverse simulation data and the mean and standard deviation reported. All tests were performed at room temperature in 150 ml of lubricant, except the MoP hip which used ~1 ml in an inverted cup (non-anatomical). There was one MoP hip control sample.

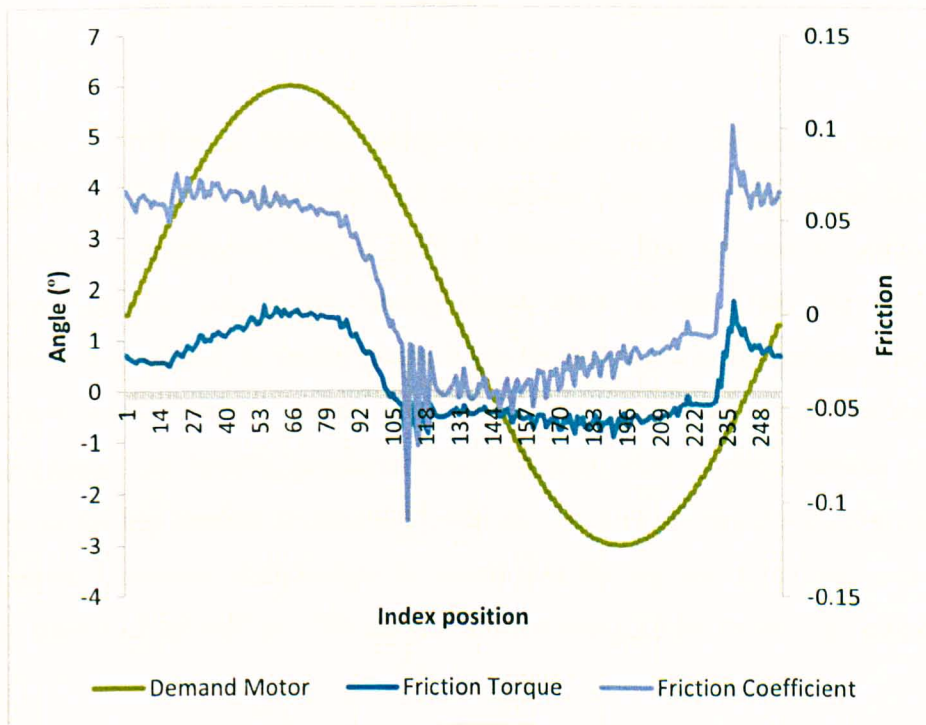


Figure 6-3 Typical friction simulator output – example shows TDR ISO waveform (Demand Motor = FE)

## 6.2.4 Control Sample

In order to verify that the friction simulator was functioning correctly, a standard control test was used before each experiment. Table 6-2 details the results of a single MoP hip tested over one day with cold oil, warm oil and for different periods of time. These tests used a single MoP THR operating with a standard hip input with 2 KN peak load and 100 N swing-phase load and frequency 1 Hz. Bovine serum diluted to 25 % was used for all testing. A minimum warm-up period was used (30 min) though there was no discernible difference between operating the machine with cold oil or warm.

**Table 6-2 MoP control hip friction factor displayed in relation to oil warmth and period of data point selection (90 seconds or 5 minutes)**

Data point	Cold oil		Warm oil	
	0 min	30 min	4 Hr	6 Hr
90 s	0.057	0.063	0.062	0.053
300 s	0.061	0.063	0.064	0.059

To assess the difference between using the hip input on a THR and the same input on a TDR the Prodisc was tested with an identical (but scaled) hip input, followed by a constant (maximum) load of 2000 N. This was done in order to observe the effect of constant load versus 'swing phase' load on the TDR. Hip and knee prostheses are subject to swing phase loads of much lower magnitude than their maximum loads. Contrary to this, the TDR ISO standard does not have a low load swing phase. The Prodisc produced lower friction when under a similar loading regime to the hip implant [Figure 6-4], and this friction increased with the constant load input. However, it should be noted that the hip input motions had to be scaled from  $\pm 25^\circ$  to  $\pm 10^\circ$  as TDR devices are not designed for these large flexions.

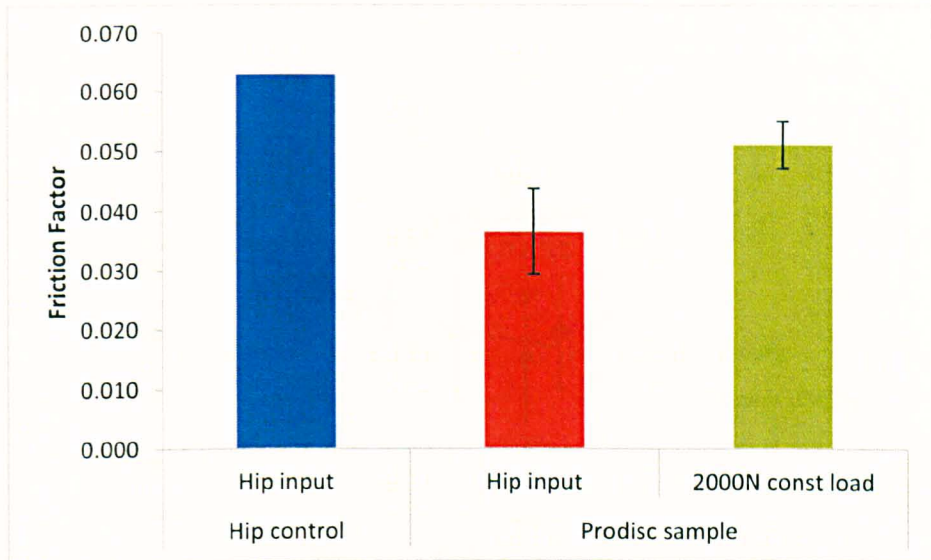


Figure 6-4 Hip control subject to hip input compared to Prodisc samples under hip input and constant load

### 6.3 Results

#### 6.3.1 Applied Load

The constant load friction factor findings for Prodisc and Charité are summarised in Figure 6-5 and Figure 6-6 respectively. The power-law relationship between friction and load is clear. The power index for the Prodisc power-law regression was lower than the Charité (-0.284 versus -0.987). Frictional torque varied from 0.6–2.4 Nm for Prodisc and 2.0–2.7 Nm for Charité [Table 6-3]. The friction factors ranged from 0.051 (2500 N) to 0.087 (500 N). The torque values for the Charité were approximately two-fold larger than the Prodisc. It may be of note that if the radius of the bearing was increased from 3.75 mm (half disc core height) to 7.5 mm (full height), the torques based on Equation 6-2 would be comparable.

Table 6-3 Frictional torque for constant load inputs, Prodisc and Charité

Axial Load (N)	500	1000	1500	2000	2500	2750	3000
Prodisc (Nm)	0.6	1.1	1.5	1.7	1.8	2.4	N/A
Charité (Nm)	2.2	2.0	2.0	2.6	2.7	N/A	2.0

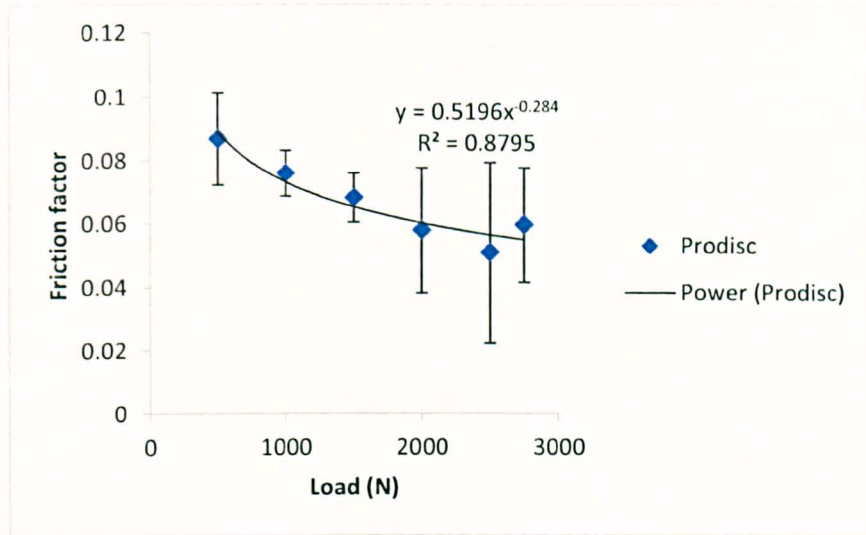


Figure 6-5 Prodisc: varying static load from 500 N – 2750 N

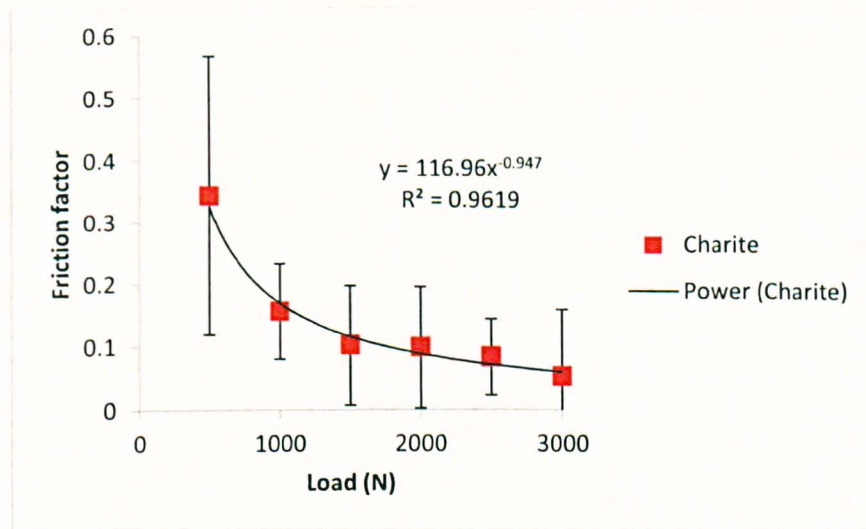


Figure 6-6 Charité: varying static load from 500 N – 3000 N

### 6.3.2 Rotational Velocity

The ISO standard, ASTM guide and *in vivo* kinematics are all lower than those used in THR and TKR testing. In order to assess the impact of small angle motions and hence slow angular velocity (i.e. slew rate) at the bearing surface, input conditions from  $\pm 2^\circ$ ,  $\pm 5^\circ$  and  $\pm 10^\circ$  at 1 Hz and  $\pm 10^\circ$  at 2 Hz were used to create different velocities, combined with a constant 1500 N axial load. Figure 6-7 and Figure 6-8 show varying velocity results for Prodisc and Charité respectively. Regression

analysis with linear and power trend lines gave  $R^2 \ll 0.1$  for the Prodisc, the Charité gave  $R^2$  of 0.93-0.94 for linear and power low relationships. However, the simulator results for the Charité should be treated with caution because of the following problems with testing an unconstrained TDR:

- the FE motion induces an AP-ML coupled motion due to inertial effects; this may have impacted on the load transducer used to measure torque;
- the radius  $R_f$  used for the calculation of friction was not based on the radius of the bearing but on the distance from the bearing surface to the CoR;
- the change in velocity came from altering the angle and frequency therefore there was a possible multi-factorial effect;
- the variance was very high for the unconstrained bearing because of its instability in the testing machine.

There was no trend between friction and rotational velocity. The slight increase seen in Figure 6-8 may be an artefact of the higher error loads on the torque transducer. High friction and frictional torque for the Charité could be attributed to the radius of moment arm used for the frictional torque calculation, or perhaps because of the two-sided bearing creating higher frictional forces.

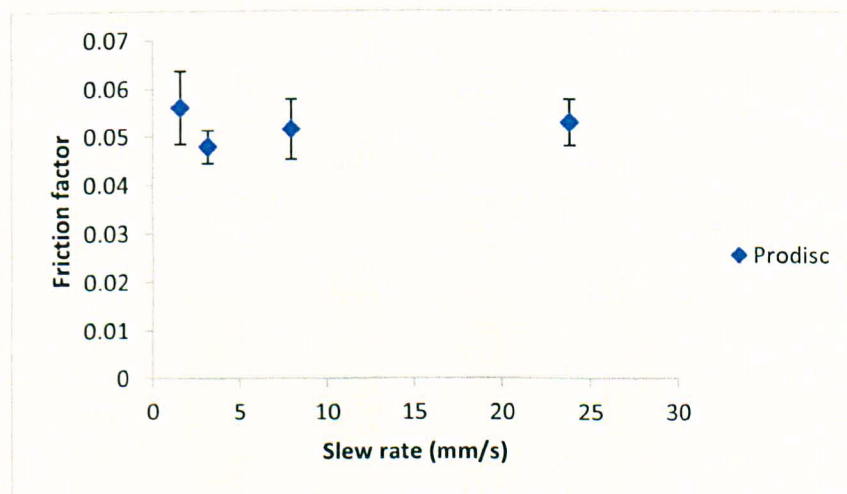


Figure 6-7 Prodisc TDR under varying bearing surface velocities (slew rate)



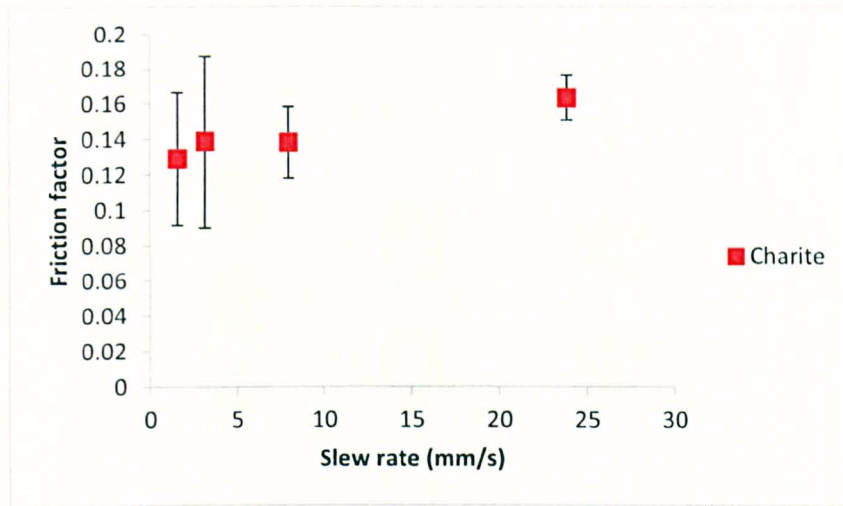


Figure 6-8 Charité TDR under varying bearing-surface velocity (slew rate)

### 6.3.3 Serum Concentration and Input Frequency

All tests for serum concentration effect were done using the Prodisc design as this was most stable in the friction simulator. No significant difference was observed between serum concentrations from 0–100 % ( $p=0.9$ ) [Figure 6-9]. There appeared to be a slight linear trend but this was also not significant (Pearson’s linear correlation,  $p=0.17$ ). The variability of the frequency of the friction simulator was limited by design to 1-2 Hz. No trend or significant difference was found for these results [Figure 6-10].

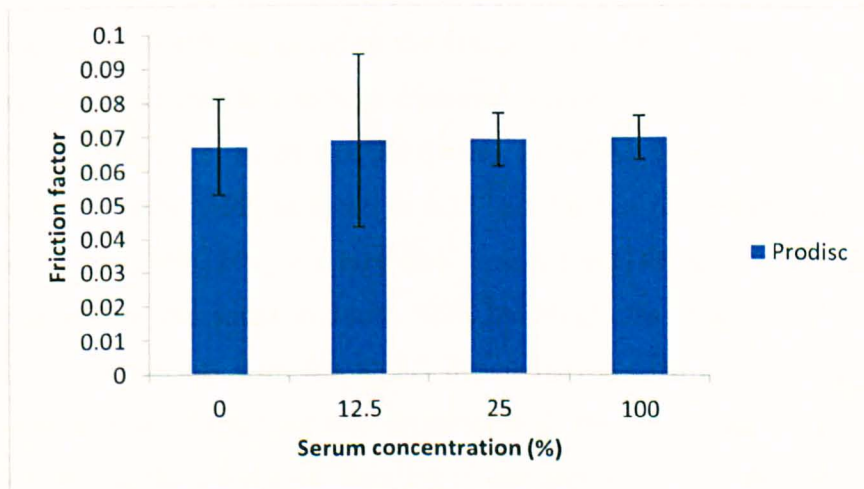


Figure 6-9 Prodisc: varying serum concentration

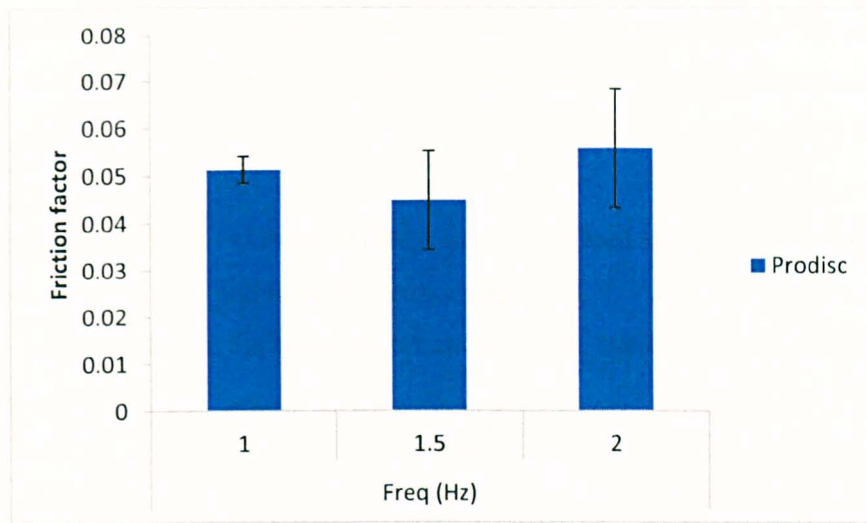


Figure 6-10 Prodisc – ISO 18192-1 input at 1, 1.5, and 2 Hz

#### 6.4 Discussion (Friction Studies)

The MoP TDR frictional torque results show that typical torque developed was ~1.5 Nm (1500 N axial load, Prodisc). This is below the torque developed in the natural IVD per 1° flexion (1.8 Nm/° [198], 1.7 Nm/° [199]). The rotational torque in THR used to be a concern since it was known that the static torque required to loosen a well cemented cup was ~100 Nm [200]. No reports exist in the literature regarding TDR implants that have been pulled out in a similar way. A lumbar spine arthroplasty is under constant compression load which should help stabilise it even in the presence of a sagittal torque, also, the rotational torques found in the *in vitro* study were much lower compared to the 100 Nm hip value. However, the cervical spine may be more sensitive to high frictional torques, especially those associated with MoM bearings. For MoM hips the friction factor and frictional torque is known to be higher than for MoP, as much as 0.12 and 3.6 Nm respectively for a 28 mm (14 mm radius) THR [201] – a size also typical for TDR bearings. High friction factors have been measured in MoM TDR by Moghadas et al. [202] who found friction factors ranging from 0.9 to 3.5 depending on load and bearing diameter (small diameter and high load was greatest) with the maximum frictional torque being 9.5 Nm for the worst case. Bending torque required to flex the natural lumbar IVD per degree has been measured to be 1.8/2.6 Nm/° for flexion and extension [198]. Therefore 9.5 Nm corresponds to the flexural torque at around 5° in the

natural disc. This suggests that the torque induced resistance of the MoM disc to rotation could be of issue *in vivo*, especially for small-angle everyday flexions such as walking.

In the present study the decrease in  $f$  with increasing load is typical of dry friction in polymers. Friction was found to be proportional to  $L^{-0.28}$  and  $L^{-0.95}$  for Prodisc and Charité respectively. In the familiar Amanton's law, where  $\mu$  and  $f$  are essentially identical:

$$F = \mu L$$

However it is known for purely elastic contact between surfaces that are either 1) a perfect spherical asperity or 2) all asperities squashed flat into a single area of contact, that:

$$F \propto L^\phi \text{ where } \phi = \frac{2}{3} \text{ and hence } f \propto L^{-1/3} [203]$$

The value of -0.28 is close to -0.033 and this suggests that the Prodisc may have been in state (2) above. This would mean that most of the surface irregularities were flat when under load. Hall et al. [204] and Weightman et al. [205] reported values of  $\phi$  of -0.232 and -0.17 for unlubricated MoP hips, however Hall et al. also found  $\phi = -0.898$  for lubricated MoP hips which is equivalent to that found for the Charité here (-0.95) however, the simulator performance with the mobile bearing was not ideal and therefore the Charité results should be treated with caution.

With all the friction data it needs to be noted that the behaviour of a ball-in-socket MoP bearing may not approximate to the existing friction formula due to other effects such as boundary protein lubrication, edge loading and changes in conformity. Boundary or mixed lubrication will exhibit complex load-friction relationships depending on the amount of 'break through' asperities involved in surface shear forces. The erratic and high friction seen in the Charité results may be indicative of the stick-slip type motion reported by O'Leary et al. [165] [discussed in Sec 3.4.2].

For Amanton's Law, it is also known that loading-dependant asperity distribution takes effect [203], i.e. the asperities exhibit full plastic flow and therefore adhesive wear predominates. The wear mechanisms of MoP TJRs are very frequently reported as showing signs of 'adhesive/abrasive wear' without further explanation. A hard rough surface articulating on a softer surface is usually expected to show abrasive wear, however, for high surface stress situations in TJR MoP bearings, it is probable that adhesion between surfaces occurs. This plasticity induced effect is responsible for the reorientation of polymer chains in PE bearings [206]. The combination of plastic flow parallel to the surface plus the elastic-like behaviour perpendicular to the surface may be the character of wear and friction generation in TDR.

The fact that the friction was not changed by increasing surface rotational velocity (and hence Sommerfeld number) suggests that the bearings were in a state of boundary lubrication; although the breadth of Sommerfeld number covered was very small and so this is not by any means conclusive. Boundary lubrication has been proposed as the most probable regime in MoP hips [201] (and all hip bearing material combinations except CoC and CoM). Unsworth et al. predicted mixed lubrication as the operating regime [207], however, they used synthetic serum (carboxy-methyl-cellulose) and this may not behave as bovine serum or synovial fluid. The friction factor appeared to increase slightly with increasing serum concentration but this trend was not significant. The same trend has also been noted in MoP THRs [201], again without significance. Brockett et al. [201] found that only hard-on-hard THR bearing combinations are influenced to any great degree by serum concentration.

#### **6.4.1 Summary**

Friction factor was found to be proportional to load raised to an index of -0.28 which suggests an elastic contact at the bearing surfaces. The reduction in  $f$  with respect to load was similar to behaviours observed in the literature in MoP hips. Rotational torque is probably not a clinical concern in terms of resistance to motion or reaction torques at the endplate-TDR interface. However, the torque-displacement characteristics are very different from the natural IVD and this may have undesirable effects. Friction was not found to be greatly influenced by serum concentration or

rotational velocity, suggesting that the TDRs under test operated in the boundary lubrication regime. Other authors have observed very high friction in MoM TDRs, but have interpreted the plotted results as demonstrating a mixed lubrication regime [202]. This is probably incorrect and MoM TDRs should be investigated further in this regard.

### *Limitations*

The friction simulator was initially designed for hip replacement testing and therefore large FE motions are more typically used. The TDR bearings had a maximum RoM much less than this. The maximum safe RoM used in the studies was  $\pm 10^\circ$  and in order to replicate ISO motions this was reduced to  $\pm 4.5^\circ$ . At motions below  $\pm 10^\circ$  the behaviour of the apparatus was less reliable. The performance of the air cylinder applying axial load was also not ideal. This device usually applies a 1 Hz half-sinusoidal load (for THR test) and was incapable of applying a reliable 2 Hz TDR ISO standard load without deformation of the cycle. Instability of the Charité design may have corrupted the results. In addition, it is not clear what value of bearing radius should be used for the friction calculations.

## 6.5 Computation of Lubrication Regimes

### 6.5.1 Introduction

To aid the understanding of the lubrication regime and hence the wear characteristics of the TDR devices under test, a computational model was developed to graphically depict a range of lubrication outcomes (known as  $\lambda$  values) as a function of clearance and FE velocity. Clearance is the radial gap between the articulating bearing surfaces of the device. FE velocity is the angular velocity of the bearing surfaces relative to each other. During *in vitro* testing the lubrication regime is difficult to ascertain and can only be inferred from surface evidence gained from the implant bearing topography. This evidence is apparent in, for example, hip replacement hard-on-hard bearings as polishing and low wear. For metal-on-UHMWPE hip and knee replacement bearings the lubrication is believed to be boundary in nature [96] due to increases in surface roughness and the relatively high volumetric wear recorded. The design of a typical articulating lumbar TDR shows similar radius of bearing to that of hips, but with reduced bearing coverage due to the shallower design [Figure 6-11].

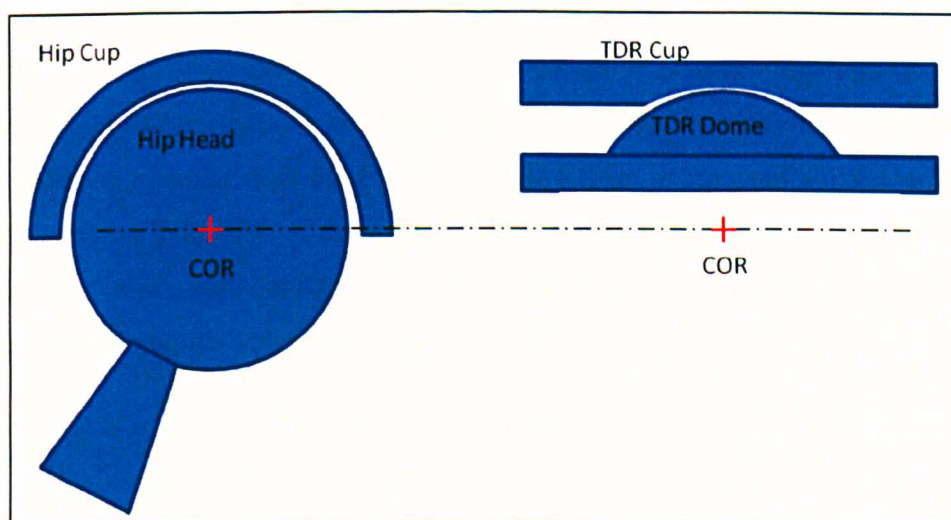


Figure 6-11 Schematic demonstration of the difference in bearing coverage of a THR (left) and TDR (right), also showing same centre of rotation (CoR)

Design rationales vary greatly between device manufacturers, from varying materials to mobile or fixed CoR. The reason stated for selecting a MoM bearing-

couple in TDR is biocompatibility [135], possibility of fluid film lubrication [82, 83, 202] and low wear [98, 135]. Experimental results have been presented for wear [Sec 3.3] and friction [Sec 6.3] in MoP TDR, but in order to complement the friction results a numerical computation of theoretical lubrication regimes was undertaken. Appendix F details the MatLab code used.

## 6.5.2 Method

Matlab code was developed based on the Hamrock-Dowson elastohydrodynamic lubrication formula [81] [Equation 6-7], where  $R$  is radius,  $n$  is viscosity,  $E$  is equivalent modulus,  $u$  is velocity and  $L$  is load. The predicted lubrication regime,  $\lambda$ , is the ratio  $h/R_a$ , where  $h$  is minimum film thickness and  $R_a$  is the average roughness. This equation uses an equivalent radius ( $R$ ) (calculated from the bearing geometries) acting on an infinitely flat plane.

$$h_{\min} = 2.798R \left( \frac{\eta u}{E' R} \right)^{0.65} \left( \frac{L}{E' R^2} \right)^{-0.21}$$

Equation 6-7

For the first set of lubrication regime data the values of average roughness ( $R_a$ ) were taken directly from Shaheen and Shepherd [83] in order to verify the computation. The following results then used roughness data from component surface analysis. These were an indication of the immediate roughness values before wear had taken place. The values used for the constants and the range of values for the variables of clearance and angular velocity are listed in Table 6-4.

**Table 6-4 Values of constants and variables in lubrication analysis (modified from Shaheen & Shepherd [83])**

Equivalent roughness ( $\mu\text{m}$ )	1.29	(MoP combined)
	0.08	(MoM combined)
Poisson's ratio	0.3	(metal)
	0.4	(UHMWPE)
Elastic modulus and equivalent (GPa)	230	(metal)
	1	(UHMWPE)
	230	(MoM combined)
	2.36	(MoP combined)
Viscosity (mPas)	1.24	
Load (KN)	1.5	
Trunk velocity (rad/s)	0–1.8	
Clearance ( $\mu\text{m}$ )	20–200	

Figure 6-12 is one plot from the Shaheen and Shepherd paper and Figure 6-13 is the Matlab plot for comparison. Further development of the Matlab code produced an easier to understand and more detailed 3D overview of the disc lubrication regime than is possible with 2D plots.

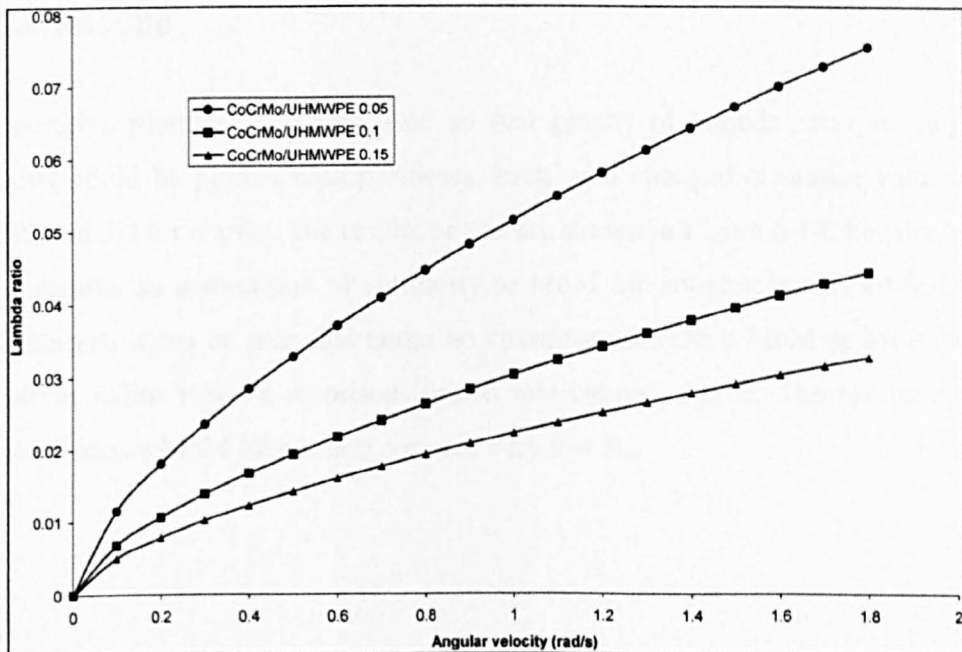


**Figure 6-12 Shaheen-Shepherd plot of lubrication regime for a 14mm radius and 0.05mm clearance – the CoCrMo/UHMWPE plot was used to verify the matlab plot [Figure 6-13]**



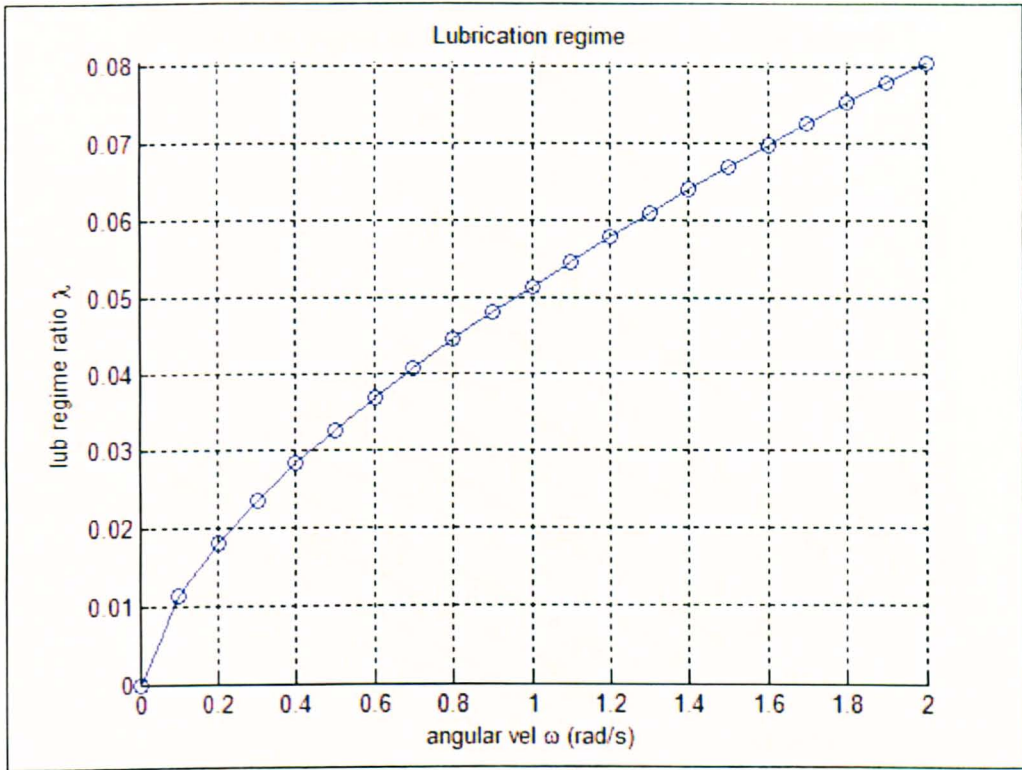


Figure 6-13 Simple MatLab plot used to verify calculations against existing data

### 6.5.3 Results

An iterative plotting code was used so that graphs of lambda ratio vs. angular velocity could be plotted multiple times, each with changed clearance values and graphed in 3D for clarity. The results of this are shown in Figure 6-14. For the MoM TDR results, an assumption of similarity to MoM hip roughness was made in the calculations. It can be seen that under no circumstances can a MoM or MoP device of 14mm radius reach a theorised ‘mixed lubrication’ regime. The results appear similar because MoM lubrication requires very low  $R_a$ .

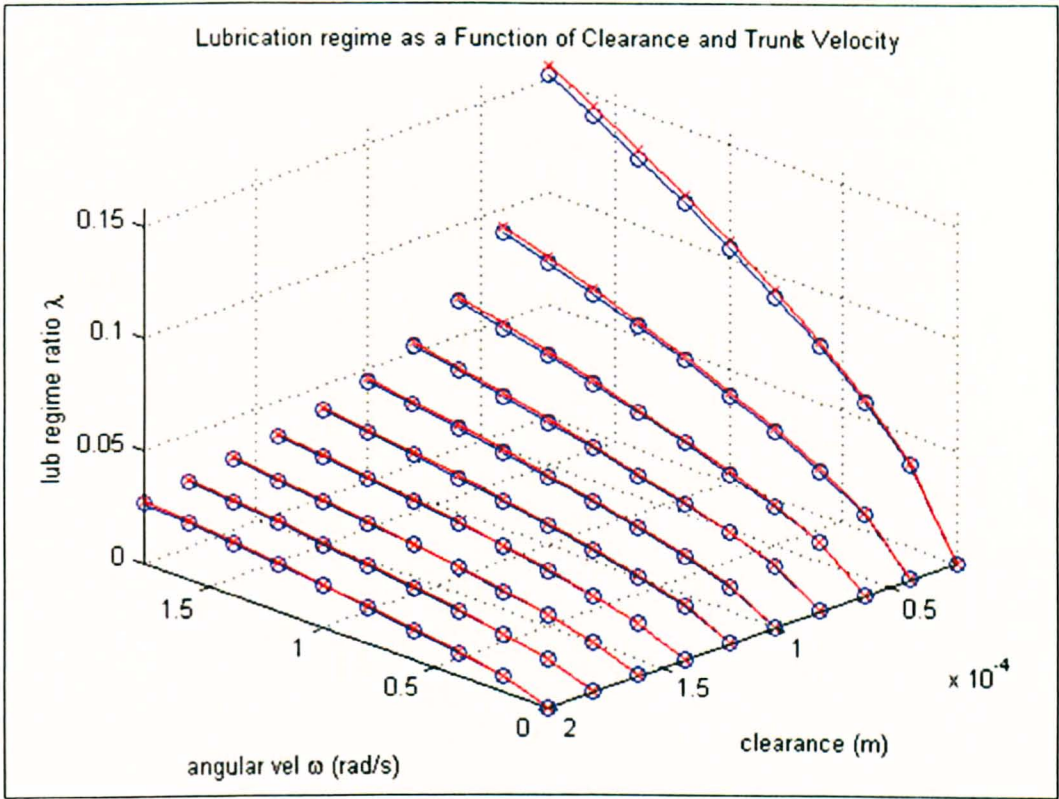


Figure 6-14 MoM (blue) and MoP (red) lubrication regime plots for a 14mm radius TDR device

The theoretical lubrication deteriorated when a more kinematically accurate input range for the angular velocity was chosen. The range selected by Shaheen & Shepherd was 0-1.8 rad/s. From the ISO standard for spine simulation it can be calculated that velocity for the FE motion will be 0.3 rad/s, with a maximum load of 2000N. A range of velocity values around 0.3 rad/s was therefore used in the model. The effect of a range of velocity values decreased to 0-0.5 rad/s and with increased load input of 2000N is demonstrated in Figure 6-15.

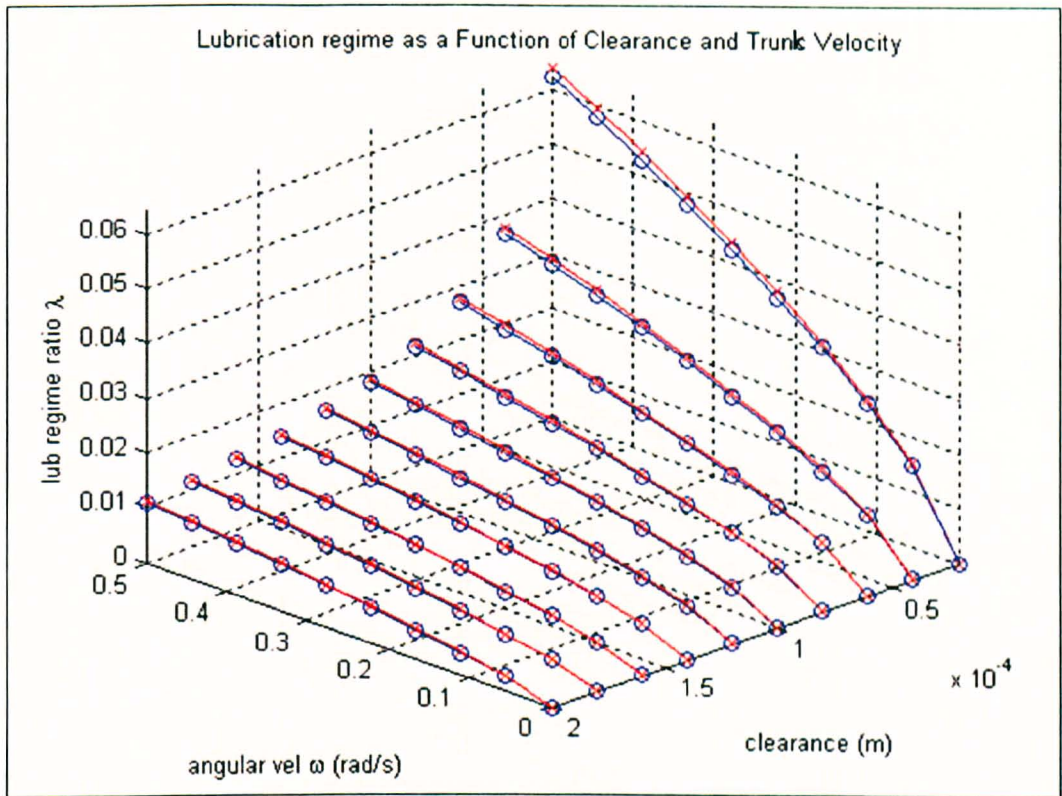


Figure 6-15 MoM (blue) and MoP (red) lubrication regime for reduced FE velocity and increased load (2000 N)

Both Shaheen & Shepherd [83] and calculations presented here predict lubrication regimes one or two orders of magnitude less than Bushelow et al. [82]. However, if the roughness values are reduced from 80 nm (Shaheen & Shepherd) to 5nm (Bushelow et al.) the results become comparable and show a weak mixed lubrication regime [Figure 6-16]. In practice, a surface finish of 5 nm, though not impossible to create, may increase after use *in vivo* and so the favourable lubrication values could be misleading.

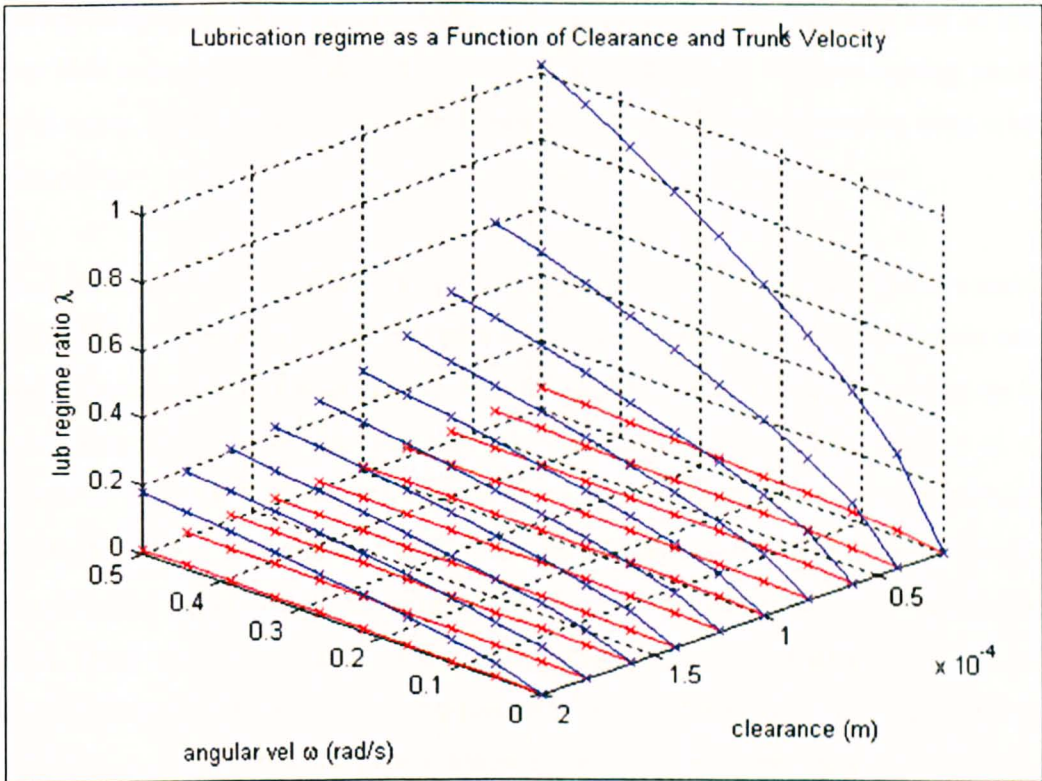


Figure 6-16 The lubrication regime for a MoM TDR after changing the roughness from 80nm (red) to 5nm (blue)

#### 6.5.4 Discussion (computational lubrication)

The results show that MoM devices (for example, Kineflex and Maverick TDRs) have a lubrication regime that is most probably boundary in nature. A study by Mathews et al. [135] describing the design rationale of the MoM Maverick disc said that the CoCr bearing materials were chosen because they were:

*“a safe combination of design and biomaterials. Both the material and the articulation geometry have enjoyed decades of clinical success in metal-on-metal hip arthroplasties”.*

The assertion that MoM hip arthroplasties are successful and low wearing is accurate, so far as well functioning devices are concerned, but the author’s conclusions that TDR devices of MoM design are superior due to low wear is suspect, because their testing methodologies were not stated. Williams et al. [132] experimented with loading and wear effects on MoM THR and found that increasing swing-phase loads increased both friction and wear. The high minimum loading

values associated with TDRs is analogous to high swing-phase loading and as such any kind of entrained fluid film lubrication is doubtful. *In vivo*, no 'swing phase' load exists, as the spine is in a state of permanent muscular compression even when prone [3].

Experiments *in vitro* by Lee et al. [98] on a generic MoM design similar in concept to the Maverick showed wear rates of 6.2 to 15.8 mm<sup>3</sup>/MC. These experiments used approximately linear inputs (based on ASTM F2423-05) which are known to be more severe than crossing path (polishing) inputs. However, Bushelow et al. observed wear rates in Maverick discs of 10-50 times that observed in equivalent THR [97] when using ISO 18192-1 inputs. These cycles have relatively large crossing path motions and should produce the best case scenario. Conversely, Paré et al. [208] investigated wear using A-Mav discs (Medtronic, Memphis, TN - very similar design to the Maverick) and reported low wear results of 0.33 mm<sup>3</sup>/MC for pure FE motions. However, their methods included a relatively low load (1200 constant load), large FE rotations ( $\pm 10^\circ$ ) and faster than typical cycles (2 Hz). All these factors are theoretically advantageous for improved lubrication regime.

Bushelow et al [82] theoretically investigated the lubrication regime in MoM TDRs. However, there were limited details as to the nature of the model used. The lubrication regime results seem to be favourable when compared to the theoretical study by Shaheen & Shepherd [83]. They found that a bearing radius of 14.5mm,  $R_a=5\text{nm}$  and diametric clearance 75 $\mu\text{m}$  (37.5 $\mu\text{m}$  radial clearance) indicated a mixed lubrication regime, which is where MoM hips are said to operate, and was therefore encouraging in terms of long-term wear rates. MoM hips do exhibit very low volumetric wear when operating in an ideal anatomical position but can become very high wearing when high inclination angle and micro separation becomes an issue [133]. Under these conditions, the bearing may operate in the boundary regime and therefore is subject to much increased friction and wear.

An experimental study by Moghadas et al. [202] compared *in vitro* friction of custom-designed MoM TDRs using dimensions based on the Maverick TDR. Using a range of bearing radii from 10-16 mm (constant radial clearance of 15  $\mu\text{m}$ ), they plotted Stribeck curves [Section 1.6.1] showing a fall and rise in friction which they

attributed to evidence of a lubrication regime between mixed or full hydrodynamic. Although appearing to indicate a minima (and hence favourable lubrication regime) in the graph, the plots used a linear-linear scale. However, Stribeck analysis requires a log scale in order to allow for a very wide range of Sommerfeld number, therefore only one order of magnitude was plotted for the Sommerfeld number and so this is probably not a reliable indication of hydrodynamic operation. Further to this, the friction factors reported were very high at almost 0.8 for the 600 N load, which is an order of magnitude more than for an equivalent hip device [201]. This suggests that the devices actually operated firmly in the boundary regime.

Ceramic on ceramic THR bearings have been demonstrated to be relatively robust in terms of wear behaviour under adverse conditions such as raised cup inclination angles and micro-separation (rim impact effects) [209]. This material combination has also been shown to have equivalent friction factors when lubricated by bovine serum and very low friction factors when lubricated with water [201]. This resilience to lubricating fluid effects would be beneficial in TDR design, although the lack of toughness of ceramics is of great concern in the spine.

### **6.5.5 Summary**

Theoretical computation of lubrication regime is not a perfect simulation of reality, but it may indicate performance differences between device designs in terms on bearing material, surface finish and rotational entrainment velocities. All bearing parameters considered suggest that TDRs probably operate in the boundary lubrication regime. Previous knowledge gained from other TJRs suggests that materials suitable for such bio-tribological application are MoP and CoC. The wear rates observed in the literature for MoM discs, and the lubrication regimes calculated for them, suggest that they are an unsuitable design for TDR. However, further testing of MoM TDRs and comparison to existing MoP designs is necessary before concrete conclusions can be drawn.

## **7 General Discussion**

The aim of the experiments presented here was to more fully characterise articulating TDR designs in terms of wear rates due to parametric testing conditions, measure contact mechanics and surface topography, investigate the effects of very short stroke lengths, compare motion tracks of semi- and unconstrained bearings and investigate friction and lubrication behaviours. These were achieved and the knowledge-base of *in vitro* artificial disc behaviour has been increased.

### **7.1 Overview of Experiments**

The new Leeds spine simulator was commissioned and verified against known TDR wear testing data. A parametric bio-tribological study was designed to study the wear characteristics of two different types of TDR design under varying kinematics and loads. Selective surface analysis was used to give a qualitative and quantitative description of wear behaviour. Motion analysis of TDRs subject to extended ISO-based motions indicated the effect of reduced cross shear, addition of AP motions and *in vivo* kinematics. A contact pressure test and PoP study were used to further investigate the hypothesis that short strokes were responsible for debris entrapment in TDR. Experimental frictional characteristics and theoretical lubrication regimes were investigated in order to explore the impact of design rationale and material selection. An attempt was made to correlate *in vitro* and *in vivo* observations and to expand on the literature the knowledge base of TDR behaviour. Debris from the tests was recovered and will be analysed by research colleagues.

### **7.2 Use of Leeds Spine Simulators**

The new spine simulator initially suffered from mechanical, software and electrical problems. However, once debugging of problems was achieved, over time the equipment became more reliable. However, the difference between wear rates from identical devices and simulators under ISO conditions was found to be 25 % (Sec 2.4.1). This was a concern but is not unusual for *in vitro* simulator work. A previous work on spine simulation using a Leeds-designed simulator found over-input of the

FE angles [122]. After inspection using video analysis of dial-gauge displacement readings this was found not to be the case (Sec 2.2.2). It is possible that previous video analysis of the FE motions was influenced by the parallax error that filming using a wide-angle lens would incur. Axial loads were found to be within the tolerances stipulated by ISO. Overall, six DoF combined with accurate electro-mechanical control, is a successful design which allows a wide range of input-cycle parameters to be studied.

Further experiments to investigate motion patterns on the bearing surfaces required design and manufacture of bespoke components and improvement in those designs over previous versions. The frictional characteristics investigation also required custom-made components and an understanding of the kinematics and loads required for testing. These challenges were overcome and now further experimentation can be undertaken using the components and methodologies created during this study.

### **7.3 Summary**

Investigation of wear behaviour in MoP TDRs was an important undertaking because the popularity of disc replacement was growing exponentially in the 2000s, but has receded recently due to reimbursement issues. The longevity *in vivo* had not been proved to be “life-time” and *in vitro* testing had shown results ranging from zero wear to wear comparable to *in vitro* THR [Sec 3.4.1]. The clinical relevance of this is that prediction, or at least indication, of performance *in vivo* is an important objective of joint replacement simulation. As has been seen with recent failure of MoM surface hip replacements, a parametric approach to testing, by expanding the envelope of the standard procedures, may give important clues to the success of TDR and its probable modes of failure.

The initial base-line (verification) experiments gave rates of wear similar to that in the literature (Sec 3.4.1) and so further studies were carried out. The first million cycles of Charité data were much lower than expected and were excluded from some analyses. No cause for this was found, but it is a feature of MoP TJR that bedding-in wear is different to MoM wear where there is usually a period of much higher wear.



Following the initial test, the low CS experiment filled the gap in knowledge between zero and high CS input cycle results. Although the CS ratio was only 0.05 (compared to  $\sim 0.2$  for other inputs) and the motion tracks were narrow, the reduction in wear was modest. This is confirmed by the wear factor-CS relationship found by Kang et al. [210] where K rises very rapidly from zero CS and begins to plateau at CS ratios above  $\sim 0.05$ , therefore for CS ratios above this it is the sliding length that dominates the resulting wear.

The following low load study found that the wear rate was not reduced by half (which was expected as this is a well-known phenomenon in MoP devices) but this had not been demonstrated in MoP TDRs and so it will supply experimental data for computational modellers to help with their verifications. It is worth noting that the TDR devices tested are actually of reverse bearing combination when compared to contemporary hips. The cup is metallic rather than PE and so a more accurate description perhaps should be PoM. The small reduction in wear seen for the halving of load suggests that patients with a factor of two mass difference should not expect to see a large change in longevity of their device in terms of wear, though other factors such as fatigue may possibly become prominent. The semi-constrained device was subject to a further test using half FE. The results show that in this instance, the very similar CS ratio meant that the traditional (Archard) wear equation was an adequate predictor of wear.

A full discussion of the clinical relevance, in terms of explants comparison, was given in Chapter 3. It was observed that explants and *in vitro* tested devices show limited similarity in terms of modes of wear (though *in vivo* and *in vitro* wear levels have been validated to some extent previously [186]), however, some evidence was present. For example, the roughened area around the pole of the UHMWPE dome on both devices tested was observed in both this work and previously by Vicars et al. [122] and Prokopovich et al. [185], but not reported by others who have tested under ISO conditions. Possible reasons for this are: Leeds universally use 25 % dilute serum, half the viscosity of the standard. This lack of lubricity is designed to more closely match results found *in vivo* for THR and TKR. Perhaps for TDR this is not the case. However the use of this serum concentration is warranted since the natural

IVD is not a synovial joint and it is a reasonable conjecture that any lubricating fluid will not be of the same viscous quality as in natural synovial joints. As stated, no other explants or *in vitro* tested disc (other than Leeds) have displayed this phenomenon, but as described in Section 3.4.2, an image from an explant [Figure 3-42] did show similarity to the SEM image of the disc tested [Figure 3-43]. Rather than not being replicated, it is possible that no other authors have reported this wear effect. The reattachment of wear debris in this way does not appear to have any obvious implications *in vivo*, but the reason behind it is indicative of the poor bio-tribological environment and has implications when choosing bearing materials at the design phase. In Section 6.5 it was observed that TDRs operate (in theory) at a boundary level lubrication. As stated, this is supported by the reattachment of debris wear mechanism. If a material other than MoP was chosen, this lack of lubrication should be considered carefully. For example, the use of MoM in lumbar TDR may be unwise unless clearance and surface roughness are at a minimum, which due to manufacturing constraints, is very difficult. Also in chapter 6 it was seen that other authors [202] have found very high friction in MoM designs, and although they interpreted this as mixed lubrication, the more probable interpretation is that friction and torque were very high because lubrication is very poor in MoM TDR. It is therefore of paramount importance that during translation of medical technology from one type of joint replacement device to another, that sound tribological principles are adhered to.

The reoccurring theme from explant failure modes is rim fracture or rim deformation. These are usually attributed to impingement due to rotation beyond the limit of the device (Prodisc) and/or anterior shear compressing the rim (Charité). No evidence of this was observed *in vitro*, even in a previous study using addition of AP force and displacement inputs [130]. However, a recent paper by Kurtz et al. [93] has highlighted the role of oxidation. They report that the rim-damaged areas were much more highly oxidised than the rest of the dome and therefore had an increased likelihood of failure. The rim is only ~1 mm thick and so surface area is relatively large compared to its volume. This may be a wear result that is only capable of simulation *in vitro* with prematurely oxidised components.

Pin-on-plate experimentation sought to highlight the effect of short stroke lengths on wear in prostheses [Chapter 5]. Although the contact pressure measurements gave an insight into the contact mechanics (plug-like pressure distribution rather than Hertzian) the results were inconclusive. No evidence of reattachment of debris was observed or any other adverse events. However, the wear factor was found to increase with the shorter stroke length and this has important implications for computational modelling.

The friction simulator gave interesting comparisons between MoP hip and MoP TDR data [Chapter 6]. The Prodisc device was successfully tested and results were in the region expected of comparable THR, with a decreasing friction for increasing load. The Charité tests were less successful; the unconstrained mobile core led to AP and some ML movement that probably made those results less than ideal. However, the trends found were similar to the Prodisc and so the principle frictional characteristics were reported. Frictional torques were found to be below that of slightly flexed spinal units [Section 6.4] and so pull-out torques, that were once a concern in other joint replacement [200], are probably not a concern for articulating TDRs. This does however reiterate the difference between a natural (or visco-elastic) joint and replacement with an articulating one. The quality of motion is not the same and the articulating TDR has no inbuilt resistance to excessive rotational inputs that are present in both natural and artificial elastomeric discs. Maintenance of quality of motion should be as important as maintaining RoM in the next generation of TDR design. The use of frictional torque measuring equipment will be useful to validate these new designs with available *in vivo* data.

#### *TDR as an alternative to fusion?*

The chain of vertebrae-disc connections of the spine results in a degree of redundancy in the spinal assembly. This means that spinal units have differing amounts of biomechanical involvement. The possible cascade of failure of IVDs (sometimes referred to as ‘fusion diseases’) due to ALDD is a problem that TDR was theorised to minimise through the preservation of motion. However, the amount of redundancy means that the lack of motion at one segment should be compensated by others. If fusion did result in a cascade of adjacent failure of discs then TDR would be a desirable intervention in theory. But, if pathology is the prime driver of

continued degeneration then the TDR procedure will not slow this inevitable disease and the future of TDRs would be in doubt.

### *Debris Analysis*

Results analysed from previous *in vitro* spine simulator testing by Tipper et al. [174] have shown equivalence to THR particles and so the potential for osteolytic reaction is present. Some limited reports have now emerged detailing adverse tissue reaction [139-142, 176, 177], but the vast majority of TDR patients appear not to have osteolytic reactions at this time-point. However, how these patients fare in 20+ years is open to conjecture. The first report of osteolysis in THRs was not seen for ~13 years [180]. Only in the last decade has TDR been implanted in any great number. The most worrisome results may be from patients with multi-level replacement discs who, if osteolysis does occur, will have very complicated and life-threatening operations ahead of them.

Overall, the case for cervical TDR is stronger, given the lower loads and easier surgical access. Countering this is the catastrophic results of failure: paraplegia, breathing function, death.

### **7.3.1 Key Results**

- The ISO wear results from the second Leeds spine simulator displayed wear rates comparable to literature when comparing tests run with three, simultaneous, out-of-phase rotations or more [Section 3.4.1]. There was no significant difference between the wear of Prodisc and Charité TDRs under ISO conditions [Section 3.3.1].
- Placing the FE and LB motions in-phase produced a low cross shear motion, the result of which was a reduction in wear, but not the order of magnitude reduction seen in the literature for zero cross shear studies. A change in CS ratio from zero to 0.05 can make a dramatic difference in terms of wear rate [Section 3.3.1.1]. The two devices showed no significant difference in wear rate.

- The experimental data confirmed that the new Leeds wear law accurately predicts the trend in wear for high CS, low CS and low loads, though the absolute values were incorrect [Section 3.4.1].
- Lowering the average axial loading of the input cycle reduced the wear only moderately and showed that MoP TDRs are not sensitive to perturbations in loading dynamics [Section 3.3.1.2].
- The halving of the FE motion in the Prodisc experiment demonstrated that the proportion reduction in wear rate was approximately equal to the proportion reduction in sliding distance [Section 3.3.1.3].
- Repeating the standard ISO input cycles tested the spine simulator's ability to maintain control accurately over many millions of cycles [Section 3.3.1.4]. The wear rates returned to those seen at the start of testing and validated the long-term results of the spine simulator.
- Continued profilometry of the bearing surfaces allowed changes of input kinetics to be correlated with surface morphology [Section 3.2.2]. Roughening of the pole area of the PE components was caused by re-attachment of wear particles and was found to occur under all inputs (except low loading on the Prodisc). However, presence of this effect appears not to impact on rates of wear. Very high magnification SEM images revealed that the roughened pole surfaces were made up from particulate debris approximately 1  $\mu\text{m}$  diameter [Section 3.3.2.3].
- Edge effects including burnishing and deformation were found on both types of bearing. Contact pressure theory suggested that the TDR bearing area of contact is too small to allow Hertzian-shaped pressure distribution [Section 5.1.1]. Experiment confirmed that pressure distribution is plug-shaped rather than Gaussian [Section 5.1.3].
- The metallic components showed little signs of wear after 15 MC of testing [Section 3.3.1.4].
- The Prodisc PE components displayed preferential wear towards the posterior, which correlates with higher CS ratio motion paths in this region compared to the anterior [Section 3.3.2 and 3.4.1]. Charité PE components were evenly worn.
- The rotation of the Charité components made the wear isotropic by distributing the wear evenly [Section 4.3].

- Some SEM images of the PE bearing surfaces matched those reported from explant analysis, however, rim damage reported in explant reports was not noted during simulator studies [Section 3.4.1].
- Microscopic scratches on the PE bearing surfaces did match those observed from explants analysis [Section 3.4.1].
- Preferential superior motion of the Charité cores was observed and confirms computational prediction by Goreham-Voss et al. [150] [Section 4.4].
- Motion tracks were found to be similar in length for ISO and Callaghan inputs. The nature of the tracks was elliptical for the Prodisc and continuous spiral for the Charité [Section 4.3].
- Frictional characterisation demonstrated that the Prodisc behaviour was similar to that of equivalent diameter MoP hip replacements with decreasing friction factors resulting from increasing loads [Section 6.3.1].
- Surface tangential torques were in the region of 1.5 Nm. The Charité device was more challenging to test and the results were less reliable, though the trends were similar to those of the Prodisc. Slew rate (rotational velocity at the 0° flexion point) and serum concentration did not affect the friction factor results.

## 8 Conclusions and Future Work

### 8.1 Conclusions

There was no significant difference between the wear rates of the semi-constrained (Prodisc) and unconstrained (Charité) designs and therefore neither disc could be considered superior based on wear performance presented here. However, previous tests conducted using additional AP inputs have highlight design-dependant differences [122]. A caveat to those results, however, was that the simulator design at that time had relatively high friction linear AP bearings that may have attenuated the load applied to the semi-constrained Prodisc samples.

The standard ISO TDR wear rates were relatively high in context to modern hip and knee replacements [Section 3.3.1], but lower than historical TKRs and THRs that have used similar non-cross linked PE materials. In general, the use of cross-linked PE in TJR may be advantageous in terms of volumetric wear reduction, but the reduced toughness and reduced fracture resistance of these materials make them high-risk for use in the spine where the effects of failure could be catastrophic.

The difference in wear results between zero cross shear, low cross shear and high cross shear was made clear from altering the phasing of the FE and LB rotations [Section 3.3.1.1]. The low cross shear kinematics produced wear rates that, although lower than the standard ISO, were still of the same magnitude, being approximately half that of the baseline test. Evidence in the literature regarding performance of TDRs subject to purely curvilinear motions indicate near-zero wear which could imply an unwise level of confidence in TDR rates of wear *in vivo*. If it is assumed that *in vivo* FSU kinematics are highly unlikely to be composed of pure curvilinear motions, then even small amounts of crossing path motion that result will produce significant amounts of wear and hence debris. However, if the rotations of an articulating TDR design could be separated into curvilinear articulations rather than coupled motions, the rates of wear could be greatly reduced.

The Prodisc and Charité implants displayed anisotropic and isotropic surface morphology respectively [Section 3.3.2]. The more equally distributed wear on the

Charité surface was due to rotation of the core in the transverse plane [Sec 4.3] and may indicate a small advantage in that no one area of the PE dome will become preferentially worn. Rotation of the core could, in theory, reduce the amount of cross shear motion at the bearing interface by allowing some separation of the motions (similar to rotating platform TKRs). However, *in vivo* FSU spinal kinematics may not necessarily result in the rotations seen *in vitro*.

The reduced loading study [Sec 3.3.1.2] demonstrated only a modest reduction in rate of wear over the ISO standard. This indicated that patient weight is unlikely to play a key role in long-term success of a TDR procedure solely in terms of volume of wear and consequent debris-production and height-loss of the device. However, increased axial loads will increase subsurface stresses and perhaps lead to an increased probability of fatigue fracture. If the rim damaged Charité samples seen in *ex vivo* reports [Sec 3.4.2] were due to anterior shear loading (allowing impingement), then this force-component would also be increased under higher axial loads. Rim impingement described in some explanted Charité discs was not found in any of the parametric simulator studies, nor was this effect noted when using additional AP displacements [122]. However, rim impingement of Charité discs *in vivo* is probably caused by a combination of mal-alignment and significant anterior shear due to flexural tilt in the sagittal plane, especially at L5-S1. Other reported instances of rim impingement could be related to loss of the rotation-torque dependency of the natural IVD when replaced by an articulating TDR with approximately constant frictional torque resistance to motion [Sec 6.4].

Tracking important surface topographical features demonstrated patterns of wear, previously un-quantified, that were measured and correlated with tribological changes resultant from loading and kinematic alterations to the input test cycle. The results highlighted the edge-effects [Sec 3.3.2] that result from a soft, convex PE bearing surface articulating against a hard, concave surface [168]. The radii of curvature at the perimeter of the hard bearing cup(s) produced a larger contact stress than predicted by Hertzian contact theory. If the bearing couple was reversed – as is the case with MoP hip and knee replacements – this edge loading could be reduced and consequently wear characteristics would change, perhaps leading to improved wear resistance.



SEM analysis [Sec 3.3.2.3] revealed that the roughened poles of the PE bearings actually consisted of particles of debris that had been smeared in layers back onto the surface. The results suggest that small rotations and high loads experienced by TDRs *in vitro* have a detrimental effect on the bio-tribological operating regime. Reduced lubrication caused re-attachment of particulate debris that would normally be released into the lubricating medium [Sec 4.1]. Entrainment of fluid into the bearing was probably limited by short motion tracks and high contact stresses, especially at the rim. The magnitude of loading affected the re-attachment of particles, with the half loading cycle showing little signs of re-attachment [Sec 3.3.2]. Explants analyses have not explicitly noted this roughening effect and therefore it could be postulated that the half load input cycle is the best representation of *in vivo* simulation. However, many parameters will be different between *in vivo* and *in vitro* operation and so it is difficult to draw conclusions. Further to this, although only one *ex vivo* SEM image [Sec 3.4.2] was found in the literature to be similar to the ones reported in the present study, the number of such example explant images is very few and therefore more evidence of debris reattachment and roughening may become known as explant numbers and surface analyses increase. The re-attachment of particles to the pole areas probably has limited *in vivo* dangers, however, if a fragment of this 0.1 mm thick skin of PE was to break away intact and enter the neural spaces, the effect is unknown.

If the 'Callaghan' waveform is a more realistic representation of spinal motions, then the finding that this waveform and the ISO one produce similar motion tracks may indicate that the production of debris *in vivo* is on the scale predicted by ISO testing [Sec 4.3]. However, the Callaghan data was gathered from an entire lumbar region and applied to a single level in the present study. A more realistic motion at a single FSU is probably much less than the full segment measured by Callaghan et al. [1]. As previously stated, the articulating discs do not have a rotation-dependant increase in flexural torque [Sec 4.4] and so this lack of restraint may induce more motion than a natural IVD during more extended motions, for example, tying shoes laces etc.

The amount of debris released into the intervertebral region has an unknown long-term effect on tissue response. Preliminary particle analysis has shown that the wear debris has osteolytic potential [174], based on previous knowledge gained from hip and knee data. Reports are starting to emerge [Sec 3.4.3] describing adverse tissue reactions *in vivo* but are still relatively uncommon. However, it remains to be seen if osteolysis will be a rare mode of failure, or, if these effects are merely in stasis at present, and will become more common in the following decades - as was the case for the first generation of UHMWPE-on-metal hip replacement.

The contact pressures experienced by TDRs [Sec 5.1.3] are of broadly similar magnitude to those reported in the literature for MoP THRs and TKRs. However, the pressure magnitude across the bearing surface is plug-shaped and not a Hertzian or a parabolic distribution [Sec 5.1.1]. This is a result of the reversal of the bearing materials used in Prodisc and Charité TDRs. The soft UHMWPE conforms to the hard CoCr cup which caused the stress distribution described. This change in contact characteristics may cause some of the wear phenomena observed in the TDRs studied.

The aim of the PoP experiments was not realised in full (no debris re-attachment was observed), but some useful data was gained. The reduction in wear factor for shorter stroke distances may be of use to computational modellers concerned with poor tribological conditions such as small rotational inputs when using MoP bearings [Sec 5.4]. Higher contact stresses, shorter stroke lengths and higher CS ratios are required in order to more accurately model the TDR regime in a simple PoP study.

Frictional torques and friction factors measured using the Prodisc samples were similar in magnitude to those reported for MoP THRs even though the FE rotations were much reduced and the bearing material combination was reversed [Sec 6.3.1]. Natural IVDs have an increasing resistance to rotational motion dependant on the amplitude of that motion. As the MoP TDR has a rotational resistance to motion that is always present (i.e. no neutral zone as in the natural IVD) this may mean that 'everyday' motions *in vivo*, such as very small FE angles during walking, may be limited by frictional forces and therefore passed on to adjacent IVDs [Sec 6.4].

Using an artificial replacement disc results in the loss of displacement-dependant resistance to flexion, and therefore an increased amount of load will probably be transferred to the other spinal structures such as the ligaments, muscles and facet joints. A visco-elastic TDR would include the quality of motion that is lacking in articulating designs and help prevent overloading of the peripheral structures of the lumbar spine.

The computational lubrication regimes calculated [Sec 6.5.3] demonstrated that under ISO conditions the TDR operates in the boundary lubrication condition. For MoM bearings this is also probably true; and as there is no 'swing phase' present in the spinal kinetics, the probability of fluid entrainment into the bearing contact region is further reduced and suggests higher wear may result, perhaps similar to poorly performing THR. If this is the case then bearing materials that are proven to respond well in adverse bio-tribological conditions should be chosen for further development. The relatively poor lubrication predicted by theory and confirmed from particle re-attachment, suggests that a bearing combination of ceramic materials would be ideal for this situation. However, ceramics have much lower fracture toughness and can result in shattering when they fail. Such risks are unacceptable given the close proximity of the device to the spinal canal and nerve networks. If this risk could be substantially reduced then CoC bearings could be a low wearing alternative to CoCr and UHMWPE based bearing materials.

## **8.2 Future Work**

- There are a small number of MoM TDR devices being implanted but there is very limited data available on their performance *in vitro*, especially under more challenging regimes. Future testing in this area should be a priority given the recent failures seen in MoM hips
- Testing of prematurely aged (oxidised) UHMWPE components would allow comparison with explant data suggesting that rim damage may be related to this phenomenon

- Application of constant anterior shear load to a higher degree than has previously been conducted, may help simulate rim damage or fracture observed *in vivo*
- The bearing combination used in commercially available lumbar TDRs is a PE dome articulating against a metallic cups(s). Due to the edge effects observed during testing, it may be prudent to check if reversal of these bearing materials will reduce these adverse effects and consequential wear
- Other material combination behaviours are relatively unknown. The next generation of articulating devices may use both PEEK-based and ceramic materials, their wear and frictional characteristics should be studied
- The ideal natural IVD replacement is probably a joint with similar quality of motion; therefore viscoelastic devices are the ideal and may become popular in time. Their longevity in terms of fatigue resistance, delamination of endplate-disc interfaces and strength in extreme rotations should be explored
- Further to this, resistance to bone ‘pull-out’ torques in visco-elastic TDRs may be a concern as was once expressed in older THR acetabula designs, due to the increased rotational torque that constrained devices will produce
- Improved access to explants, especially those that have performed reasonably well *in vivo*, would be a great step forward in validating *in vitro* results and predicting performance
- Further analysis of explants surfaces using the techniques described in this thesis may help explain, and therefore improve, the bio-tribological wear behaviour in future designs

## References

1. Callaghan, J.P., A.E. Patla, and S.M. McGill, *Low back three-dimensional joint forces, kinematics, and kinetics during walking*. *Clinical Biomechanics*, 1999. **14**(3): p. 203-216.
2. NHS. *NHS Back Pain Introduction*. 08/09/2008 [cited 2009 01/10/09]; Available from: <http://www.nhs.uk/conditions/Back-pain/Pages/Introduction.aspx>.
3. White, A. and M. Panjabi, *Clinical Biomechanics of the Spine*. 1990: J. B. Lippincott Co.
4. Buttner-Janzen, K., S. Hochschuler, and P.C. McAfee, *The Artificial Disc*. 2004: Springer.
5. Maniadakis, N. and A. Gray, *The economic burden of back pain in the UK*. *Pain*, 2000. **84**(1): p. 95-103.
6. Dagenais, S., J. Caro, and S. Haldeman, *A systematic review of low back pain cost of illness studies in the United States and internationally*. 2008. **8**: p. 8-20.
7. Katz, J.N. and J.N. Katz, *Lumbar disc disorders and low-back pain: socioeconomic factors and consequences*. *Journal of Bone & Joint Surgery - American Volume*, 2006. **88 Suppl 2**: p. 21-4.
8. van Tulder, M., B. Koes, and C. Bombardier, *Low back pain*. *Best Practice & Research Clinical Rheumatology*, 2002. **16**(5): p. 761-775.
9. Deyo, R.A., A. Nachemson, and S.K. Mirza, *Spinal-Fusion Surgery--The Case for Restraint*. *The Spine Journal*, 2004. **4**(Supplement 1): p. S138-S142.
10. Krishna, M., *Posterior Lumbar Arthroplasty*, in *Motion Preservation Surgery of the Spine: Advanced Techniques and Controversies*, J.J. Yue, et al., Editors. c2008, Elsevier: Philadelphia.
11. Gibson, J.N.A., I.C. Grant, and G. Waddell, *The Cochrane Review of Surgery for Lumbar Disc Prolapse and Degenerative Lumbar Spondylosis*. *Spine*, 1999. **24**(17): p. 1820.
12. Carreon, L.Y., S.D. Glassman, and J. Howard, *Fusion and nonsurgical treatment for symptomatic lumbar degenerative disease: a systematic review of Oswestry Disability Index and MOS Short Form-36 outcomes*. *The Spine Journal*, 2008. **8**(5): p. 747-755.
13. Fritzell, P., O. Hägg, P. Wessberg, and A. Nordwall, *2001 Volvo award winner in clinical studies: Lumbar fusion versus nonsurgical treatment for chronic low back pain. A multicenter randomized controlled trial from the Swedish Lumbar Spine Study Group*. *Spine*, 2001. **26**(23): p. 2521-2534.
14. Kwon, B., J.N. Katz, D.H. Kim, and L.G. Jenis, *A review of the 2001 Volvo Award winner in clinical studies: lumbar fusion versus nonsurgical treatment for chronic low back pain: a multicenter randomized controlled trial from the Swedish lumbar spine study group*. *Spine*, 2006. **31**(2): p. 245-9.
15. Brox, J.I., R. Sorensen, A. Friis, O. Nygaard, A. Indahl, A. Keller, T. Ingebrigtsen, H.R. Eriksen, I. Holm, A.K. Koller, R. Riise, and O. Reikeras, *Randomized clinical trial of lumbar instrumented fusion and cognitive intervention and exercises in patients with chronic low back pain and disc degeneration*. *Spine*, 2003. **28**(17): p. 1913-21.

16. Anderson, P.A., J.P. Rouleau, P.A. Anderson, and J.P. Rouleau, *Intervertebral disc arthroplasty*. Spine, 2004. **29**(23): p. 2779-86.
17. Errico, T.J. and T.J. Errico, *Why a mechanical disc?* Spine Journal: Official Journal of the North American Spine Society, 2004. **4**(6 Suppl): p. 151S-157S.
18. Neal, C.J., M.K. Rosner, and T.R. Kuklo, *Magnetic resonance imaging evaluation of adjacent segments after disc arthroplasty*. J Neurosurgery Spine, 2005. **3**(5): p. 342-7.
19. Regan, J.J. and J.J. Regan, *Clinical results of charite lumbar total disc replacement*. Orthopedic Clinics of North America, 2005. **36**(3): p. 323-40.
20. Frelinghuysen, P., R.C. Huang, F.P. Girardi, and F.P. Cammisa Jr, *Lumbar Total Disc Replacement Part I: Rationale, Biomechanics, and Implant Types*. Orthopedic Clinics of North America, 2005. **36**(3): p. 293-299.
21. Huang, R.C., M.R. Lim, F.P. Girardi, F.P. Cammisa, Jr., R.C. Huang, M.R. Lim, F.P. Girardi, and F.P. Cammisa, Jr., *The prevalence of contraindications to total disc replacement in a cohort of lumbar surgical patients*. Spine, 2004. **29**(22): p. 2538-41.
22. Fras, C.I., J.D. Auerbach, C.I. Fras, and J.D. Auerbach, *Prevalence of lumbar total disc replacement candidates in a community-based spinal surgery practice*. Journal of Spinal Disorders & Techniques, 2008. **21**(2): p. 126-9.
23. Harms, J. and G. Tabasso, *Instrumented Spinal Surgery*. 1999.
24. training.seer.cancer.gov. *Vertebral Column*. [cited 2009 01/08/09]; Available from: <http://training.seer.cancer.gov/anatomy/skeletal/divisions/axial.html>.
25. Filler, A.G. and A.G. Filler, *Homeotic evolution in the mammalia: diversification of therian axial seriation and the morphogenetic basis of human origins*. PLoS ONE [Electronic Resource], 2007. **2**(10): p. e1019.
26. Smeathers, J.E., *Shocking news about discs*. Current Orthopaedics, 1994. **8**(1): p. 45-48.
27. Smeathers, J.E., *Transient vibrations caused by heel strike*. Proc Inst Mech Eng [H], 1989. **203**(4): p. 181-6.
28. Middleditch, A. and J. Oliver, *Functional anatomy of the spine*. 2nd ed. ed. 2005: Elsevier Butterworth-Heinemann.
29. Boos, N., *Spinal Disorders Fundamentals of Diagnosis and Treatment*, ed. M. Aebi. 2008.
30. Adams, M., N. Bogduk, K. Burton, and P. Dolan, *The Lumbar Vertebral Column and Sacrum*, in *The biomechanics of back pain*. c2006, Churchill Livingstone Elsevier: Edinburgh.
31. Adams, M., N. Bogduk, K. Burton, and P. Dolan, *The biomechanics of back pain*. 2nd ed. ed. c2006, Edinburgh: Churchill Livingstone Elsevier.
32. Bogduk, N., *Clinical Anatomy of the Lumbar Spine and Sacrum*. 1997: Elsevier.
33. Heylings, D.J., *Supraspinous and interspinous ligaments of the human lumbar spine*. Journal of Anatomy, 1978. **125**(Pt 1): p. 127-31.
34. Jenkins, D., *Functional Anatomy of the Limbs and Back*. 8th ed. 2002, Illinois: W. B. Saunders.
35. Adams, M.A., *The effect of posture on the role of the apophysial joints in resisting intervertebral compressive forces*. J Bone Joint Surg Br, 1980. **62**: p. 358-362.

36. Drake, R., A. Vogl, and A. Mitchell, *Greys Anatomy for Students*. 2 ed. 2005: Churchill Livingstone Elsevier.
37. Bogduk, N., *Clinical Anatomy of the Lumbar Spine and Sacrum*. 2008: Elsevier.
38. Bogdanov, K., *Bone*, in *Biology in Physics*. 2000, Academic Press: San Diego. p. 151-167.
39. O'Brien, F.J., D. Taylor, and T. Clive Lee, *Bone as a composite material: The role of osteons as barriers to crack growth in compact bone*. *International Journal of Fatigue*, 2007. **29**(6): p. 1051-1056.
40. Gordon, J.E., *The New Science of Strong Materials*. 1968: Pelican Books.
41. Pal, G.P., L. Cosio, and R.V. Routil, *Trajectory architecture of the trabecular bone between the body and the neural arch in human vertebrae*. *Anat Rec*, 1988. **222**(4): p. 418-25.
42. Gornet, M., *Maverick Total Disc Replacement*, in *Motion Preservation Surgery of the Spine: Advanced Techniques and Controversies*, J.J. Yue, et al., Editors. c2008, Elsevier: Philadelphia. p. 354.
43. Roaf, R., *A STUDY OF THE MECHANICS OF SPINAL INJURIES*. *J Bone Joint Surg Br*, 1960. **42-B**(4): p. 810-823.
44. Farfan, H.F., *Mechanical disorders of the low back*. 1973, Philadelphia: Lea and Febiger.
45. Putz, R., *Function-related morphology of the intervertebral discs*. *Radiologe*, 1993. **33**(10): p. 563-566.
46. Palastanga, N., D. Field, and R. Soames, *Anatomy and human movement*. 5th ed.: Butterworth-Heinemann.
47. Callaghan, J.P. and S.M. McGill, *Low back joint loading and kinematics during standing and unsupported sitting*. *Ergonomics*, 2001. **44**(3): p. 280 - 294.
48. Urban, J.P. and J.F. McMullin, *Swelling pressure of the lumbar intervertebral discs: influence of age, spinal level, composition, and degeneration*. *Spine*, 1976. **13**(2): p. 179-87.
49. McNally, D.S. and M.A. Adams, *Internal intervertebral disc mechanics as revealed by stress profilometry*. *Spine*, 1976. **17**(1): p. 66-73.
50. Miller, J.A., C. Schmatz, and A.B. Schultz, *Lumbar disc degeneration: correlation with age, sex, and spine level in 600 autopsy specimens*. *Spine*, 1976. **13**(2): p. 173-8.
51. Ferguson, S.J. and T. Steffen, *Biomechanics of the aging spine*. *Eur Spine J*, 2003. **12**(2): p. S97-S103.
52. Klein, J.A., D.S. Hickey, and D.W.L. Hukins, *Radial bulging of the annulus fibrosus during compression of the intervertebral disc*. *Journal of Biomechanics*, 1983. **16**(3): p. 211-217.
53. Ochia, R.S. and R.P. Ching, *Rate dependence of hydraulic resistance in human lumbar vertebral bodies*. *Spine*, 2006. **31**(22): p. 2569-2574.
54. Wilke, H.J., K. Wenger, and L. Claes, *Testing criteria for spinal implants: recommendations for the standardization of in vitro stability testing of spinal implants*. *European Spine Journal*, 1998. **7**(2): p. 148-54.
55. Morlock, M.M., V. Bonin, G. Deuretzbacher, G. Muller, M. Honl, and E. Schneider, *Determination of the in vivo loading of the lumbar spine with a new approach directly at the workplace--first results for nurses*. *Clin Biomech*, 2000. **15**(8): p. 549-58.

56. Cobian, D., B. Heiderscheit, N. Daehn, and P.A. Anderson, *Comparison of Daily Motion of the Cervical and Lumbar Spine to ASTM F2423-11 and ISO 18192-1.2011 Standard Testing*. JAI, 2011. **9**(1): p. 10.
57. Cassinelli, E.H. and J.D. Kang, *Current understanding of lumbar disc degeneration*. Operative Techniques in Orthopaedics, 2000. **10**(4): p. 254-262.
58. Freemont, A.J., T.E. Peacock, P. Goupille, J.A. Hoyland, J. O'Brien, and M.I.V. Jayson, *Nerve ingrowth into diseased intervertebral disc in chronic back pain*. The Lancet, 1997. **350**(9072): p. 178-181.
59. Freemont, T.J., C. LeMaitre, A. Watkins, and J.A. Hoyland, *Degeneration of intervertebral discs: current understanding of cellular and molecular events, and implications for novel therapies*. Expert Reviews in Molecular Medicine, 2001. **3**(11): p. 1-10.
60. Martin, M.D., C.M. Boxell, and D.G. Malone, *Pathophysiology of lumbar disc degeneration: a review of the literature*. Neurosurgical Focus, 2002. **13**(2): p. E1.
61. Siemionow, K., H. An, K. Masuda, G. Andersson, and G. Cs-Szabo, *The effects of age, sex, ethnicity, and spinal level on the rate of intervertebral disc degeneration: a review of 1712 intervertebral discs*. Spine, 2011. **36**(17): p. 1333-1339.
62. Park, P.e.a., *Adjacent segment disease after lumbar or lumbrosacral fusion: review of the literature*. Spine, 2004. **29**(17): p. 1938-44.
63. Lee, C.K., *Accelerated degeneration of the segment adjacent to a lumbar fusion*. Spine, 1988. **13**(3): p. 375-7.
64. Kumar, M.N., A. Baklanov, and D. Chopin, *Correlation between sagittal plane changes and adjacent segment degeneration following lumbar spine fusion*. European Spine Journal, 2001. **10**(4): p. 314-9.
65. Harrop, J.S.M.D., J.A.M.D. Youssef, M.P. Maltenfort, P.B.S. Vorwald, P.M.D. Jabbour, C.M.M.D. Bono, N.B.S. Goldfarb, A.R.M.D. Vaccaro, and A.S. Hilibrand, *Lumbar Adjacent Segment Degeneration and Disease After Arthrodesis and Total Disc Arthroplasty*. Spine, 2008. **33**(15): p. 1701-1707.
66. Gillett, P., *The fate of the adjacent motion segments after lumbar fusion*. J Spinal Disorders and Techniques, 2003. **16**(4): p. 338-45.
67. Freeman, B.J.C. and J. Davenport, *Total disc replacement in the lumbar spine: a systematic review of the literature*. European Spine Journal, 2006. **15** **Suppl 3**: p. S439-47.
68. Hilibrand, A.S. and M. Robbins, *Adjacent segment degeneration and adjacent segment disease: the consequences of spinal fusion?* The Spine Journal. **4**(6, Supplement 1): p. S190-S194.
69. Cunningham, B.W., G.L. Lowery, H.A. Serhan, A.E. Dmitriev, C.M. Orbegoso, P.C. McAfee, R.D. Fraser, R.E. Ross, and S.S. Kulkarni, *Total disc replacement arthroplasty using the AcroFlex lumbar disc: a non-human primate model*. Eur Spine J, 2002. **11**(2): p. 20.
70. Fraser, R.D., E.R. Ross, G.L. Lowery, B.J. Freeman, and M. Dolan, *AcroFlex design and results*. The Spine Journal, 2004. **4**(6, Supplement 1): p. S245-S251.
71. Bhuhan, B., *Introduction to Tribology*. 2002, New York: Wiley.
72. Harris, W.H. and W.H. Harris, *The first 50 years of total hip arthroplasty: lessons learned*. Clinical Orthopaedics & Related Research, 2009. **467**(1): p. 28-31.



73. Dowson, D. and V. Wright, *Bio-tribology*. in *Proceedings of the conference on the rheology of lubrication. The Institute of Petroleum, The Institution of Mechanical Engineers and the British Society of Rheology*. 1973.
74. Brown, C., J. Fisher, and E. Ingham, *Biological effects of clinically relevant wear particles from metal-on-metal hip prostheses*. Proceedings of the Institution of Mechanical Engineers Part H - Journal of Engineering in Medicine, 2006. **220**(2): p. 355-69.
75. Ingham, E. and J. Fisher, *Biological reactions to wear debris in total joint replacement*. Proceedings of the Institution of Mechanical Engineers Part H - Journal of Engineering in Medicine, 2000. **214**(1): p. 21-37.
76. Karuppiah, K., S. Sundararajan, Z.-H. Xu, and X. Li, *The effect of protein adsorption on the friction behavior of ultra-high molecular weight polyethylene*. Tribology Letters, 2006. **22**(2): p. 181-188.
77. Dowson, D., *Biotribology of natural and replacement synovial joints*. Biomechanics of diarthrodial joints (Eds V. C. Mow, S. L. Y. Woo), 1990. **Springer Verlag, New York**: p. 303-345.
78. Yan, Y., A. Neville, and D. Dowson, *Biotribocorrosion of CoCrMo orthopaedic implant materials--Assessing the formation and effect of the biofilm*. Tribology International, 2007. **40**(10-12): p. 1492-1499.
79. Bowden, F.P. and D. Tabor, *The area of contact between stationary and between moving surfaces*. Proceedings of the Royal Society of London Series a-Mathematical and Physical Sciences, 1939. **169**(938): p. 391-413.
80. Archard, J.F., *Contact and rubbing of flat Surfaces*. J. Applied Sciences, 1953. **24**: p. 981-988.
81. Hamrock, B.J., Dowson, D., *Elastohydrodynamic lubrication of elliptical contacts for materials of low elastic modulus. 1: Fully flooded conjunction. y* Journal of Lubrication Technology - Transactions of the ASME, 1978. **100**: p. 236-245.
82. Bushelow, M., W. Nechtow, and J. Walker, *P8. Metal-on-Metal Lumbar TDR Design: A Theoretical Analysis of the Affect of Diameter Clearance and Surface Finish on Lubrication*. The Spine Journal, 2008. **8**(5, Supplement 1): p. 105S-105S.
83. Shaheen, A. and D.E.T. Shepherd, *Lubrication regimes in lumbar total disc arthroplasty*. Proceedings of the I MECH E Part H Journal of Engineering in Medicine, 2007. **221**: p. 621-627.
84. Wang, A., *A unified theory of wear for ultra-high molecular weight polyethylene in multi-directional sliding*. Wear, 2001. **248**(1-2): p. 38-47.
85. Huang, R.C., P. Tropiano, T. Marnay, F.P. Girardi, M.R. Lim, and J.F.P. Cammisa, *Range of motion and adjacent level degeneration after lumbar total disc replacement*. The Spine Journal, 2006. **6**(3): p. 242-247.
86. Bertagnoli, R., *Dynamic Reconstruction of the Spine*, in *Dynamic Reconstruction of the Spine*, F.C.J. Daniel Kim, Richard Fessler, Editor. 2006, Thieme Medical publishers, Inc: New York.
87. Cunningham, B.W., *Basic scientific considerations in total disc arthroplasty*. The Spine Journal, 2004. **4**(6, Supplement 1): p. S219-S230.
88. Palepu, V., M. Kodigudla, and V.K. Goel, *Biomechanics of disc degeneration*. Adv Orthop. **2012**(726210): p. 17.
89. Rundell, S.A., J.D. Auerbach, R.A. Balderston, S.M. Kurtz, S.A. Rundell, J.D. Auerbach, R.A. Balderston, and S.M. Kurtz, *Total disc replacement positioning affects facet contact forces and vertebral body strains*. Spine, 2008. **33**(23): p. 2510-7.

90. Rousseau, M.-A., D.S. Bradford, R. Bertagnoli, S.S. Hu, and J.C. Lotz, *Disc arthroplasty design influences intervertebral kinematics and facet forces*. *The Spine Journal*, 2006. **6**(3): p. 258-266.
91. Dooris, A.P., V.K. Goel, N.M. Grosland, L.G. Gilbertson, and D.G. Wilder, *Load-sharing between anterior and posterior elements in a lumbar motion segment implanted with an artificial disc*. *Spine*, 2001. **26**(6): p. E122-9.
92. Premnath, V., W.H. Harris, M. Jasty, and E.W. Merrill, *Gamma sterilization of UHMWPE articular implants: an analysis of the oxidation problem*. *Biomaterials*, 1996. **17**(18): p. 1741-1753.
93. Kurtz, S.M., J.M. Toth, R. Siskey, L. Ciccarelli, D. MacDonald, J. Isaza, T. Lanman, I. Punt, M. Steinbeck, J. Goffin, and A. van Ooij, *The Latest Lessons Learned from Retrieval Analyses of Ultra-High Molecular Weight Polyethylene, Metal-on-Metal, and Alternative Bearing Total Disc Replacements*. *Seminars in Spine Surgery*, 2012. **24**(1): p. 57-70.
94. Pinchuk, *Tribology and biophysics of artificial joints*.
95. Cooper, J.R., D. Dowson, and J. Fisher, *The effect of transfer film and surface roughness on the wear of lubricated ultra-high molecular weight polyethylene*. *Clinical Materials*, 1993. **14**(4): p. 295-302.
96. Fisher, J. and D. Dowson, *Tribology of total artificial joints*. *Proceedings of the Institution of Mechanical Engineers Part H - Journal of Engineering in Medicine*, 1991. **205**(2): p. 73-9.
97. Bushelow, M., J. Walker, J. Coppes, M. Hinter, W. Nechtow, and C. Kaddick, *P32. Comparison of Wear Rates: Metal/UHMWPE and Metal-on-Metal Total Disc Arthroplasty*. *The Spine Journal*, 2008. **7**(5, Supplement 1): p. 97S-98S.
98. Lee, J.L., F. Billi, S.N. Sangiorgio, W. McGarry, D.J. Krueger, P.T. Miller, H. McKellop, E. Ebramzadeh, J.L. Lee, F. Billi, S.N. Sangiorgio, W. McGarry, D.J. Krueger, P.T. Miller, H. McKellop, and E. Ebramzadeh, *Wear of an experimental metal-on-metal artificial disc for the lumbar spine*. *Spine*, 2008. **33**(6): p. 597-606.
99. Blumenthal, S., P.C. McAfee, R.D. Guyer, S.H. Hochschuler, F.H. Geisler, R.T. Holt, R. Garcia, Jr., J.J. Regan, D.D. Ohnmeiss, S. Blumenthal, P.C. McAfee, R.D. Guyer, S.H. Hochschuler, F.H. Geisler, R.T. Holt, R. Garcia, Jr., J.J. Regan, and D.D. Ohnmeiss, *A prospective, randomized, multicenter Food and Drug Administration investigational device exemptions study of lumbar total disc replacement with the CHARITE artificial disc versus lumbar fusion: part I: evaluation of clinical outcomes.[erratum appears in Spine. 2005 Oct 15;30(20):2356]*. *Spine*, 2005. **30**(14): p. 1565-75; discussion E387-91.
100. Cinotti, G., T. David, and F. Postacchini, *Results of disc prosthesis after a minimum follow-up period of 2 years*. *Spine*, 1996. **21**(8): p. 995-1000.
101. Lemaire, J.P., W. Skalli, F. Lavaste, A. Templier, F. Mendes, A. Diop, V. Sauty, and E. Laloux, *Intervertebral disc prosthesis. Results and prospects for the year 2000*. *Clinical Orthopaedics & Related Research*, 1997(337): p. 64-76.
102. Zeegers, W.S., L.M. Bohnen, M. Laaper, and M.J. Verhaegen, *Artificial disc replacement with the modular type SB Charite III: 2-year results in 50 prospectively studied patients*. *European Spine Journal*, 1999. **8**(3): p. 210-7.
103. Zigler, J.M.D., R.M.D. Delamarter, J.M.M.D. Spivak, R.J.M.D.F. Linovitz, G.O.I.I.M.D. Danielson, T.T.M.D. Haider, F.M.D. Cammisa, J.M.D. Zuchermann, R.M.D. Balderston, S.M.D. Kitchel, K.M.D. Foley, R.M.D.

- Watkins, D.M.D. Bradford, J.M.D. Yue, H.M.D. Yuan, H.M.D. Herkowitz, D.M.D. Geiger, J.M.D. Bendo, T.M.D. Peppers, B.M.D. Sachs, F.M.D. Girardi, M.M.D. Kropf, and J.M.D. Goldstein, *Results of the Prospective, Randomized, Multicenter Food and Drug Administration Investigational Device Exemption Study of the ProDisc(R)-L Total Disc Replacement Versus Circumferential Fusion for the Treatment of 1-Level Degenerative Disc Disease*. Spine, 2007. **32**(11): p. 1155-1162.
104. Marnay, T., *4:19 Lumbar disc replacement: 7 to 11-year results with Prodisc*. The Spine Journal. **2**(5, Supplement 1): p. 94-94.
105. Bertagnoli, R., S. Kumar, R. Bertagnoli, and S. Kumar, *Indications for full prosthetic disc arthroplasty: a correlation of clinical outcome against a variety of indications*. European Spine Journal, 2002. **11 Suppl 2**: p. S131-6.
106. Mayer, H.M., K. Wiechert, A. Korge, and I. Qose, *Minimally invasive total disc replacement: surgical technique and preliminary clinical results*. European Spine Journal, 2002. **11 Suppl 2**: p. S124-30.
107. Zigler, J.E., T.A. Burd, E.N. Vialle, B.L. Sachs, R.F. Rashbaum, D.D. Ohnmeiss, J.E. Zigler, T.A. Burd, E.N. Vialle, B.L. Sachs, R.F. Rashbaum, and D.D. Ohnmeiss, *Lumbar spine arthroplasty: early results using the ProDisc II: a prospective randomized trial of arthroplasty versus fusion*. Journal of Spinal Disorders & Techniques, 2003. **16**(4): p. 352-61.
108. Le Huec, J.C., H. Mathews, Y. Basso, S. Aunoble, D. Hoste, B. Bley, and T. Friesem, *Clinical results of Maverick lumbar total disc replacement: two-year prospective follow-up*. Orthopedic Clinics of North America, 2005. **36**(3): p. 315-22.
109. Guyer, R.D., R.J. Banco, F.D. Bitan, S.L. Blumenthal, A. Cappucino, F.H. Geisler, S. Hochschuler, R.T. Holt, L.G. Jenis, M.E. Majd, P.C. McAfee, B.B. Mullin, J.J. Regan, N. Stadlan, S.G. Tromanhauser, and D. Wong, *Lumbar Arthroplasty versus Anterior Interbody Fusion at One-Level: Clinical Results at 5-Year Follow-Up From the IDE Study of the Charité Artificial Disc*. The Spine Journal, 2006. **6**(5, Supplement 1): p. 16S-16S.
110. Pettine, K. and E.J. Donner, *172. Prospective Randomized Series Comparing Maverick(TM) Lumbar Total Disc Replacement (TDR) with Anterior Lumbar Interbody Fusion (ALIF)*. The Spine Journal. **7**(5, Supplement 1): p. 82S-82S.
111. Cunningham, B.W., G. Demuth, P.C. McAfee, M. Scott-Young, K. Yoon, S. Blumenthal, R.D. Guyer, F. Geisler, J. Regan, B. Conix, R. Hes, L. Pimenta, R. Diaz, I.L. Fedder, and P.J. Tortolani, *171. Survivorship Analysis of the Charité Artificial Disc: Review of 1,938 Patients from Eight Leading International Spine Centers*. The Spine Journal. **7**(5, Supplement 1): p. 81S-82S.
112. Delamarter, R.B., J. Zigler, D. Ohnmeiss, L.E.A. Kanim, and B.B. Pradhan, *P95. Lumbar total disc replacement: a 2 to 3 year report from 2 centers in the United States clinical trial for the Prodisc-II prosthesis*. The Spine Journal 2005. **5** (Proceedings of the NASS 20th Annual Meeting): p. 1S-189S.
113. Green, T.R., J. Fisher, M. Stone, B.M. Wroblewski, and E. Ingham, *Polyethylene particles of a critical size' are necessary for the induction of cytokines by macrophages in vitro*. Biomaterials, 1998. **19**(24): p. 2297-2302.

114. Boynton, E., J.P. Waddell, J. Morton, and G.W. Gardiner, *Aseptic loosening in total hip implants: the role of polyethylene wear debris*. *Can J Surg*, 1991. **34**(6): p. 599-605.
115. Boynton, E.L., M. Henry, J. Morton, and J.P. Waddell, *The inflammatory response to particulate wear debris in total hip arthroplasty*. *Can J Surg*, 1995. **38**(6): p. 507-15.
116. Schmalzried, T.P., M. Jasty, and W.H. Harris, *Periprosthetic bone loss in total hip arthroplasty. Polyethylene wear debris and the concept of the effective joint space*. *Journal of Bone & Joint Surgery - American Volume*, 1992. **74**(6): p. 849-63.
117. Fisher, J., J. Bell, P.S. Barbour, J.L. Tipper, J.B. Matthews, A.A. Besong, M.H. Stone, and E. Ingham, *A novel method for the prediction of functional biological activity of polyethylene wear debris*. *Proceedings of the Institution of Mechanical Engineers Part H - Journal of Engineering in Medicine*, 2001. **215**(2): p. 127-32.
118. Hall, R.M., T.D. Brown, J. Fisher, E. Ingham, S.A. Mendoza, and H.M. Mayer, *Introduction to lumbar total disc replacement: factors that affect tribological performance*. *Proceedings of the Institution of Mechanical Engineers Part J-Journal of Engineering Tribology*, 2006. **220**(J8): p. 775-786.
119. Nechtow, W., M. Hintner, M. Bushelow, and C. Kaddick, *IVD Replacement Mechanical Performance Depends Strongly on Input Parameters*. *Trans 52nd Annual meeting of the orthopaedic research society*, Chicago, IL, 2006.
120. Grupp, T.M., J.J. Yue, R. Garcia, Jr., J. Basson, J. Schwiesau, B. Fritz, and W. Blomer, *Biotribological evaluation of artificial disc arthroplasty devices: influence of loading and kinematic patterns during in vitro wear simulation*. *European Spine Journal*, 2009. **18**(1): p. 98-108.
121. Goreham-Voss, C.M., P.J. Hyde, R.M. Hall, J. Fisher, and T.D. Brown, *Cross-shear implementation in sliding-distance-coupled finite element analysis of wear in metal-on-polyethylene total joint arthroplasty: Intervertebral total disc replacement as an illustrative application*. *Journal of Biomechanics*, 2010. **43**(9): p. 1674-1681.
122. Vicars, R., *Wear simulation of lumbar total disc replacements*, in *School of Mechanical Engineering 2009*, University of Leeds: Leeds.
123. Serhan, H.A., A.P. Dooris, M.L. Parsons, P.J. Ares, and S.M. Gabriel, *In vitro wear assessment of the Charite Artificial Disc according to ASTM recommendations*. *Spine*, 2006. **31**(17): p. 1900-10.
124. Kang, L., A.L. Galvin, T.D. Brown, Z. Jin, and J. Fisher, *Quantification of the effect of cross-shear on the wear of conventional and highly cross-linked UHMWPE*. *Journal of Biomechanics*, 2008. **41**(2): p. 340-346.
125. Turell, M., A. Wang, and A. Bellare, *Quantification of the effect of cross-path motion on the wear rate of ultra-high molecular weight polyethylene*. *Wear*. **255**(7-12): p. 1034-1039.
126. Wang, A., D.C. Sun, S.S. Yau, B. Edwards, M. Sokol, A. Essner, V.K. Polineni, C. Stark, and J.H. Dumbleton, *Orientation softening in the deformation and wear of ultra-high molecular weight polyethylene*. *Wear*, 1997. **203**: p. 230-241.
127. ISO-18192-1, *Implants for surgery – wear of total intervertebral spinal disc prostheses, Part 1: Loading and displacement parameters for wear testing and corresponding environmental conditions for test*, D.C. Kaddick, Editor 2008-01-29, ISO.

128. Vicars, R., P.J. Hyde, T. Brown, J. Tipper, E. Ingham, J. Fisher, and R.M. Hall, *The effect of anterior-posterior shear load on the wear of ProDisc-L TDR*. *European Spine Journal*, 2010. **19**(8): p. 2010, 1356-1362.
129. Rawlinson, J.J., K.P. Punga, K.L. Gunsallus, D.L. Bartel, and T.M. Wright, *Wear simulation of the ProDisc-L disc replacement using adaptive finite element analysis*. *Journal of Neurosurgery: Spine*, 2007. **7**(2): p. 165-173.
130. Vicars, R., P. Prokopovich, T.D. Brown, J.L. Tipper, E. Ingham, J. Fisher, and R.M. Hall, *The Effect of Anterior-Posterior Shear on the Wear of Charite Total Disc Replacement*. *Spine*, 2012. **37**(9): p. E528-E534  
10.1097/BRS.0b013e31823cbd6e.
131. Kurtz, S.M., A. Patwardhan, D. MacDonald, L. Ciccarelli, A. Van Ooij, M. Lorenz, M. Zindrick, P. O'Leary, J. Isaza, and R. Ross, *What is the correlation of in vivo wear and damage patterns with in vitro TDR motion response?* *Journal*, 2008. **33**(5): p. 481-489.
132. Williams, S., D. Jalali-Vahid, C. Brockett, Z. Jin, M.H. Stone, E. Ingham, and J. Fisher, *Effect of swing phase load on metal-on-metal hip lubrication, friction and wear*. *Journal of Biomechanics*, 2006. **39**(12): p. 2274-2281.
133. Leslie, I., S. Williams, J. Anderson, G. Isaac, E. Ingham, and J. Fisher, *Increased wear of hip surface replacements with high cup angle and head lateralisation in vitro*. *Journal of Biomechanics*, 2008. **41**(Supplement 1): p. S6-S6.
134. Dowson, D., M.P.G.D. D. Dowson, and A.A. Lubrecht, *The relationship between steady-state wear rate and theoretical film thickness in metal-on-metal total replacement hip joints*, in *Tribology and Interface Engineering Series*. 2003, Elsevier. p. 273-280.
135. Mathews, H.H., J.-C. LeHuec, T. Friesem, T. Zdeblick, and L. Eisermann, *Design rationale and biomechanics of Maverick Total Disc arthroplasty with early clinical results*. *The Spine Journal*, 2004. **4**(6, Supplement 1): p. S268-S275.
136. Anderson, P.A., S.M. Kurtz, and J.M. Toth, *Explant Analysis of Total Disc Replacement*. *Seminars in Spine Surgery*, 2006. **18**(2): p. 109-116.
137. Tipper, J.L., E. Ingham, Z.M. Jin, and J. Fisher, *(iv) The science of metal-on-metal articulation*. *Current Orthopaedics*, 2005. **19**(4): p. 280-287.
138. Kurtz, S.M., M. Steinbeck, A. Ianuzzi, A. van Ooij, I.M. Punt, J. Isaza, and E.R.S. Ross, *Retrieval Analysis of Motion Preserving Spinal Devices and Periprosthetic Tissues*. *SAS Journal*, 2009. **In Press, Accepted Manuscript**.
139. Devin, C.J., T.G. Myers, and J.D. Kang, *Chronic failure of a lumbar total disc replacement with osteolysis. Report of a case with nineteen-year follow-up*. *Journal of Bone & Joint Surgery - American Volume*, 2008. **90**(10): p. 2230-4.
140. Punt, I.M., J.P.M. Cleutjens, T. de Bruin, P.C. Willems, S.M. Kurtz, L.W. van Rhijn, G.W.H. Schurink, and A. van Ooij, *Periprosthetic tissue reactions observed at revision of total intervertebral disc arthroplasty*. *Biomaterials*, 2009. **30**(11): p. 2079-2084.
141. Punt, I., R. Baxter, A.v. Ooij, P. Willems, L.v. Rhijn, S. Kurtz, and M. Steinbeck, *Submicron sized ultra-high molecular weight polyethylene wear particle analysis from revised SB Charité III total disc replacements*. *Acta Biomaterialia*, 2011. **In Press, Uncorrected Proof**.
142. van Ooij, A., S.M. Kurtz, F. Stessels, H. Noten, L. van Rhijn, A. van Ooij, S.M. Kurtz, F. Stessels, H. Noten, and L. van Rhijn, *Polyethylene wear debris and long-term clinical failure of the Charite disc prosthesis: a study*

- of 4 patients. [erratum appears in *Spine*. 2007 Apr 20;32(9):1052]. *Spine*, 2007. **32**(2): p. 223-9.
143. Fisher, J., A. Galvin, J. Tipper, T. Stewart, M. Stone, and E. Ingham, *Comparison of the Functional Biological Activity and Osteolytic Potential of Ceramic on Ceramic and Cross Linked Polyethylene Bearings in the Hip*, in *Bioceramics and Alternative Bearings in Joint Arthroplasty*. 2005. p. 21-24.
  144. Ingham, E. and J. Fisher, *The role of macrophages in osteolysis of total joint replacement*. *Biomaterials*, 2005. **26**(11): p. 1271-1286.
  145. Fisher, J., *A stratified approach to pre-clinical tribological evaluation of joint replacements representing a wider range of clinical conditions advancing beyond the current standard*. *Faraday Discussions*, 2012. **156**(0): p. 59-68.
  146. Wang, A., V.K. Polineni, A. Essner, C. Stark, and J.H. Dumbleton. *The impact of lubricant protein concentration on the outcome of hip joint simulator testing*. in *45th Annual Meeting of the Orthopaedic Research Society*. 1999. Anaheim, California.
  147. Paré, P.E., F.W. Chan, S. Bhattacharya, and V.K. Goel, *Surface slide track mapping of implants for total disc arthroplasty*. *Journal of Biomechanics*, 2009. **42**(2): p. 131-139.
  148. Vicars, R., J. Fisher, N. Heyes, R. Birrell, and R.M. Hall, *Verification of a novel spine wear simulator*, in *British Orthopaedic Research Society Annual Conference 2007*: Manchester, UK.
  149. Cornwall, G.B., J.T. Bryant, C.M. Hansson, J. Rudan, L.A. Kennedy, and T.D. Cooke, *A quantitative technique for reporting surface degradation patterns of UHMWPE components of retrieved total knee replacements*. *J Appl Biomater*, 1995. **6**(1): p. 9-18.
  150. Goreham-Voss, C., R. Vicars, R. Hall, and T. Brown, *Preferential superior surface motion in wear simulations of the Charité total disc replacement*. *European Spine Journal*, 2009.
  151. Galvin, A.L., J.L. Tipper, L.M. Jennings, M.H. Stone, Z.M. Jin, E. Ingham, and J. Fisher, *Wear and biological activity of highly crosslinked polyethylene in the hip under low serum protein concentrations*. *Proceedings of the Institution of Mechanical Engineers, Part H: Journal of Engineering in Medicine*, 2007. **221**(1): p. 1-10.
  152. Endo, M., J.L. Tipper, D.C. Barton, M.H. Stone, E. Ingham, and J. Fisher, *Comparison of wear, wear debris and functional biological activity of moderately crosslinked and non-crosslinked polyethylenes in hip prostheses*. *Proceedings of the Institution of Mechanical Engineers Part H - Journal of Engineering in Medicine*, 2002. **216**(2): p. 111-22.
  153. Essner, A., G. Schmidig, and A. Wang, *The clinical relevance of hip joint simulator testing: In vitro and in vivo comparisons*. *Wear*, 2005. **259**(7-12): p. 882-886.
  154. McKellop, H.A.P., P.B. Campbell, S.-H.P. Park, T.P.M.D. Schmalzried, P.M.D.P. Grigoris, H.C.M.D. Amstutz, and A.M.D. Sarmiento, *The Origin of Submicron Polyethylene Wear Debris in Total Hip Arthroplasty*. *Clinical Orthopaedics & Related Research* February, 1995. **311**: p. 3-20.
  155. Bell, C.J., P.S. Walker, S. Sathasivam, G.W. Blunn, and P.A. Campbell, *Differences in wear between fixed bearing and mobile bearing knees*. *Journal of Biomechanics*, 1998. **31**, Supplement 1(0): p. 24.

156. Fisher, J., H. McEwen, J. Tipper, L. Jennings, R. Farrar, M. Stone, and F. Ingham, *Wear-simulation analysis of rotating-platform mobile-bearing knees*. Orthopedics, 2006. **29**(9): p. S36-S41.
157. Grupp, T.M., C. Kaddick, J. Schwiesau, A. Maas, and S.D. Stulberg, *Fixed and mobile bearing total knee arthroplasty - Influence on wear generation, corresponding wear areas, knee kinematics and particle composition*. Clinical Biomechanics, 2009. **24**(2): p. 210-217.
158. Grupp, T.M., S.D. Stulberg, C. Kaddick, J. Schwiesau, B. Fritz, A. Maas, and W. Blömer, *Biotribology in total knee arthroplasty - in vitro wear generation, knee kinematics and particle composition for fixed and mobile bearing designs*. Journal of Biomechanics, 2008. **41**(Supplement 1): p. S230-S231.
159. McEwen, H.M.J., P.I. Barnett, C.J. Bell, R. Farrar, D.D. Auger, M.H. Stone, and J. Fisher, *The influence of design, materials and kinematics on the in vitro wear of total knee replacements*. Journal of Biomechanics, 2005. **38**(2): p. 357-365.
160. Galvin, A.L., L. Kang, I. Udofia, L.M. Jennings, H.M. McEwen, Z. Jin, and J. Fisher, *Effect of conformity and contact stress on wear in fixed-bearing total knee prostheses*. J Biomech, 2009. **42**(12): p. 1898-902.
161. Barbour, P.S., D.C. Barton, and J. Fisher, *The influence of stress conditions on the wear of UHMWPE for total joint replacements*. J Mater Sci Mater Med, 1997. **8**(10): p. 603-11.
162. Vassiliou, K. and A. Unsworth, *Is the wear factor in total joint replacements dependent on the nominal contact stress in ultra-high molecular weight polyethylene contacts?* Proceedings of the Institution of Mechanical Engineers Part H - Journal of Engineering in Medicine, 2004. **218**(2): p. 101-7.
163. Abdelgaied, A., F. Liu, C. Brockett, L. Jennings, J. Fisher, and Z. Jin, *Computational wear prediction of artificial knee joints based on a new wear law and formulation*. Journal of Biomechanics. **44**(6): p. 1108-1116.
164. Kurtz, S., A. Patwardhan, A. Van Ooij, M. Lorenz, M. Zindrick, O.L. Patrick, J. Peloza, R. Ross, L. Ciccarelli, R. Siskey, and M.L. Villarraga, *4:2887. What Is the Correlation of In Vivo Wear and Fracture Patterns With In Vitro TDR Motion Response?* The Spine Journal, 2006. **6**(5, Supplement 1): p. 43S-43S.
165. O'Leary, P., M. Nicolakis, M.A. Lorenz, L.I. Voronov, M.R. Zindrick, A. Ghanayem, R.M. Havey, G. Carandang, M. Sartori, I.N. Gaitanis, S. Fronczak, and A.G. Patwardhan, *Response of Charité total disc replacement under physiologic loads: prosthesis component motion patterns*. The Spine Journal, 2005. **5**(6): p. 590-599.
166. Garling, E.H., B.L. Kaptein, R.G.H.H. Nelissen, and E.R. Valstar, *Limited rotation of the mobile-bearing in a rotating platform total knee prosthesis*. Journal of Biomechanics, 2007. **40**, **Supplement 1**(0): p. S25-S30.
167. Barbour, P.S.M., D.C. Barton, and J. Fisher, *The influence of contact stress on the wear of UHMWPE for total replacement hip prostheses*. Wear, 1995. **181-183**(1): p. 250-257.
168. Hyde, P., R. Vicars, J. Fisher, and R. Hall, *Wear simulation of total disc arthroplasties: Sensitivity to device design and test parameters*. Journal of ASTM International, 2011. **9**(2): p. 51-65.

169. Kurtz, S.M., A. van Ooij, R. Ross, J. de Waal Malefijt, J. Pelozo, L. Ciccarelli, and M.L. Villarraga, *Polyethylene wear and rim fracture in total disc arthroplasty*. The Spine Journal, 2007. 7(1): p. 12-21.
170. Kurtz, S.M., J. Pelozo, R. Siskey, and M.L. Villarraga, *Analysis of a retrieved polyethylene total disc replacement component*. The Spine Journal, 2005. 5(3): p. 344-350.
171. Scott-Young, M. *Clinical outcome of two-level total disc replacement in 84 patients with minimum 5 years follow-up*. in ISASS2012. 2012. Barcelona.
172. Choma, T.J., J. Miranda, R. Siskey, R. Baxter, M.J. Steinbeck, S.M. Kurtz, T.J. Choma, J. Miranda, R. Siskey, R. Baxter, M.J. Steinbeck, and S.M. Kurtz, *Retrieval analysis of a ProDisc-L total disc replacement*. Journal of Spinal Disorders & Techniques, 2009. 22(4): p. 290-6.
173. Fisher, J., H.M.J. McEwen, P.I. Barnett, C.J. Bell, T.D. Stewart, M.H. Stone, and E. Ingham, *(i) Wear of polyethylene in artificial knee joints*. Current Orthopaedics, 2001. 15(6): p. 399-405.
174. Tipper, J.L., R.E. Vicars, T.D. Brown, E. Ingham, J. Fisher, and R.M. Hall. *Quantitative comparison of UHMWPE wear particles from Prodisc-L total disc replacements tested under ISO and ISO plus anterior-posterior shear*. in BORS. 2012. Cambridge: Journal of Bone & Joint Surgery, British Volume.
175. Austen, S., I.M. Punt, J.P. Cleutjens, P.C. Willems, S.M. Kurtz, D.W. Macdonald, L.W. van Rhijn, and A. van Ooij, *Clinical, radiological, histological and retrieval findings of Activ-L and Mobidisc total disc replacements: a study of two patients*. Eur Spine J. 4: p. 513-20.
176. Berry, M.R., B.G. Peterson, and D.H. Alander, *A Granulomatous Mass Surrounding a Maverick Total Disc Replacement Causing Iliac Vein Occlusion and Spinal Stenosis: A Case Report*. J Bone Joint Surg Am, 2010. 92(5): p. 1242-1245.
177. Guyer, R.D., J. Shellock, B. MacLennan, D. Hanscom, R.Q. Knight, P. McCombe, J.J. Jacobs, R.M. Urban, D. Bradford, and D.D. Ohnmeiss, *Early failure of metal-on-metal artificial disc prostheses associated with lymphocytic reaction: diagnosis and treatment experience in four cases*. Spine, 2011. 36(7): p. E492-7.
178. Morlock, M.M., N. Bishop, J. Zustin, M. Hahn, W. Ruther, and M. Amling, *Modes of implant failure after hip resurfacing: morphological and wear analysis of 267 retrieval specimens*. J Bone Joint Surg Am, 2008. 3: p. 89-95.
179. Golish, S.R. and P.A. Anderson, *Bearing surfaces for total disc arthroplasty: metal-on-metal versus metal-on-polyethylene and other biomaterials*. The Spine Journal, (0).
180. Harris, W.H., A.L. Schiller, J.M. Scholler, R.A. Freiberg, and R. Scott, *Extensive localized bone resorption in the femur following total hip replacement*. The Journal of bone and joint surgery. American volume, 1976. 58(5): p. 612-618.
181. Pare, P.E.C., F. W. Buchholz, P. Kurtz, S. Peter, M., *Surface Texture Analysis of Artificial Discs Wear-Tested under Different Conditions and Comparison to a Retrieved Implant*. Journal of ASTM International, 2006. 3(5): p. 65-74.
182. Dowson, D., C. Hardaker, M. Flett, and G.H. Isaac, *A hip joint simulator study of the performance of metal-on-metal joints: Part II: design*. J Arthroplasty, 2004. 19(8 Suppl 3): p. 124-30.



183. St John, K.R., L.D. Zardiackas, and R.A. Poggie, *Wear evaluation of cobalt-chromium alloy for use in a metal-on-metal hip prosthesis*. J Biomed Mater Res B Appl Biomater, 2004. **68**(1): p. 1-14.
184. Kurtz SM, S.R., Ciccarelli L, van Ooij A, Pelozo J, Villarraga ML, *Retrieval Analysis of Total Disc Replacements: Implications for Standardized Wear Testing*. JAI, 2006. **3**(3): p. 12.
185. Prokopovich, P., S. Perni, J. Fisher, and R.M. Hall, *Spatial variation of wear on Charit<sup>Å</sup> lumbar discs*. Acta Biomaterialia, 2012. **7**(11): p. 3914-3926.
186. Vicars, R.K., Steven; MacDonald, Dan; Brown, Tom; Tipper, Joanne; Fisher, John; Ingham, Eileen; Hall, Richard. *Height loss comparison between ex-vivo and in-vitro TDR*. in ORS. 2010. New Orleans, LA.
187. McKellop, H., S.H. Park, R. Chiesa, P. Doorn, B. Lu, P. Normand, P. Grigoris, and H. Amstutz, *In vivo wear of three types of metal on metal hip prostheses during two decades of use*. Clin Orthop Relat Res, 1996. **329**(40): p. S128-40.
188. Kang, L., A.L. Galvin, T.D. Brown, J. Fisher, and Z.M. Jin, *Wear simulation of ultra-high molecular weight polyethylene hip implants by incorporating the effects of cross-shear and contact pressure*. Proceedings of the Institution of Mechanical Engineers Part H - Journal of Engineering in Medicine, 2008. **222**(7): p. 1049-64.
189. Brockett, C., *Tribology of Large Diameter Metal-on-Metal Hip Resurfacing Replacements*, in *Mechanical Engineering 2007*, University of Leeds: Leeds.
190. Zdero, R., P.V. Fenton, J. Rudan, and J.T. Bryant, *Fuji film and ultrasound measurement of total knee arthroplasty contact areas*. The Journal of Arthroplasty, 2001. **16**(3): p. 367-375.
191. Wang, A., A. Essner, V.K. Polineni, C. Stark, and J.H. Dumbleton, *Lubrication and wear of ultra-high molecular weight polyethylene in total joint replacements*. Tribology International, 1998. **31**(1-3): p. 17-33.
192. Fisher, J., *Wear of ultra high molecular weight polyethylene in total artificial joints*. Current Orthopaedics, 1994. **8**(3): p. 164-169.
193. Sathasivam, S. and P.S. Walker, *Optimization of the bearing surface geometry of total knees*. Journal of Biomechanics, 1994. **27**(3): p. 255-264.
194. Wenzel, S.A., D.E. Shepherd, and D.E.T. Shepherd, *Contact stresses in lumbar total disc arthroplasty*. Bio-Medical Materials & Engineering, 2007. **17**(3): p. 169-73.
195. Hall, R.M., A. Unsworth, B.M. Wroblewski, and C. Hardaker, *Tribological characterisation of explanted charnley hip prostheses*. Journal of Biomechanics, 1994. **27**(6): p. 831-831.
196. Saikko, V. and T. Ahlroos, *Type of motion and lubricant in wear simulation of polyethylene acetabular cup*. Proceedings of the Institution of Mechanical Engineers Part H - Journal of Engineering in Medicine, 1999. **213**(4): p. 301-10.
197. Udofia, I.J. and Z.M. Jin, *Elastohydrodynamic lubrication analysis of metal-on-metal hip-resurfacing prostheses*. Journal of Biomechanics, 2003. **36**(4): p. 537-544.
198. Schmidt, T.A., H.S. An, T.H. Lim, B.H. Nowicki, and V.M. Haughton, *The stiffness of lumbar spinal motion segments with a high-intensity zone in the anulus fibrosus*. Spine, 1976. **23**(20): p. 2167-73.
199. Panjabi, M.M., M.H. Krag, and T.Q. Chung, *Effects of disc injury on mechanical behavior of the human spine*. Spine, 1984. **9**(7): p. 707-713.

200. Andersson, G.B.J., M.A.R. Freeman, and S.A.V. Swanson, *Loosening of the cemented acetabular cup in total hip replacement*. Journal of Bone & Joint Surgery, British Volume, 1972. **54-B(4)**: p. 590-599.
201. Brockett, C., S. Williams, Z. Jin, G. Isaac, and J. Fisher, *Friction of total hip replacements with different bearings and loading conditions*. J Biomed Mater Res B Appl Biomater, 2007. **81(2)**: p. 508-15.
202. Moghadas, P., A. Mahomed, D.W.L. Hukins, and D.E.T. Shepherd, *Friction in metal-on-metal total disc arthroplasty: Effect of ball radius*. Journal of Biomechanics, 2012. **45(3)**: p. 504-509.
203. Archard, J.F., *Elastic Deformation and the Laws of Friction*. Proceedings of the Royal Society of London. Series A, Mathematical and Physical Sciences, 1957. **243(1233)**: p. 190-205.
204. Hall, R.M., A. Unsworth, B.M. Wroblewski, and I.C. Burgess, *Frictional characterisation of explanted Charnley hip prostheses*. Wear, 1994. **175(1-2)**: p. 159-166.
205. B. Weightman, S.S., I. Paul, R. Rose, E. Radin, *Lubrication mechanisms of hip joint replacement prostheses*. J. Lubrication Technol., 1972. **4**: p. 131-135.
206. Kurtz, S.M., C.M. Rimnac, L. Pruitt, C.W. Jewett, V. Goldberg, and A.A. Edidin, *The relationship between the clinical performance and large deformation mechanical behavior of retrieved UHMWPE tibial inserts*. Biomaterials, 2000. **21(3)**: p. 283-91.
207. Unsworth, A., R.M. Hall, I.C. Burgess, B.M. Wroblewski, R.M. Streicher, and M. Semlitsch, *Frictional resistance of new and explanted artificial hip joints*. Wear, 1995. **190(2)**: p. 226-231.
208. Pare, P.E., F.W. Chan, and M.L. Powell, *Wear characterization of the A-MAVâ, ç anterior motion replacement using a spine wear simulator*. Wear, 2007. **263(7â€“12)**: p. 1055-1059.
209. Al-Hajjar, M., I.J. Leslie, J. Tipper, S. Williams, J. Fisher, and L.M. Jennings, *Effect of cup inclination angle during microseparation and rim loading on the wear of BIOLOX® delta ceramic-on-ceramic total hip replacement*. Journal of Biomedical Materials Research Part B: Applied Biomaterials, 2011. **95B(2)**: p. 263-268.
210. Kang, L., A.L. Galvin, Z.M. Jin, and J. Fisher, *Computational modelling and experimental measurement of effect of cross-shear on wear of polyethylene*. Journal of Biomechanics, 2006. **39(Supplement 1)**: p. S143-S143.

## Appendix A: Publications Arising From Thesis

### Published Papers

- Hyde, P., R. Vicars, J. Fisher, and R. Hall. *Wear simulation of total disc arthroplasties: Sensitivity to device design and test parameters*. 2010, San Antonio, TX, United states: American Society for Testing and Materials. 2011. 9(2)
- Goreham-Voss, C.M., P.J. Hyde, R.M. Hall, J. Fisher, and T.D. Brown, *Experimental Validation of a Computational Wear Model for Total Disc Replacements Under Low- and High-Cross-Shear Conditions*, 2009, Departments of Orthopaedics and Biomedical Engineering, University of Iowa, Iowa City, IA. <sup>2</sup>Institute of Medical and Biological Engineering, University of Leeds, Leeds, UK.
- Goreham-Voss, C.M., P.J. Hyde, R.M. Hall, J. Fisher, and T.D. Brown, *Cross-shear implementation in sliding-distance-coupled finite element analysis of wear in metal-on-polyethylene total joint arthroplasty: Intervertebral total disc replacement as an illustrative application*. *Journal of Biomechanics*, 2010. 43(9): p. 1674-1681.
- Vicars, R., P.J. Hyde, T. Brown, J. Tipper, E. Ingham, J. Fisher, and R.M. Hall, *The effect of anterior-posterior shear load on the wear of ProDisc-L TDR*. *European Spine Journal*, 2010. 19(8): p. 2010, 1356-1362.

### Published Abstracts

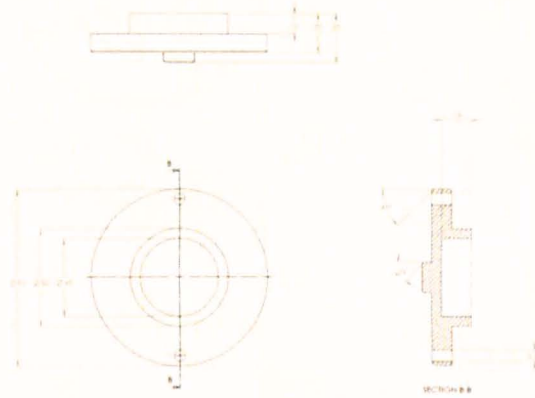
- Hyde, P., R. Vicars, J. Fisher, T. Brown, and R.M. Hall. *Prodisc-L lumbar total disc replacement wear sensitivity to changes in input kinematics and loading*. in *BORS*. 2012. Cardiff: Journal of Bone & Joint Surgery, British Volume.
- Hyde, P., J. Fisher, and R. Hall. *Friction in metal-on-polyethylene lumbar total disc replacements*. *BORS 2012*. Cambridge: Journal of Bone & Joint Surgery, British Volume.

- Hyde, P., R. Vicars, J. Fisher, and R. Hall. *Total disc replacement wear sensitivity to device design and input kinematics*. 2010. San Antonio, TX, United States: American Society for Testing and Materials. 2010
- Hyde, P., J. Fisher, and R. Hall. *Investigating TDR wear-rate sensitivity to phasing, loading and forward bending*. 2011. Las Vegas, NA, United States, Journal of ISASS
- Tipper, J.L., R.E. Vicars, T.D. Brown, E. Ingham, J. Fisher, and R.M. Hall. *Quantitative comparison of UHMWPE wear particles from Prodisc-L total disc replacements tested under ISO and ISO plus anterior-posterior shear*. in *BORS*. 2012. Cambridge: Journal of Bone & Joint Surgery, British Volume.

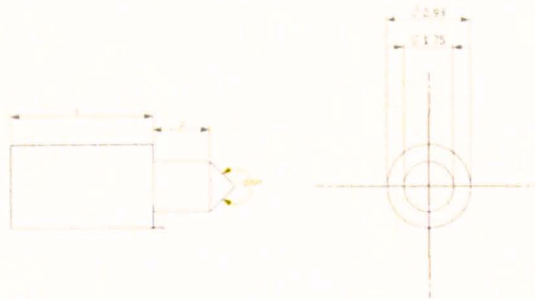
#### International Oral Presentations

- ASTM, Static and Dynamic Spinal Implants: Are We Evaluating Them Appropriately? *Total disc replacement wear sensitivity to device design and input kinematics*. San Antonio, Nov 2010
- International Society for the Advancement of Spine Surgery. *Investigating Lumbar TDR wear-rate sensitivity to phasing, loading and forward bending*. Las Vegas, May 2011
- International Society for the Advancement of Spine Surgery. *In Vitro Lumbar TDA Wear Rate Susceptibility Depends on Phasing of Motions and Device Design*. Barcelona, March 2012


## Appendix B: Motion Tracking Equipment



New inferior holder needed to mount motion track components in spine simulator

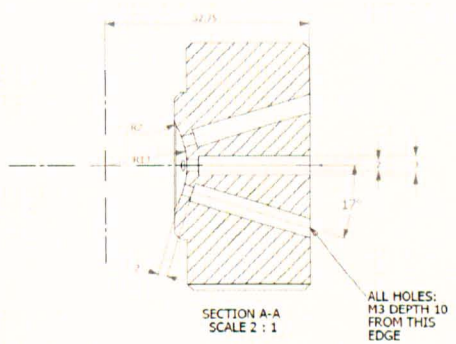
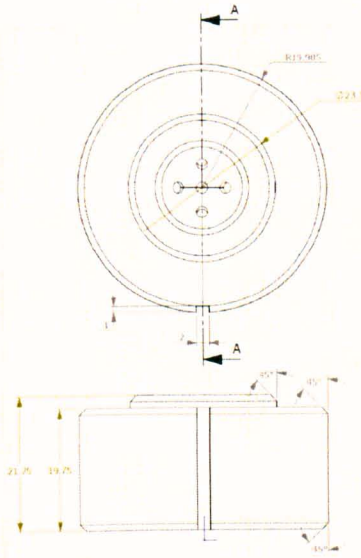


MATERIAL: DELRIN  
20 REQUIRED  
REMOVE ALL BURS AND  
SHARP EDGES

 UNIVERSITY OF LEEDS School of Mechanical Engineering

NAME SCRIBER  
DATE

Scriber used to mark surface of the bearings



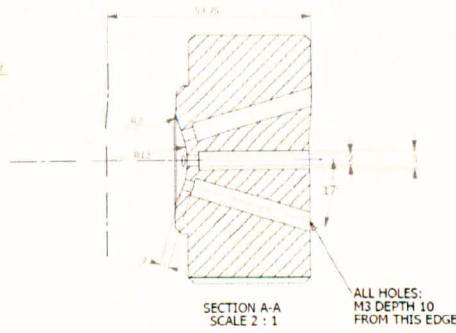
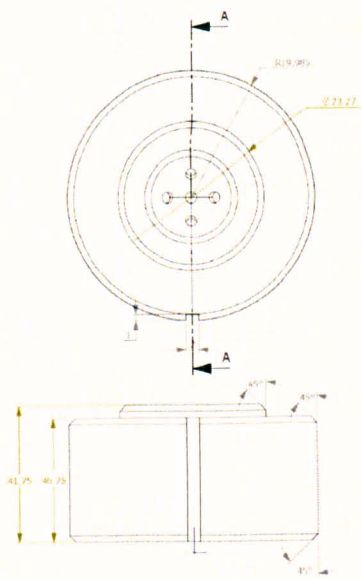
ALL HOLES:  
M3 DEPTH 10  
FROM THIS  
EDGE

MATERIAL: 303 STEEL  
ENSURE EDGES OF HOLES  
ON DISH HAVE FILET  
REMOVE ALL BURS AND  
SHARP EDGES

UNIVERSITY OF LEEDS School of Mechanical Engineering

NAME CHARITE LOWER  
DATE

Inferior Charité component



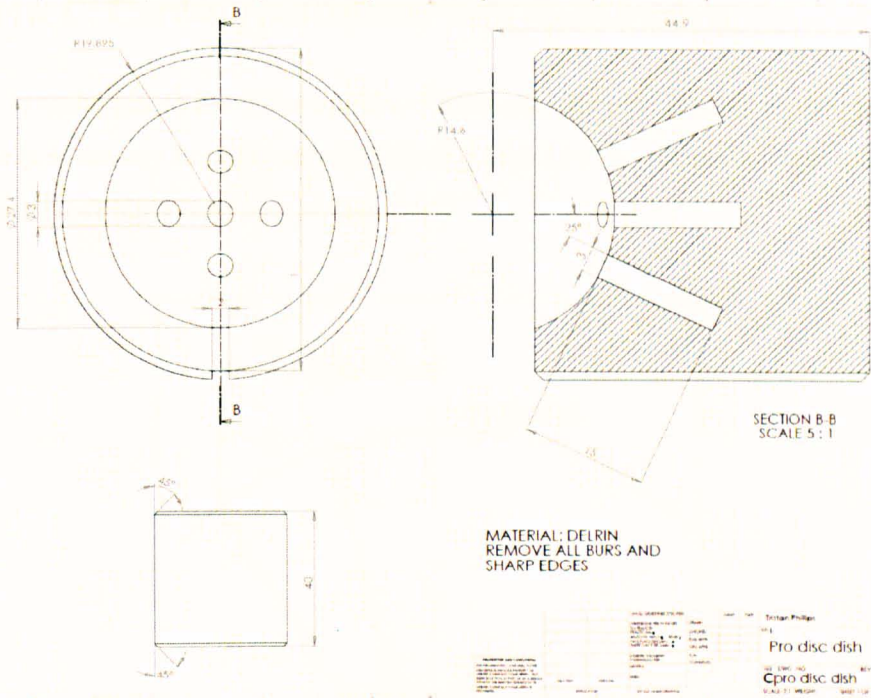
ALL HOLES:  
M3 DEPTH 10  
FROM THIS  
EDGE

MATERIAL: 303 STEEL  
ENSURE HOLES ON DISH  
HAVE FILET EDGE  
REMOVE ALL BURS AND  
SHARP EDGES

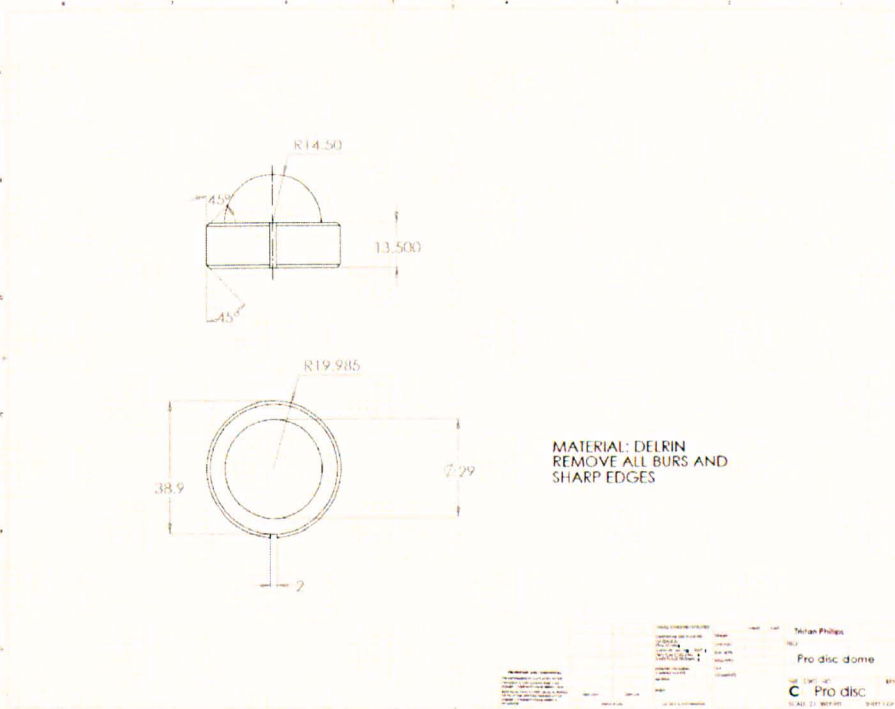
UNIVERSITY OF LEEDS School of Mechanical Engineering

NAME UPPER CHARITE  
DATE

Superior Charité component



Superior Prodisc component



Inferior Prodisc component

## Appendix C: Curvature of Motion Path Measurement

In order to compensate for the curvature of the bearing surface in the motion path image, it is necessary to apply some basic trigonometry. A schematic representation of the bearing surface is shown in Figure 8-1.

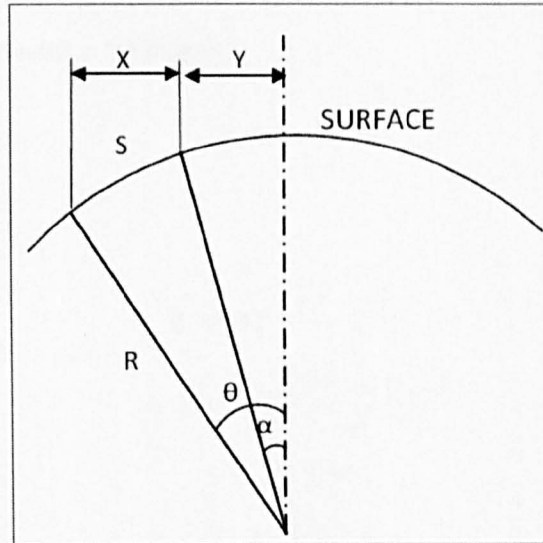


Figure 8-1 Bearing surface with motion path length shown Y mm away from the central position

1.

$$1s = R(\theta - \alpha)$$

Using trigonometry :

2.

$$\sin\theta = \frac{x+y}{R}$$

3.

$$\sin\alpha = \frac{y}{R}$$

4.

$$\theta = \sin^{-1}\left(\frac{x+y}{R}\right)$$

5.

$$\alpha = \sin^{-1}\left(\frac{y}{R}\right)$$

Substitute equation (4) & (5) into (1) :



6.

$$s = R[\sin^{-1}\left(\frac{x+y}{R}\right) - \sin^{-1}\left(\frac{y}{R}\right)]$$

Equation 6 will be used to calculate the actual length for three length of motion track in position 1 and 3 and the width for position 2 and 4.

An example calculation for the width of motion track on charite disc under pure ISO motions. Measured width = 0.698mm

$$x = 0.698\text{mm}$$

$$y = 4.2\text{mm}$$

$$R = 13\text{mm}$$

$$\theta = \sin^{-1}\left(\frac{x+y}{R}\right)$$

$$\theta = \sin^{-1}\frac{0.698 + 4.2}{13}$$

$$\theta = 22.134^\circ$$

$$\alpha = \sin^{-1}\left(\frac{y}{R}\right)$$

$$\alpha = \sin^{-1}\left(\frac{4.2}{13}\right)$$

$$\alpha = 18.849^\circ$$

$$s = R(\theta - \alpha)$$

$$S = 13(22.134^\circ - 18.849^\circ)$$

$$S = 0.745252\text{mm}$$

Therefore the actual length of the motion track is 0.745252mm.

## Appendix D: Possible Source of Error in Friction Simulator Design

The friction measurement is based on loads recorded at the transducer ( $F+F_e$ ). The error load ( $F_e$ ) is a result of an offset (from CoR) load, demonstrated in Figure 8-2 by  $L$ . The resultant torque produced by the offset  $L$  is  $F_e \cdot x_e$  and therefore can give rise to systemic error. To avoid this, knowledge of how the measurement of friction is made and how to cancel the effect of the error is needed. Outlined below is a systematic description of how error occurs and the method by which it is reduced or eliminated.

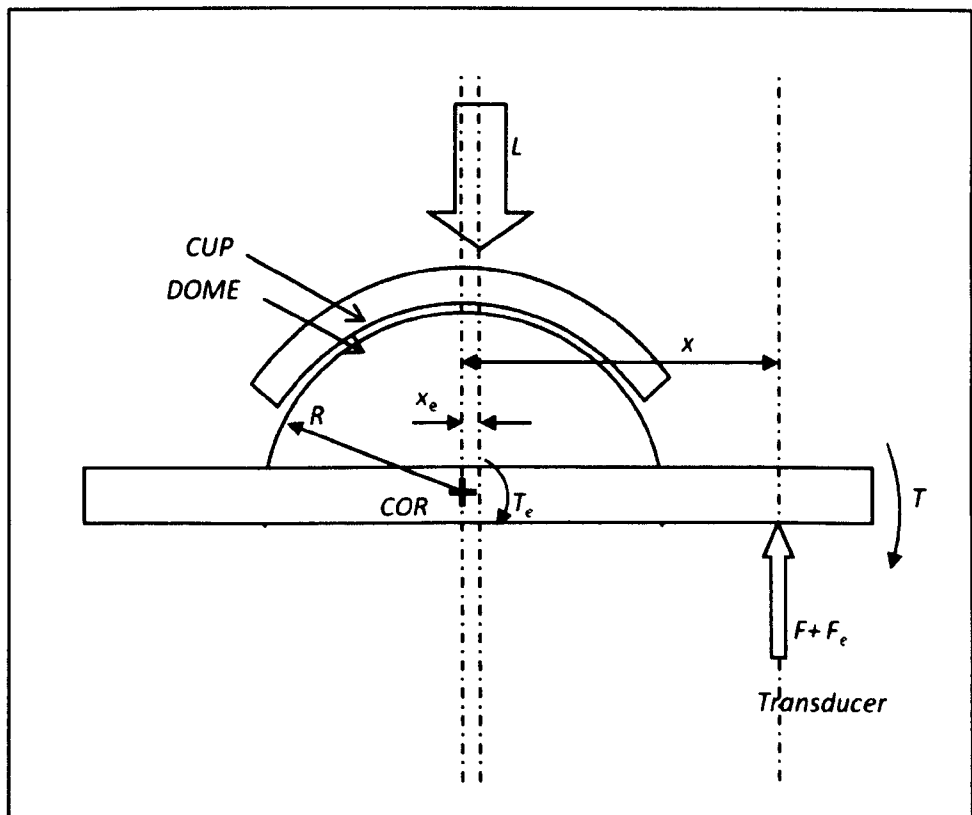


Figure 8-2 Simplified friction simulator with TDR cup and dome components – the cup is loaded (offset centre loading shown) and rotated against the dome with the resulting torque on the dome measured at the transducer ( $F+F_e$ )

Peizelectric force transducer measures friction force,  $F$

Length from  $CoR$ ,  $x$

Length from  $CoR$  to line of action of load,  $x_e$

$CoR$  offset by  $x_e$  gives rise to force error component,  $F_e$

Friction factor,  $f$ , calculated from  $F$

Torque at transducer,  $T = F \cdot x$

Force at transducer,  $F = f \cdot L$

For friction simulator, friction factor,  $f = T/r \cdot L$

Torque from eccentric loading,  $T_e = L \cdot x_e$

Reaction forces at transducer due to offset load (Figure 8-3):

$$F_e = T_e/x_e \quad T_e = L \cdot x_e \quad \text{therefore } F_e = L \cdot x_e/x \quad (x_e \text{ is variable, } x \text{ is constant})$$

Positive cycle, friction force is +ve, error is +ve:  $F + F_e$

Positive cycle, friction force is -ve, error is +ve:  $-F + F_e$

When using a constant load ( $L$ ) the friction force ( $F$ ) is half of the difference between fwd (+ve) and rev (-ve) values:  $[(F + F_e) - (-F + F_e)]/2 = 2F/2 = F$

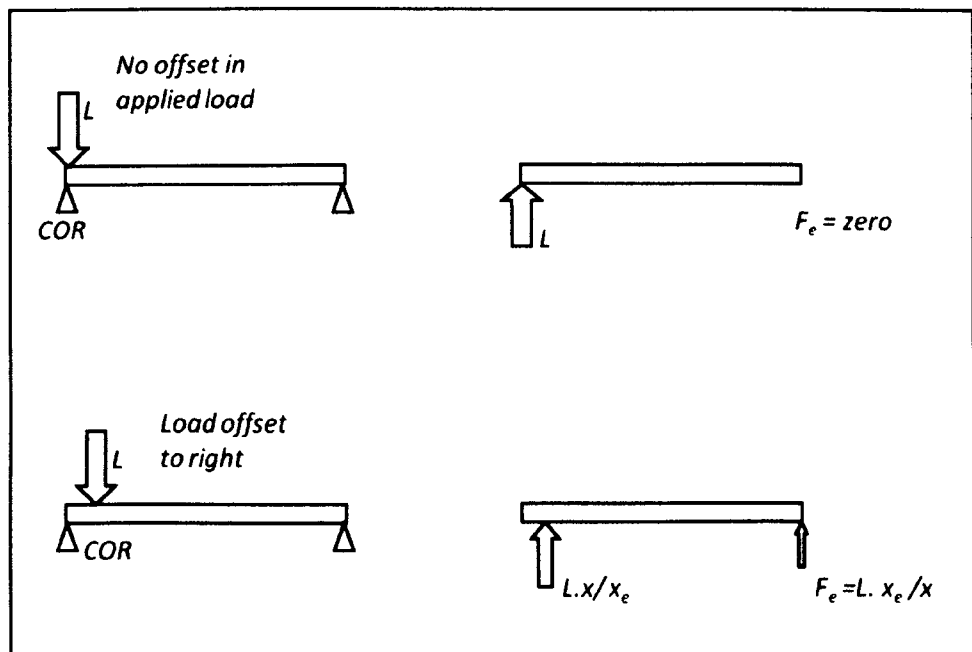
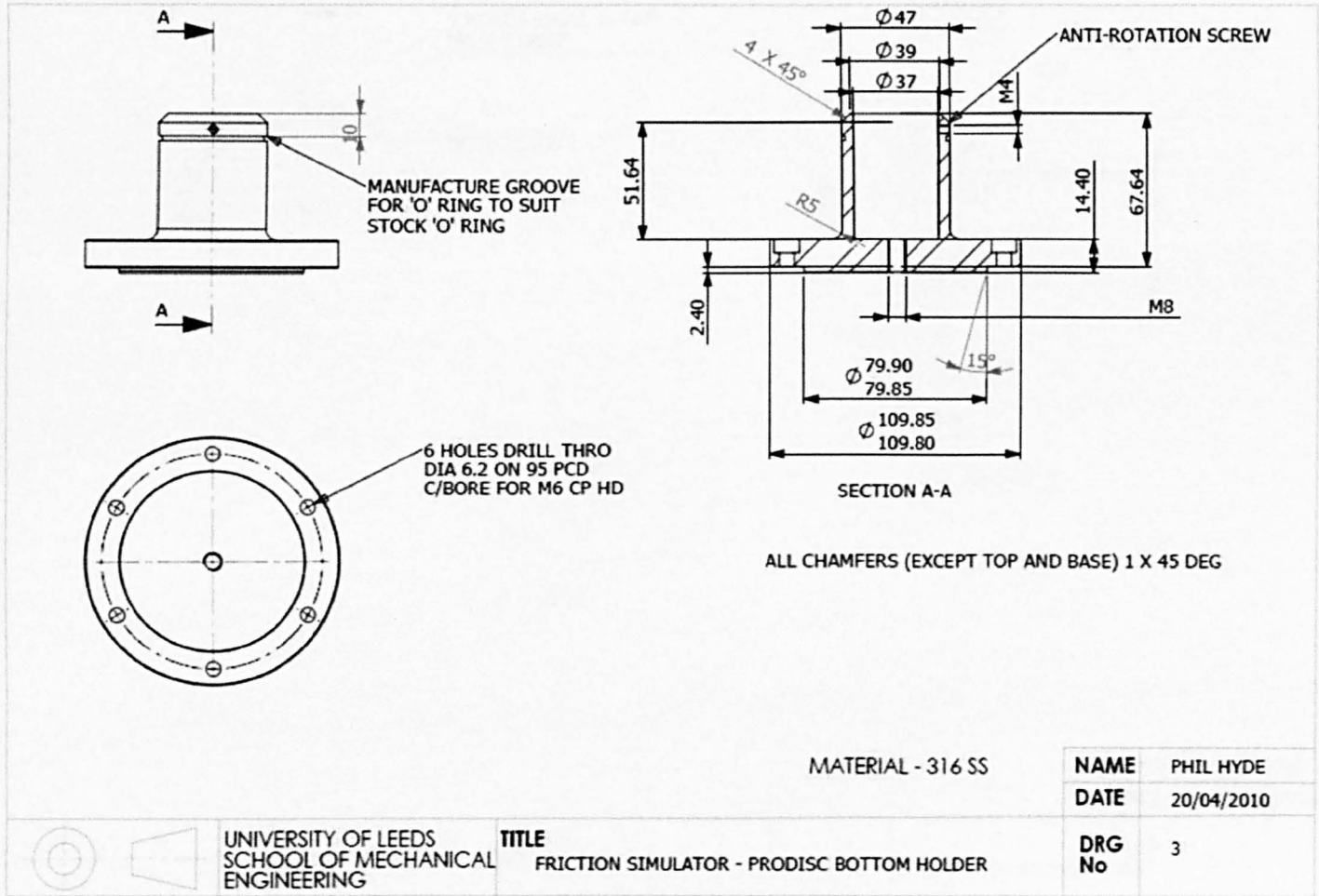


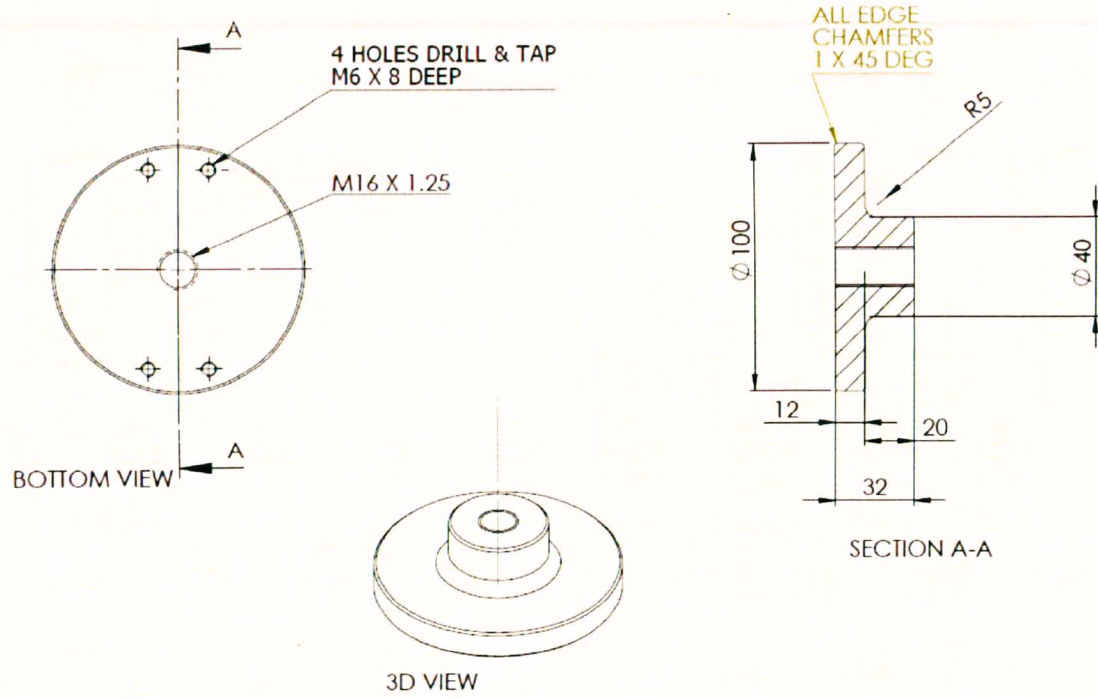
Figure 8-3 The free body diagram shows the forces required to prevent the (mass less) beam falling

As can be seen, the error force is cancelled this way. The value of  $f$  measured at forward and reverse points of cycle = difference/2



Bottom holder is used in conjunction with a bath with holds the lubricant

Top base plate used in conjunction with threaded upper holder



MATERIAL - 316 SS

**NAME** PHIL HYDE

**DATE** 20/04/2010

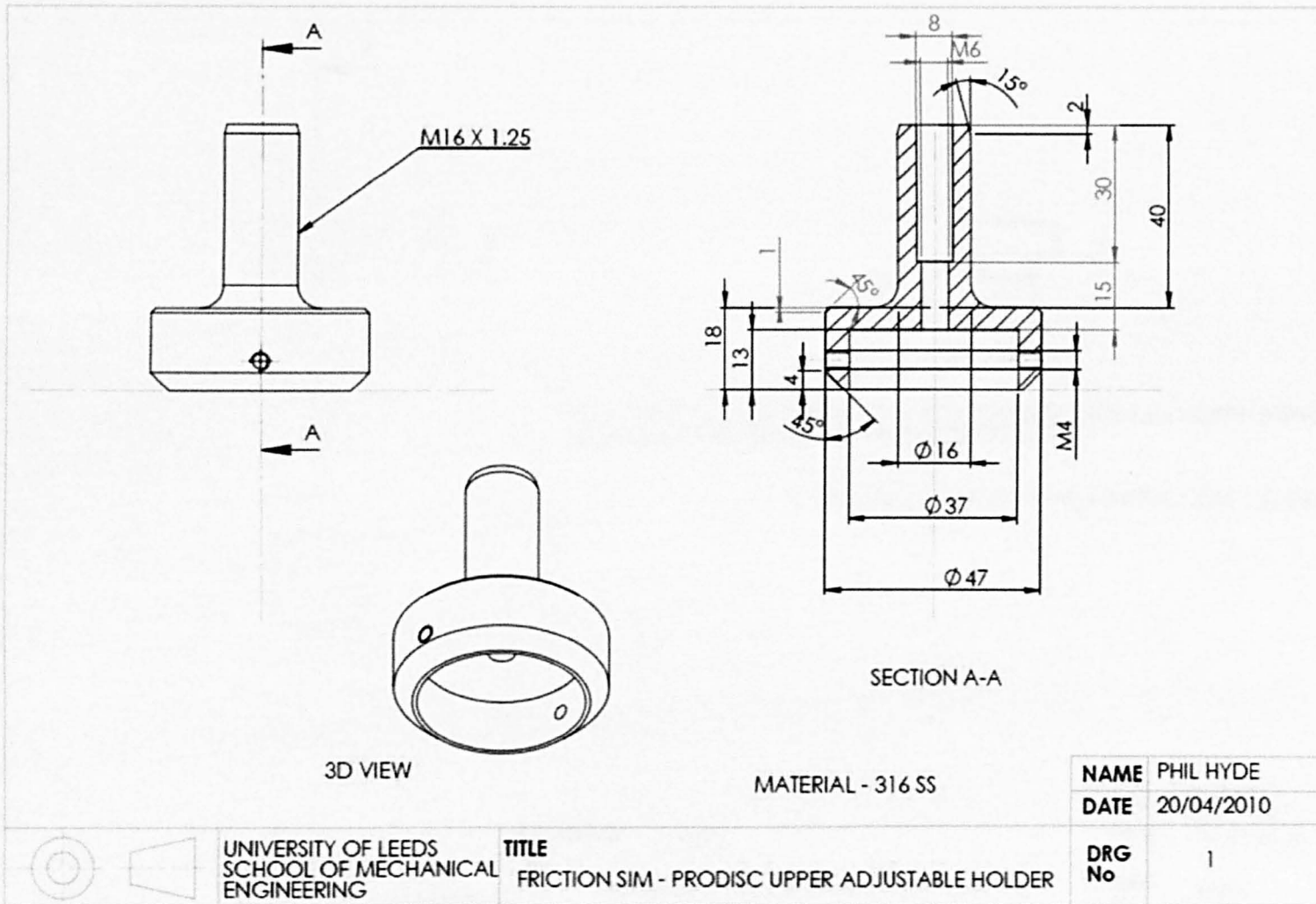


UNIVERSITY OF LEEDS  
SCHOOL OF MECHANICAL  
ENGINEERING

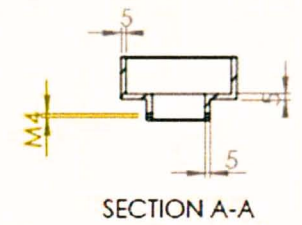
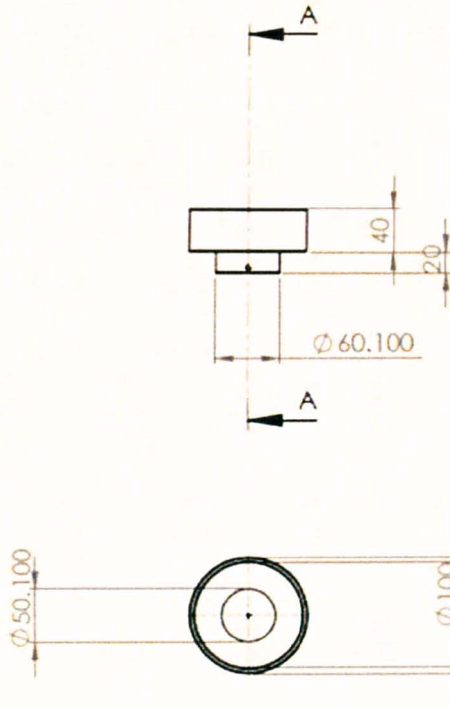
**TITLE**  
FRICTION SIM - UPPER BASE FOR ADJUSTABLE HOLDER

**DRG No** 2

Upper holder is screwed into upper base plate and allows adjustment of CoR





Serum bath fits over bottom holder and is sealed to the sides by use of o rings



NB THIS BATH HOLDS THE SERUM - TO FIT OVER THE BOTTOM COMPONENT OF THE FRICTION SIM SPINAL DISC COMPONENTS

NB - ALL CHAMFERS TO BE APPROX 1 MM / 45 DEG

 	UNIVERSITY OF LEEDS SCHOOL OF MECHANICAL ENGINEERING	<b>MATERIAL</b> Delrin	<b>NAME</b> Phil Hyde
		<b>TITLE</b> Serum bath for spine disc friction sim test	<b>DATE</b> 07 06 2010
			<b>DRG No</b> bath

## Appendix F: MATLAB Code for Lubrication Regime

Note: Several versions of this code were compiled and combined for different bearing material combinations.

```
% To calculate the lubrication regime for MoPE
clear all;
clc;

% Ra1 = 0.0000060;
% Ra2 = 0.000000020;
% Rax = (Ra1^2 + Ra2^2)^0.5 %eqv roughness
for s=1:2;
    if s==1;
        Rax = 0.00000129% shepherd - where he get values from?
        E1 = 210e9; %modulus metal
        E2 = 1e9; %modulus PE
    else if s==2;
        Rax(2) = 0.00000008
        E2 = 210e9; %modulus PE
    end
end

v1 = 0.3; %poisson ratio metal
v2 = 0.4; %poisson ratio PE
Ex = (0.5*((1-v1^2)/E1 + (1-v2^2)/E2))^-1

w = 0:0.2:1.8;

L = 1500;

n = (1.24e-3);

hold on;
for q=1:10;

    clearance = 0.000020: 0.000020: 0.000200; %VECTOR length 10
    R1 = 0.014;
```



```

U = w.*R1/2; %VECTOR
R2 = R1 + clearance(q);
Rx = (1/R1 - 1/R2)^-1;

%fill vector with 1st value of clearance, then repeat for 2nd
3rd etc
for i = 1:10;
    c(i) = clearance(q);
end

%iterated
hmin = 2.789.*Rx.*(n.*U./(Ex.*Rx)).^0.65 .* (L./(Ex.*Rx^2)).^-0.21;

%VECTOR
lambda = hmin./Rax;

plot3(w,c,lambda,'b o'); %VECTOR, iterated, %iterated
% axis ([0 2 0 0.000200 0 2]);
axis tight;
view(-135,30)

end
hold off;

title ('Lubrication regime as a Function of Clearance and Trunc
Velocity');
xlabel('angular vel \omega (rad/s)');
zlabel('lub regime ratio (\lambda)'); [NB bracket changed]
ylabel('clearance (m)');

grid on;
%create a table to display
EntrainingVel_LambdaRatio = [U;lambda]' %NB dash makes list
vertical
end

```